Imperial College London

Department of Mechanical Engineering

Uncertainty Quantification in Nuclear Criticality Modelling Using Methods of Polynomial Chaos

Daniel A F Ayres

August 27, 2015

Supervised by:

Dr Matthew D. Eaton, Prof. Christopher C. Pain and Prof. Kevin Hesketh

EngD Thesis

Declaration

I herewith certify that all material in this dissertation that is not my own work has been properly acknowledged.



Daniel A F Ayres

The copyright of this thesis rests with the author and is made available under a Creative Commons Attribution Non-Commercial No Derivatives licence. Researchers are free to copy, distribute or transmit the thesis on the condition that they attribute it, that they do not use it for commercial purposes and that they do not alter, transform or build upon it. For any reuse or redistribution, researchers must make clear to others the licence terms of this work.

To my girlfriend, Emma,

for all of your love and

support.

Abstract

In this thesis we use polynomial chaos expansions to represent the response of criticality calculations when they are subject to large numbers (many hundreds) of correlated nuclear data uncertainties. An adaptive high dimensional model representation (HDMR) is used to decompose the response parameter k_{eff} into a superposition of lower dimensional subspaces which are in-turn projected on to a polynomial basis. These projections are evaluated using an adaptive quadrature scheme which is used to infer the polynomial orders of the basis. The combination of adaptive HDMR and adaptive quadrature techniques results in a sparse polynomial expansion which has been optimised to represent the variance of the response with the minimum number of polynomials. The combined application of these techniques is illustrated using UOX and MOX pin cell problems with evaluated nuclear covariance data. We show that this approach to calculating the variance in k_{eff} is an order of magnitude more efficient when compared to Latin hypercube sampling with the same number of samples for problems involving up to 988 random dimensions. In the final chapter of this thesis, the adaptive HDMR and quadrature methods combined with polynomial chaos are applied to an industrially relevant problem; the computation of k_{eff} uncertainties due to evaluated covariance data. Uncertainties and first order sensitivities are computed from the polynomial chaos expansion which are compared to the results from the first order sensitivity method imple-

mented in the Monte Carlo code MONK. We found that the local sensitivities and uncertainties derived from the PCE compare well with the MONK sensitivity method. These uncertainty quantification approaches were applied to fast spectrum uranium, plutonium and americium-241 critical assemblies. Comparisons between the uranium/plutonium and americium-241 uncertainties were made in the context of the 0.95 sub-critical limit. Suggestions for new sub-critical limits based on differing numbers of standard deviations below the mean values were proposed.

Acknowledgements

First of all I would like to thank my supervisor Dr. Matthew Eaton. Matt has invested a lot in this project and myself and was always happy to help in any way he could. I would also like to acknowledge the help and support of Prof. M.M.R Williams and Prof. A.K Prinja. Prof. Williams was a constant source of ideas and inspiration during the early years of my project and it was always a pleasure to work with Prof. Prinja when he visited Imperial from the University of New Mexico. I would like to thank the National Nuclear Laboratory for their financial support and, more specifically, I would like to thank Prof. Kevin Hesketh for being my industrial supervisor and Dr. A. Barnes for his help with the americium-241 problems investigated in this thesis.

The last two years of my project were spent with the Answers software team at Winfrith which is a part of Amec Foster Wheeler. I would like to take this opportunity to thank the whole of the Answers team, they have been very welcoming and were always happy to help with any questions I had about their software and the physics and numerics involved. I would now like to single-out some people who have been instrumental in completing the work presented in this thesis. Firstly, and foremost, I would like to thank Mr. Richard Hiles and Dr. Brian Turland, without their help I

would not been have able to achieve as much as I have. I would also like to thank Prof. Paul Smith for inviting me to work at Winfrith, it has been a pleasure working with the Answers team. I would also like to thank Dr. Chris Baker and Dr. Brendan Tollit for answering my questions about the Answers software (on an almost daily basis) and for helping to keep me sane during the writing-up phase of my project.

Finally I would like to extend a huge thank you to my friends and family, particularly my girlfriend, Emma, who has supported me throughout.

Contents

Declaration **i**

Abstract **v**

Acknowledgements **vii**

Contents **ix**

List of Tables **xv**

List of Figures **xxi**

List of Algorithms **xxix**

Glossary **xxxi**

Symbols xxxi

Abbreviations xxxiv

1. Introduction **1**

1.1. Nuclear Data and Covariances 4

1.2. Criticality Calculations 7

1.3. Numerical Methods for Uncertainty Quantification 11

1.3.1. Sampling Methods 13

1.3.1.1. Latin Hypercube Sampling (LHS) 14

1.3.2. Perturbation/Sensitivity Methods 16
1.3.2.1. Direct Numerical Perturbation 19
1.3.2.2. Adjoint Sensitivity Analysis Procedure (ASAP) 20
1.3.2.3. Monte Carlo Sensitivities 22
1.3.3. Polynomial Chaos Methods 23
1.3.3.1. Intrusive Methods 25
1.3.3.2. Non-Intrusive Methods 27
1.4. Summary and Overview of the Thesis 30

2. The Neutron Transport Equation and Uncertain Nuclear Data **33**

2.1. Introduction 33
2.2. The Neutron Transport Equations 34
2.3. Modelling Correlated Nuclear Data 43
2.3.1. The Karhunen Loéve Expansion (KLE) 48
2.4. Transforming to Standard Normal Variables 55
2.5. Summary and Conclusions 60

3. Polynomial Chaos **61**

3.1. Introduction 61
3.2. Theory 62
3.3. Post-Processing 67
3.3.1. Mean, Variance and Covariance 68
3.3.2. Sensitivity Coefficients 69
3.3.3. Probability Density Function 70
3.4. The Stochastic Eigenvalue Problem 70
3.4.1. Solution of the System of Equations 72

3.5. Example: Static and Dynamic Criticality 77
3.5.1. Time Eigenvalues 81
3.5.2. Static Eigenvalues 84
3.5.3. Results 87
3.6. Summary and Conclusions 103

4. Non-Intrusive Spectral Projection (NISP) 107
4.1. Introduction 107
4.2. Theory 108
4.3. Quadrature Methods 110
4.3.1. Uni-variate Rules 111
4.3.2. Tensor Product Quadrature Rules 113
4.3.3. Smolyak Sparse Grids 114
4.3.4. Adaptive Sparse Grids 117
4.3.4.1. Error Measures 119
4.4. Computing Polynomial Chaos Expansions Using Sparse Grid Quadratures 122
4.5. Numerical Examples 124
4.5.1. Test Set 1 124
4.5.2. Test Set 2 126
4.5.3. Test Set 3 129
4.6. Discussion and Conclusions 131

5. High Dimensional Model Representation (HDMR) 133
5.1. Introduction 133
5.2. Theory 134
5.3. Adaptive HDMR 141
5.4. Combining Polynomial Chaos with HDMR 146

5.5. Numerical Examples 148
5.5.1. Verification Tests 149
5.5.1.1. Choice of Cut Point 150
5.5.1.2. Structure of Response Function 150
5.5.1.3. Magnitude of the Uncertainty 152
5.5.1.4. Adaptive HDMR 153
5.5.1.5. Combination with Adaptive Quadrature . . . 155
5.5.1.6. Building a Sparse Polynomial Chaos Expansion 158
5.5.2. Rowlands' Pin Cell Problems 159
5.5.2.1. Nuclear Data Covariances 165
5.5.2.2. HDMR Versus Latin Hypercube Sampling (LHS) 170
5.5.2.3. Log-Normal Versus Gaussian Distributed Uncertainties 179
5.6. Discussion and Conclusions 184

6. Uncertainty Quantification in Nuclear Criticality Assessment of Americium-241 Spheres 187

6.1. Introduction 187
6.1.1. Computing k_{eff} 192
6.1.2. Modelling and Processing Covariance Data 194
6.1.3. Calculating k_{eff} Sensitivities and Uncertainties 199
6.2. The FLATTOP Experiments 202
6.2.1. Sensitivity Studies and Uncertainty Quantification . . 209
6.2.2. Relationship of Uncertainties to the Sub-Critical Limit 219

6.3. Americium 241 222
6.3.1. Critical Mass Calculations 223
6.3.2. Sensitivity Studies and Uncertainty Quantification . . 239
6.4. Comparison of Americium-241 and FLATTOP Problems . . . 255
6.5. Conclusions 259

7. Summary and Conclusions **263**

Bibliography **283**

Appendices **285**

A. Transformations between Log-Normal and Normal Distributions **287**

B. Propagation of input model uncertainties with different marginal distributions using a hybrid polynomial chaos expansion **291**
B.1. Introduction 291
B.2. Theory 292
B.3. Numerical Example 295
B.4. Discussion and Conclusions 300

C. Integration of Functions with Associated Statistical Uncertainties **303**

List of Tables

3.1. Description of the Wiener-Askey or generalised polynomial chaoses. 67
3.2. Cross section and geometry data for the one dimensional slab problem from [1]. 88
3.3. Delayed neutron data, 8-groups. $\beta = 0.007046$. 88
3.4. Summary of execution times for the 1,2 and 3 random variable static and dynamic eigenvalue problems computed using both NKLS and NISP methods. Results are in seconds (s). . 94
3.5. Average values of the w eigenvalue and reactivity, ρ, and their standard deviations as a function of the relative uncertainty, R, in the cross section data. 96
3.6. Mean and variance of the time eigenvalue w and static reactivity, ρ. Results have been calculated using a $p = 15$ PCE with one random dimension. 97
3.7. Mean and variance of the time eigenvalue w and static reactivity, ρ. Results have been calculated using a $p = 15$ PCE with a relative uncertainty $R = 0.01$. 97

5.1. Material compositions for the fuel, clad and coolant regions of the Rowlands' PWR square pin-cell problem. 162
5.2. Isotopic abundance of natural Zirconium. 162

5.3. Hierarchy of Rowlands' pin-cell problems with differing numbers of stochastic dimensions, M. We define: U=^{235}U + ^{238}U, Pu=^{238}Pu + ^{239}Pu + ^{240}Pu + ^{241}Pu + ^{242}Pu. 171

5.4. Mean, variance and relative standard deviation R of k_{eff} for the problems defined in Table (5.3). These are the reference values calculated using 10^6 Latin hypercube samples. 172

5.5. The number of realisations used in the HDMR and LHS calculations presented in Figs. (5.19) and (5.20) for the Rowlands' pin cell problems. 173

6.1. Inferred critical masses for ^{241}Am spheres quoted from [2]. The density of ^{241}Am is taken to be 13.67g/cc. 190

6.2. Geometrical description of the uranium core FLATTOP benchmark, FLATTOP U, and the plutonium core FLATTOP benchmark, FLATTOP Pu. 202

6.3. FLATTOP criticality benchmarks calculated using MONK10A. The differences from critical are quoted in pcm and MONK standard deviations (SD). 204

6.4. Statistics of k_{eff} from the range of MONK calculations for different evaluations in Table (6.3). 205

6.5. FLATTOP k_{eff} calculations using WIMS with 172 and 26 group WIMS nuclear data. The route **HEAD** - **FLURIG** - **PIP** has been used. 206

6.6. Statistics of the WIMS k_{eff} calculations given in Table (6.5). . 207

6.7. Relative uncertainties R(%) in the results of k_{eff} due to ENDF/B-VII.1 and JENDL 4.0 covariance data for the FLATTOP problems. Results are calculated using the MONK sensitivity method, the PCE and its derived first order sensitivities (FOS) are calculated using EVENT. 211

6.8. Statistics of k_{eff} using ENDF/B-VII.1 and JENDL 4.0 covariance data calculated using polynomial chaos. 212

6.9. Contribution of each reaction and nuclide to the total relative uncertainty for the FLATTOP uranium problem using ENDF/B-VII.1 and JENDL 4.0 covariance data. 213

6.10. Probabilities of k_{eff} being below the sub-critical limit,0.95, for the FLATTOP problems using ENDF/B-VII.1 and JENDL 4.0 evaluations. 221

6.11. Difference between the mean value and sub-critical limit of k_{eff} =0.95 in standard deviations for the FLATTOP problems. 222

6.12. Critical radius and critical mass values for bare and water reflected ^{241}Am spheres. 226

6.13. Critical radius and critical mass values for graphite and steel reflected ^{241}Am spheres. 227

6.14. Statistics of the MONK americium-241 critical radius calculations for a range of data evaluations. 228

6.15. WIMS k_{eff} calculations using MONK-calculated critical radii. 228

6.16. Coefficients of the linear fit $r = a(k_{\text{eff}}\text{-}1)+r_c$ where r is the radius, a is the gradient and r_c is the critical radius. 232

6.17. Critical radius and critical mass values for graphite and steel reflected ^{241}Am spheres calculated using WIMS. 233

6.18. Statistics of the WIMS americium-241 critical radius calculations for a range of data evaluations. 234

6.19. Spatial and angular discretisation parameters for the EVENT americium-241 problems. 237

6.20. Statistics of k_{eff} for the americium-241 problems based on the use of covariance data. 240

6.21. Statistics of the critical radius for the americium-241 problems. 244

6.22. Relative uncertainties R(%) in the results of k_{eff} due to JENDL 4.0 covariance data for the ^{241}Am problems. Results are calculated using the MONK sensitivity method, the PCE and its derived first order sensitivities (FOS) are calculated using EVENT. 246

6.23. Relative uncertainties R(%) in the results of k_{eff} due to ENDF/B-VII.1 covariance data for the ^{241}Am problems. Results are calculated using the MONK sensitivity method, the PCE and its derived first order sensitivities (FOS) are calculated using EVENT. 247

6.24. Probabilities of k_{eff} being below the sub-critical limit, k_{eff} =0.95, for the americium-241 problems using ENDF/B-VII.1 and JENDL 4.0 data evaluations. 254

6.25. Difference between the mean value and sub-critical limit of k_{eff} =0.95 in standard deviations for the americium-241 problems. 255

6.26. Sub-critical limits and masses estimated using k_{eff} uncertainties calculated using ENDF/B-VII.1 and JENDL 4.0 covariance data for the americium-241 problems. 259

C.1. Mean and variance in k_∞ of a homogeneous, mono-energetic problem due to uncertainty in the fission cross section. 304

List of Figures

1.1. Representation of response variables subject to arbitrary input data uncertainties. 13

1.2. Examples of Latin Hypercube and conventional sampling procedures in two dimensions. 15

2.1. Example realisation of a cross section. 46

3.1. Number of PC coefficients, N_P, versus dimension, M. 66

3.2. Convergence of the PCE as a function of polynomial order p for 1,2 and 3 stochastic dimensions. 90

3.3. Response of the time eigenvalue, w, to changes in the random variable ξ and reactivity ρ. 91

3.4. Comparison of intrusive NK, NKLS and the reference quadrature solution which is denoted by "Exact". The fundamental time eigenvalue is calculated for a range of relative uncertainties R with one random variable. 93

3.5. PDF of the 9^{th} time eigenvalue with input relative uncertainties of $R = 0.01$ for 1 and 3 random variables. 98

3.6. PDF of the 8^{th} time eigenvalue with input relative uncertainties of $R = 0.01$ for 1 and 3 random variables. 98

3.7. PDF of the 7^{th} time eigenvalue with input relative uncertainties of $R = 0.01$ for 1 and 3 random variables. 99

3.8. PDF of the 6^{th} time eigenvalue with input relative uncertainties of $R = 0.01$ for 1 and 3 random variables. 99

3.9. PDF of the 5^{th} time eigenvalue with input relative uncertainties of $R = 0.01$ for 1 and 3 random variables. 99

3.10. PDF of the 4^{th} time eigenvalue with input relative uncertainties of $R = 0.01$ for 1 and 3 random variables. 100

3.11. PDF of the 3^{rd} time eigenvalue with input relative uncertainties of $R = 0.01$ for 1 and 3 random variables. 100

3.12. PDF of the 2^{nd} time eigenvalue with input relative uncertainties of $R = 0.01$ for 1 and 3 random variables. 100

3.13. PDF of fundamental time eigenvalue with input relative uncertainties of $R = 0.01$ for 1 and 3 random variables. 101

3.14. Probability distribution function for the reactivity ρ. 102

4.1. Hierarchical difference spaces of a level $\mathcal{L}$=4 univariate Newton-Cotes quadrature rule. 114

4.2. Example of a Smolyak [3] sparse grid construction with a level $\mathcal{L} = 3$ Newton-Cotes quadrature. Allowed indices are below the red line. 116

4.3. Example of an adaptive sparse grid procedure showing the active and old index sets. The current index is also shown with the admissible forward neighbours denoted by a forward pointing arrow. 118

4.4. Convergence of the test integrals using sparse grid quadrature schemes for increasing level. 126

4.5. Convergence of the test integrals using adaptive sparse grid quadrature schemes for decreasing adaptive tolerance, δ_{Quad} . 127

4.6. Example of a generalised sparse grid construction for isotropic integrands using Gauss-Patterson and combined Gauss-Patterson and Genz-Keister quadratures. 128

4.7. Example of a generalised sparse grid construction for anisotropic integrands using Gauss-Patterson and combined Gauss-Patterson and Genz-Keister quadratures. 129

4.8. Convergence of the variance calculated using a polynomial chaos expansion built with conventional sparse grid and adaptive sparse grid indices. 132

5.1. Graphical examples of the adaptive HDMR strategies. 145

5.2. Mean value and relative, ϵ, error in the mean versus the cut point c for the first four HDMR orders. A level 5 Gauss-Legendre sparse grid has been used to calculate integrals and a value of $l = 2$ has been used for the structure parameter. . . 151

5.3. Variance and relative error, ϵ, in the variance versus the cut point c for the first four HDMR orders. A level 5 Gauss-Legendre sparse grid has been used to calculate integrals and a value of $l = 2$ has been used for the structure parameter. . . 151

5.4. Relative error versus HDMR order for various values of structure parameter l. A level 5 Gauss-Legendre sparse grid has been used to calculate integrals. 152

5.5. Mean value and relative error in the mean versus the relative standard deviation (σ) of the input parameters for the first four HDMR orders. A level 5 Gauss-Legendre sparse grid has been used to calculate integrals. 152

5.6. Variance and relative error in the variance versus the relative standard deviation (σ) of the input parameters for the first four HDMR orders. A level 5 Gauss-Legendre sparse grid has been used to calculate integrals. 153

5.7. Convergence of the relative error versus the number of realisations, N. 154

5.8. Convergence of the relative error versus the adaptive HDMR threshold, δ_{HDMR}. 155

5.9. Relative error, ϵ, versus the number of realisations, N. Values of $\sigma = 0.1$ and $l = 2.0$ have been used whilst integration has been performed with Gauss-Patterson rules. 156

5.10. Relative error, ϵ, versus the adaptive HDMR tolerance, δ_{HDMR}. Values of $\sigma = 0.1$ and $l = 2.0$ have been used whilst integration has been performed with Gauss-Patterson rules. 157

5.11. Relative error in the variance versus the number of realisations (N). 159

5.12. Relative error in the variance versus the number of polynomials in the PCE (N_P). 160

5.13. Relative error in the variance versus execution time for HDMR and NISP using adaptive quadrature. 160

5.14. Two-dimensional xy geometry of the LWR Rowlands pin-cell problem. 161

5.15. Discretised geometry of the Rowlands' pin-cell problems for EVENT calculations. 163
5.16. Convergence of EVENT calculations for the UOX and MOX Rowlands' pin-cell problems with space and angle. 164
5.17. Correlation matrix C from Eqn.(6.1.2) of ^{235}U for 3, 9 and 26 groups. 170
5.18. Cumulative graph of the eigenspectra of H, ^{239}Pu, ^{240}Pu, ^{235}U and ^{238}U for the covariance matrix defined by Eqn.(6.1.2). There are 26 energy groups for each reaction and $\overline{\nu}$. Only the first 30 eigenvalues have been plotted. 170
5.19. Relative error in the mean versus number of stochastic dimensions M for the problems in Table(5.3) calculated using both HDMR and LHS. 173
5.20. Relative error in the variance versus number of stochastic dimensions M for the problems in Table(5.3) calculated using both HDMR and LHS. 174
5.21. Relative contributions of the variance of each HDMR order ν, the variance of each polynomial order p, the relative number of HDMR terms, the relative number of quadrature points and the relative number of polynomials. 177
5.22. Probability density functions for the problems in Table (5.3) calculated using polynomial chaos and LHS. Adaptive HDMR threshold $\delta_{\text{HDMR}} = 10^{-5}$ and adaptive quadrature threshold, $\delta_{\text{Quad}} = 10^{-5}$. 178
5.23. Relative error versus number of realisations for the UOX_{42} Rowlands' pin-cell problem using Log-Normal and Gaussian distributed uncertainties. 181

5.24. HDMR component and variance ratios for the Rowlands' UOX_{12} problem using Gaussian and Log-Normal nuclear data uncertainties. 183

6.1. Convergence of EVENT-k_{eff} with spatial and angular discretisation for the uranium FLATTOP problems. 207

6.2. Convergence of EVENT-k_{eff} with spatial and angular discretisation for the plutonium FLATTOP problems. 208

6.3. First order sensitivities of k_{eff} to ^{235}U fission and nu-bar for the FLATTOP uranium problem. 216

6.4. First order sensitivities of k_{eff} to ^{239}Pu fission and nu-bar for the FLATTOP plutonium problem. 217

6.5. First order sensitivities of k_{eff} to capture reactions for ^{235}U in the uranium FLATTOP problem and ^{239}Pu in the plutonium FLATTOP problem. 218

6.6. Probability density functions for k_{eff} for the plutonium and uranium FLATTOP experiments calculated using ENDF/B-VII.1 and JENDL 4.0 covariance data. The shaded regions correspond to $\overline{k}_{\text{eff}} \pm$ 1 standard deviation. 220

6.7. Radius versus k_{eff} -1.0 for the un-reflected and water reflected ^{241}Am spheres. 224

6.8. Radius versus -1.0 for the Graphite reflected and Steel reflected ^{241}Am spheres. 224

6.9. Critical mass calculations for the Bare and Water reflected americium-241 spheres using WIMS. 229

6.10. Critical mass calculations for the steel and graphite reflected americium-241 spheres using WIMS. 229

6.11. Calculated versus experimental values for WIMS and MONK critical mass calculations. 235

6.12. Convergence of EVENT calculations for the bare americium-241 sphere. 236

6.13. Convergence of EVENT calculations for the americium-241 sphere with a water reflector. 237

6.14. Convergence of EVENT calculations for the americium-241 sphere with a graphite reflector. 237

6.15. Convergence of EVENT calculations for the americium-241 sphere with a steel reflector. 238

6.16. Probability density functions of the radius for the bare and water reflected ^{241}Am spheres for ENDF/B-VII.1 and JENDL 4.0 data evaluations. A region of $\overline{r}\pm$ 2 standard deviation have been shaded. 242

6.17. Probability density functions of radius for the graphite and steel reflected ^{241}Am spheres for ENDF/B-VII.1 and JENDL 4.0 data evaluations. A region of $\overline{r}\pm$ 2 standard deviation have been shaded. 243

6.18. First order sensitivities of k_{eff} to ^{241}Am capture, fission and nu-bar for the bare americium-241 sphere. 248

6.19. First order sensitivities of k_{eff} to ^{241}Am capture, fission and nu-bar for the water reflected americium-241 sphere. 249

6.20. First order sensitivities of k_{eff} to ^{241}Am capture, fission and nu-bar for the graphite reflected americium-241 sphere. 250

6.21. First order sensitivities of k_{eff} to ^{241}Am capture, fission and nu-bar for the steel reflected americium-241 sphere. 251

6.22. Probability density functions of k_{eff} for the bare and water reflected ^{241}Am spheres for ENDF/B-VII.1 and JENDL 4.0 data evaluations. The mean k_{eff} is high-lighted using a dashed line and the regions defined by $\overline{k}_{\text{eff}} \pm$ 1 standard deviation have been shaded. 252

6.23. Probability density functions of k_{eff} for the graphite and steel reflected ^{241}Am spheres for ENDF/B-VII.1 and JENDL 4.0 data evaluations. The mean k_{eff} is high-lighted using a dashed line and the regions defined by $\overline{k}_{\text{eff}} \pm$ 1 standard deviation have been shaded. 253

B.1. Convergence of the Hermite-Legendre polynomial expansion for relative uncertainties $R = 5\%, 10\%$ and 15%. 298

B.2. Convergence of the Hermite-Hermite and Hermite-Legendre expansions for relative uncertainties $R = 5\%, 10\%$ and 15%. . 301

C.1. Polynomial approximation of a response surface using function evaluations with no statistical uncertainty. 306

C.2. Polynomial chaos representation of a stochastic response surface with standard deviation $\sigma = 1 \times 10^{-2}$ 307

C.3. Polynomial chaos representation of a stochastic response surface with standard deviation $\sigma = 1 \times 10^{-3}$ 308

C.4. Relative error in the parameter variance calculated using stochastic integration points. 309

List of Algorithms

1. Newton-Krylov algorithm for the stochastic eigenvalue problems. Superscript (k) denotes iterative index. 76
2. Newton-Krylov algorithm with the backtracking line-search method. 77
3. Adaptive sparse grid algorithm proposed by Gerstner [4]. . . 121
4. Conventional adaptive HDMR as outlined by Ma [5] and Yang [6]. 144
5. Modified adaptive HDMR algorithm. 147

Glossary

Symbols

- $\mathcal{D}$: Input data parameters.
- p_ξ: Probability density function of the random variable ξ
- P_ξ: Cumulative distribution function of the random variable ξ
- N_G: Number of energy groups
- N_{KL}: Number of terms in the Karhunen Loéve expansion
- Σ: Macroscopic cross section
- σ: Microscopic cross section
- ψ: Angular neutron flux
- d, r, etc.: Lower case symbols are used to represent deterministic variables / realisations of random variables. Bold notation ($\boldsymbol{d}$, $\boldsymbol{r}$, etc.) represents a vector of values.
- D, R, etc.: Upper case symbols are used to represent random variables. Bold notation ($\boldsymbol{D}$, $\boldsymbol{R}$, etc.) represents a vector of values.
- $\mathcal{A}$: Index set of polynomial basis functions.

- δ_{New}: Convergence tolerance for the Newton iteration of the Newton-Krylov solver.
- δ_{Kry}: Convergence tolerance for the Krylov iteration of the Newton-Krylov solver.
- δ_{Quad} : Convergence tolerance for the adaptive quadrature method.
- δ_{HDMR}: Convergence tolerance for the HDMR method.

Abbreviations

- ASAP: adjoint sensitivity analysis procedure
- BINGO: continuous energy nuclear data library used with the MONK code
- CDF: cumulative distribution function
- DICE: discrete energy (multi-group) nuclear data library used with the MONK code
- ENDF: evaluated nuclear data file
- ESA: European Space Agency
- EVENT: even parity neutron transport code
- HDMR: high dimensional model representation
- IID: independent, identically distributed
- JENDL: Japan evaluated nuclear data file
- KL/KLE: Karhunen Loéve /Karhunen Loéve expansion

- LHS: Latin Hypercube sampling
- MCS: Monte Carlo sampling
- MONK: Monte Carlo criticality code
- MOX: mixed oxide
- MT: nuclear reaction identifier in ENDF format
- NISP: non-intrusive spectral projection
- NJOY: Nuclear data processing code
- NK: Newton Krylov
- NKLS: Newton Krylov with line search
- NNL: National Nuclear Laboratory
- PC/PCE: polynomial chaos/polynomial chaos expansion
- pcm: per-cent millie
- PDF: probability density function
- PWR: pressurised water reactor
- RSD(s): relative standard deviation(s)
- RTG: radioisotope thermoelectric generator
- SD(s): standard deviation(s)
- SSFEM: spectral stochastic finite element method
- UOX: Uranium oxide
- UQ: uncertainty quantification

- WIMS: Winfrith improved multigroup scheme

Chapter 1

Introduction

In the past few decades great strides have been made in the development of computational resources for scientific computing particularly in the areas of numerical methods and in the power and availability of computational devices. This has led to an increase in the size of physical problems which may be tackled and the level of precision to which they may be computed. The increased size and fidelity of problems that can be modelled have allowed engineers to simulate physical systems which may be too costly or even impossible to perform during early design stages. However, numerical simulations must be stringently verified and validated against experiment and/or exact results before one may be confident a simulation is yielding useful and reliable information. In fact, the confidence the analyst has in the numerical results is a key aspect when interpreting simulation results.

In reality, all numerical simulations will be subject to error. Quantifying the effect of these errors is crucial if we wish to understand the differences between numerical predictions and the actual system behaviour. The errors which cause the discrepancy in the simulation results can be grouped into three broad categories which have been ordered as a list below.

- **Data:** The mathematical model requires additional data and parameters that describe the physical characteristics of the problem, for

example, the materials involved, the geometry, boundary conditions and initial conditions. In many situations these data will not be exactly specified, e.g. due to limitations in the available experimental data or from some inherent variability due to manufacturing or assembly processes. Use of inexact data values will induce an error in the computed result.

- **Numerical errors:** Mathematical models are solved on computers using numerical methods. The resolution of the numerical method then introduces an error in the predictions since the numerical methods are usually only an approximation to the exact solution. The error due to the numerical discretisation can be reduced, at least in theory, to an arbitrarily low level by increasing the resolution.

- **Model approximations:** Simulations rely on the solution of mathematical models which account for the physical characteristics of the system being studied. These phenomenon may be very complicated and simplifications which facilitate the solution of the model are often used, e.g. a diffusion equation may be used to model the passage of radiation through media which is physically a transport phenomenon. In other situations, physical phenomenon may be neglected if they are deemed to have a negligible effect, for example, the neutron flux within a reactor is assumed to be sufficiently dilute such that neutron-neutron interactions may be ignored. Modelling errors are difficult to quantify but the predictions based upon a simplified model will be accurate if the assumptions are appropriately validated.

In this thesis, we concentrate on the quantification of errors introduced due to the input data, in particular, we are interested in quantifying the ef-

fect that nuclear data uncertainties have on the nuclear criticality coefficient k_{eff} . The criticality coefficient, or k_{eff} , provides a description of the neutron balance of a fissioning nuclear system indicating whether the chain reaction is critical, sub-critical or super-critical. Therefore, uncertainty quantification (UQ) is an important task in criticality problems where optimistic assumptions about data uncertainties could have serious implications for nuclear safety and design. The nuclear data we are interested in here are the average number of neutrons produced per fission, $\overline{\nu}$, and microscopic reaction cross sections, σ_r. The main source of information available about these data comes in the form of a central estimate (or mean value), the uncertainty in the central estimate, represented by its variance, and then correlations between the uncertainties, e.g in different energy groups, or for different reactions, represented by the covariance matrix.

The main focus of this thesis is the investigation of state-of-the-art spectral-based uncertainty quantification methods known as polynomial chaos. Uncertainties represented by polynomial chaos take the form of a polynomial expansion; in this work, methods for optimising this expansion are investigated with the aim of applying them to industrially relevant problems. To test the developed methods, uncertainties in several critical assemblies of americium-241 were studied in the context of criticality safety. Americium-241 is being investigated by the National Nuclear Laboratory (NNL) in a contract awarded by the European Space Agency (ESA) as a potential fuel source for radioisotope thermoelectric generators (RTGs) or, more colloquially, space batteries.. Americium-241 is a fissionable material with very little experimental validation data. In such a situation uncertainty studies may aid in the assessment of sub-critical limits for criticality safety assessments.

1.1. Nuclear Data and Covariances

As we have mentioned, the main focus of this work is quantifying the uncertainty introduced in computed values of k_{eff} due to input nuclear data uncertainties. Firstly, we introduce some of the basic quantities used to describe neutron interactions with nuclei; this will aid in the description of some of the methods introduced later in this chapter. Secondly, we briefly describe the origins of the nuclear data and their uncertainties and explain how they are processed into a form applicable for our applications.

To simulate the behaviour of neutrons within a nuclear reactor we must understand the mechanisms through which they interact with matter. The type and likelihood of a nuclear reaction depends on the energy of the incident neutron, the nuclear structure of the incident nucleus and the temperature of the host material. The probability of a particular reaction with a nucleus at a given energy is described by a microscopic cross section which we denote, for reaction r, by σ_r (which has units of area and is usually given in units of barns (10^{-24} cm^2)). The macroscopic cross section for a reaction r, denoted by Σ_r, of a material is defined as

$$\Sigma_r = \sum_i N_i \sigma_i \tag{1.1.1}$$

where the sum extends over all nuclides present in the material with N_i being the number density of the i^{th} nuclide. The macroscopic cross section has units of inverse length. The probability that a neutron survives a distance x without interaction is given by

$$\exp(-\Sigma_t x) \tag{1.1.2}$$

where the total cross section, Σ_t, is the sum over all reactions r. Likewise, the probability of a neutron, that has survived without any interaction until a distance x, having an interaction r in dx is given by

$$\Sigma_r dx. \tag{1.1.3}$$

Values of microscopic cross sections as a function of energy are generally derived from measurements in experimental facilities all over the world. The data are held in databases such as EXFOR [7]. EXFOR is the exchange format for the transmission of experimental nuclear reaction data between national and international nuclear data centres. The data of interest to the criticality analyst contained in EXFOR is neutron induced reaction data which is in the form of resonance parameters and transmission and capture yields. Before these data may be used by the analyst for the calculation of the effective multiplication factor, it must be approved by a nuclear data centre and processed into an evaluated nuclear data library (ENDL). There are several nuclear data centres including the National Nuclear Data Centre (NNDC) at Brookhaven National Laboratory which is responsible for the Evaluated Nuclear Data File [8] (ENDF), the Nuclear Energy Agency (NEA) which is responsible for the Joint Evaluated Fission and Fusion file [9] (JEFF), the Japan Atomic Energy Agency which is responsible for the Japanese Evaluated Nuclear Data File [10] (JENDL) and others.

The role of the evaluator, in a very broad and simplified sense, is to produce a recommended set of reaction cross sections that comply as closely as possible with available experimental data whilst, at the same time, ac-

curately matching the results of integral benchmark experiments. To this end, measured data are processed by the evaluator using codes such as SAMMY [11] and REFIT [12] which are also supplemented, where appropriate, using nuclear model codes. For a detailed description of the role of the data evaluator see [13] and for the methods they use see [14]. The SAMMY code is capable of producing covariances [15] from EXFOR data for both resonance parameters and cross sections. There is no functionality, as of yet, in REFIT for generating covariances for nuclear data although a statistical sampling procedure has been used in combination with REFIT to produce covariances in the resonance range [16].

Microscopic cross sections for reactor applications can also be predicted using theoretical nuclear model codes such as TALYS [17] and EMPIRE [18]. The TALYS code has been used to generate evaluated nuclear data libraries (ENDL), complete with covariances, called TENDL for applications with criticality and reactor physics [19]. The production of a TENDL is completely automated and begins by assigning default nuclear model parameters or choosing values that give the best global fit to the experimental (EXFOR) data. The nuclear model parameters are assumed to have uncertainties which are obtained either directly from experimental data or by increasing the standard deviation of random TALYS evaluations until the range covers available experimental data for all nuclides. The nominal values and uncertainties can be used to define a probability distribution which is then sampled n times to produce n ENDLs. This ensemble of libraries is then used to produce a nominal TENDL with associated covariances. The TENDL process provides a rigorous approach to producing data for nuclides and reactions where no experimental data exists. A downside to

this approach is that the nuclear models may themselves include modelling error due to a lack of understanding / information about the nuclear forces. For important nuclides and reactions, such as $^{238}\mathrm{U}(n,\gamma)$ (radiative neutron capture), the TENDL results are normalised to experimental data.

The final stage in the nuclear data processing route is to process evaluated data into a format specific to the application physics code. This task is performed using nuclear data processing codes such as NJOY [20], CALENDF [21] and PREPRO [22]. The operations performed by these codes are many and varied and are dependent upon the choice of application physics code. Some common manipulations to the evaluated data include Doppler broadening of the resonances from 0 kelvin (as used by convention in evaluated files) to the temperature of the problem, reduction of the continuous energy data to a discrete form and production of covariance matrices. The production of covariances is performed using the ERROR module of NJOY which is the only processing code out of the three mentioned that is capable of processing evaluated covariance data.

1.2. Criticality Calculations

Criticality is a term used to described the balance of neutrons in a fissioning nuclear system and may be interpreted as the ratio of the production of neutrons due to fission to the loss of neutrons. If these terms are exactly equal, i.e. if the ratio is one, then the system is said to be critical; a ratio less than one and the system is sub-critical and conversely, a ratio of greater than one and the system is super-critical. For any ratio other than one, the system is of course time dependent. To avoid explicitly representing the

time dependence, it is customary in criticality calculations to modify the neutron sources such that the system is in a pseudo equilibrium. The two most commonly used methods are the k_{eff} -eigenvalue method and the w-eigenvalue method.

The k_{eff} method modifies the fission source such that the system is time independent and the w-eigenvalue method adds a pseudo production/absorption term to force balance. Both methods result in an eigenvalue equation. However, the w-eigenvalue is physically more rigorous whereas the k_{eff} method is only accurate at, or very close to, critical. The computational expense and difficulty involved when computing the w-eigenvalue is greater than compared to the k_{eff} -method. It is for this reason and the fact that most criticality calculations will be in a regime where the k_{eff} method is accurate, that the k_{eff} method is used in the criticality community.

There are two main computational techniques for evaluating k_{eff} . These are the deterministic method and the Monte Carlo method. The deterministic approach solves an integro-differential equation, known as the neutron transport equation, which may be written in operator form as follows [23]

$$L\psi = \frac{1}{k_{\text{eff}}} F\psi \tag{1.2.1}$$

here L accounts for the leakage, scatter and transport of neutrons, F accounts for the production of neutrons due to fission and ψ is the neutron flux. A more detailed explanation of this equation will be given in Chapter (2.2). To be amenable to numerical solution, the state space (energy, angle and volume) is discretised using a suitable numerical technique.

For example, the spatial (volume) dependence of the neutron flux may be represented using the finite element [24] or finite difference methods, the angular dependence using a discrete ordinate [25], spherical harmonic or even parity method [26] and the energy dependence using the multi-group method. There are many codes available which compute k_{eff} and ψ using a combination of these approaches, examples of which are RADIANT [27], EVENT [26] and WIMS [28]. The amount of input data these codes require is of course problem dependent but a typical calculation may require 10 nuclear species (nuclides), 6 reactions and an energy resolution of several hundred discrete energy groups. Thus, there may be many thousands of input parameters used in a k_{eff} calculation.

The Monte Carlo method simulates the passage of neutrons through materials determining the type of interactions the neutron experiences from probability laws. Certain characteristics of the neutron population are counted or scored (termed estimators), such as the number of neutrons leaking from the system or the number of fission children produced. A statistical estimate of k_{eff} is then represented as a function of these estimators, for example

$$k_{\text{eff}} \approx f(E_1, \cdots, E_n) \tag{1.2.2}$$

where each E_i is an estimator of some physically relevant score with n being the total number of estimators. Each estimator may be regarded as a sequence of events each having a probability p_i of occurring. The estimator is the expected value of the physical event and may be expressed as the sum of scores from all possible sequences of events multiplied by their

probabilities, namely

$$E = \sum_{\text{all tracks}} p_1 \cdots p_n p_E \tag{1.2.3}$$

where p_E is the probability of the event corresponding to estimator E, for example, the number of fission children produced. For an example of the practical implementation of the Monte Carlo method to neutron transport see [29] and for the mathematical basis of the method see [30]. Examples of the probabilities in Eqn.(1.2.3) are given by Eqns.(1.1.2) and (1.1.3). There are many examples of codes which determine k_{eff} in this manner, some examples are SCALE [31], MCNP [32], MONK [33] and TRIPOLI [34].

There are obvious distinctions between the two approaches described above, each has its benefits depending on the application. The deterministic approach requires a discrete representation of the state space which ultimately requires averaging of the continuous parameter input data. The most significant of these averaging procedures is the energy dependence of the nuclear data, which is also weighted with respect to the averaged neutron flux. This introduces an approximation error in the input data, with the discrete representation of the problem geometry introducing additional error. The Monte Carlo method represents the problem geometry exactly, uses an exact continuous energy representation of the evaluated nuclear data and models the physics of neutron transport exactly. The downside to Monte Carlo simulations is that all response parameters are subject to a statistical uncertainty. For integral parameters this error can be reduced to a reasonable tolerance but for differential results, the number of simulations (or particle histories) may become computationally impractical.

Conversely, the response of a deterministic calculation has no statistical error and a simulation will return the same result each time it is run under the same conditions. The deterministic method simultaneously computes the solution throughout the entirety of the state space making it much better suited to computing differential results.

1.3. Numerical Methods for Uncertainty Quantification

In the following section we describe some of the methods available for calculating the statistics of the response to a mathematical model due to uncertain input data. These include sampling methods, perturbation/sensitivity analysis methods and spectral based (polynomial chaos) methods. As we have mentioned, physical systems may be represented using mathematical models. In this work, we use models which are mappings denoted by $\mathcal{M}$ from $\mathbb{R}^M$ to $\mathbb{R}^Q$, where $M, Q \geq 1$. The model depends upon M input parameters denoted by $\boldsymbol{d} = \{d_1, \cdots, d_M\}$ which represent the nuclear data parameters in this work. Each evaluation of the model $\mathcal{M}(\boldsymbol{d})$ returns Q output quantities $\boldsymbol{r} = \{r_1, \cdots, r_Q\}$ which are the response parameters of the model. The response vector $\boldsymbol{r}$ may represent reactions rates and/or neutron fluxes at points on a finite element mesh for example. In this work we are only concerned with a single response parameter, the criticality coefficient k_{eff} , but we will consider the general case for now for the purpose of illustration. The problem may be stated generally as

$$\mathcal{M}(\boldsymbol{d}, \boldsymbol{r})\psi = 0 \tag{1.3.1}$$

where ψ is the state variable, for example the neutron flux, and $\mathcal{M}$ is an operator which maps the state variable and input parameters to the response vector. To completely define the problem, boundary conditions must also be specified but consideration of these is not necessary for the points discussed below.

Each of the input parameters, $\boldsymbol{d}$, are now assumed to be subject to an uncertainty and are treated as random variables which we denote $\boldsymbol{D} = \{D_1, \cdots, D_M\}$. This leads us to seek the probability law of the response vector $\boldsymbol{R} = \{R_1, \cdots, R_Q\}$ whose elements are now random variables. The polynomial chaos methods, which are the central theme in this thesis, are based on a parametrisation of the uncertain input data using a set of independent random variables (RVs) which we denote $\boldsymbol{\xi} = \{\xi_1, \cdots, \xi_{M'}\}$ where $M' \leq M$. The uncertain input data may be expressed as

$$\boldsymbol{D}(\boldsymbol{\xi}) = \{D_1(\boldsymbol{\xi}), \cdots, D_M(\boldsymbol{\xi})\}. \tag{1.3.2}$$

Because the input data are a function of $\boldsymbol{\xi}$, from (1.3.1), so must the state variable. It also follows that if the state variable is a function of $\boldsymbol{\xi}$ then so will the response $\boldsymbol{R}(\boldsymbol{\xi})$. A point to note is that the random variables $\boldsymbol{\xi}$ do not necessarily have the same probability distribution function as the input data themselves.

A graphical representation of the effect of uncertain input data on a model's responses is shown in Fig.(1.1). Here we can see that if the input data is characterised by a probability densisty function (PDF), then the response variables will also be distributed according to some probability

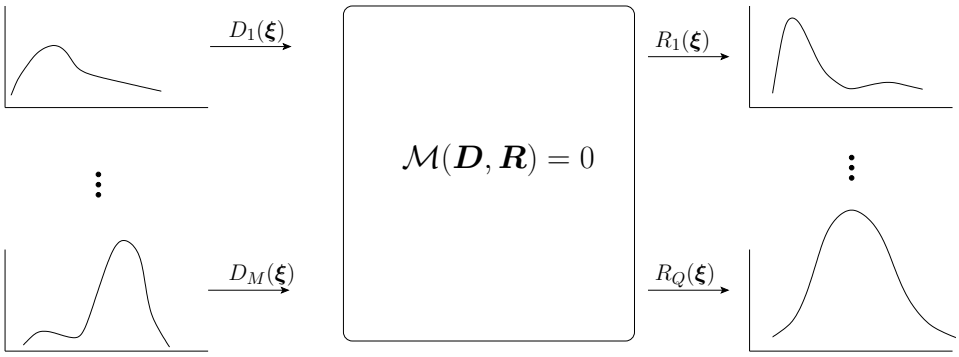


Figure 1.1.: Representation of response variables subject to arbitrary input data uncertainties.

law.

1.3.1. Sampling Methods

Sampling based techniques are probably the most simple approach for calculating the statistical quantities of the response variables. These methods approximate statistical moments through ensemble averages of independent realisations of the deterministic system. This makes the method simple to implement, allows for maximum re-usability of existing code and is straightforward to parallelise. Of all the sampling methods the Monte Carlo sampling (MCS) method [35] is the simplest. The asymptotic numerical error of the Monte Carlo method is approximately

$$\mathcal{O}(N^{-\frac{1}{2}})$$

where N is the number of realisations or samples. The advantage of this approach is that the convergence rate is independent of the number of random dimensions in the problem. The downside, however, is that MCS will require a large number of samples to achieve a good representation of the statistics. With a long execution time for each sample, this method would

be undesirable.

Simple expressions for the mean and variance of the response parameter using the ensemble of samples are as follows:

$$\overline{\boldsymbol{R}} = \frac{1}{N}\sum_{i=1}^{N} \boldsymbol{R}(\boldsymbol{\xi}^i) \tag{1.3.3}$$

$$\mathrm{Var}[\boldsymbol{R}] = \frac{1}{N-1}\sum_{i=1}^{N} \boldsymbol{R}^2(\boldsymbol{\xi}^i) - \overline{\boldsymbol{R}}^2 \tag{1.3.4}$$

here the over line, $\bar{\cdot}$, denotes the sample mean, Var denotes the sample variance and the superscript in $\boldsymbol{\xi}^i$ denotes the i^{th} sample or realisation of the vector of random variables $\boldsymbol{\xi}$. When using the sample mean instead of the true mean, we are underestimating the true variance by the variance of the sample mean. To obtain an unbiased estimator of the variance, the correction $1/N-1$ is applied. The probability density function of the response parameter is approximated using a histogram of the ensemble of samples.

1.3.1.1. Latin Hypercube Sampling (LHS)

An improvement to the basic MCS procedure is the Latin Hypercube sampling (LHS) technique [36]. In this method each dimension is split into d equiprobable intervals forming a vector of possible samples. Each of the M vectors (one vector for each dimension in the response) is then randomly shuffled. Pairing all M vectors then forms a set of equiprobable sampling locations distributed across the M dimensional space. Thus the number of samples, N, is equal to the number of partitions, d. This technique has been extensively used for uncertainty quantification in many fields for several decades. For a thorough review of applications and the history of the

development of LHS see [37].

As an example we consider $M = 2$ dimensions each split into to $d = 4$

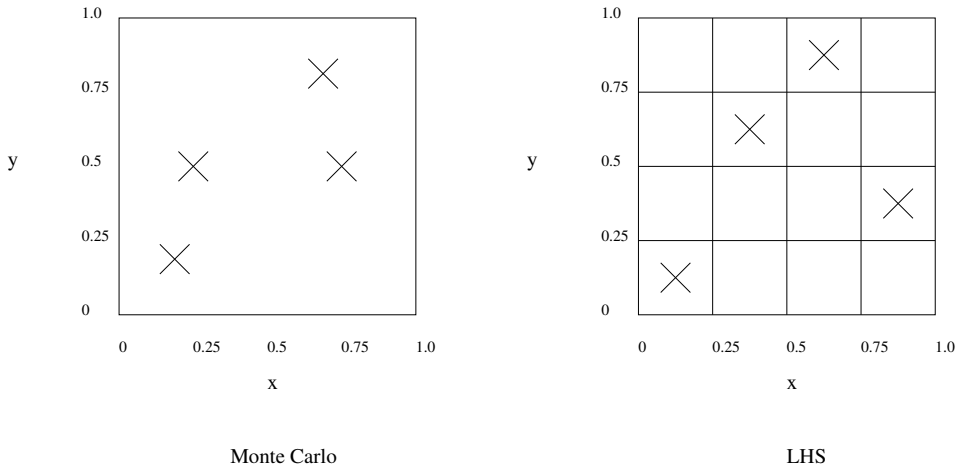


Figure 1.2.: Examples of Latin Hypercube and conventional sampling procedures in two dimensions.

intervals. In Figure (1.2) a two dimensional space is sampled using both MCS and LHS. The example shows that the LHS samples are more evenly distributed across the parameter space as opposed to the MCS which may cluster. The more even distribution of samples obtained when using LHS over MCS results in a faster convergence rate hence reducing the total number of samples required for a given accuracy. (This is particularly true for a small number of samples but will asymptotically produce the MCS results when the number of samples becomes large.) However, unlike MCS, LHS requires all $N = d$ samples otherwise the selection of points in the parameter space will be biased. This is not the case with MCS where any number of samples can be conducted and appended further at any time.

1.3.2. Perturbation/Sensitivity Methods

There are numerous examples of the use of perturbation/sensitivity techniques for reactor physics applications (see [38, 39, 40]) with the decades of research culminating with the implementation in large-scale industrial codes such as SCALE [41]. These methods are also termed "local" sensitivity methods since they analyse system responses locally around a nominal value in the combined phase space of data parameters and state variables. The object of sensitivity analysis is to calculate the sensitivity of the model's response to changes in the model's parameters. In the following we briefly describe three methods for calculating the response sensitivities; two are based upon deterministic perturbations and one is based upon statistical sampling.

Once the response sensitivities have been computed, the uncertainties in the response parameters due to uncertainties in the input parameters may be calculated. The error propagation formula for the perturbation/sensitivity methods is derived from the Taylor expansion of the response vector. If the variation or uncertainty in the response vector, $\boldsymbol{R}$, is thought of as an explicit function of a realisation of the input data, $\boldsymbol{d}$, then we may expand

in a multivariate Taylor expansion as follows:

$$
\begin{aligned}
R(\boldsymbol{d}) \approx R(\boldsymbol{d}^0) &+ \sum_{i_1=1}^{N} \left.\frac{\partial R(\boldsymbol{d})}{\partial d_{i_1}}\right|_{\boldsymbol{d}^0} \Delta d_{i_1} \\
&+ \frac{1}{2!} \sum_{i_1=1}^{N} \sum_{i_2=1}^{N} \left.\frac{\partial^2 R(\boldsymbol{d})}{\partial d_{i_1} \partial d_{i_2}}\right|_{\boldsymbol{d}^0} \Delta d_{i_1} \Delta d_{i_2} \\
&+ \frac{1}{3!} \sum_{i_1=1}^{N} \sum_{i_2=1}^{N} \sum_{i_3=1}^{N} \left.\frac{\partial^3 R(\boldsymbol{d})}{\partial d_{i_1} \partial d_{i_2} \partial d_{i_3}}\right|_{\boldsymbol{d}^0} \Delta d_{i_1} \Delta d_{i_2} \Delta d_{i_3} + \ldots \\
&+ \frac{1}{n!} \sum_{i_1=1}^{N} \ldots \sum_{i_n=1}^{N} \left.\frac{\partial^N R(\boldsymbol{d})}{\partial d_{i_1} \ldots \partial d_{i_n}}\right|_{\boldsymbol{d}^0} \Delta d_{i_1} \ldots \Delta d_{i_n} + \ldots \quad \forall R \in \boldsymbol{R}
\end{aligned}
\tag{1.3.5}
$$

where

$$
\Delta d_i = d_i - d_i^0 \tag{1.3.6}
$$

and $d_i^0 \equiv \overline{D}_i$ is the mean value.

The unknowns in the expansion are the partial derivatives of the response with respect to the input parameters. Once the partial derivatives in (1.3.5), evaluated to a specific order, have been determined, a formula can be used to compute the statistical moments of the response vector $\boldsymbol{R}$. If only the first order derivatives are retained from (1.3.5), namely

$$
R(\boldsymbol{d}) \approx R(\boldsymbol{d}^0) + \sum_{i_1=1}^{N} \left.\frac{\partial R(\boldsymbol{d})}{\partial d_{i_1}}\right|_{\boldsymbol{d}^0} \Delta d_{i_1} \tag{1.3.7}
$$

the statistics of the response vector may be calculated by integrating with respect to $\boldsymbol{d}$ over the probability space of $\boldsymbol{D}$. The covariance of the response

vector may be calculated using the following [39]:

$$\mathrm{Cov}(\boldsymbol{R}, \boldsymbol{R}) = S\,\mathrm{rCov}(\boldsymbol{D}, \boldsymbol{D})S^T \tag{1.3.8}$$

where the superscript "T" denotes transposition and $\mathrm{rCov}(D_i, D_j)$ denotes the relative covariance between the parameters D_i and D_j. The object S is a rectangular matrix of order $M \times Q$ with elements representing the sensitivity of the j^{th} response to the i^{th} input parameter. The sensitivity matrix, S, is given explicitly as

$$S_{ij} = \frac{d_i^0}{R_j(\boldsymbol{d}^0)} \frac{\partial R_j(d_i)}{\partial d_i} \tag{1.3.9}$$

The accuracy of the results obtained from the perturbation method depend on the fidelity of the underlying Taylor expansion. If the response to the input parameters is highly non-linear then many terms in the Taylor expansion may be needed. However, as more high order terms are considered, the approximations to the moments of the response vector become very complicated and usually only terms up to second order are retained [42].

Often the most difficult and costly part of performing a perturbation analysis is the computation of the partial derivatives. As such, much of the research in this field has been devoted to developing techniques for evaluating these derivatives such as adjoint methods [43, 39] and Green's function methods. In what follows, we briefly discuss some of the most commonly used techniques.

1.3.2.1. Direct Numerical Perturbation

The most basic of the sensitivity calculation techniques is the direct perturbation where the sensitivities are represented using a simple difference relation. The process proceeds as follows:

- The response vector is calculated using Eqn. (1.3.1) using nominal or mean values of the input data, $\boldsymbol{d}^0$.

- An element of the input data, d_j, is perturbed, usually by around 1%, and the response function is again calculated using the modified input data.

- The element d_j is returned to its nominal value and the procedure repeats for all elements of $\boldsymbol{d}^0$.

The partial differential of the response vector relative to each element of the input data may be approximated using the following relation

$$\frac{\partial \boldsymbol{R}(\boldsymbol{d}^0)}{\partial d_j} \approx \frac{\boldsymbol{R}(\boldsymbol{d}^0 + \Delta d_j) - \boldsymbol{R}(\boldsymbol{d}^0)}{\Delta d_j} \tag{1.3.10}$$

This approach requires $M + 1$ function evaluations to calculate the sensitivities of the response vector to all M input data parameters. For large M, this obviously becomes computationally prohibitive if the cost of a single model evaluation is high. The approach does allow all Q response parameters to be calculated for each evaluation of the quotient in Eqn. (1.3.10) and the physics code can be treated as a "black box" requiring little if no modification to existing code. This method has been used in conjunction with CASMO-5 [44] to propagate nuclear data uncertainties.

1.3.2.2. Adjoint Sensitivity Analysis Procedure (ASAP)

The motivation behind the ASAP is to derive an expression for the response sensitivities that avoids repeatedly solving the physics model as in Eqn.(1.3.10). A description of this method is most simply achieved through example; consider the neutron transport equation from Eqn.(1.2.1)

$$L_0\psi_0 = \frac{1}{k_0}F_0\psi_0 \tag{1.3.11}$$

where $k_{\text{eff}} \equiv k_0$. The adjoint equation may be written as

$$L_0^\dagger\psi_0^\dagger = \frac{1}{k_0^\dagger}F_0^\dagger\psi_0^\dagger \tag{1.3.12}$$

where $\psi_0^\dagger$ is the adjoint flux which has the physical meaning of "importance" of neutrons in the system, $L_0^\dagger$ and $F_0^\dagger$ are the adjoint operators corresponding to L_0 and F_0 and, according to [23], $k_0 = k_0^\dagger$. The subscript zero e.g. "X_0", corresponds to the unperturbed state i.e. the input data are chosen to be their nominal/mean values. The solution of Eqn. (1.3.12) is independent of the state vector, ψ_0, of the original system and of any perturbations in this state vector. Therefore, the adjoint system can be solved independently of the state vector ψ_0. The general theory for linear and non-linear operators is outlined in [39].

When the input data, $\boldsymbol{d}_0$, is perturbed by an amount $\delta\boldsymbol{d}$, perturbations are induced in the state variables and operators, namely

$$\begin{aligned} \psi &= \psi_0 + \delta\psi \qquad & L &= L_0 + \delta L \\ F &= F_0 + \delta F \qquad & k &= k_0 + \delta_k \end{aligned} \tag{1.3.13}$$

where the perturbations in the operators, δF and δL are due directly to the perturbation in the input data, $\delta \boldsymbol{d}$.

If we insert Eqns.(1.3.13) into (1.2.1) and subtract (1.2.1), after regrouping, we have

$$-\frac{\delta k}{k_0^2} F_0 \psi_0 \approx \left(\delta L - \frac{1}{k_0}\delta F\right)\psi_0 + \left(L_0 - \frac{1}{k_0}F_0\right)\delta\psi \tag{1.3.14}$$

where any δ^2 terms have been ignored. If we multiply (1.3.14) by $\psi^\dagger$ and integrate over the state space (energy, angle and volume), which is denoted by $< \cdot >$, we have

$$-\frac{\delta k}{k_0^2} < \psi_0^\dagger F_0 \psi_0 > \approx \left\langle \psi_0^\dagger \left(\delta L - \frac{1}{k_0}\delta F\right)\psi_0 \right\rangle + \left\langle \psi_0^\dagger \left(L_0 - \frac{1}{k_0}F_0\right)\delta\psi \right\rangle . \tag{1.3.15}$$

The quantity we wish to calculate is the perturbation in k_{eff} , δk. Equation (1.3.14) defines a relationship for δk which is a function of the perturbation in the state variable $\delta\psi$ which will therefore require the solution of (1.2.1) every time the input data is perturbed. Using the following property of adjoint operators

$$\left\langle \psi_0^\dagger \left(L_0 - \frac{1}{k_0}F_0\right)\delta\psi \right\rangle = \left\langle \delta\psi_0 \left(L_0^\dagger - \frac{1}{k_0^\dagger}F_0^\dagger\right)\psi^\dagger \right\rangle , \tag{1.3.16}$$

and noting that from Eqn.(1.3.12) the left hand term in Eqn.(1.3.16) is zero, Eqn.(1.3.15) reduces to the following

$$\frac{\delta k}{k_0^2} = \frac{\left\langle \psi_0^\dagger \left(\frac{1}{k_0}\delta F - \delta L\right)\psi_0 \right\rangle}{< \psi_0^\dagger F_0 \psi_0 >}. \tag{1.3.17}$$

Substituting the perturbation terms with partial derivatives with respect to the input data, $\boldsymbol{d}$, the sensitivity of k_{eff} to the input data may be calculated using the following

$$S_k = \frac{\boldsymbol{d}_0}{k_0}\frac{\partial k}{\partial \boldsymbol{d}} = \frac{k_0 \boldsymbol{d}_0}{\delta \boldsymbol{d}} \frac{\left\langle \psi_0^\dagger \left(\frac{1}{k_0} \left.\frac{\partial F(\boldsymbol{d})}{\partial \boldsymbol{d}}\right|_{\boldsymbol{d}_0} - \left.\frac{\partial L(\boldsymbol{d})}{\partial \boldsymbol{d}}\right|_{\boldsymbol{d}_0} \right) \psi_0 \right\rangle}{\left\langle \psi_0^\dagger F_0 \psi_0 \right\rangle}. \tag{1.3.18}$$

Equation (1.3.18) expresses the sensitivity of k_{eff} in terms of the neutron flux ψ, the adjoint neutron flux $\psi^\dagger$, the unperturbed operator F_0 and differentials of the unperturbed operators L_0 and F_0. Thus, the calculation of S_k only requires two numerical computations, the solution of the neutron flux and its adjoint. The number of numerical computations is independent of the number of input data parameters. However, it does depend upon the number of physical response parameters (e.g. k_{eff}) and this approach becomes inefficient compared with the direct perturbation when the number of response parameters is greater then the number of input parameters.

1.3.2.3. Monte Carlo Sensitivities

A method for estimating the k_{eff} sensitivities in a Monte Carlo calculation, known as differential operator sampling, was devised by Hall [45]. This is the method which is used in the Monte Carlo neutron transport code MONK. In this method, a neutron has a number of "sensitivity weights", one for each variable parameter. These weights are updated during the neutron history and are used to calculate the sensitivities as described below. As we have mentioned in Section (1.2), k_{eff} may be approximated using a function of scored physical quantities or estimators; the sensitivity of k_{eff} is therefore a function of the sensitivities to each estimator. Equation (1.2.3) defines a

generic expression for an estimator E which may be written as

$$E = \sum_{\text{all tracks}} p_E \prod_{j=1}^{n} p_j \tag{1.3.19}$$

where n is the number of interactions preceding the event E. Differentiating Eqn.(1.3.19) with respect to the input data $\boldsymbol{d}$ and multiplying by the factor $\boldsymbol{d}/E$ yields

$$\frac{\boldsymbol{d}}{E}\frac{dE}{d\boldsymbol{d}} = \frac{1}{E}\sum_{\text{all tracks}} \left(\sum_{i=1}^{n} \frac{\boldsymbol{d}}{p_i}\frac{dp_i}{d\boldsymbol{d}} + \frac{\boldsymbol{d}}{p_E}\frac{dp_E}{d\boldsymbol{d}} \right) p_E \prod_{j=1}^{n} p_j \tag{1.3.20}$$

If we now define the sensitivity weight, W, as

$$W = \sum_{i=1}^{n} \frac{\boldsymbol{d}}{p_i}\frac{dp_i}{d\boldsymbol{d}} + \frac{\boldsymbol{d}}{p_E}\frac{dp_E}{d\boldsymbol{d}} \tag{1.3.21}$$

then the sensitivity to the estimator E, S_E, may be written as

$$S_E = \frac{\boldsymbol{d}}{E}\frac{dE}{d\boldsymbol{d}} = \frac{\sum_{\text{all tracks}} W p_E \prod_{j=1}^{n} p_j}{\sum_{\text{all tracks}} p_E \prod_{j=1}^{n} p_j}. \tag{1.3.22}$$

Because the estimators are only a statistical estimate of the actual physical quantity, the sensitivities will also only be a statistical representation of the true sensitivity and will therefore have an associated statistical error.

1.3.3. Polynomial Chaos Methods

An alternative approach to the sampling and perturbation methods are the so-called spectral stochastic expansion techniques. These methods represent the response variables (and/or inputs) in a suitable function space spanned by a polynomial basis [46]. Each of the polynomials, which are known as a polynomial chaos, are orthogonal with respect to the PDF of the input

variables and form a complete set. The response surface is approximated using a truncated expansion of the polynomial chaoses as follows:

$$\boldsymbol{r}(\boldsymbol{\xi}) = \sum_{i=0}^{N_P} r_i \psi(\boldsymbol{\xi}) \tag{1.3.23}$$

where $\boldsymbol{\xi}$ are random variables representing the uncertainty, $N_P + 1$ is the number of polynomials in the expansion, $\psi_i(\boldsymbol{\xi})$ are the polynomial chaoses and r_i are coefficients to be determined.

The methods of polynomial chaos are akin to the spectral methods used in the numerical analysis of partial differential equations. Like their deterministic counterparts, the stochastic spectral methods exhibit exponential convergence with respect to the order of the approximating polynomial basis. However, with respect to the number of polynomials in the expansion, this rate of convergence deteriorates rapidly as the number of dimensions increases. Once the coefficients of the expansion are computed, they may be used to calculate the statistics of the response variables. The maximum number of coefficients in the expansion is a function of the number of dimensions of the response surface, M, and the maximum polynomial order p. Depending upon the manner in which the polynomial expansion is built, the number of coefficients can increase exponentially with M and p. This is known as the "curse of dimensionality" and is illustrated in Figure (3.1) for up to 30 dimensions.

There are many methods for calculating the coefficients in the polynomial chaos expansion (PCE) all of which can be broadly split into two categories: intrusive methods and non-intrusive methods.

1.3.3.1. Intrusive Methods

The intrusive methods are so called because they replace the response variables in the governing equation(s) directly with a PCE requiring a complete reformulation of the system of equations. This approach uses a Galerkin technique to reduce the stochastic problem to a system of coupled equations for the coefficients in the PCE. Early examples of this approach, which is regarded as a discretisation in the stochastic space, were combined with a finite element approach in the spatial domain for structural mechanics problems [47]. This combination is known as the spectral stochastic finite element method (SSFEM) with the general framework described in [48]. SSFEM has been used for a variety of applications including transport in random media, fluid flow and structural mechanics. The method has also seen increased use in the field of neutron transport with application to diffusion problems [49], transport problems [50], linear discontinuous discrete ordinates [1], the method of characteristics[51] and also criticality calculations [51, 52, 53]. Although SSFEM is based upon a sound mathematical framework, the technique may result in a huge increase in the number of degrees of freedom, particularly for large M or p. Further complications can also arise in time dependent problems, non-linear problems, discontinuous problems and also stochastic eigenvalue problems.

In an effort to decrease the computational expense of the intrusive PCE method, adaptive selection of the chaos polynomials has been explored. Some of these methods, including the adaptive wavelet and adaptive multi-element method are described below.

The adaptive wavelet expansion uses, instead of a polynomial basis with

global support, a compact piecewise-smooth polynomial basis which has a local support. Because the response is not yet determined, the adaptive procedure commences with a calculation using an initial coarse basis. This coarse basis is iteratively "enriched" until a required error threshold is met [54, 55]. Both the resolution of the wavelet basis is adapted (h-refinement) and also the polynomial order of each basis function (p-refinement) is adapted. For smooth functions, wavelets are expected to have a slower rate of convergence than global polynomial basis functions since a local basis is only non-zero on a particular interval and therefore requires many functions to represent a function globally. However, one may expect that in a situation where the response shows localised sharp gradients or discontinuities the wavelet expansion may be more efficient than a spectral expansion whose convergence rate may be significantly deteriorated due to Gibbs type phenomena. Here the Gibbs phenomenon refers to the oscillations which are observed when approximating discontinuous functions using a finite series of continuous polynomials. This method has been implemented in [55] and applied to the Lorenz system with three random parameters. The results show that the adaptive wavelet approach accurately captures the random behaviour in the response variable and is more efficient than the corresponding LHS solution. However, the number of terms in the expansion increases rapidly as the resolution and polynomial order increase, faster than the analogous global basis expansion.

In the multi-element approach, the random parameter space is split into a number of subspaces or elements. The solution within each element is then represented using a global PCE [56, 57]. This theory does not need to guarantee the absolute continuity between each element, the solutions in

each can therefore be computed independently of one another. This fact is beneficial when designing methods for parallel computation. However, the number of elements will depend exponentially on the number of random dimensions in the problem. This limitation may be alleviated to some extent by adaptively partitioning the random parameter space. For high dimensional problems which, in an ideal case, may be modelled with very few elements, the number of terms in the PCE will still be dependent on the number of dimensions, M, and will ultimately become impractical for large M.

1.3.3.2. Non-Intrusive Methods

The non-intrusive methods evolved from the effort to couple the fast convergence of the intrusive Galerkin techniques with the decoupled nature of Monte Carlo sampling. The PCE coefficents can be determined using either a projection method known as non-intrusive spectral projection (NISP) [58, 59, 60, 61] or via a regression approach [62, 63, 64, 65].

The use of NISP to compute the PCE expansion coefficients consists of a projection of the response surface on to the multivariate polynomial basis, hence a multidimensional integration is required. This integration can be performed using any method, such as Monte Carlo, but the most common approach in the literature is to use quadrature. This task is non trivial, especially in high dimensions where it is vital to minimise the number of model evaluations for a given approximation error. In [66] the authors used a tensor product of one dimensional Gaussian quadratures to form the multidimensional quadrature rule. Although this approach showed exponential

convergence with polynomial order, the number of model evaluations increases as a power of the number of dimensions. Alternatively a sparse construction of a multidimensional rule from 1D quadratures is possible using the Smolyak algorithm [3]. This approach constructs the multivariate quadrature isotropically, i.e. all dimensions are treated equally. Using this isotropic method, quadrature schemes can be constructed with orders of magnitude fewer model evaluations (up to a logarithmic factor) compared to quadrature on a tensor grid [4, 67]. For the 5 and 11 dimensional problems analysed in [67] the authors showed that sparse grid quadratures consistently outperformed the Monte Carlo approach even when the structure of the response exhibited some anisotropy. However, when a large degree of anisotropy was present, the anisotropic full tensor product quadrature out performed the sparse construction. To address the issue of integrating anisotropic functions, a more general method [68, 69] was developed. This method can further reduce the number of model evaluations by adaptively selecting the important dimensions and producing sparse grids accordingly. In [69] the authors showed that the adaptive anisotropic method outperformed the Monte Carlo method for a range of problems up to 121 random dimensions.

An alternative representation of the stochastic response variables which has recently received attention in the fields of structural/mechanical reliability, chemical systems and finance is the high dimensional model representation (HDMR) [70, 71, 72, 73, 74, 75]. The HDMR method is used to capture high dimensional relationships between input and output model parameters using a hierarchical expansion of increasing dimension. If the cooperative effect of many input parameters upon the output is weak then

the HDMR provides a very efficient representation of the system response allowing the physical model to be captured by an expansion of only low order component functions.

Each component function is calculated via an integration of the response function with the final form of the HDMR expansion determined by the type of integration measure used. There are two commonly used measures, the Lebesgue measure which results in ANOVA-HDMR and the Dirac measure which results in the cut-HDMR expansion. For an M dimensional response function, the ANOVA (ANalysis Of VAriance) method requires the evaluation of an M dimensional integral for each component function which is expensive for even modest values of M. Whereas, the cut-HDMR method evaluates each component function along a cut or plane through the M dimensional space and only requires a multidimensional integration equal to the order of the component function. In other words, a third order cut-HDMR component will require a three dimensional integration.

For some engineering applications [74] it is stated that component functions of order 3 or greater are negligible but this is obviously problem dependent. To tailor the truncation of the HDMR expansion to specific problems, adaptive strategies have been used [6]. The adaptive cut-HDMR expansion has also been used for problems with a discontinuous response function [5] where an adaptive sparse-grid quadrature method was used to compute the HDMR component functions. The adaptive quadrature method used a local hierarchical basis combined with the Smolyak algorithm. The statistical moments were calculated directly from quadrature hence the solution was not projected onto a polynomial chaos basis. The purpose of this work was

to capture discontinuities in the response surface rather than minimising the total number model evaluations. Here the authors were able to solve a fluid flow problem with 500 uncertain input parameters each with a relative uncertainty of 1%. To achieve a 1% L_2 error in the standard deviation of the response variable required 3000 model evaluations. A 0.1% L_2 error in the standard deviation of the response required 10000 model evaluations.

1.4. Summary and Overview of the Thesis

A typical k_{eff} calculation requires many hundreds, if not, thousands of input data parameters resulting in a high dimensional stochastic parameter space for the response. Many of the nuclear data parameters have been measured to a reasonable degree of accuracy, around 2%, but some are still relatively unknown and a large spread in the available data exists.

The random sampling procedures are obviously well suited to this situation since their rate of convergence is independent of the number of dimensions M. However, their rate of convergence can be slow resulting in significant computational effort. The direct numerical perturbation approach will perform poorly for this type of application since the number of samples is directly related to the number of dimensions. The ASAP approach will be very efficient in this situation because there is only a single response parameter, k_{eff} , requiring only a forward and adjoint solution of the problem. The downside, of course, is that modifications to the physics code are required to compute the adjoint which may not always be available for the particular problem. The sensitivity based approaches are of course only valid locally around the nominal point in the response space which may be an insufficient

representation when the input uncertainties are large.

With regard to the polynomial chaos methods described in Section (1.3.3), the main factor prohibiting their implementation is the number of uncertain parameters/dimensions in the problem. This is a direct consequence of the curse of dimensionality mentioned above which causes the number of unknowns (hence computational expense) to increase rapidly with the number of dimensions, M. The number of data parameters for typical k_{eff} problems is expected to be very large presenting a potentially intractable problem for the polynomial chaos methods. To address this issue, an adaptive-HDMR method will be implemented to reduce the effective number of dimensions in the problem or, more specifically, limit the number of high-order interactions in the response variable. To compute the coefficients in the PCE, non-intrusive methods are favoured over intrusive methods for two reasons: Firstly, non-intrusive methods treat the physics code as a "black box" requiring no modification to existing codes and are trivial to parallelise. Secondly, the polynomial coefficients computed using the non-intrusive method are de-coupled which enables the polynomial expansion to be adaptively enriched without re-computing existing coefficients.

In view of the issues described above, the objectives of the following work can be classified as follows: A technique will be developed which utilises a non-intrusive spectral projection (NISP) type approach to calculate the uncertainty on the criticality coefficient k_{eff} due to all appropriate nuclear data uncertainties. The term appropriate here refers to those parameters that are expected to produce the largest sensitivity with respect to k_{eff} . The method should be capable of computing uncertainties to industrially

relevant problems reproducing results computed with existing methodologies and should be competitive with other sampling-based techniques such as Latin Hypercube.

Chapter 2

The Neutron Transport Equation and Uncertain Nuclear Data

2.1. Introduction

In this chapter we present the forms of the neutron transport equation used in the examples of this work along with a probabilistic representation of the input nuclear data. The multi-group forms of the k-eigenvalue and time-eigenvalue neutron transport equations are derived from the continuous energy, time dependent neutron transport equation in Section (2.2). In Section (2.3) a probabilistic representation of the nuclear data is presented along with a derivation of the Karhunen Loéve expansion for a discrete energy random process. In Section (2.4) we define methods for transforming random variables between probability distributions and then derive the special case of transforming correlated Log-Normal random fields to correlated Gaussian random fields.

2.2. The Neutron Transport Equations

In this section we derive two expressions for the time-independent balance of neutrons in a fissioning nuclear system known as the k-eigenvalue/k_{eff} and the w-eigenvalue/time-eigenvalue methods. We start from the time-dependent, integro-differential, form of the neutron transport equation which is written as [76]:

$$\left[\frac{1}{v(E)}\frac{\partial}{\partial t} + \boldsymbol{\Omega}\cdot\nabla + \Sigma_t(\boldsymbol{r},E)\right]\psi(\boldsymbol{r},\boldsymbol{\Omega},E,t) = Q(\boldsymbol{r},\boldsymbol{\Omega},E,t) \tag{2.2.1}$$

where the source density $Q(\boldsymbol{r},\boldsymbol{\Omega},E,t)$ is defined as

$$\begin{aligned} Q(\boldsymbol{r},\boldsymbol{\Omega},E,t) = &\int_0^\infty dE' \int_{4\pi} d\boldsymbol{\Omega}'\Sigma_s(\boldsymbol{r},\boldsymbol{\Omega}'\to\boldsymbol{\Omega},E'\to E)\psi(\boldsymbol{r},\boldsymbol{\Omega}',E',t) \\ &+ \frac{1}{4\pi}\left\{\chi^p(E)\int_0^\infty dE' \int_{4\pi} d\boldsymbol{\Omega}'\overline{\nu}^p(\boldsymbol{r},E')\Sigma_f(\boldsymbol{r},E')\psi(\boldsymbol{r},\boldsymbol{\Omega}',E',t)\right. \\ &\left. + \sum_{i=1}^{N_d}\chi_i^d(E)\lambda_i c_i(\boldsymbol{r},E,t) + q(\boldsymbol{r},\boldsymbol{\Omega},E,t)\right\} \end{aligned} \tag{2.2.2}$$

which describes the production of neutrons per volume, angle, energy and time from fission, scattering, the decay chains of fission products and from any extraneous sources. A further balance equation is required to describe the production rate of neutrons from fission product or "precursor" decays. The set of N_d precursor equations are written as

$$\frac{\partial c_i(\boldsymbol{r},E,t)}{\partial t} = \int_0^\infty dE\overline{\nu}^d(\boldsymbol{r},E)\Sigma_f(\boldsymbol{r},E)\int_{4\pi} d\boldsymbol{\Omega}'\psi(\boldsymbol{r},\boldsymbol{\Omega}',E,t) - \lambda_i c_i(\boldsymbol{r},E,t) \quad i=1,N_d. \tag{2.2.3}$$

The parameters in Eqns. (2.2.1), (2.2.2) and (2.2.3) are defined as follows:

- $v(E)$ is the neutron speed ($\mathrm{cm.s^{-1}}$).
- $\boldsymbol{\Omega}$ is a vector representing the direction of neutron travel.
- $\Sigma_t(\boldsymbol{r}, E)$, $\Sigma_f(\boldsymbol{r}, E')$ are the macroscopic total and fission cross-sections respectively and $\Sigma_s(\boldsymbol{r}, \boldsymbol{\Omega}' \rightarrow \boldsymbol{\Omega}, E' \rightarrow E)$ is the scattering kernel ($\mathrm{cm^{-1}}$).
- $\boldsymbol{r}$ represents the spatial location.
- $\chi^p(E)$ is the prompt fission spectrum. The integral over all energy of the prompt fission spectrum is unity by definition $\int_0^\infty \chi^p(E)\, dE = 1$ which is a physical constraint.
- $\chi_i^d(E)$ is the delayed emission spectrum for neutrons emitted by precursors in group i and subject to the following normalisation: $\int_0^\infty \chi_i^d(E)\, dE = 1$
- λ_i is the radioactive decay constant for precursor group i.
- $\overline{\nu}^p(\boldsymbol{r}, E)$ is the average number of prompt neutrons produced per fission event.
- $\overline{\nu}^d(\boldsymbol{r}, E)$ is the average number of delayed neutrons produced per fission event.
- $\psi(\boldsymbol{r}, \boldsymbol{\Omega}, E, t)$ is the angular neutron flux ($\mathrm{cm^{-3}.eV^{-1}.Sr^{-1}.s^{-1}}$).
- $Q(\boldsymbol{r}, \boldsymbol{\Omega}, E, t)$ is an external source of neutrons ($\mathrm{cm^{-3}.eV^{-1}.Sr^{-1}.s^{-1}}$).

where we have ignored any time dependence of the nuclear data.
In the steady state, the average number of neutrons produced during a fission event will have a component due to prompt neutrons and one due to

delayed neutrons; this may be written as

$$\overline{\nu}(\boldsymbol{r}, E) = \overline{\nu}^p(\boldsymbol{r}, E) + \sum_{i=1}^{N_d} \overline{\nu}_i^d(\boldsymbol{r}, E). \tag{2.2.4}$$

We may also define a similar expression for the steady state fission spectrum; taking into account both prompt and delayed neutrons, this may be written as

$$\chi(E) = \left[1 - \sum_{i=1}^{N_d} \beta_i\right] \chi^p(E) + \sum_{i=1}^{N_d} \beta_i \chi_i^d(E). \tag{2.2.5}$$

The fraction of delayed neutrons for a precursor group i is defined as

$$\beta_i = \frac{\int_0^\infty dE \overline{\nu}_i^d(\boldsymbol{r}, E)\Sigma_f(\boldsymbol{r}, E)\phi(\boldsymbol{r}, E)}{\int_0^\infty dE \overline{\nu}(\boldsymbol{r}, E)\Sigma_f(\boldsymbol{r}, E)\phi(\boldsymbol{r}, E)}. \tag{2.2.6}$$

In isotropic media, the scattering cross section is only a function of the scattering angle, therefore, the scattering kernel may be written as follows

$$\Sigma_s(\boldsymbol{r}, \boldsymbol{\Omega}' \to \boldsymbol{\Omega}, E' \to E, t) = \sum_{l=0}^{L} \frac{2l+1}{4\pi} \Sigma_{s,l}(\boldsymbol{r}, E' \to E) \sum_{m=-l}^{l} R_l^m(\boldsymbol{\Omega}) \phi_l^m(\boldsymbol{r}, E') \tag{2.2.7}$$

where R_l^m are the spherical harmonic functions and the scattering and scalar flux moments, $\Sigma_{s,l}$ and ϕ_l^m, are given by the following:

$$\phi_l^m(\boldsymbol{r}, E, t) = \int_{4\pi} d\boldsymbol{\Omega} R_l^m(\boldsymbol{\Omega}) \psi(\boldsymbol{r}, E, \boldsymbol{\Omega}, t) \tag{2.2.8}$$

$$\Sigma_{s,l}(\boldsymbol{r}, E' \to E) = \int_{-1}^{1} d\mu \Sigma_s(\boldsymbol{r}, E' \to E, \mu) P_l(\mu) \tag{2.2.9}$$

Using Eqns. (2.2.4), (2.2.5), (2.2.6) and (2.2.7), the source density from (2.2.2) may now be written as

$$
\begin{aligned}
Q(\boldsymbol{r},\boldsymbol{\Omega},E,t) = & \int_0^\infty dE' \sum_{l=0}^{L} \frac{2l+1}{4\pi} \Sigma_{s,l}(\boldsymbol{r},E'\to E) \sum_{m=-l}^{l} R_l^m(\boldsymbol{\Omega})\phi_l^m(\boldsymbol{r},E') \\
& + \frac{1}{4\pi}\left\{ \chi^p(E)\left[1-\sum_{l=1}^{N_d}\beta_l\right]\right. \\
& \times \int_0^\infty dE'\overline{\nu}(E')\Sigma_f(\boldsymbol{r},E') \int_{4\pi} d\boldsymbol{\Omega}'\psi(\boldsymbol{r},\boldsymbol{\Omega}',E',t) \\
& \left. + \sum_{i=1}^{N_d} \chi_i^d(E)\lambda_i c_i(\boldsymbol{r},E,t) + q(\boldsymbol{r},\boldsymbol{\Omega},E,t)\right\} \qquad (2.2.10)
\end{aligned}
$$

with the corresponding set of precursor equations

$$
\frac{\partial c_i(\boldsymbol{r},E,t)}{\partial t} = \beta_i \int_0^\infty dE\overline{\nu}(\boldsymbol{r},E)\Sigma_f(\boldsymbol{r},E) \int_{4\pi} d\boldsymbol{\Omega}'\psi(\boldsymbol{r},\boldsymbol{\Omega}',E,t) - \lambda_i c_i(\boldsymbol{r},E,t) \qquad (2.2.11)
$$

The solution of Eqn.(2.2.10) is determined by the geometry of the problem, the composition of the macroscopic cross sections within the geometry and the boundary conditions. The macroscopic cross-sections are a weighted sum of the individual microscopic nuclear cross-sections associated with each isotope composing the host material. The microscopic nuclear cross-sections vary significantly with neutron speed $v(E)$ or kinetic energy (E) and their dependence on (E) is often extremely complicated especially in the resonance energy region. For a generally applicable treatment of energy-dependent neutron transport problems the representation used for the energy variable must be convenient for numerical methods of solution. Such a representation is provided by the multi-group [23] model of the neutron transport equation. This numerical discretisation method for the energy variable E is the one most used in the field of numerical methods

development for neutron transport. Instead of the energy range $E \in [0, \infty]$ used in the exact neutron transport equation the energy range is assumed to be finite $E \in [E_{\min}, E_{\max}]$. The energies $E_{\max}$ and $E_{\min}$ are chosen such that neutrons with energies greater than $E_{\max}$ and less than $E_{\min}$ may be neglected. In the multi-group approach the energy domain $E \in [E_{\min}, E_{\max}]$ is subdivided or partitioned into intervals or energy groups. The multi-group neutron transport equations are obtained by integrating the energy dependent neutron transport equation over each energy group. The group angular flux $\psi_g(\boldsymbol{r}, \boldsymbol{\Omega}, t)$ for the g^{th} group is defined in terms of the angular flux $\psi(\boldsymbol{r}, \boldsymbol{\Omega}, E, t)$ by the following expression:

$$\psi_g(\boldsymbol{r}, \boldsymbol{\Omega}, t) = \int_{E_{g-1}}^{E_g} \psi(\boldsymbol{r}, \boldsymbol{\Omega}, E, t)\, dE \tag{2.2.12}$$

Therefore, integrating the neutron transport equation over the energy range $[E_{g-1}, E_g]$ yields the following equation:

$$\int_{E_{g-1}}^{E_g} \left[\frac{1}{v(E)} \frac{\partial}{\partial t} + \boldsymbol{\Omega} \cdot \nabla + \Sigma_t(\boldsymbol{r}, E) \right] \psi(\boldsymbol{r}, \boldsymbol{\Omega}, E, t)\, dE = \int_{E_{g-1}}^{E_g} Q(\boldsymbol{r}, \boldsymbol{\Omega}, E, t)\, dE \tag{2.2.13}$$

In order to preserve reaction rates within an energy group, the group-averaged cross sections are divided by the energy-averaged flux within each group. For the isotropic fission source, the energy average of the scalar flux is used which is defined as

$$\phi_g(\boldsymbol{r}, t) = \int_{E_{g-1}}^{E_g} dE \phi(\boldsymbol{r}, E, t) \tag{2.2.14}$$

where

$$\phi(\boldsymbol{r}, E, t) = \int_{4\pi} d\boldsymbol{\Omega}\psi(\boldsymbol{r}, \boldsymbol{\Omega}, E, t) \tag{2.2.15}$$

The scattering kernel is weighted with respect to the energy-average angular flux moments

$$\phi_{lg}^{m}(\boldsymbol{r}, t) = \int_{E_{g-1}}^{E_g} dE\phi_{l}^{m}(\boldsymbol{r}, E, t) \tag{2.2.16}$$

The collision term is slightly more complicated. None of the widely used transport methods are designed to treat angular dependence of the total cross section which is what results if one divides by the angular flux. Instead, for the purposes of our discussion, we weight with respect to the scalar flux. We may now define the group averaged total cross-section, the number of prompt neutrons per fission multiplied by the fission cross-section, fission spectrum, differential scattering cross-section, extraneous (external) source and velocity terms as:

$$\Sigma_{tg}(\boldsymbol{r}) = \frac{\int_{E_{g-1}}^{E_g} \Sigma_t(\boldsymbol{r}, E)\phi(\boldsymbol{r}, E, t)\, dE}{\phi_g(\boldsymbol{r}, t)} \tag{2.2.17}$$

$$\overline{\nu}_g\Sigma_{fg}(\boldsymbol{r}) = \frac{\int_{E_{g-1}}^{E_g} \overline{\nu}(E)\Sigma_f(\boldsymbol{r}, E)\phi(\boldsymbol{r}, E, t)\, dE}{\phi_g(\boldsymbol{r}, t)} \tag{2.2.18}$$

$$\frac{1}{v_g} = \frac{\int_{E_{g-1}}^{E_g} \frac{1}{v(E)}\phi(\boldsymbol{r}, \boldsymbol{\Omega}, E, t)\, dE}{\phi_g(\boldsymbol{r}, t)} \tag{2.2.19}$$

$$\Sigma_{sl,h\to g}^{m}(\boldsymbol{r}) = \frac{\int_{E_{g-1}}^{E_g}\int_{E_{h-1}}^{E_h} \Sigma_{sl}(\boldsymbol{r}, E' \to E)\phi_{l}^{m}(\boldsymbol{r}, E', t)\, dE'\, dE}{\phi_{lh}^{m}(\boldsymbol{r})} \tag{2.2.20}$$

$$\chi_g^p = \int_{E_{g-1}}^{E_g} \chi^p(E)\, dE \tag{2.2.21}$$

$$\chi_g^d = \int_{E_{g-1}}^{E_g} \chi^d(E)\, dE \tag{2.2.22}$$

Using Eqns.(2.2.17) to (2.2.22), the multi-group form of the transport equation becomes:

$$\left[\frac{1}{v_g}\frac{\partial}{\partial t} + \mathbf{\Omega}\cdot\nabla + \Sigma_{tg}(\boldsymbol{r})\right]\psi_g(\boldsymbol{r},\mathbf{\Omega},t) = Q_g(\boldsymbol{r},\mathbf{\Omega},t) \quad (g=1,\ldots,G) \tag{2.2.23}$$

where the source and auxillary precursor equations are

$$\begin{aligned} Q_g(\boldsymbol{r},\mathbf{\Omega},t) = &\sum_{h=1}^{G}\sum_{l=0}^{L}\frac{2l+1}{4\pi}\sum_{m=-l}^{l}\Sigma^m_{s,l,h\to g}(\boldsymbol{r})R^m_l(\mathbf{\Omega})\phi^m_{l,h}(\boldsymbol{r}) \\ &+ \frac{1}{4\pi}\left\{\chi^p_g\left[1-\sum_{l=1}^{N_d}\beta_l\right]\sum_{h=1}^{G}\overline{\nu}_h\Sigma_{f,h}(\boldsymbol{r})\phi_h(\boldsymbol{r},t)\right. \\ &\left.+\sum_{l=1}^{N_d}\chi^d_{l,g}\lambda_l c_l(\boldsymbol{r},t) + q_g(\boldsymbol{r},\mathbf{\Omega},t)\right\} \end{aligned} \tag{2.2.24}$$

and

$$\frac{\partial c_i(\boldsymbol{r},t)}{\partial t} = \beta_i\sum_{h=1}^{G}\overline{\nu}_h(\boldsymbol{r})\Sigma_{f,h}(\boldsymbol{r})\int_{4\pi}d\mathbf{\Omega}'\psi_h(\boldsymbol{r},\mathbf{\Omega}',t) - \lambda_i c_i(\boldsymbol{r},t) \quad i=1,N_d. \tag{2.2.25}$$

As we can see, the group averaged input cross sections depend upon the output angular flux. In other words, the group averaged cross sections depend upon how the angular flux varies within each group. Usually the approach within the deterministic case is that a simulation has been performed in a large number of groups in a simplified geometry to determine an "approximated" flux to average the input variables over energy. This takes account of complex issues such as resonance self-shielding effects in the resonance region.

At this point, Eqns. (2.2.23) and (2.2.25) describe the explicit time dependence of the neutron and precursor density within a fissioning system. Computing the solution to this time dependent problem would enable the analyst to assess the balance of neutrons and hence determine the criticality of the system. A more convenient approach to assessing whether the neutron population is sub or super critical is to use either the k-eigenvalue or w-eigenvalue methods. We start by defining the w-eigenvalue method where it is assumed that the solutions of Eqns, (2.2.23) and (2.2.25) have the following form

$$\psi_h(\boldsymbol{r},\boldsymbol{\Omega},t) = \psi_h(\boldsymbol{r},\boldsymbol{\Omega})\exp(wt) \quad \text{and} \quad c_i(\boldsymbol{r},t) = c_i(\boldsymbol{r})\exp(wt). \tag{2.2.26}$$

Inserting Eqn.(2.2.26) into (2.2.23) and (2.2.25) yields

$$\left[\frac{w}{v_g} + \boldsymbol{\Omega}\cdot\nabla + \Sigma_{tg}(\boldsymbol{r})\right]\psi_g(\boldsymbol{r},\boldsymbol{\Omega}) = Q_g(\boldsymbol{r},\boldsymbol{\Omega}) \quad (g = 1,\ldots,G) \tag{2.2.27}$$

and

$$wc_i(\boldsymbol{r}) = \beta_i \sum_{h=1}^{G} \overline{\nu}_h(\boldsymbol{r})\Sigma_{f,h}(\boldsymbol{r}) \int_{4\pi} d\boldsymbol{\Omega}'\psi_h(\boldsymbol{r},\boldsymbol{\Omega}') - \lambda_i c_i(\boldsymbol{r}) \quad i = 1, N_d. \tag{2.2.28}$$

The source density, $Q_g(\boldsymbol{r},\boldsymbol{\Omega})$, has the same form as (2.2.24) except for the omission of the time dependence of the the neutron flux.

For the application we present in Chapter (3), it is more convenient to reduce the transport equation to a first order approximation known as the diffusion approximation. In this situation, we know that the angular neutron

flux may be represented using a P1 approximation [77] which is written as

$$\psi_g(\boldsymbol{r},\boldsymbol{\Omega}) = \frac{1}{4\pi}\psi_g^0(\boldsymbol{r}) + \frac{3}{4\pi}\boldsymbol{\Omega}\cdot\psi_g^1(\boldsymbol{r}) \tag{2.2.29}$$

where ψ^0 and ψ^1 are the isotropic and linearly anisotropic neutron angular fluxes respectively. Now, assuming that the source density is isotropic in angle, namely

$$\begin{aligned} Q_g(\boldsymbol{r}) = &\sum_{h=1}^{G}\Sigma_{s,0,h\to g}(\boldsymbol{r})\psi_h^0(\boldsymbol{r}) + \chi_g^p\left[1-\sum_{l=1}^{N_d}\beta_l\right]\sum_{h=1}^{G}\overline{\nu}_h\Sigma_{f,h}(\boldsymbol{r})\psi_h^0 \\ &+\sum_{l=1}^{N_d}\chi_{l,g}^d\lambda_l c_l(\boldsymbol{r}) + q_g(\boldsymbol{r}) \end{aligned} \tag{2.2.30}$$

we may insert Eqn.(2.2.29) into Eqns. (2.2.27) and (2.2.28) to yield

$$\left[\frac{w}{v_g} - \nabla\cdot D_g(\boldsymbol{r})\nabla + \Sigma_t(\boldsymbol{r})\right]\psi_g^0(\boldsymbol{r}) = Q_g(\boldsymbol{r}) \tag{2.2.31}$$

and

$$wc_i(\boldsymbol{r}) = \beta_i\sum_{h=1}^{G}\overline{\nu}_h(\boldsymbol{r})\Sigma_{f,h}(\boldsymbol{r})\psi_h^0(\boldsymbol{r}) - \lambda_i c_i(\boldsymbol{r}). \tag{2.2.32}$$

where D_g is the diffusion coefficient in energy group g.

A complementary method of defining sub- or super-criticality is via the effective multiplication factor k_{eff} . In this instance, the transport equation

for a system with the same properties as the time dependent one is written

$$[\boldsymbol{\Omega}\cdot\nabla+\Sigma_{tg}(\boldsymbol{r})]\,\psi_g(\boldsymbol{r},\boldsymbol{\Omega})=\sum_{h=1}^{G}\sum_{l=0}^{L}\frac{2l+1}{4\pi}\Sigma_{s,l,h\to g}(\boldsymbol{r})\sum_{m=-l}^{l}R_l^m(\boldsymbol{\Omega})\phi_{l,h}^m(\boldsymbol{r})$$
$$+\frac{\chi_g}{4\pi k_{\text{eff}}}\sum_{h=1}^{G}\int_{4\pi}d\boldsymbol{\Omega}'\overline{\nu}_h\Sigma_{fh}(\boldsymbol{r})\psi_h(\boldsymbol{r},\boldsymbol{\Omega}')+q_g(\boldsymbol{r},\boldsymbol{\Omega})\qquad(g=1,\ldots,N_G)\tag{2.2.33}$$

The term k_{eff} is the effective multiplication coefficient. This term artificially alters the source of fission neutrons to ensure the system is in a steady state. The effective multiplication factor is therefore a measure of the degree of criticality but only yields accurate results when the system is close to critical [78].

Again, for the applications we present in Chapter (3), it is more convenient to reduce the transport equation in (2.2.33) to a diffusion equation. All source terms are isotropic in angle and the angular flux is represented using the P1 approximation from Eqn.(2.2.29). Using these simplifications, the transport equation given by Eqn.(2.2.33) reduces to

$$-\nabla\cdot D_g(\boldsymbol{r})\nabla\psi_g^0(\boldsymbol{r})+\Sigma_{tg}\psi_g^0(\boldsymbol{r})=\sum_{h=1}^{G}\Sigma_{s,0,h\to g}(\boldsymbol{r})\psi_h^0(\boldsymbol{r})$$
$$+\frac{\chi_g}{k_{\text{eff}}}\sum_{h=1}^{G}\overline{\nu}_h\Sigma_{fh}\psi_h^0(\boldsymbol{r})+q_g(\boldsymbol{r})\qquad(g=1,\ldots,N_G)\tag{2.2.34}$$

2.3. Modelling Correlated Nuclear Data

From the neutron transport equation in (2.2.1), we can see that the macroscopic nuclear data (cross sections and $\overline{\nu}$) are a function of energy, time, space and, in the special case of scattering, angle. Microscopic nuclear data

are solely a function of energy and, in the case of scattering cross sections, angle. The time and space dependencies in the macroscopic cross sections are introduced via the number density of each nuclide present in the material. In this work we will only be considering uncertainties in the energy variable which we will model using the notion of a random field.

For all of the problems considered in this work, the energy dependence of all input and output model parameters are represented using the multi-group method. From the definition of the multi-group nuclear data in Eqns.(2.2.17) to (2.2.22), we can see that they are piece-wise continuous functions of energy, i.e. they are represented using averaged values over discrete, non-overlapping energy regions. From physical arguments, all values of energy are positive and real valued which we index by the piece-wise continuous variable $\boldsymbol{E} \in \Gamma$ where Γ is a subset of the positive real line, $\Gamma \subseteq \mathbb{R}^+$. For example, the domain of allowed energies is defined as $\boldsymbol{E} = \{E; E_g > E \geq E_{g-1}; g = 1, N_G\}$ where N_G is the total number of energy groups, $E_0 = E_{\min}$ and $E_{N_G} = E_{\max}$.

The uncertainties in the input nuclear data are represented parametrically using a set of independent, identically distributed (IID) random variables $\boldsymbol{\xi} = \{\xi, \cdots, \xi_M\}$ where M is the total number of data parameters. As we have discussed previously, each datum (cross section or $\overline{\nu}$ etc.) is itself a random variable. There may also exist a linear dependence between the uncertainties of any two input data, (known as a correlation) meaning each datum will be a function of some or all of the set $\boldsymbol{\xi}$.

We now define the uncertain input nuclear data as a function of energy,

which we denote by $\boldsymbol{\mathcal{D}}(\boldsymbol{E}, \boldsymbol{\xi}(\theta))$, on a probability space denoted by $(\Theta, \mathcal{B}, P)$. Here Θ is the set of all possible outcomes (called the sample space), θ is a random event belonging to Θ and $\mathcal{B}$ is the closure of countable unions of subsets of Θ and is called a sigma-field on Θ. The symbol P is a finite probability measure on $\mathcal{B}$ and is a function that maps $\mathcal{B}$ onto the real space $[0, 1]$. The random field $\boldsymbol{\mathcal{D}}(\boldsymbol{E}, \boldsymbol{\xi}(\theta))$ corresponds to any of the input nuclear data be it cross sections or nu-bar. The random field can be thought of as a set of correlated random variables, $\boldsymbol{\mathcal{D}}(\boldsymbol{E}, \boldsymbol{\xi}(\theta)) = \{\mathcal{D}_g; g = 1, \cdots N_G\}$ where $\mathcal{D}_g = \boldsymbol{\mathcal{D}}(E_g, \boldsymbol{\xi}(\theta))$ is a random variable, representing the uncertainty in each energy group g.

For a fixed event θ, the function $\boldsymbol{\mathcal{D}}(\cdot, \boldsymbol{\xi}(\theta))$ is called a realization of the random process. The inner product over the space Γ is defined as

$$\langle A, B \rangle = \sum_{E_i \in \boldsymbol{E}} A(E_i) B(E_i) \quad \forall \boldsymbol{E} \in \Gamma \tag{2.3.1}$$

and we assume that the square root of the inner product (L_2 norm) of all functions in the space Γ are finite. This means that Γ is a Hilbert space which will be important in Section (2.3.1) when deriving the Karhunen Loéve representation of $\boldsymbol{\mathcal{D}}$. Corollary to the above, for any fixed value $\boldsymbol{E} \in \Gamma$, the function $\boldsymbol{\mathcal{D}}(\boldsymbol{E}; \cdot)$ is a random variable. The inner product over the space Θ is defined as

$$\begin{aligned} \langle A, B \rangle &= \int_{\Theta} A(\boldsymbol{\xi}(\theta)) B(\boldsymbol{\xi}(\theta)) dP(\theta) \quad \forall A, B \in L_2(\Theta, P) \\ &= \prod_{i=1}^{M} \int_{\Theta} A(\xi_i) B(\xi_i) p_{\xi}(\xi_i) d\xi_i \\ &= \mathbb{E}\left[A(\boldsymbol{\xi}) B(\boldsymbol{\xi})\right] \end{aligned} \tag{2.3.2}$$

where $\mathbb{E}[\cdot]$ is the mathematical expectation and $p_\xi(\xi)$ is the probability density function (PDF) of the random variable ξ. We assume that all random variables, $\boldsymbol{\mathcal{D}}(\boldsymbol{E};\cdot)$, are in the Hilbert space $L_2(\Theta,\mathcal{B},P)$ which implies that all uncertain data parameters for each energy group have a finite variance. An example realisation of an arbitrary cross section is given in Fig.(2.1).

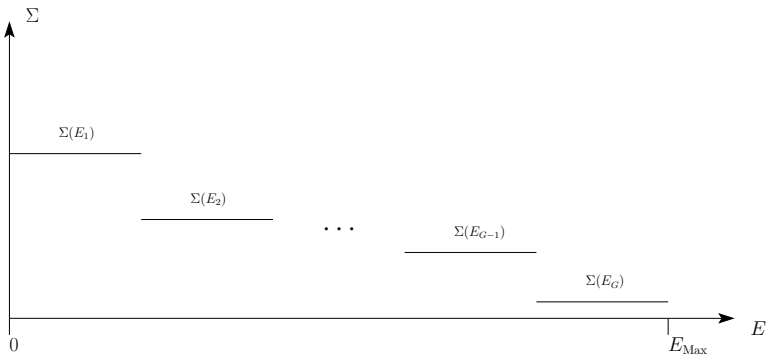


Figure 2.1.: Example realisation of a cross section.

The mathematical expectation which was denoted by $\mathbb{E}[\cdot]$ yields the following expression for the mean value of the random process $\boldsymbol{\mathcal{D}}(\boldsymbol{E};\boldsymbol{\xi})$:

$$\begin{aligned}\mathbb{E}\left[\boldsymbol{\mathcal{D}}(\boldsymbol{E};\boldsymbol{\xi})\right] &= \int_\Theta \boldsymbol{\mathcal{D}}(\boldsymbol{E};\boldsymbol{\xi}) p_{\boldsymbol{\xi}}(\boldsymbol{\xi})\, d\boldsymbol{\xi} \\ &= \overline{\boldsymbol{\mathcal{D}}}(\boldsymbol{E}) \end{aligned} \tag{2.3.3}$$

The autocorrelation function of the random process $\boldsymbol{\mathcal{D}}(\boldsymbol{E};\cdot)$ which is denoted as $C_{\boldsymbol{\mathcal{D}}\boldsymbol{\mathcal{D}}}$ is defined as:

$$C_{\boldsymbol{\mathcal{D}}\boldsymbol{\mathcal{D}}}(E_g,E_h) = \mathbb{E}\left[\boldsymbol{\mathcal{D}}(E_g;\cdot)\boldsymbol{\mathcal{D}}(E_h;\cdot)\right] \quad \forall E_g,E_h \in \boldsymbol{E} \tag{2.3.4}$$

The closely related covariance function is defined as:

$$\mathrm{Cov}_{\boldsymbol{\mathcal{D}}\boldsymbol{\mathcal{D}}}(E_g, E_h) = \mathbb{E}\left[\boldsymbol{\mathcal{D}}(E_g;\boldsymbol{\xi}) - \mathbb{E}\left[\boldsymbol{\mathcal{D}}(E_g;\boldsymbol{\xi})\right]\right]\mathbb{E}\left[\boldsymbol{\mathcal{D}}(E_h;\boldsymbol{\xi}) - \mathbb{E}\left[\boldsymbol{\mathcal{D}}(E_h;\boldsymbol{\xi})\right]\right] \tag{2.3.5}$$

which can be re-written as:

$$\begin{aligned}\mathrm{Cov}_{\boldsymbol{\mathcal{D}}\boldsymbol{\mathcal{D}}}(E_g, E_h) &= \mathbb{E}\left[\boldsymbol{\mathcal{D}}(E_g;\boldsymbol{\xi})\boldsymbol{\mathcal{D}}(E_h;\boldsymbol{\xi})\right] - \mathbb{E}\left[\boldsymbol{\mathcal{D}}(E_g;\boldsymbol{\xi})\right]\mathbb{E}\left[\boldsymbol{\mathcal{D}}(E_h;\boldsymbol{\xi})\right] \\ &= C_{\boldsymbol{\mathcal{D}}\boldsymbol{\mathcal{D}}}(E_g, E_h) - \overline{\boldsymbol{\mathcal{D}}}(E_g)\overline{\boldsymbol{\mathcal{D}}}(E_h).\end{aligned} \tag{2.3.6}$$

Another useful quantity is the relative covariance which is defined as

$$\mathrm{rCov}_{\boldsymbol{\mathcal{D}}\boldsymbol{\mathcal{D}}}(E_g, E_h) = \frac{\mathrm{Cov}_{\boldsymbol{\mathcal{D}}\boldsymbol{\mathcal{D}}}(E_g, E_h)}{\overline{\boldsymbol{\mathcal{D}}}(E_g)\overline{\boldsymbol{\mathcal{D}}}(E_h)}. \tag{2.3.7}$$

When $E_h = E_g$ the variance of a random process is given by

$$\mathrm{Var}_{\boldsymbol{\mathcal{D}}}(E_g) = \mathrm{Cov}_{\boldsymbol{\mathcal{D}}\boldsymbol{\mathcal{D}}}(E_g, E_g) = C_{\boldsymbol{\mathcal{D}}\boldsymbol{\mathcal{D}}}(E_g, E_g) - \overline{\boldsymbol{\mathcal{D}}}(E_g)\overline{\boldsymbol{\mathcal{D}}}(E_g) \tag{2.3.8}$$

Dividing the covariance function by $\sqrt{\mathrm{Var}(E_g)}$ and $\sqrt{\mathrm{Var}(E_h)}$ yields the dimensionless coefficient of correlation between E_g and E_h

$$\rho_{\boldsymbol{\mathcal{D}}\boldsymbol{\mathcal{D}}}(E_g, E_h) = \frac{\mathrm{Cov}_{\boldsymbol{\mathcal{D}}\boldsymbol{\mathcal{D}}}(E_g, E_h)}{\sqrt{\mathrm{Var}(E_g)}\sqrt{\mathrm{Var}(E_h)}} \tag{2.3.9}$$

The coefficient of correlation measures the degree of linear dependence between the standard deviations of two random variables.

As well as being symmetric, the covariance matrix has the following properties:

- It has real eigenvalues λ_i

- The eigenvalues λ_i are non-negative and can be arranged in decreasing order $\lambda_1 \geq \lambda_2 \geq \ldots \to 0$
- The eigenvalues are countable and are such that $\sum_{j\geq 1} \lambda_j^2 < +\infty$
- For each eigenvalue there exists a finite number of linearly independent eigenvectors
- The collection of eigenvectors $\{\varphi_i,\ i \geq 1\}$ constitutes an orthogonal basis of the Hilbert space $H = L_2(\Gamma)$. Furthermore, the eigenvectors may be normalized so that $(\varphi_i, \varphi_j) = \delta_{ij}$.

The covariance matrix also admits the following spectral decomposition which is known as Mercer's theorem:

$$\mathrm{Cov}_{\boldsymbol{\mathcal{D}}\boldsymbol{\mathcal{D}}}(E_g, E_h) = \sum_{i\geq 1} \lambda_i \varphi_i(E_g)\varphi_j(E_h) \tag{2.3.10}$$

where λ and φ are the eigenvalues and eigenvectors respectively.

The above equations describe some integral properties of the random variables in a second-order random field such as mean, variance and covariance. To simulate such a random field, we require a parametric representation in terms of IID random variables which produces realisations with exactly the same statistics as the original random field. This can be achieved using the Karhunen Loéve expansion which is described in the next section.

2.3.1. The Karhunen Loéve Expansion (KLE)

In this section we derive a method for parametrically representing a second order random process in terms of a linear sum of Gaussian variables. For the proceeding discussion it is assumed that $\boldsymbol{\mathcal{D}}(\boldsymbol{E};\boldsymbol{\xi})$ is a centred random

process which is defined as a process where the mean or expectation value is zero:

$$\mathbb{E}\left[\boldsymbol{\mathcal{D}}(\boldsymbol{E};\boldsymbol{\xi})\right] = \int_{\Theta} \boldsymbol{\mathcal{D}}(\boldsymbol{E};\boldsymbol{\xi}) p_{\boldsymbol{\xi}}(\boldsymbol{\xi})\, d\boldsymbol{\xi} = 0. \tag{2.3.11}$$

If a random process $\boldsymbol{\mathcal{D}}'(\boldsymbol{E};\boldsymbol{\xi})$ is not a centred random process it can be written as a sum of a centred random process $\boldsymbol{\mathcal{D}}(\boldsymbol{E};\boldsymbol{\xi})$ and the expectation value of the original random process $\boldsymbol{\mathcal{D}}'(\boldsymbol{E};\boldsymbol{\xi})$:

$$\boldsymbol{\mathcal{D}}'(\boldsymbol{E};\boldsymbol{\xi}) = \overline{\boldsymbol{\mathcal{D}}'}(\boldsymbol{E}) + \boldsymbol{\mathcal{D}}(\boldsymbol{E};\boldsymbol{\xi}) \tag{2.3.12}$$

where $\boldsymbol{\mathcal{D}}(\boldsymbol{E};\boldsymbol{\xi})$ is a centred random process and $\overline{\boldsymbol{\mathcal{D}}'}(\boldsymbol{E})$ is the expectation or mean value of the non-centred random process $\boldsymbol{\mathcal{D}}'(\boldsymbol{E};\boldsymbol{\xi})$.

From Section (2.3) we assumed that every realization of a random process representing the input nuclear data belongs to the $L_2(\Gamma)$ space of square integrable functions. To find good representations of these realizations we must project each $\boldsymbol{\mathcal{D}}(\cdot,\theta)$ onto candidate basis vectors. In essence, each realisation of the random process is represented using a set of known basis vectors, $\{\varphi_j(\boldsymbol{E})\}_{j=1}^{\infty}$, which form a complete set within the function space $L_2(\Gamma)$. Following the derivation for continuous parameter random fields in [79] we seek an expansion such as

$$\hat{\boldsymbol{\mathcal{D}}}(\boldsymbol{E},\theta) = \sum_{i=1}^{\infty} a_i \varphi_i(\boldsymbol{E}) \xi_i(\theta) \tag{2.3.13}$$

which is optimal in the sense that it describes realisations of the random field better than representations of the same dimension in any other basis. In the above, it is assumed that the set of parameters $\{\xi_i, i = 1, \cdots, \infty\}$ are an orthogonal set of random variables with zero mean and unit variance,

namely

$$\mathbb{E}\left[\xi_i\right] = 0; \qquad \mathbb{E}\left[\xi_i \xi_j\right] = \delta_{ij} \tag{2.3.14}$$

which means the set of random variables $\boldsymbol{\xi}$ are orthogonal. However, they are generally not independent (except in the particular case of Gaussian processes). To proceed, we project the random field $\boldsymbol{\mathcal{D}}(\boldsymbol{E}, \theta)$ onto the basis $\varphi(\boldsymbol{E})$ and compute the variance using the relation in Eqn.(2.3.8). We seek the largest possible amount of variation of the random process, $\boldsymbol{\mathcal{D}}(\boldsymbol{E}, \theta)$, which may be represented by a single function, $\varphi(\boldsymbol{E})$, therefore we choose the $\boldsymbol{\mathcal{D}}(\boldsymbol{E}, \theta)$ that maximises the variance, i.e

$$\max_{\varphi \in L_2(\Gamma)} \frac{\mathbb{E}[(\boldsymbol{\mathcal{D}}(\boldsymbol{E}, \theta), \varphi(\boldsymbol{E}))^2]}{||\varphi||^2} \tag{2.3.15}$$

where the norm $||\cdot||$ and inner product $(\cdot, \cdot)$ are taken over the domain Γ. Solving (2.3.15) as stated would yield only the best approximation to the random field by a single function, but the other critical points of this functional are also physically important, for they correspond to a set of functions which, when taken together, provide the desired basis.

We now wish to extremise $\mathbb{E}[(\boldsymbol{\mathcal{D}}(\boldsymbol{E}, \boldsymbol{\xi}), \varphi(\boldsymbol{E}))^2]$ subject to the constraint $||\varphi||^2 = 1$. The corresponding functional for this constrained variational problem is

$$J[\varphi] = \mathbb{E}[(\boldsymbol{\mathcal{D}}(\boldsymbol{E}, \boldsymbol{\xi}), \varphi(\boldsymbol{E}))^2] - \lambda(||\varphi||^2 - 1) = 0 \tag{2.3.16}$$

A necessary condition for an extrema is that the functional derivatives van-

ish for all variations $\varphi + \delta\varphi \in \ L_2(\Gamma), \quad \delta \in \mathbb{R}$ which may be written as

$$\frac{d}{d\delta} J[\varphi + \delta\varphi]|_{\delta=0} = 0. \tag{2.3.17}$$

From (2.3.16) we have

$$\begin{aligned}
&\frac{d}{d\delta} J[\varphi + \delta\varphi]|_{\delta=0} \\
&\quad = \frac{d}{d\delta}\Big[\mathbb{E}[(\boldsymbol{\mathcal{D}}, \varphi + \delta\varphi)(\varphi + \delta\varphi, \boldsymbol{\mathcal{D}})] - \lambda(\varphi + \delta\varphi, \varphi + \delta\varphi)\Big]\Big|_{\delta=0} \\
&\quad = 2[\mathbb{E}[(\boldsymbol{\mathcal{D}}, \varphi)(\boldsymbol{\mathcal{D}}, \varphi)] - \lambda(\varphi, \varphi)] \\
&\quad = 2\mathbb{E}\left[\sum_{g=1}^{N_G} \boldsymbol{\mathcal{D}}(E_g, \boldsymbol{\xi})\varphi(E_g) \sum_{h=1}^{N_G} \boldsymbol{\mathcal{D}}(E_h, \boldsymbol{\xi})\varphi(E_h)\right] - \lambda \sum_{g=1}^{N_G} \varphi(E_g)\varphi(E_g) \\
&\quad = 2\sum_{h=1}^{N_G}\Big[\sum_{g=1}^{N_G} \mathbb{E}[\boldsymbol{\mathcal{D}}(E_g, \boldsymbol{\xi})\boldsymbol{\mathcal{D}}(E_h, \boldsymbol{\xi})]\varphi(E_h) - \lambda\varphi(E_g)\Big]\varphi(E_g) = 0
\end{aligned} \tag{2.3.18}$$

Since the variation is arbitrary, the condition reduces to

$$\sum_{g=1}^{N_G} \mathbb{E}[\boldsymbol{\mathcal{D}}(E_g, \boldsymbol{\xi})\boldsymbol{\mathcal{D}}(E_h, \boldsymbol{\xi})]\varphi(E_h) = \lambda\varphi(E_g)$$

or in matrix form

$$\mathrm{C}_{\boldsymbol{\mathcal{D}}\boldsymbol{\mathcal{D}}}\boldsymbol{\varphi} = \lambda\boldsymbol{\varphi} \tag{2.3.19}$$

Equation (2.3.19) is a matrix eigenvalue equation where $\mathrm{C}_{\boldsymbol{\mathcal{D}}\boldsymbol{\mathcal{D}}}$ is the auto-covariance function of the random process given by Eqn.(2.3.4), $\boldsymbol{\varphi}$ are the eigenvectors and λ are the eigenvalues. Because we have assumed that the random process is centred, the optimal basis for the expansion

in Eqn.(2.3.13) are the eigenfunctions of the covariance matrix, namely

$$\mathrm{Cov}_{\boldsymbol{\mathcal{D}}\boldsymbol{\mathcal{D}}}\boldsymbol{\varphi} = \lambda\boldsymbol{\varphi}. \tag{2.3.20}$$

We also note that the infinite sum in Eqn.(2.3.13) now only extends to the size of the covariance matrix, N_G. This means the maximum number of IID random variables in the KLE is equal to N_G which is to be expected since the uncertainty in the nuclear data is represented using a single random variable for each energy group.

Now that the basis functions for the expansion in Eqn.(2.3.13) are defined, it remains to calculate the expansion coefficients, a_i. Starting from Mercer's Theorem (2.3.10) and using the definition of covariance:

$$\begin{aligned}
\mathrm{Cov}_{\boldsymbol{\mathcal{D}}\boldsymbol{\mathcal{D}}}(E_g, E_h) = \sum_{i=1}^{N_G} \lambda_i \varphi(E_g)\varphi_i(E_h) &= \int_\Theta \left(\sum_{i=1}^{N_G} a_i\varphi_i(E_g)\xi_i\right) \\
&\quad \times \left(\sum_{j=1}^{N_G} a_j\varphi_j(E_h)\xi_j\right) p_{\boldsymbol{\xi}}(\boldsymbol{\xi})d\boldsymbol{\xi} \\
&= \sum_{i=1}^{N_G}\sum_{j=1}^{\infty} a_i a_j \varphi_i(E)\varphi_j(E) \int_\Theta \xi_i\xi_j p_{\boldsymbol{\xi}}(\boldsymbol{\xi})d\boldsymbol{\xi} \\
&= \sum_{i=1}^{N_G} a_i^2 \varphi_i(E_g)\varphi_i(E_h).
\end{aligned}$$

Therefore the optimal expansion is

$$\hat{\boldsymbol{\mathcal{D}}}(\boldsymbol{E}, \xi(\theta)) = \sum_{i=1}^{N_G} \sqrt{\lambda_i}\varphi_i(\boldsymbol{E})\xi_i(\theta). \tag{2.3.21}$$

The Karhunen Loéve expansion in Eqn.(2.3.21) is optimal in the mean square sense. This means that, when truncating the expansion after a finite

number of terms $N_{KL} \leq N_G$, the resulting approximation of the random process $\hat{\boldsymbol{\mathcal{D}}}(\boldsymbol{E};\boldsymbol{\xi})$ minimizes the mean square error i.e.

$$\epsilon^2_{N_{KL}} = \mathbb{E}\left[\left(\sum_{g=1}^{N_G} \boldsymbol{\mathcal{D}}(E_g;\cdot) - \hat{\boldsymbol{\mathcal{D}}}(E_g;\cdot)\right)^2\right] = \sum_{i,j>N_{KL}} \sqrt{\lambda_i\lambda_j}\,(\varphi_i,\varphi_j)\,\mathbb{E}\left[\xi_i(\theta)\xi_j(\theta)\right]$$
$$= \sum_{i,j>N_{KL}} \sqrt{\lambda_i\lambda_j}\delta_{ij}\delta_{ij} = \sum_{i>N_{KL}} \lambda_i. \tag{2.3.22}$$

Therefore, no other approximation of the random process $\boldsymbol{\mathcal{D}}(\boldsymbol{E};\boldsymbol{\xi})$ in a series of N_{KL} terms results in a smaller mean square error. The mean square truncation error decreases monotonically with the number of terms retained in the expansion at a rate that depends on the decay of the spectrum of the covariance matrix. The higher the rate of spectral decay the smaller the number of terms needed in the expansion to produce a representation of a desired accuracy. Specifically, the number of terms to achieve a specified error threshold depends on the correlation function of the random process. The more correlated the random process the smaller the number of terms needed to achieve the desired threshold. Conversely, if the random process is poorly correlated, a higher number of terms is needed.

The KLE can also be used to remove any degeneracy present in the random field by ignoring those eigenvectors whose eigenvalues are zero. This reduces the number of IID random variables which may ultimately lead to a reduction in the computational effort. The number of non zero eigenvalues corresponds to the rank of the covariance matrix which is also equal to the size of the largest collection of linearly independent columns or rows of the covariance matrix.

From Eqn.(2.3.12), a non-centred random process can be factored into a mean or expectation value plus a centred random process. Therefore, for a non-centred random process $\boldsymbol{\mathcal{D}'}(\boldsymbol{E};\boldsymbol{\xi})$ the Karhunen Loéve expansion would be:

$$\boldsymbol{\mathcal{D}'}(\boldsymbol{E};\boldsymbol{\xi}) = \overline{\boldsymbol{\mathcal{D}'}}(\boldsymbol{E}) + \sum_{i=1}^{N_{KL}} \sqrt{\lambda_i}\varphi_i(\boldsymbol{E})\xi_i(\theta) \quad N_{KL} \leq \text{size}(\text{Cov}_{\boldsymbol{\mathcal{D}'}\boldsymbol{\mathcal{D}'}}) \quad (2.3.23)$$

where $\text{size}(\text{Cov}_{\boldsymbol{\mathcal{D}'}\boldsymbol{\mathcal{D}'}})$ is the number of rows/columns in the covariance matrix.

As we have mentioned above, the KLE can be used to remove any degeneracy in the random field by reducing the number of terms, N_{KL} such that $\lambda_i = 0$ modes are not included. The KLE can also be used to produce a reduced order representation of the random field which reproduces only a proportion of the total variation described by the original covariance matrix. Using the following relation

$$\frac{\text{Var}_{KL}}{\text{Var}_T} = \frac{\sum_{i=1}^{N_{KL}} \lambda_i}{\sum_{i=1}^{\text{size}(\text{Cov}_{\boldsymbol{\mathcal{D}'}\boldsymbol{\mathcal{D}'}})} \lambda_i} \quad (2.3.24)$$

any given proportion of the total variation of the random field may be represented by choosing the appropriate number of eigenvalues λ. However, choosing the value of N_{KL} in this fashion allows one to specify the variation of the input random fields which is modelled but, without knowing the sensitivities of each eigen-mode of the Karhunen Loéve expansion to the response parameters, this may have no bearing on the amount variation observed in the response parameters.

2.4. Transforming to Standard Normal Variables

In section (2.3) the input nuclear data uncertainties are represented using the concept of a random field which is described parametrically using a set of IID random variables $\boldsymbol{\xi}$. In the limit, where each random variable in the random processes is independent of every other, the random variable representing the uncertainty in a given energy group, $\mathcal{D}_g$, may be represented parametrically using a single unit variable, ξ_g. In general, the random variables $\mathcal{D}_g$ and ξ_g will belong to different probability spaces but it is assumed that the marginal probability distributions of both are known. In order to represent $\mathcal{D}_g$ in terms of ξ_g, we must define the transform t such that $\mathcal{D}_g = t(\xi_g)$. To begin we let p_ξ and $p_{\mathcal{D}_g}$ be the probability density functions of ξ_g and $\mathcal{D}_g$ respectively. We may now equate infinitesimal units of probability, namely

$$p_\xi(x)dx = p_{\mathcal{D}_g}(y)dy. \tag{2.4.1}$$

Integrating Eqn.(2.4.1) yields

$$\int_{-\infty}^{\xi} p_\xi(x)dx = \int_{-\infty}^{\mathcal{D}_g} p_{\mathcal{D}_g}(y)dy \tag{2.4.2}$$

which are the cumulative density functions

$$P_\xi(\xi) = \int_{-\infty}^{\xi} p_\xi(x)dx \quad \text{and} \quad P_{\mathcal{D}_g}(\mathcal{D}_g) = \int_{-\infty}^{\mathcal{D}_g} p_{\mathcal{D}_g}(y)dy \tag{2.4.3}$$

of the random variables ξ_g and $\mathcal{D}_g$ respectively. Therefore, the transform t is defined by

$$\mathcal{D}_g(\xi) = P^{-1}_{\mathcal{D}_g} P_\xi(\xi). \tag{2.4.4}$$

As we have seen above, the method for calculating the transform, t, between two random variables involves the inversion of the CDF of one of the random variables. For many combinations of probability density functions in Eqn.(2.4.1), expressions for t can be found analytically.

In this work, members of a realisation of the multi-group nuclear data parameters, which we denote by $\boldsymbol{\mathcal{D}} = \{\mathcal{D}_g; g = 1, N_G\}$ with $\mathcal{D}_g = \boldsymbol{\mathcal{D}}(E_g, \theta)$, will, in general, be correlated. If the marginal distribution of the members of the set $\boldsymbol{\mathcal{D}}$ are Gaussian distributed, the Karhunen Loéve expansion may be used to transform the correlated variables $\boldsymbol{\mathcal{D}}$ into a set of IID Gaussian variables $\boldsymbol{\xi}$ directly.

If, however, the marginal distributions of the members of $\boldsymbol{\mathcal{D}}$ are non-Gaussian then the Karhunen Loéve expansion cannot be used directly. This constraint can be understood by considering the central limit theorem [80] which states that, in the limit $n \to \infty$, a linear combination of n random variables, X_i, will be Normally distributed regardless of the original distribution of the X_i's. Therefore, only a linear combination of Normally distributed random variables will ultimately result in the same (Gaussian) PDF. A linear combination of random variables with any other (non-Gaussian) distribution will result in a random variable with a different marginal distribution (Gaussian in the limit of an infinite combination).

To express a random field with non-Gaussian marginal distributions, the field must be transformed to an equivalent random field with Gaussian marginals. The field can then be represented using the Karhunen Loéve expansion in terms of a set of IID Gaussian variables $\boldsymbol{\xi}$. A realisation of the field using the KLE can then be transformed back to the original marginal distribution. The transform from non-Gaussian correlated variables to uncorrelated standard Gaussian variables is denoted as follows $\boldsymbol{\xi} = T(\boldsymbol{\mathcal{D}})$ with the reverse transformation defined as $\boldsymbol{\mathcal{D}} = T^{-1}(\boldsymbol{\xi})$. These transforms are generally non-linear and may be calculated with one of the following: Rosenblatt [81], Nataf [82], or Box-Cox [83]. To avoid these complicated transforms, which often require numerical treatment, we assume that the correlated variables $\boldsymbol{\mathcal{D}}$ in this work are either Gaussian or log-normally distributed. In theses cases closed form expressions for the transform T and its inverse can be found.

In section (2.3.1) we have seen that if the marginal distributions of the variables in the random field are Gaussian, the random field may be represented using a linear expansion of Gaussian random variables. In this case, the inverse transform T^{-1} will simply consist of a shift and a scaling of the set of standard Gaussian variables $\boldsymbol{\xi}$, namely

$$\mathcal{D}_g = \overline{\mathcal{D}}_g + \sum_h L_{gh}\xi_h \tag{2.4.5}$$

here L is a coefficient matrix formed from a decomposition of the covariance matrix of the variables $\boldsymbol{\mathcal{D}}$ and $\overline{\mathcal{D}}_g = \mathbb{E}[\mathcal{D}_g]$ is the mean value of the Gaussian random variable $\mathcal{D}_g$. Using the Karhunen Loéve expansion from

Eqn.(2.3.23), the components of the coefficient matrix L_{gh} are given by

$$L_{gh} = \sqrt{\lambda_h}\varphi_h(E_g). \tag{2.4.6}$$

If we now assume that $\mathcal{D}_g$ and ξ_h are log-normally distributed then we may transform back to the space of Gaussian variables by taking logarithms. Using this fact and Eqn.(2.4.5) we may now write

$$\ln(\mathcal{D}_g^{(LN)}) = \overline{\mathcal{D}}_g^{(N)} + \sum_{k=1}^{N} L_{ik}^{(N)} \ln(\xi_k) \tag{2.4.7}$$

or alternatively

$$\mathcal{D}_g^{(LN)} = \exp\left(\overline{\mathcal{D}}_g^{(N)} + \sum_{k=1}^{N} L_{ik}^{(N)} \ln(\xi_k)\right) \tag{2.4.8}$$

In Eqns.(2.4.7) and (2.4.8) the superscipts "(N)" and "(LN)" represent the Normally/Gaussian distributed and Log-Normally distributed random variables respectively. Since $\ln(\boldsymbol{\xi})$ are Gaussian distributed, we note that Eqn.(2.4.8) is the inverse transform: $\boldsymbol{\mathcal{D}} = T^{-1}(\ln(\boldsymbol{\xi}))$ which is the KLE of the Gaussian random field as the exponent of the base of natural logarithms. At this point we note that Eqn.(2.4.8) is a function of the mean value of the Gaussian random field and also the spectral decomposition of its covariance matrix. Therefore the covariance matrix of the Gaussian random field, $\mathrm{Cov}_{\boldsymbol{\mathcal{D}}\boldsymbol{\mathcal{D}}}^{(N)}$, and the mean values, $\overline{\boldsymbol{\mathcal{D}}}^{(N)}$, must be calculated from the available information about the Log-Normal random field, namely the Covariance, $\mathrm{Cov}_{\boldsymbol{\mathcal{D}}\boldsymbol{\mathcal{D}}}^{(LN)}$, and mean values, $\overline{\boldsymbol{\mathcal{D}}}^{(LN)}$. A derivation of the mapping between Log-Normal and Gaussian means and covariances is given in Appendix (A).

The covariance matrix $\mathrm{Cov}^{(N)}_{\boldsymbol{\mathcal{D}}\boldsymbol{\mathcal{D}}}$ is given by the following

$$\mathrm{Cov}^{(N)}_{\boldsymbol{\mathcal{D}}\boldsymbol{\mathcal{D}}}(E_g, E_h) = \ln\left[\frac{\mathrm{Cov}^{(LN)}_{\boldsymbol{\mathcal{D}}\boldsymbol{\mathcal{D}}}(E_g, E_h)}{\overline{\mathcal{D}}^{(LN)}_g \overline{\mathcal{D}}^{(LN)}_h} + 1\right] \tag{2.4.9}$$

along with the mean value

$$\overline{\mathcal{D}}^{(N)}_g = \ln\left[\frac{\overline{\mathcal{D}}^{(LN)}_g \overline{\mathcal{D}}^{(LN)}_g}{\sqrt{\mathrm{Cov}^{(LN)}_{\boldsymbol{\mathcal{D}}\boldsymbol{\mathcal{D}}}(E_g, E_g) + \overline{\mathcal{D}}^{(LN)}_g}}\right]. \tag{2.4.10}$$

It is important to stress that the transform in Eqn.(2.4.9) is undefined for values of

$$\frac{\mathrm{Cov}^{(LN)}_{\boldsymbol{\mathcal{D}}\boldsymbol{\mathcal{D}}}(E_g, E_h)}{\overline{\mathcal{D}}^{(LN)}_g \overline{\mathcal{D}}^{(LN)}_h} \leq -1. \tag{2.4.11}$$

To make more physical sense of this constraint, we may rewrite Eqn.(2.4.11) using Eqn.(2.3.9) as follows:

$$\frac{\mathrm{Cov}^{(LN)}_{\boldsymbol{\mathcal{D}}\boldsymbol{\mathcal{D}}}(E_g, E_h)}{\overline{\mathcal{D}}^{(LN)}_g \overline{\mathcal{D}}^{(LN)}_h} = \rho_{\boldsymbol{\mathcal{D}}\boldsymbol{\mathcal{D}}}(E_g, E_h) R_g R_h \tag{2.4.12}$$

where $\rho_{\boldsymbol{\mathcal{D}}}$ is the coefficient of correlation and R_g is the relative standard deviation defined as

$$R_g = \frac{\sqrt{\mathrm{Var}(E_g)}}{\overline{\mathcal{D}}_g}. \tag{2.4.13}$$

Because $\rho_{\boldsymbol{\mathcal{D}}\boldsymbol{\mathcal{D}}}$ is bounded on $[-1:1]$ and values of R_g are strictly positive, the coefficient of correlation must be negative and the product $R_g R_h > 1$ to break the constraint in Eqn.(2.4.11). This condition corresponds to a situation where the relative uncertainties are greater than 100%.

2.5. Summary and Conclusions

In Section (2.2) multi-group diffusion equations were derived from the time dependent transport equation using both w-eigenvalue and k_{eff} -eigenvalue methods. The multi-group method averages the transport/diffusion equation over discrete energy regions resulting in a piece-wise continuous energy representation of the input nuclear data. In section (2.3) the uncertainties in the nuclear data were described using the concept of a random field provided that the random variables describing the nuclear data had finite variances and their energy dependence is bounded and has a finite L_2 norm. In Section (2.3.1) the Karhunen Loéve expansion (KLE), which is an expansion in terms of IID Gaussian random variables, was derived for a discrete energy random field. The maximum number of random variables in the random field is equal to the rank of the covariance matrix, if the random field is degenerate, this number will be less than the number of random variables in the random field. In the final section of this chapter, the mappings for correlated Log-Normally distributed random variables to Gaussian distributed random variables were defined.

Chapter 3

Polynomial Chaos

3.1. Introduction

In Chapter (1), uncertainty quantification methods based upon random sampling and local perturbations were described. Random sampling can exhibit slow convergence rates and perturbation techniques may be inaccurate due to their inherently local nature. These issues prompted the investigation of alternative methods which have global support and fast convergence rates. One such method is the method of polynomial chaos.

The polynomial chaos technique approximates the response of a model due to random input parameters using a spectral expansion of orthogonal polynomial basis functions. The basis functions are known as polynomial chaoses and are defined in a suitable finite dimensional space. The spectral expansion of the random model response is known as a polynomial chaos expansion or PCE. The original polynomial chaos method, also termed homogeneous chaos or Wiener chaos, was first developed by Wiener [84]. Wiener chaos was shown to produce optimal representations in the L_2 sense of Gaussian random processes. For random processes with non-Gaussian marginals, Wiener chaos was generalised by Xiu and Karniadakis [85].

In the following chapter we give the general theory for the Wiener chaos and generalised polynomial chaos expansions outlining how the expansion coefficients may be used to determine the mean, variance, covariance, probability density functions and local sensitivity coefficients of the model responses. We then outline how the PCE method may be used to compute the statistical moments of stochastic eigenvalue problems. All of the above theory is then illustrated using an example; the calculation of the statistics of the k_{eff} and w-eigenvalues due to uncertain macroscopic cross sections.

3.2. Theory

To begin, consider an $\mathbb{R}$-valued output random variable R defined on a probability space $(\Theta, \mathcal{B}, P)$ such that $R : \Theta \to \mathbb{R}$. Let $\{\xi\}_{i=1}^{\infty}$ be a set of orthogonal (independent) zero mean unit variance Gaussian random variables. Let $\hat{\Gamma}_p$ be the space of polynomials in $\{\xi\}_{i=1}^{\infty}$ having degree not exceeding p. Let Γ_p be the set of polynomials in $\hat{\Gamma}_p$ orthogonal to Γ_{p-1} and $\widetilde{\Gamma}_p$ be the space spanned by Γ_p . Conventionally the space $\widetilde{\Gamma}_p$ is known as the p^{th} Homogeneous Chaos and Γ_p is known as the Polynomial Chaos of order p. Thus, the Polynomial Chaos of order p consists of all polynomials of order p involving all combinations of the random variables $\{\xi\}_{i=1}^{\infty}$.

The Homogeneous chaos or Wiener chaos may be used to represent a second order random process in terms of Hermite polynomials using Normal

random variables [84, 47], namely

$$\begin{aligned} R(\boldsymbol{x},\boldsymbol{\xi}) = r_0(\boldsymbol{x})\Gamma_0 &+ \sum_{i_1=1}^{\infty} r_{i_1}(\boldsymbol{x})\Gamma_1(\xi_{i_1}) \\ &+ \sum_{i_1=1}^{\infty}\sum_{i_2=1}^{i_1} r_{i_1 i_2}(\boldsymbol{x})\Gamma_2(\xi_{i_1},\xi_{i_2}) \\ &+ \sum_{i_1=1}^{\infty}\sum_{i_2=1}^{i_1}\sum_{i_3=1}^{i_2} r_{i_1 i_2 i_3}(\boldsymbol{x})\Gamma_3(\xi_{i_1},\xi_{i_2},\xi_{i_3}) \\ &+ \cdots \end{aligned} \tag{3.2.1}$$

where $\Gamma_n(\xi_{i_1},\cdots,\xi_{i_n})$ denotes the polynomial chaos of order n. For notational convenience we may write

$$R(\boldsymbol{x},\boldsymbol{\xi}) = \sum_{\boldsymbol{\alpha}\in\mathcal{A}^M} r_{\boldsymbol{\alpha}}(\boldsymbol{x})\Phi_{\boldsymbol{\alpha}}(\boldsymbol{\xi}) \tag{3.2.2}$$

where there is a one-to-one correspondence between the functions $\Gamma_n(\xi_{i_1},\cdots,\xi_{i_n})$ and $\Phi_{\boldsymbol{\alpha}}(\boldsymbol{\xi})$. Here $\mathcal{A}^M$ is the set of all polynomial indexes which is defined as $\mathcal{A}^M \equiv \{\boldsymbol{\alpha}\in\mathbb{N}^M\}$ where M is the number of dimensions. The multi-index $\boldsymbol{\alpha}$ is defined as $\boldsymbol{\alpha} = (\alpha_1,\cdots,\alpha_M)$ where α_i is the index of a univariate polynomial; this results in the following form for the functions $\Phi_{\boldsymbol{\alpha}}(\boldsymbol{\xi})$:

$$\Phi_{\boldsymbol{\alpha}}(\boldsymbol{\xi}) = \prod_{i=1}^{M}\Phi_{\alpha_i}(\xi_i) \tag{3.2.3}$$

which is a product of the appropriate one-dimensional polynomial basis. These basis functions are orthogonal which implies

$$\langle\Phi_{\boldsymbol{\alpha}},\Phi_{\boldsymbol{\beta}}\rangle = \prod_{i=1}^{M} N_{\alpha_i}^2\delta_{\alpha_i\beta_j} \tag{3.2.4}$$

where $\delta_{\alpha_i\beta_j}$ is the Kronecker delta and $N_{\alpha_i}^2$ is a normalisation constant. The

term $\langle \cdot, \cdot \rangle$ denotes the ensemble average which is the inner product in the Hilbert space of variables $\boldsymbol{\xi}$ and defined as

$$\langle \mathrm{X}(\boldsymbol{x}, \boldsymbol{\xi}), \mathrm{Y}(\boldsymbol{x}, \boldsymbol{\xi}) \rangle = \int \mathrm{X}(\boldsymbol{x}, \boldsymbol{\xi}) \mathrm{Y}(\boldsymbol{x}, \boldsymbol{\xi}) p(\boldsymbol{\xi}) d\boldsymbol{\xi} \tag{3.2.5}$$

where $p(\boldsymbol{\xi})$ is the probability density function of the random variables $\boldsymbol{\xi}$. The set of variables $\boldsymbol{\xi}$ are independent so the multivariate PDF, $p(\boldsymbol{\xi})$ is simply the product of the univariate PDFs, namely:

$$p(\boldsymbol{\xi}) = \prod_{i=1}^{M} p(\xi_i). \tag{3.2.6}$$

For the purposes of numerical computation, the series given by Eqn.(3.2.2) must be truncated. The most commonly used approach is to restrict the maximum total order of the multivariate polynomial basis to $\leq p$. This imposes the following restriction on the index sets

$$\mathcal{A}^{M,p} \equiv \{ \boldsymbol{\alpha} \in \mathbb{N}^M : ||\boldsymbol{\alpha}||_1 \leq p \} \quad ; \quad ||\boldsymbol{\alpha}||_1 \equiv \sum_{i=1}^{M} \alpha_i \tag{3.2.7}$$

The response function $R(\boldsymbol{x}, \boldsymbol{\xi})$ is now approximated by the following expansion:

$$R(\boldsymbol{x}, \boldsymbol{\xi}) \approx \sum_{\boldsymbol{\alpha} \in \mathcal{A}^{M,p}} R_{\boldsymbol{\alpha}}(\boldsymbol{x}) \Phi_{\boldsymbol{\alpha}}(\boldsymbol{\xi}) \tag{3.2.8}$$

For a number of random dimensions M and maximum polynomial order p the total number of coefficients in the expansion given by (3.2.8) is as follows

$$N_P + 1 = \frac{(M+p)!}{M!p!} = \begin{pmatrix} M+p \\ M \end{pmatrix} \tag{3.2.9}$$

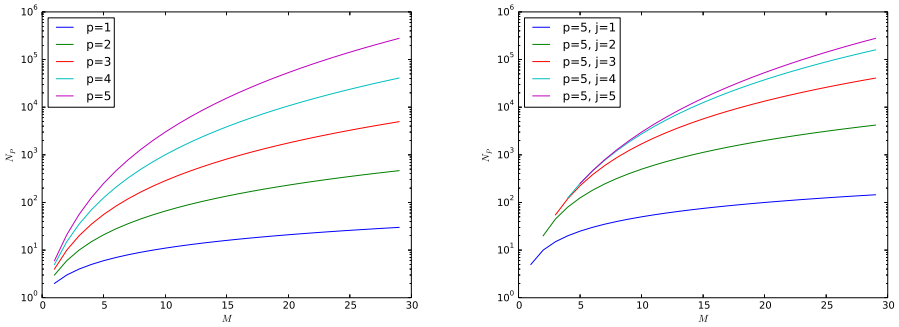
Alternative methods which can further reduce the number of polynomial basis functions have been proposed and investigated in [86, 62, 63, 64]. These approaches form a sparse PCE by imposing additional restrictions on the formation of the index set $\mathcal{A}$. One such method computes a so called low rank index set. Here an additional parameter $j = 1, 2, \cdots, \min(M, p)$ is introduced such that

$$\mathcal{A}^{M,p,j} \equiv \{\boldsymbol{\alpha} \in \mathbb{N}^M : ||\boldsymbol{\alpha}||_1 \leq p, ||\boldsymbol{\alpha}||_0 \leq j\} \quad ; \quad ||\boldsymbol{\alpha}||_0 \equiv \sum_{i=1}^{M} 1_{(\alpha_i > 0)}$$

Here we can see that the parameter j controls the order of allowed multivariate interactions, i.e. j=2 includes all bi-variate and univarite interactions and all possible combinations thereof. The disadvantage of using a low rank set is that the PCE is not convergent for ranks $j < \min(M, p)$. That is, multivariate interactions of order $> j$ are neglected. The total number of coefficients is now given by

$$N_P = \sum_{i=1}^{j} \frac{M!p!}{i!i!(M-i)!(p-i)!} \tag{3.2.10}$$

In Fig.(3.1a) Eqn.(3.2.9) is plotted as a function of the number of dimensions M for polynomial orders up to $p = 5$. This shows the exponential increase in the number of coefficients in the PCE with the number of dimensions, M. Using this index set requires many thousands of coefficients for even a modest number of dimensions. In Figure (3.1b) the number of coefficients from Eqn.(3.2.10) is plotted versus dimension, M, for values of $j = 1, \cdots, 5$ and $p = 5$. From this example we can see that limiting the maximum order of multivariate interactions can reduce the number of coefficients significantly as M increases. This approach does require some



(a) Conventional PCE (b) Low rank set

Figure 3.1.: Number of PC coefficients, N_P, versus dimension, M.

pre-existing knowledge of the response function so that the value of j can be appropriately chosen.

According to the Cameron-Martin theorem [87], the homogeneous chaos expansion can approximate any functionals in the continuously differentiable L_2 space and converges in the L_2 sense, namely

$$\lim_{p\to\infty} \left|\left| R(\boldsymbol{x},\boldsymbol{\xi}) - \sum_{\boldsymbol{\alpha}\in\mathcal{A}^{M,p}} R_{\boldsymbol{\alpha}}(\boldsymbol{x})\Phi_{\boldsymbol{\alpha}}(\boldsymbol{\xi}) \right|\right|_{L_2}^2 = 0 \tag{3.2.11}$$

This means the homogeneous chaos expansion converges to any stochastic process with finite second order moments.

Although this expansion converges in the L_2 sense to any arbitrary stochastic process with second order moments, it has been demonstrated that the optimal convergence rate is obtained only for Gaussian processes [85]. For non Gaussian processes an extension to Wiener's chaos using the Askey family of orthogonal polynomials has been proposed [85]. Here the underlying random variables are chosen according to the weighting function of

the polynomial chaos. If the polynomial chaos expansion is used with its corresponding stochastic process (Table(3.1)), optimal (exponential) convergence is observed [85] with respect to the polynomial order p. This extended method is known as Wiener-Askey chaos or generalised polynomial chaos (gPC). In the case where the uncertain input parameters are described using different probability distributions, a mixture of the optimal polynomials may be used to construct a basis [88]. A derivation and a simple example is given in Appendix B.

	Random variables $\boldsymbol{\xi}$	Askey Chaos $\{\Phi(\xi)\}$	Support
Continuous	Gaussian	Hermite	$(-\infty, \infty)$
	Gamma	Laguerre	$[0, \infty)$
	Beta	Jacobi	$[a, b]$
	Uniform	Legendre	$[a, b]$
Discrete	Poisson	Charlier	$\{0, 1, 2, \cdots\}$
	Binomial	Krawtchouk	$\{0, 1, 2, \cdots, N\}$
	Negative Binomial	Meixner	$\{0, 1, 2, \cdots\}$
	Hypergeometric	Hahn	$\{0, 1, 2, \cdots, N\}$

Table 3.1.: Description of the Wiener-Askey or generalised polynomial chaoses.

We note that, in general, the probability distribution of the response is not known *a priori*, therefore, it is not possible to select the optimal polynomial basis for the output process. However, the form of the input stochastic process is known, or at least partially known, and it is standard practice to use the optimal basis for the input process to construct the output polynomial basis.

3.3. Post-Processing

The main benefit of representing the response variables in the semi-analytic form of Eqn.(3.2.2) is the ability it provides to perform analytic manip-

ulations on the solution. In this section we provide expressions for computing the mean, variance/covariance, local sensitivity coefficients and also the PDF of the response variable(s). We start with the expansion of the response variable $R(\boldsymbol{x}, \boldsymbol{\xi})$

$$R(\boldsymbol{x}, \boldsymbol{\xi}) \approx \sum_{\boldsymbol{\alpha} \in \mathcal{A}^M} R_{\boldsymbol{\alpha}}(\boldsymbol{x}) \Phi_{\boldsymbol{\alpha}}(\boldsymbol{\xi}) \tag{3.3.1}$$

Here $\mathcal{A}^M$ is a generic index set corresponding to a polynomial basis spanning M dimensions and may be pre-defined or built up iteratively via some adaptive procedure. The statistics of $R(\boldsymbol{x}, \boldsymbol{\xi})$ are calculated in the following subsections.

3.3.1. Mean, Variance and Covariance

Once the expansion coefficients in Eqn.(3.3.1) are known, the mean, variance and covariance may be calculated using the following relations:

$$\overline{R}(\boldsymbol{x}) = R_0(\boldsymbol{x}) \tag{3.3.2}$$

$$\begin{aligned} \mathrm{Var}(\boldsymbol{x}) &= \left(\sum_{\boldsymbol{\alpha} \in \mathcal{A}^{M,p}} R_{\boldsymbol{\alpha}} \Phi_{\boldsymbol{\alpha}}(\boldsymbol{\xi}) \right)^2 - \overline{R}(\boldsymbol{x})^2 \\ &= \sum_{\boldsymbol{\alpha} \in \mathcal{A}^{M,p}} R_{\boldsymbol{\alpha}}^2(\boldsymbol{x}) N_{\boldsymbol{\alpha}}^2 \end{aligned} \tag{3.3.3}$$

$$\mathrm{Cov}(\boldsymbol{x}, \boldsymbol{x'}) = \sum_{\boldsymbol{\alpha} \in \mathcal{A}^{M,p}} R_{\boldsymbol{\alpha}}(\boldsymbol{x}) R_{\boldsymbol{\alpha}}(\boldsymbol{x'}) N_{\boldsymbol{\alpha}}^2 \tag{3.3.4}$$

Expressions for higher order moments such as skew and kurtosis may also be calculated [89].

3.3.2. Sensitivity Coefficients

In many engineering applications it is important to assess the impact that randomly varying input parameters have on the response variables. This impact may be expressed as a local sensitivity coefficient. Specifically, the local sensitivity of the response $R(\boldsymbol{x}, \boldsymbol{\xi})$ as expressed in (3.3.1) with respect to the parameter Σ_j may be calculated by taking the derivative, namely

$$\left.\frac{\partial R(\boldsymbol{x}, \boldsymbol{\xi})}{\partial \Sigma_j(\boldsymbol{x}, \boldsymbol{\xi})}\right|_{\Delta\Sigma=0} = \sum_{i=1}^{M} \left.\frac{\partial R(\boldsymbol{x}, \boldsymbol{\xi})}{\partial \xi_i}\right|_{\boldsymbol{\xi}=0} \left.\frac{\partial \xi_i}{\partial \Sigma_j(\boldsymbol{x}, \boldsymbol{\xi})}\right|_{\boldsymbol{\xi}=0} \tag{3.3.5}$$

An exact expression for the derivative of R with respect to the random variables ξ can be calculated from the PCE:

$$\left.\frac{\partial R(\boldsymbol{x}, \boldsymbol{\xi})}{\partial \xi_i}\right|_{\boldsymbol{\xi}=0} = \sum_{\boldsymbol{\alpha} \in \mathcal{A}^{M,p}} R_{\boldsymbol{\alpha}}(\boldsymbol{x}) \left.\frac{\partial \Phi_{\alpha_i}(\xi_i)}{\partial \xi_i}\right|_{\boldsymbol{\xi}=0} \tag{3.3.6}$$

which is just a sum of the differentials of the polynomial basis functions with respect to ξ_i. The differential of ξ_i with respect Σ can be obtained from the representation of the input uncertainties, i.e. the Karhunen Loéve expansion. The input uncertainties will have the general form:

$$\Sigma_j(\boldsymbol{\xi}) = \overline{\Sigma}_j + \sum_i L_{ij} \xi_i. \tag{3.3.7}$$

Therefore, (3.3.5) can now be written

$$\left.\frac{\partial R(\boldsymbol{x}, \boldsymbol{\xi})}{\partial \Sigma_j(\boldsymbol{x}, \boldsymbol{\xi})}\right|_{\Delta\Sigma=0} = \sum_{i=1}^{M} L_{ij}^{-1} \sum_{\boldsymbol{\alpha} \in \mathcal{A}^{M,p}} R_{\boldsymbol{\alpha}}(\boldsymbol{x}) \left.\frac{\partial \Phi_{\alpha_i}(\xi_i)}{\partial \xi_i}\right|_{\boldsymbol{\xi}=0} \tag{3.3.8}$$

3.3.3. Probability Density Function

In order to obtain a graphical representation of the PDF, the random response R as represented by (3.3.1) may be simulated using a Monte Carlo scheme. This provides an ensemble of response quantities $\{R_1, \cdots, R_N\}$ which are then used to construct a histogram. In practice a large number of samples are required to obtain an accurate representation, say N=10,000 - 100,000.

3.4. The Stochastic Eigenvalue Problem

Eigenvalue problems occur in many engineering and physics problems including structural mechanics, dynamical systems and of course criticality calculations. In Section (2.2) equations for the w-eigenvalue and k_{eff} - eigenvalue were derived from the time dependent transport equation. For notational convenience, k_{eff} -eigenvalue problems will be referred to as k-eigenvalue problems for the remainder of this section. Both systems, w and k eigenvalues, may be written generally as (noting the w-eigenvalue will have an auxiliary equation for the neutron precursors):

$$L(\boldsymbol{x}, \boldsymbol{\xi})\psi(\boldsymbol{x}, \boldsymbol{\xi}) = \lambda(\boldsymbol{\xi})F(\boldsymbol{x}, \boldsymbol{\xi})\psi(\boldsymbol{x}, \boldsymbol{\xi}) \tag{3.4.1}$$

which is an eigenvalue problem with the eigenvalue λ and the eigenvector ψ. The eigenvector may be dependent upon many variables which we denote $\boldsymbol{x}$ such as space, $\boldsymbol{r}$, energy, E and angle, Ω. In the presence of input data uncertainties, both eigenvalue and eigenvector will also depend upon a vector of IID random variables $\boldsymbol{\xi}$. This results in a stochastic eigenvalue problem. For a fixed elementary event, θ, the deterministic functions in space angle

and energy may be approximated by the following:

$$\psi(\boldsymbol{x},\theta) \approx \sum_{i=1}^{N_{\boldsymbol{r}}} \sum_{j=1}^{N_{\boldsymbol{\Omega}}} \sum_{g=1}^{N_G} \psi(\theta) N_i(\boldsymbol{r}) N_j(\Omega) N_g(E) \equiv \boldsymbol{\psi}^T(\theta) \boldsymbol{N}(\boldsymbol{x}) \tag{3.4.2}$$

where $N_i(\boldsymbol{r})$, $N_j(\Omega)$, $N_g(E)$ are typical shape functions for space, angle and energy and $N_{\boldsymbol{r}}$, N_Ω and N_G are the number of spatial, angular and energy degrees of freedom respectively. The following vector notation has also been used:

$$\boldsymbol{\psi}^T(\theta) = \{\psi_{111}(\theta), \cdots, \psi_{N_{\boldsymbol{r}} N_\Omega N_G}(\theta)\}^T \tag{3.4.3}$$

$$\boldsymbol{N}(\boldsymbol{x}) = \{N_1(\boldsymbol{r}) N_1(\Omega) N_1(E), \cdots, N_{N_{\boldsymbol{r}}}(\boldsymbol{r}) N_{N_\Omega}(\Omega) N_G(E)\}^T. \tag{3.4.4}$$

Inserting Eqn.(3.4.2) into (3.4.1) and projecting onto a basis, $M(\boldsymbol{x})$, given by (3.4.4) yields the following matrix eigenvalue problem:

$$\boldsymbol{L}(\boldsymbol{\xi})\boldsymbol{\psi}(\boldsymbol{\xi}) = \lambda(\boldsymbol{\xi})\boldsymbol{F}(\boldsymbol{\xi})\boldsymbol{\psi}(\boldsymbol{\xi}). \tag{3.4.5}$$

The matrices $\boldsymbol{L}(\boldsymbol{\xi})$ and $\boldsymbol{F}(\boldsymbol{\xi})$ are stochastic matrices formed from the discretisation of the deterministic variables and from the parametric representation of the uncertain input data and are defined as follows:

$$\boldsymbol{L}(\boldsymbol{\xi}) = \int d\boldsymbol{r} \int d\Omega \int dE\, M(\boldsymbol{x}) L(\boldsymbol{x},\boldsymbol{\xi}) N(\boldsymbol{x}) \tag{3.4.6}$$

$$\boldsymbol{F}(\boldsymbol{\xi}) = \int d\boldsymbol{r} \int d\Omega \int dE\, M(\boldsymbol{x}) F(\boldsymbol{x},\boldsymbol{\xi}) N(\boldsymbol{x}). \tag{3.4.7}$$

At this point we note that the integrations over energy define the multi-group method given in Section (2.2) of Chapter (2). The explicit form of the stochastic matrices in (3.4.6) and (3.4.7) will depend upon the probabilistic nature of the input data and the way in which they are modelled.

For example, if the uncertainties are described using Gaussian marginal distributions then the Karhunen Loéve expansion may be used to generate realisations of the correlated random data which is a linear function of $\boldsymbol{\xi}$. Conversely, for random data described by any other marginal distribution, the representation of a realisation may be a highly non-linear function of the random variables $\boldsymbol{\xi}$.

3.4.1. Solution of the System of Equations

For stochastic eigenvalue problems, we are interested in calculating the statistics of both the eigenvalue and eigenvector. There are several, very general, methods available for computing these quantities; some are based upon local perturbations of the eigen-pair such as the ASAP method in Section (1.3.2.2), others may be based upon computing an ensemble of eigen-pairs via random sampling such as Latin Hypercube sampling (LHS) from Section (1.3.1.1). More specific research has examined the combination of dimensional decomposition methods and quadrature methods to compute the statistical moments of the random eigen-pair [90].

The methods we are interested in involve using a PCE to represent the variation of the response variables in the parameter space of the variables $\boldsymbol{\xi}$. As such, we expand the eigenvector and eigenvalue as follows:

$$\lambda(\boldsymbol{\xi}) = \sum_{\boldsymbol{\alpha}\in\mathcal{A}^{M,p}} \lambda_{\boldsymbol{\alpha}}\Phi_{\boldsymbol{\alpha}}(\boldsymbol{\xi}) \quad \psi(\boldsymbol{\xi}) = \sum_{\boldsymbol{\alpha}\in\mathcal{A}^{M,p}} \psi_{\boldsymbol{\alpha}}\Phi_{\boldsymbol{\alpha}}(\boldsymbol{\xi}) \tag{3.4.8}$$

which are then substituted into the stochastic eigenvalue equation (3.4.5)

yielding:

$$\sum_{\boldsymbol{\alpha}\in\mathcal{A}^{M,p}} L(\boldsymbol{\xi})\psi_{\boldsymbol{\alpha}}\Phi_{\boldsymbol{\alpha}}(\boldsymbol{\xi}) = \sum_{\boldsymbol{\alpha}\in\mathcal{A}^{M,p}}\sum_{\boldsymbol{\beta}\in\mathcal{A}^{M,p}} \lambda_{\boldsymbol{\beta}}\Phi_{\boldsymbol{\beta}}(\boldsymbol{\xi})F(\boldsymbol{\xi})\psi_{\boldsymbol{\beta}}\Phi_{\boldsymbol{\beta}}(\boldsymbol{\xi}). \tag{3.4.9}$$

The residual in (3.4.9) is minimised requiring it to be orthogonal to the approximation subspace spanned by $\{\psi\}$, resulting in

$$\begin{aligned}\sum_{\boldsymbol{\alpha}\in\mathcal{A}^{M,p}} \psi_{\boldsymbol{\alpha}} &< \Phi_{\boldsymbol{\alpha}}(\boldsymbol{\xi})L(\boldsymbol{\xi})\Phi_{\boldsymbol{\omega}}(\boldsymbol{\xi}) > \\ &= \sum_{\boldsymbol{\alpha},\boldsymbol{\beta}\in\mathcal{A}^{M,p}} \lambda_{\boldsymbol{\beta}}\psi_{\boldsymbol{\alpha}} < F(\boldsymbol{\xi})\Phi_{\boldsymbol{\alpha}}(\boldsymbol{\xi})\Phi_{\boldsymbol{\beta}}(\boldsymbol{\xi})\Phi_{\boldsymbol{\omega}}(\boldsymbol{\xi}) > \quad \omega \in \mathcal{A}^{M,p}\end{aligned} \tag{3.4.10}$$

which can be written as

$$\hat{\boldsymbol{L}}\hat{\boldsymbol{\psi}} = \sum_{\boldsymbol{\beta}\in\mathcal{A}^{M,p}} \lambda_{\boldsymbol{\beta}}\hat{\boldsymbol{F}}_{\boldsymbol{\beta}}\hat{\boldsymbol{\psi}}. \tag{3.4.11}$$

Here $\boldsymbol{\psi}$ is an $\mathcal{N} = (N_P+1)N_{\boldsymbol{r}}N_\Omega N_G$ dimensional vector where N_P is given by Eqn.(3.2.9), $\hat{\boldsymbol{L}}$ is a $(\mathcal{N}\times\mathcal{N})$ matrix, $\hat{\boldsymbol{F}}$ is a $(\mathcal{N}\times\mathcal{N}\times\mathcal{N})$ matrix and the total number of PCE coefficients for the eigenvalue λ is N_P+1. At this point we note that Eqn.(3.4.11) is not a conventional eigen problem. This type of problem has been solved using power type methods [91, 92] and pseudo time dependent methods [52, 93] but in this example we employ a non-linear root-finding technique known as the Newton-Krylov method. This approach has been used to characterise the solution of stochastic eigenvalue problems [94, 95] and particularly, has been used to solve the stochastic k-eigenvalue problem in neutron transport [1].

From equation (3.4.11) we can see that there are $\mathcal{N}+N_P+1$ unknowns but

only $\mathcal{N}$ equations. To derive the additional $N_P + 1$ equations we introduce the constraint:

$$\boldsymbol{\psi}\boldsymbol{\psi}^T = 1 \tag{3.4.12}$$

Expanding the above using a PCE and projecting on to the basis $\Phi_{\boldsymbol{\omega}}$ yields the following $N_P + 1$ equations

$$\sum_{\boldsymbol{\alpha}\in\mathcal{A}^{M,p}} \sum_{\boldsymbol{\beta}\in\mathcal{A}^{M,p}} \boldsymbol{\psi}_{\boldsymbol{\alpha}}\boldsymbol{\psi}_{\boldsymbol{\beta}} \left\langle \Phi_{\boldsymbol{\omega}}(\boldsymbol{\xi})\Phi_{\boldsymbol{\alpha}}(\boldsymbol{\xi})\Phi_{\boldsymbol{\beta}}(\boldsymbol{\xi})\right\rangle = \delta_{\boldsymbol{\omega}0} \tag{3.4.13}$$

It is now convenient to define the solution vector, $\vec{x}$, as follows:

$$\vec{x} = [\boldsymbol{\psi}_0, \cdots, \boldsymbol{\psi}_{N_P}, \lambda_0, \cdots, \lambda_{N_P}]^T \tag{3.4.14}$$

where $\boldsymbol{\psi}_i$ is given by Eqn. (3.4.3).
The residual, $\mathcal{R}(\vec{x})$, of the system of equations then has the form

$$\mathcal{R}_{\psi}(\vec{x}) = \hat{\boldsymbol{L}}\boldsymbol{\psi} - \sum_{\boldsymbol{\beta}\in\mathcal{A}^{M,p}} \lambda_{\boldsymbol{\beta}}\hat{\boldsymbol{F}}_{\boldsymbol{\beta}}\boldsymbol{\psi} \tag{3.4.15}$$

$$\mathcal{R}_{w}(\vec{x}) = \sum_{\boldsymbol{\alpha}\in\mathcal{A}^{M,p}} \sum_{\boldsymbol{\beta}\in\mathcal{A}^{M,p}} \boldsymbol{\psi}_{\boldsymbol{\alpha}}\boldsymbol{\psi}_{\boldsymbol{\beta}} \left\langle \Phi_{\boldsymbol{\omega}}(\boldsymbol{\xi})\Phi_{\boldsymbol{\alpha}}(\boldsymbol{\xi})\Phi_{\boldsymbol{\beta}}(\boldsymbol{\xi})\right\rangle - \delta_{\boldsymbol{\omega}0}. \tag{3.4.16}$$

To linearise the system, the residual is expanded in a tailor series

$$\mathcal{R}(\vec{x} + \vec{\delta x}) = \mathcal{R}(\vec{x}) + J\vec{\delta x} + \mathcal{O}^2 \tag{3.4.17}$$

where J is the Jacobian matrix and is given by the following

$$J = \begin{bmatrix} \frac{\partial \mathcal{R}_{\psi}}{\partial \psi} & \frac{\partial \mathcal{R}_{\psi}}{\partial w} \\ \frac{\partial \mathcal{R}_{w}}{\partial \psi} & \frac{\partial \mathcal{R}_{w}}{\partial w} \end{bmatrix}. \tag{3.4.18}$$

The elements of the Jacobian may, in some circumstances, be calculated exactly by differentiating expressions (3.4.15) and (3.4.16). In general this may not be possible, in which case the elements of the Jacobian may be approximated using the following finite difference relation:

$$J_{ij} \approx \frac{\mathcal{R}_i(x_j + h) - \mathcal{R}_i(x_j)}{h} \tag{3.4.19}$$

To find the solution vector $\vec{x}$ we require the residual of the vector $\mathcal{R}(\vec{x} + \vec{\delta x}) = 0$. This condition yields the following equation for the update vector $\vec{\delta x}$

$$J\vec{\delta x} = -\mathcal{R}(\vec{x}). \tag{3.4.20}$$

Given an initial guess for the solution vector which we denote $\vec{x}^{(0)}$, the solution is updated iteratively by repeatedly solving Eqn.(3.4.20) and updating the solution via

$$\vec{x}^{(k)} = \vec{x}^{(k-1)} + \vec{\delta x} \tag{3.4.21}$$

where $k = 1, \cdots$ is the iteration index. The procedure stops when the L_2 inner product of the residual denoted $||\mathcal{R}(\vec{x}^{(k)}||$ falls below some threshold δ_{NK}. The solution of Eqn. (3.4.20) is performed using an iterative Krylov method and is referred to as the inner Krylov iteration; equation (3.4.21) is the update equation for the solution vector and is referred to as the outer Newton iteration. The solution procedure is outlined in Algorithm (1).

The major strength of the Newton method lies in its local convergence properties. If the initial solution is not sufficiently close to the exact solution, the method described in Algorithm (1) may converge to the wrong solution

Algorithm 1 Newton-Krylov algorithm for the stochastic eigenvalue problems. Superscript (k) denotes iterative index.

1: Initial guess of the solution vector $\vec{x}^{(0)}$
2: **while** $||\mathcal{R}(\vec{x}^{(k)})|| > \delta_{NK}$ **do**
3: Calculate the Jacobian, J.
4: Solve the linear system: $J\vec{\delta x}^{(k)} = -\mathcal{R}(\vec{x}^{(k)})$
5: Update the solution vector: $\vec{x}^{(k+1)} = \vec{x}^{(k)} + \vec{\delta x}^{(k)}$
6: **end while**

or may not converge at all. To improve the radius of convergence, a globally convergent strategy can be combined with the local Newton strategy in a way which derives the benefits of both [96, 97]. One of the simplest of these globalisation procedures is the line search. In this method the Newton update vector, $\vec{\delta x}$, is assumed to be a good direction in which to move. The line search algorithm then produces a scalar value, s, which is used in

$$\vec{x}^{(k+1)} = \vec{x}^{(k)} + s\vec{\delta x}^{k}. \tag{3.4.22}$$

The selection criteria for s requires a reduction in the non-linear residual, namely

$$\mathcal{R}(\vec{x}^{k} + s\vec{\delta x}^{k}) < \mathcal{R}(\vec{x}^{k}). \tag{3.4.23}$$

The value of the scalar s starts as 1. If the criterion from (3.4.23) is not met, s is reduced by a scalar value ρ. This process repeats until the update criterion from (3.4.23) is met or a maximum iteration count is met. The Newton algorithm is now given by Algorithm (2). In practice the value of ρ should be calculated each time within the line search but, from the following arguments, we will show how it may be approximated with a constant. If we assume that s varies quadratically in $[0, 1]$, for the situation where $||\mathcal{R}(\vec{x} + s\vec{\delta x})|| > ||\mathcal{R}(\vec{x})||$, it can be shown [96] that the value of ρ that minimizes $||\mathcal{R}(\vec{x} + s\vec{\delta x})||$ is $\rho \in (0, 0.5]$. As a more conservative estimate we

Algorithm 2 Newton-Krylov algorithm with the backtracking line-search method.

Initial guess of the solution vector $\vec{x}^{(0)}$
while $||\mathcal{R}(\vec{x}^{(\alpha)})|| > \delta_{NK}$ **do**
  Calculate the Jacobian, J, using differencing.
  Solve the linear system: $J\vec{\delta x}^{(\alpha)} = -\mathcal{R}(\vec{x}^{(\alpha)})$
  $s = 1$
  while $||\mathcal{R}(\vec{x}^{(\alpha)} + s\vec{\delta x}^{(\alpha)})|| > ||\mathcal{R}(\vec{x}^{(\alpha)})||$ **do**
    $s = \rho s$
  end while
  Update the solution vector: $\vec{x}^{(\alpha+1)} = \vec{x}^{(\alpha)} + s\vec{\delta x}^{(\alpha)}$
end while

shall take $\rho = 0.5$.

Although the Newton algorithm, with the addition of the line search procedure, now has an improved radius of convergence, it still requires and initial guess of the solution vector $\vec{x}^{(0)}$. The better this guess the smaller the number of Newton iterations needed to converge the solution.

3.5. Example: Static and Dynamic Criticality

In this section we illustrate the above theory using the time eigenvlue and k_{eff} eigenvalue models of criticality. For the present purpose it is sufficient to consider mono-energetic problems in homogeneous media. If we let the energy group boundaries from Eqn.(2.2.13) $[E_{g-1}, E_g] = [0, E_{\max}]$ then Eqns. (2.2.30), (2.2.31) and (2.2.32) for the dynamic (time-eigenvalue) criticality model become

$$\left[\frac{w}{v} - D\nabla^2 + \Sigma_a\right]\psi(\boldsymbol{r}) = (1-\beta)\overline{\nu}\Sigma_f\psi(\boldsymbol{r}) + \sum_{i=1}^{N_d}\lambda_i c_i(\boldsymbol{r}) \tag{3.5.1}$$

and

$$wc_i(\boldsymbol{r}) = \beta_i \overline{\nu} \Sigma_f \psi(\boldsymbol{r}) - \lambda_i c_i(\boldsymbol{r}). \tag{3.5.2}$$

where we have made use of the following relations

$$1 - \beta = \left[1 - \sum_{i=1}^{N_d} \beta_i \right] \tag{3.5.3}$$

and

$$\Sigma_a = \Sigma_t - \Sigma_{s,0}. \tag{3.5.4}$$

Equation (2.2.34) for the static (k_{eff} -eigenvalue) criticality model becomes

$$-D\nabla^2\psi(\boldsymbol{r}) + \Sigma_a \psi(\boldsymbol{r}) = \frac{1}{k_{\text{eff}}} \overline{\nu} \Sigma_f \psi(\boldsymbol{r}). \tag{3.5.5}$$

In both cases, the isotropic neutron flux ψ^0 and the isotropic scattering cross section $\Sigma_{s,0}$ are written simply as ψ and Σ_s. The extraneous source term q has also been ignored and, due to the homogeneity of the problems considered, the spatial dependence of the macroscopic cross sections has been removed.

We now assume that the absorption, scattering and fission cross sections have an associated uncertainty which we represent parametrically using the set of random variables $\boldsymbol{\xi} = \{\xi_1, \xi_2, \xi_3\}$. Each random variable ξ_i is described using a uniform probability distribution of

$$p(\xi_i) = \frac{1}{2} \quad \xi \in [-1, 1]. \tag{3.5.6}$$

Each of the cross sections are modelled as statistically independent with explicit expressions for their uncertainty as a function of $\boldsymbol{\xi}$ given by:

$$\Sigma_a(\xi_1) = \Sigma_a(1 + \sqrt{3}R\xi_1) \tag{3.5.7}$$

$$\Sigma_s(\xi_2) = \Sigma_s(1 + \sqrt{3}R\xi_2) \tag{3.5.8}$$

$$\Sigma_f(\xi_3) = \Sigma_f(1 + \sqrt{3}R\xi_3). \tag{3.5.9}$$

The range of variation in the cross sections is controlled by the relative standard deviation, R, which is defined as

$$R = \frac{\sigma_r}{\overline{\Sigma}_r} \tag{3.5.10}$$

where $\overline{\Sigma}_r$ and σ_r are the mean and standard deviation of the cross section for reaction r.

Now that the uncertainty in the input data has been defined, Eqns. (3.5.1), (3.5.2) and (3.5.5) may be written as

$$\left[\frac{w(\boldsymbol{\xi})}{v} - D(\xi_1, \xi_2)\nabla^2 + \Sigma_a(\xi_1)\right]\psi(\boldsymbol{r}, \boldsymbol{\xi}) = (1-\beta)\overline{\nu}\Sigma_f(\xi_3)\psi(\boldsymbol{r}, \boldsymbol{\xi}) + \sum_{i=1}^{N_d}\lambda_i c_i(\boldsymbol{r}, \boldsymbol{\xi}) \tag{3.5.11}$$

$$wc_i(\boldsymbol{r}, \boldsymbol{\xi}) = \beta_i\overline{\nu}\Sigma_f(\xi_3)\psi(\boldsymbol{r}, \boldsymbol{\xi}) - \lambda_i c_i(\boldsymbol{r}, \boldsymbol{\xi}). \tag{3.5.12}$$

and

$$-D(\xi_1, \xi_2)\nabla^2\psi(\boldsymbol{r}, \boldsymbol{\xi}) + \Sigma_a(\xi_1)\psi(\boldsymbol{r}, \boldsymbol{\xi}) = \frac{1}{k_{\text{eff}}(\boldsymbol{\xi})}\overline{\nu}\Sigma_f(\xi_3)\psi(\boldsymbol{r}, \boldsymbol{\xi}) \tag{3.5.13}$$

noting that the diffusion coefficient D may be approximately expressed in

terms of the absorption and scattering cross sections, namely

$$D(\xi_1, \xi_2) = \frac{1}{3(\Sigma_a(\xi_1) + \Sigma_s(\xi_2))}.$$

At this point it is useful to assume that the system is bare, in which case we may write

$$\psi(\boldsymbol{r}, \boldsymbol{\xi}) = \sum_{s=1}^{\infty} \varphi_s(\boldsymbol{r})\phi_s(\boldsymbol{\xi}) \qquad C_i(\mathbf{r}, \boldsymbol{\xi}) = \sum_{s=1}^{\infty} \varphi_s(\boldsymbol{r})c_{is}(\boldsymbol{\xi}) \tag{3.5.14}$$

where the spatial eigenfunctions $\varphi_s(\boldsymbol{r})$ obey the following conditions

$$\nabla^2\varphi_s(\mathbf{r}) + B_s^2\varphi_s(\mathbf{r}) = 0 \quad \text{and} \quad (\varphi_s(\mathbf{r}), \varphi_q(\mathbf{r})) = \delta_{sq}. \tag{3.5.15}$$

Inserting (3.5.14) into (3.5.11) and (3.5.12) and considering only the fundamental mode (i.e. s=1) yields the following

$$\frac{w(\boldsymbol{\xi})}{v}\phi(\boldsymbol{\xi}) = H(\boldsymbol{\xi}) - \Sigma_a(\xi_1)\phi(\boldsymbol{\xi}) + (1-\beta)\overline{\nu}\Sigma_f(\xi_3)\phi(\boldsymbol{\xi}) + \sum_{i=1}^{M} \lambda_i c_{is}(\boldsymbol{\xi}) \tag{3.5.16}$$

$$w(\boldsymbol{\xi})c_{is}(\boldsymbol{\xi}) = -\lambda_i c_{is}(\boldsymbol{\xi}) + \beta_i\overline{\nu}\Sigma_f(\xi_3)\phi(\boldsymbol{\xi}) \tag{3.5.17}$$

for the time eigenvalue equations and

$$D(\xi_1, \xi_2)B^2\phi(\boldsymbol{\xi}) + \Sigma_a(\xi_1)\phi(\boldsymbol{\xi}) = \frac{1}{k_{\text{eff}}(\boldsymbol{\xi})}\overline{\nu}\Sigma_f(\xi_3)\phi(\boldsymbol{\xi}) \tag{3.5.18}$$

for the k_{eff} eigenvalue equation. In Eqn. (3.5.16) we have made use of the term $H(\boldsymbol{\xi})$ which will help to simplify expressions later when expanding the stochastic variables using PCE. This additional term is defined by the

following relation

$$\frac{-3}{B^2}(\Sigma_a(\xi_1) + \Sigma_s(\xi_2))H(\boldsymbol{\xi}) = \phi(\boldsymbol{\xi}). \tag{3.5.19}$$

3.5.1. Time Eigenvalues

To compute the statistics of the stochastic time eigenvalue and its eigenvector, we use PCE methods combined with the Newton-Krylov algorithms as outlined in Section (3.4.1). To start, we expand the following quantities using PC as follows

$$\begin{aligned} \phi(\boldsymbol{\xi}) &= \sum_{n=0}^{N_P} \phi_n \Phi_n(\boldsymbol{\xi}) \quad C_i(\boldsymbol{\xi}) = \sum_{n=0}^{N_P} c_{in} \Phi_n(\boldsymbol{\xi}) \\ w(\boldsymbol{\xi}) &= \sum_{n=0}^{N_P} w_n \Phi_n(\boldsymbol{\xi}) \quad H(\boldsymbol{\xi}) = \sum_{n=0}^{N_P} H_n \Phi_n(\boldsymbol{\xi}). \end{aligned} \tag{3.5.20}$$

Inserting these expressions into (3.5.16), (3.5.17), (3.5.18) and (3.5.19), projecting onto the orthogonal basis Φ_k and integrating over the probability space yields the following set of coupled non-linear equations

$$\begin{aligned} \frac{1}{v}\sum_{n=0}^{N_P}\sum_{m=0}^{N_P} w_n\phi_m < \Phi_k(\boldsymbol{\xi})\Phi_n(\boldsymbol{\xi})\Phi_m(\boldsymbol{\xi}) > =& < \Phi_k^2(\boldsymbol{\xi}) > H_k \\ &+ \sum_{m=0}^{N_P} \phi_m < \Phi_k(\boldsymbol{\xi}) b(\xi_1, \xi_3)\Phi_m(\boldsymbol{\xi}) > \\ &+ < \Phi_k^2(\boldsymbol{\xi}) > \sum_{i=1}^{M} \lambda_i c_{ik} \end{aligned} \tag{3.5.21}$$

$$\sum_{n=0}^{N_P}\sum_{m=0}^{N_P} w_n c_{im} < \Phi_k(\boldsymbol{\xi})\Phi_n(\boldsymbol{\xi})\Phi_m(\boldsymbol{\xi}) >= -\lambda_i c_i < \Phi_k^2(\boldsymbol{\xi}) > + \beta_i \sum_{m=0}^{N_P} \phi_m < \Phi_k(\boldsymbol{\xi})\overline{\nu}\Sigma_f(\xi_3)\Phi_m(\boldsymbol{\xi}) > \tag{3.5.22}$$

$$\sum_{n=0}^{N_P} < \Phi_k(\boldsymbol{\xi})\tilde{d}(\xi_1,\xi_2)\Phi_n(\boldsymbol{\xi}) > H_n =< \Phi_k^2(\boldsymbol{\xi}) > \phi_k \tag{3.5.23}$$

where

$$\tilde{d}(\xi_1,\xi_2) = \frac{-3}{B^2}(\Sigma_a(\xi_1) + \Sigma_s(\xi_2)) \tag{3.5.24}$$

$$b(\xi_1,\xi_3) = (1-\beta)\overline{\nu}\Sigma_f(\xi_3) - \Sigma_a(\xi_1). \tag{3.5.25}$$

Equations (3.5.21), (3.5.22) and (3.5.23) can be written more conveniently in matrix form as

$$\frac{1}{v}\sum_{n=0}^{N_P} w_n \mathbf{A}_n \vec{\phi} = \vec{H} + \mathbf{B}\vec{\phi} + \sum_{i=1}^{M} \lambda_i \vec{c_i} \tag{3.5.26}$$

$$\sum_{n=0}^{N_P} w_n \mathbf{A}_n \vec{c_i} = -\lambda_i \vec{c_i} + \beta_i \mathbf{F}\vec{\phi} \tag{3.5.27}$$

$$\mathbf{D}\vec{J} = \vec{\phi} \tag{3.5.28}$$

where the matrices are defined as follows:

$$\mathbf{A}_n = \frac{< \Phi_k(\boldsymbol{\xi})\Phi_n(\boldsymbol{\xi})\Phi_m(\boldsymbol{\xi}) >}{< \Phi_k^2(\boldsymbol{\xi}) >} \tag{3.5.29}$$

$$\mathbf{B} = \frac{< \Phi_k(\boldsymbol{\xi})b(\xi_1,\xi_3)\Phi_m(\boldsymbol{\xi}) >}{< \Phi_k^2(\boldsymbol{\xi}) >} \tag{3.5.30}$$

$$\mathbf{F} = \frac{< \Phi_k(\boldsymbol{\xi})\overline{\nu}\Sigma_f(\xi_3)\Phi_m(\boldsymbol{\xi}) >}{< \Phi_k^2(\boldsymbol{\xi}) >} \tag{3.5.31}$$

$$\mathbf{D} = \frac{< \Phi_k(\boldsymbol{\xi})\tilde{d}(\xi_1,\xi_2)\Phi_m(\boldsymbol{\xi}) >}{< \Phi_k^2(\boldsymbol{\xi}) >} \tag{3.5.32}$$

Again, following the procedure in Section (3.4.1), we form a residual from Eqns.(3.5.26), (3.5.27) and (3.5.28) as follows

$$\begin{aligned}\mathcal{R}_\phi(\vec{x}) &= \frac{1}{v}\sum_{n=0}^{N_P} w_n\mathbf{A}_n\vec{\phi} - (\mathbf{D}^{-1}+\mathbf{B})\vec{\phi} - \sum_{i=1}^{M}\lambda_i\vec{c_i} \\ &= \frac{1}{v}\sum_{n=0}^{N_P} w_n\mathbf{A}_n\vec{\phi} - (\mathbf{D}^{-1}+\mathbf{B})\vec{\phi} - \sum_{i=1}^{M}\lambda_i\left[\sum_{n=0}^{N_P} w_n\mathbf{A}_n + \lambda_i\mathbf{I}\right]^{-1}\beta_i\mathbf{F}\vec{\phi}\end{aligned} \tag{3.5.33}$$

$$\mathcal{R}_w(\vec{x}) = \sum_{n=0}^{N_P}\sum_{m=0}^{N_P}\phi_n\phi_m\left\langle\Phi_l(\xi)\Phi_n(\xi)\Phi_m(\xi)\right\rangle - \delta_{l0} \tag{3.5.34}$$

where $\boldsymbol{I}$ is the identity matrix and we have again included the constraint on the stochastic eigenvector to close the system of equations. The PCE coefficients for the delayed precursor concentrations, $\vec{c_i}$, have also been eliminated from the eigenvector residual, $\mathcal{R}_\phi(\vec{x})$, using Eqn.(3.5.27). It is also worth noting that for each residual evaluation, N_d linear systems of equations must be computed, namely:

$$\left[\sum_{n=0}^{N_P} w_n\mathbf{A}_n + \lambda_i\mathbf{I}\right]\vec{c_i} = \beta_i\mathbf{F}\vec{\phi} \qquad (i = 1,\cdots,N_d) \tag{3.5.35}$$

However, the inverse of the matrix $\mathbf{D}$ only needs to be calculated at the

beginning of the NK algorithm.

3.5.2. Static Eigenvalues

Following the same procedure as in Section (3.5.1), we calculate the statistics of the k_{eff} eigenvalue using the PCE method combined with a NK algorithm. We start by using Eqn.(3.5.19) to re-write Eqn.(3.5.18) as follows

$$\Sigma_a(\xi_1)\phi(\boldsymbol{\xi}) - H(\boldsymbol{\xi}) = \lambda(\boldsymbol{\xi})\overline{\nu}\Sigma_f(\xi_3)\phi(\boldsymbol{\xi}) \tag{3.5.36}$$

where

$$\frac{-3}{B^2}(\Sigma_a(\xi_1) + \Sigma_s(\xi_2))H(\boldsymbol{\xi}) = \phi(\boldsymbol{\xi}) \tag{3.5.37}$$

is the transcendental equation for the parameter H. Expanding the response parameters in Eqns.(3.5.36) and (3.5.37) with the following PCEs

$$\lambda(\boldsymbol{\xi}) = \sum_m \lambda_m \Phi_m(\boldsymbol{\xi}) \quad , \quad \phi(\boldsymbol{\xi}) = \sum_n \phi_n \Phi_n(\boldsymbol{\xi}) \quad , \quad H(\boldsymbol{\xi}) = \sum_n H_n \Phi_n(\boldsymbol{\xi})$$

and performing the usual projections yields the following matrix equations

$$(\tilde{\mathbf{B}} - \tilde{\mathbf{D}}^{-1})\vec{\phi} = \sum_n \lambda_n \tilde{\mathbf{A}}_n \vec{\phi} \tag{3.5.38}$$

$$\tilde{\mathbf{D}}J = \phi \tag{3.5.39}$$

where the matrices $\tilde{\mathbf{B}}$, $\tilde{\mathbf{A}}$ and $\tilde{\mathbf{D}}$ are given by the following

$$\tilde{\mathbf{B}} = \frac{< \Phi_k(\boldsymbol{\xi})\Sigma_a(\xi_1)\Phi_n(\xi) >}{< \phi_k^2(\boldsymbol{\xi}) >}$$
$$\tilde{\mathbf{A}}_n = \frac{< \Phi_k(\boldsymbol{\xi})\overline{\nu}\Sigma_f(\xi_3)\Phi_m(\boldsymbol{\xi})\Phi_n(\boldsymbol{\xi}) >}{< \Phi_k^2(\boldsymbol{\xi}) >}$$
$$\tilde{\mathbf{D}} = \frac{< \Phi_k(\boldsymbol{\xi})\tilde{d}(\xi_1,\xi_2)\Phi_m(\boldsymbol{\xi}) >}{< \Phi_k^2(\boldsymbol{\xi}) >}.$$

To solve Eqn.(3.5.38) we follow the same procedure as for the w eigenvalue and introduce the constraint $\phi\phi^T = 1$. We can now define the residual

$$\mathcal{R}_\phi(\vec{x}) = \sum_m \lambda_m \tilde{\mathbf{A}}_m \vec{\phi} - (\tilde{\mathbf{B}} - \tilde{\mathbf{D}}^{-1})\vec{\phi} \tag{3.5.40}$$
$$\mathcal{R}_\lambda(\vec{x}) = \sum_{n=0}^{N_P}\sum_{m=0}^{N_P} \phi_n\phi_m \left\langle \Phi_l(\xi)\Phi_n(\xi)\Phi_m(\xi)\right\rangle - \delta_{l0} \tag{3.5.41}$$

In this situation the components of the Jacobian matrix have an exact form and are given by the following expressions:

$$\frac{\partial \mathcal{R}_\phi}{\partial \phi} = \sum_m \lambda_m \tilde{\mathbf{A}}_m - \tilde{\mathbf{B}} + \tilde{\mathbf{D}}^{-1}$$
$$\frac{\partial \mathcal{R}_\phi}{\partial \lambda_j} = \tilde{\mathbf{A}}_j \vec{\phi}$$
$$\frac{\partial \mathcal{R}_{\lambda_l}}{\partial \phi_p} = 2\phi_p \left\langle \Phi_l(\xi)\Phi_p(\xi)\Phi_p(\xi)\right\rangle + 2\sum_{j\neq p}^{N_P} \phi_j \left\langle \Phi_l(\xi)\Phi_j(\xi)\Phi_p(\xi)\right\rangle$$
$$\frac{\partial \mathcal{R}_\lambda}{\partial \lambda} = 0$$

Equation (3.5.2) may be substituted into (3.5.1) which, after some rearrangement, yields an expression for the reactivity, ρ, in terms of the time eigenvalues, w. This equation is known as the in-hour equation since the solutions, w are usually expressed in inverse hours. The in-hour equation is

the characteristic polynomial for the w-eigenvalue equation with each root corresponding to each eigenvalue w. The number of roots is equal to N_d+1, one more than the number of precursor equations. All roots are strictly negative except for the one corresponding to the fundamental mode which may take a positive value. The reactivity may also be defined in terms of the static k_{eff} eigenvalue as follows:

$$\rho(\boldsymbol{\xi}) = 1 - \frac{1}{k(\boldsymbol{\xi})} = 1 - \lambda(\boldsymbol{\xi}) \tag{3.5.42}$$

expanding in PCE, projecting onto the basis $\Phi_j(\boldsymbol{\xi})$ and integrating yields the following

$$\rho_j = \frac{\delta_{j0}}{< \Phi_j^2 >} - \lambda_j \tag{3.5.43}$$

The solution we obtain from the residuals in (3.5.40) and (3.5.41) via the Newton-Krylov method contains λ. We are also interested in the statistics of k_{eff} which is the inverse of λ. The moments of the inverse expansion, $1/\sum_{i=0}^{N_P} k_i\Phi_i(\boldsymbol{\xi})$, can be recovered via a Galerkin inversion [89]. Starting from the following equation:

$$k\lambda = 1 \tag{3.5.44}$$

we may expand using PCE as follows

$$\sum_{i=0}^{N_P} k_i\Phi_i(\boldsymbol{\xi}) \sum_{j=0}^{N_P} \lambda_j\Phi_j(\boldsymbol{\xi}) = 1. \tag{3.5.45}$$

Projecting (3.5.45) onto the basis $\Phi_j(\boldsymbol{\xi})$ yields the following system of linear

equations

$$\begin{bmatrix} \sum_{i=0}^{N_P} G_{i,0,0}\lambda_i & \cdots & \sum_{i=0}^{N_P} G_{i,N_P,0}\lambda_i \\ \vdots & \ddots & \vdots \\ \sum_{i=0}^{N_P} G_{i,0,N_P}\lambda_i & \cdots & \sum_{i=0}^{N_P} G_{i,N_P,N_P}\lambda_i \end{bmatrix} \begin{bmatrix} k_0 \\ \vdots \\ k_{N_P} \end{bmatrix} = \begin{bmatrix} 1 \\ \vdots \\ 0 \end{bmatrix}. \tag{3.5.46}$$

In the above expression G_{ijk} is the Galerkin multiplication tensor and is given by

$$G_{ijk} = \frac{< \Phi_i \Phi_j \Phi_k >}{< \Phi_k \Phi_k >}. \tag{3.5.47}$$

3.5.3. Results

To illustrate the application of polynomial chaos to stochastic eigenvalue problems we consider a one dimensional slab. The nuclear and geometry data are given in Table (3.2) and the delayed neutron data is given in Table (3.3). The slab has a finite width and, complying with the assumption made in Section (3.5), we assume that the boundaries are bare. Following from this assumption we may define the geometrical buckling, B, as

$$B = \frac{\pi}{a + 2z_0} \quad \text{where} \quad z_0 = \frac{2}{3(\Sigma_a + \Sigma_s)} \tag{3.5.48}$$

is the extrapolation distance.

The uncertainty in the stochastic eigenvalue problems that we consider here comes from the variability in the cross section data. In Eqn.(3.5.48) we can see that the buckling is a function of the cross section data meaning it is also an uncertain quantity. However, for convenience and to reduce the complexity of the resulting expressions, we have assumed that the buckling

is a deterministic quantity calculated from the mean values of the cross section data.

Parameter	Value
Absorption, Σ_a	0.081942 cm^{-1}
Scatter, Σ_s	0.464338 cm^{-1}
Fission, Σ_f	0.054628 cm^{-1}
$\overline{\nu}$	1.718915
Slab width, a	20.0 cm
Velocity, v	2.2×10^5 cm s^{-1}

Table 3.2.: Cross section and geometry data for the one dimensional slab problem from [1].

The nuclear data have been adapted from a problem used by Fichtl [1] in their thesis work. Specifically, the value of ν has been modified to ensure that the deterministic value of k_{eff} =1, i.e. the system is exactly critical using the average value of the cross sections presented in Table (3.2). Thus any uncertainty in the cross sections will give values of k_{eff} or w which differ from one or zero respectively. Uncertainty is introduced into the equations by writing the cross section in the forms described in Eqns. (3.5.7)-(3.5.9).

i	$T^{1/2}(s)$	β_i	λ_i (s^{-1})
1	55.6	0.000230970	1.246667590×10^{-2}
2	24.5	0.001084433	2.829172165×10^{-2}
3	16.3	0.000643618	4.252436690×10^{-2}
4	5.21	0.001387229	0.133041685
5	2.37	0.002330828	0.292467164
6	1.04	0.000635872	0.666487673
7	0.424	0.000571792	1.634781086
8	0.195	0.000161257	3.554600925

Table 3.3.: Delayed neutron data, 8-groups. $\beta = 0.007046$.

As was discussed in Section (3.4.1), the Newton-Krylov method is only locally convergent and therefore requires an initial guess of the solution. In

other words, an approximation of the coefficients in the PCE for both the eigenvalue and eigenvector are required. To produce such approximations, we use the non-intrusive method. This method will be discussed in more detail in Chapter (4) but for now we will acknowledge that the coefficients in the k_{eff} and w eigenvalue expansions may be computed via the following:

$$k_j = \frac{\langle k(\boldsymbol{\xi})\Phi_j(\boldsymbol{\xi})\rangle}{\left\langle \Phi_j^2(\boldsymbol{\xi})\right\rangle} \tag{3.5.49}$$

$$w_j = \frac{\langle w(\boldsymbol{\xi})\Phi_j(\boldsymbol{\xi})\rangle}{\left\langle \Phi_j^2(\boldsymbol{\xi})\right\rangle} \tag{3.5.50}$$

where the notation $< \cdot >$ denotes integration over the probability space. The denominators in equations (3.5.49) and (3.5.50) will, for most common polynomials, have analytic expressions whereas the numerators, in this case, will be evaluated using quadrature. Many types of quadrature are available and are discussed in Section (4.3). For this application we use a non-adaptive sparse grid scheme [3] based upon a Gauss-Legendre quadrature.

The number of dimensions in the integrals of Eqns.(3.5.49) and (3.5.50) is the same as the number of independent random variables used to describe the uncertainty. We consider three situations corresponding to 1,2 and 3 random dimensions. The first situation involves the use of a single random variable to represent the uncertainty in each cross section resulting in all cross section uncertainties being completely correlated. The second situation assumes that the scattering cross section is deterministic, the uncertainty in fission and absorption are modelled independently with their own random variable. The third situation allows all three cross sections to

vary independently of one another resulting in three random dimensions.

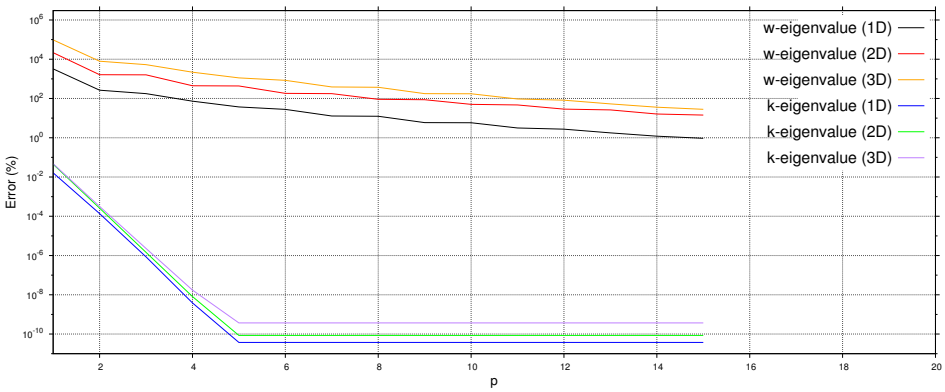
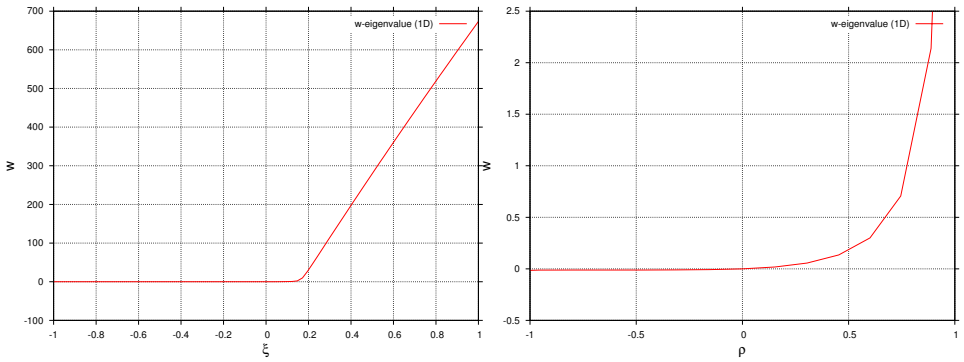


Figure 3.2.: Convergence of the PCE as a function of polynomial order p for 1,2 and 3 stochastic dimensions.

It is important to study the convergence of the PCE as the order of the maximum polynomial increases to ensure the solution is representative of the real answer. In the following example, the non-intrusive approach is used to calculate the coefficients in the PCE. The mean and variance are calculated using Eqns.(3.3.2) and (3.3.3) and compared with a reference solution to yield an error measure for the PCE. The reference solution is computed by directly integrating the eigenvalue (k and w) over the probability space using a high order quadrature scheme. A relative uncertainty in the input parameters of $R = 10\%$ has been used. The percentage errors in the variance of the PCE for 1, 2 and 3 random dimensions are presented in Figure (3.2) for various values of polynomial order p for both k and w eigenvalues. Only the fundamental mode of the time eigenvalues is considered for this example, i.e the largest value of w.

The results in Figure (3.2) show the error in the PCE solution decreases as the maximum polynomial order increases which is to be expected. However, the rate of decrease is significantly different for the k and w eigenvalues.

These differences can be explained if we examine the response of the w-eigenvalue to changes in the uncertain parameters via the random variable $\boldsymbol{\xi}$. In Figure (3.3) the w-eigenvalue is plotted against $\boldsymbol{\xi}$ and also against the reactivity induced from $\boldsymbol{\xi}$. A value of $\boldsymbol{\xi} = 0$ corresponds to the nominal cross section and results in zero values for reactivity and w.



(a) Random variable, ξ (b) Reactivity, ρ

Figure 3.3.: Response of the time eigenvalue, w, to changes in the random variable ξ and reactivity ρ.

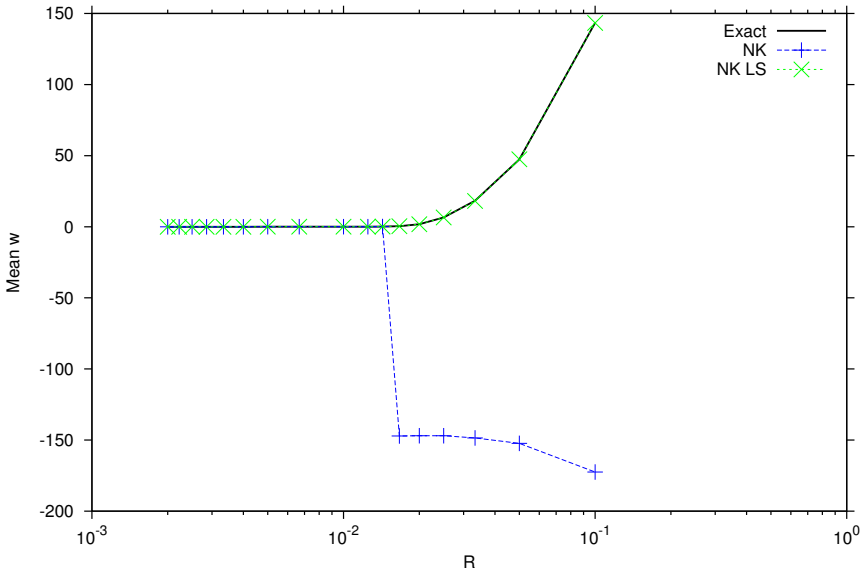
From Figure (3.3a) we can see that as the parameter $\boldsymbol{\xi}$ moves through its range of allowed values, the eigenvalue w exhibits a sharp gradient around $\boldsymbol{\xi} = 0.2$. This sharp gradient is highly non-linear and requires many polynomials to approximate its true shape resulting in the slow convergence rates seen in Fig. (3.2). If we now consider the response of w to the reactivity corresponding to the variations in $\boldsymbol{\xi}$ as in Fig. (3.3a) we may explain the sharp gradients. The reactivity has been normalised by the total delayed neutron fraction β, i.e. it is in units of \$s. We can see that as the reactivity approaches β or 1 dollar of reactivity, a sharp gradient in w occurs. This is because the effect of delayed neutrons is no longer required to make the system critical and the period of the reactor system is proportional to the prompt neutron generation time and independent of the delayed neutron

half lives.

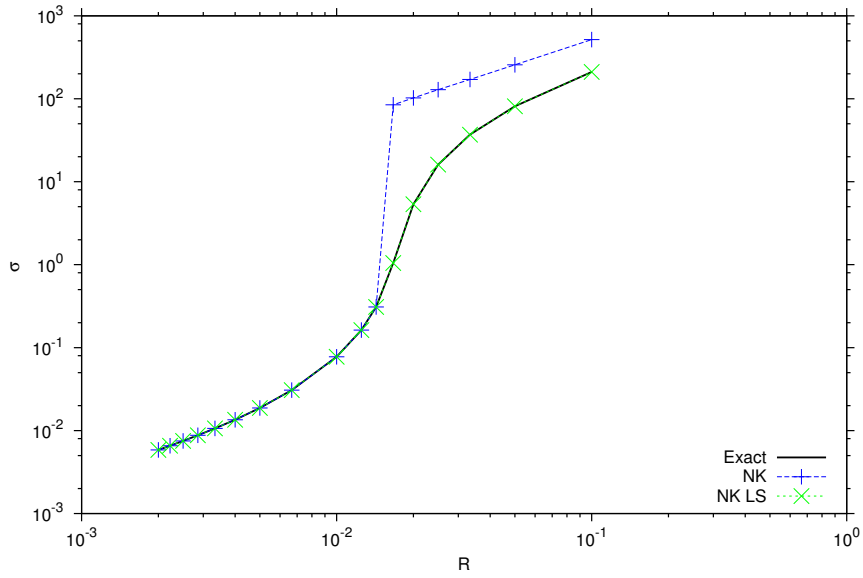
The problems considered so far have been solved using the NISP approach. The purpose of this study, however, is to examine the feasibility of using intrusive methods which utilise Newton-Krylov (NK) algorithms. As such, we start by computing the mean and standard deviations of the fundamental time eigenvalue for a range of relative uncertainties in the cross section data which are represented using a single random variable. Results for the Newton-Krylov (NK) method defined in Algorithm (1) and the NK method with line searching (NKLS) defined in Algorithm (2) are given in Fig.(3.4).

In Figure (3.4a) the mean value of the fundamental time-eigenvalue is plotted as a function of R. Here we can see that the NK algorithm matches the exact/reference solution and then diverges as R increases. The reference solution for the mean and standard deviation were computed by directly integrating over the probability space using a high order quadrature method. The NKLS algorithm corrects this divergence and matches the reference solution for all values of R. The NISP approach does not suffer from this divergence issue. A similar phenomenon is observed in Fig.(3.4b) for the error in the standard deviation of the time-eigenvalue.

The NK and NKLS algorithms, which are used for all of the following examples, have a fixed convergence tolerance of 1.0×10^{-6} for both the outer Newton solve and the inner Krylov solve. The line search algorithm has an additional constraint in the form of the number of times the search direction is bisected. The maximum number of times the line search may be performed was set to 20.



(a) Mean



(b) Standard deviation

Figure 3.4.: Comparison of intrusive NK, NKLS and the reference quadrature solution which is denoted by "Exact". The fundamental time eigenvalue is calculated for a range of relative uncertainties R with one random variable.

M	w eigenvalue		k eigenvalue	
	NKLS	NISP	NKLS	NISP
1	180	170	0.012	$\simeq 0$
2	1600	724	0.18	0.1
3	$20,000^*$	3148	156	5

Table 3.4.: Summary of execution times for the 1,2 and 3 random variable static and dynamic eigenvalue problems computed using both NKLS and NISP methods. Results are in seconds (s).

Table (3.4) presents the execution times for the 1,2 and 3 random variable time eigenvalue and static eigenvalue problems. Both eigenvalue problems are solved using the NISP and NKLS methods. The timing results are an average value computed over many different values of R ranging from $2 \times 10^{-3} \rightarrow 0.1$. Obviously the structure of the stochastic space will change as the relative uncertainty is varied and, as such, the solution times and accuracies will change. However, these results are only meant to give a qualitative comparison of the NISP and NKLS methods whilst increasing the number of dimensions, M. The number of quadrature points in the NISP calculations were chosen to give an accuracy of at least 1.0×10^{-6}, the accuracy set for the NKLS algorithm. The maximum polynomial order $p = 15$ was used for all calculations.

From Table (3.4) we can see that the NISP approach is consistently faster than the NKLS approach for both w and k eigenvalues. We also note that the computation of the w eigenvalue is more expensive than the k eigenvalue, this is for two reasons. Firstly, the initial guess of the solution requires repeated computation of the in-hour equation and secondly, the computation of the Jacobian required for the NKLS algorithm must be performed by differencing of the residual equation. The residual itself requires the

solution of N_d linear systems making the Jacobian computation a costly operation. The results for 3 random dimensions computed using the NKLS algorithm, marked in Table (3.4) with an *, failed to converge for all but the very smallest values of R. The results produced were not significantly more accurate, according to the residual in Eqns.(3.5.33) and (3.5.34), than the initialising NISP solution.

In Table (3.5) the average values and standard deviations of the w eigenvalue and reactivity, ρ, as a function of the relative uncertainty are listed. These have been calculated using the NKLS method defined above with a single random variable used to represent the uncertainty. As R increases, the mean value of the time eigenvalue, $< w >$, is positive and increases whilst the mean value of reactivity, $< \rho >$, is negative and decreases. Thus an uncritical use of static reactivity as a measure of safety margin can be misleading. Of course, once the standard deviation in the reactivity is known then it is obvious that the mean by itself may not be a very useful concept.

In the examples above we have concentrated on the dominant w eigenvalue which determines the asymptotic value of the neutron flux as time increases. However, the NK-algorithm allows us to examine the other w eigenvalues provided we have a sufficient initial guess of the solution vector. As well as the mean and variance, we take the opportunity to calculate the PDF of each of the w modes.

Table (3.6) shows the values of the mean, $< w >$, and standard deviation, σ_w, of all of the roots of the stochastic in-hour equation for values of $R = 0.1$ and $R = 0.01$; we also give the deterministic values of the eigenvalues, w_{det}. From these results it is concluded that the non-fundamental eigenvalues (1-8) are not very sensitive to values of R. In Table (3.7) the mean and

R	$< w >$	σ_w	$< \rho >$ (\$)	σ_ρ
2.0000×10^{-03}	0.001120	0.005840	-0.000117	0.072301
2.2222×10^{-03}	0.001386	0.006565	-0.000167	0.080335
2.5000×10^{-03}	0.001761	0.007507	-0.000239	0.090377
2.8571×10^{-03}	0.002316	0.008785	-0.000342	0.103289
3.3333×10^{-03}	0.003185	0.010624	-0.000502	0.120505
4.0000×10^{-03}	0.004668	0.013518	-0.000767	0.144610
5.0000×10^{-03}	0.007531	0.018742	-0.001255	0.180769
6.6667×10^{-03}	0.014343	0.030748	-0.002310	0.241047
1.0000×10^{-02}	0.039874	0.077626	-0.005324	0.361661
1.2500×10^{-02}	0.081021	0.162737	-0.008376	0.452191
1.4286×10^{-02}	0.142049	0.309508	-0.010973	0.516900
1.6667×10^{-02}	0.384593	1.048937	-0.014975	0.603251
2.0000×10^{-02}	1.817259	5.351786	-0.021616	0.724300
2.5000×10^{-02}	6.573116	16.097176	-0.033854	0.906293
3.3333×10^{-02}	18.312399	37.090311	-0.060351	1.211044
5.0000×10^{-02}	47.383311	81.141142	-0.136486	1.828018
1.0000×10^{-01}	143.385325	210.703288	-0.558918	3.783977

Table 3.5.: Average values of the w eigenvalue and reactivity, ρ, and their standard deviations as a function of the relative uncertainty, R, in the cross section data.

standard deviations of the non-fundamental eigenvalues are shown for a relative uncertainty of $R = 0.01$ for both 1 and 3 random variables. A comparison between the two data sets shows that the mean of eigenvalues 1 to 8 are relatively insensitive to the number of random variables but their standard deviations are certainly sensitive.

In Figs. (3.5) - (3.13) we show the probability density functions of the time-eigenvalues subject to a relative uncertainty of $R = 0.01$ for both one and three random variables. The cases for three random variables have considerably more structure than the one variable cases. We also note that the range of values of w for the 9^{th} to the 2^{nd} eigenvalues when going from 1 to 3 random variables increases by about a factor of 2. However, the range of values of w for the fundamental eigenvalues increases by several orders of

Root	R=0.1		R=0.01		w_{det}
	$< w >$	σ_w	$< w >$	σ_w	
1	-3.172×10^2	3.627×10^2	-1.463×10^2	5.098×10^1	-1.459
2	-2.789	8.630×10^{-1}	-3.472	3.014×10^{-2}	-3.481
3	-1.217	4.225×10^{-1}	-1.504	4.556×10^{-2}	-1.516
4	-5.202×10^{-1}	1.459×10^{-1}	-6.126×10^{-1}	1.637×10^{-2}	-6.165×10^{-1}
5	-2.073×10^{-1}	5.949×10^{-2}	-2.070×10^{-1}	1.793×10^{-2}	-2.082×10^{-1}
6	-8.446×10^{-2}	3.860×10^{-2}	-8.087×10^{-2}	1.773×10^{-2}	-8.200×10^{-2}
7	-3.583×10^{-2}	5.468×10^{-3}	-3.660×10^{-2}	1.802×10^{-3}	-3.678×10^{-2}
8	-1.929×10^{-2}	6.875×10^{-3}	-1.586×10^{-2}	3.017×10^{-3}	-1.435×10^{-2}
9	1.434×10^2	2.107×10^2	3.985×10^{-2}	7.759×10^{-2}	0.0

Table 3.6.: Mean and variance of the time eigenvalue w and static reactivity, ρ. Results have been calculated using a $p = 15$ PCE with one random dimension.

Root	1 Dimension		3 Dimensions	
	$< w >$	σ_w	$< w >$	σ_w
1	-1.463×10^2	5.098×10^1	-1.999×10^2	2.036×10^2
2	-3.472	3.014×10^{-2}	-3.006	7.714×10^{-1}
3	-1.504	4.556×10^{-2}	-1.296	3.642×10^{-1}
4	-6.126×10^{-1}	1.637×10^{-2}	-5.512×10^{-1}	1.166×10^{-1}
5	-2.070×10^{-1}	1.793×10^{-2}	-2.049×10^{-1}	4.696×10^{-2}
6	-8.087×10^{-2}	1.773×10^{-2}	-8.235×10^{-2}	3.348×10^{-2}
7	-3.660×10^{-2}	1.802×10^{-3}	-3.598×10^{-2}	4.459×10^{-3}
8	-1.586×10^{-2}	3.017×10^{-3}	-1.826×10^{-2}	6.126×10^{-3}
9	3.985×10^{-2}	7.759×10^{-2}	5.297×10^1	1.046×10^2

Table 3.7.: Mean and variance of the time eigenvalue w and static reactivity, ρ. Results have been calculated using a $p = 15$ PCE with a relative uncertainty $R = 0.01$.

magnitude. This supports the quoted uncertainties in Table (3.7).

Figures (3.14a) and (3.14b) show the PDFs of the k-eigenvalue for three and one random variables, respectively, for values of $R = 0.01$ and $R = 0.002$. From (3.14a) we can see that the PDFs vary approximately linearly whereas for the 3 dimensional case in (3.14b) the PDFs have a more tri-abgular shape. This is a consequence of the central limit theorem whereby

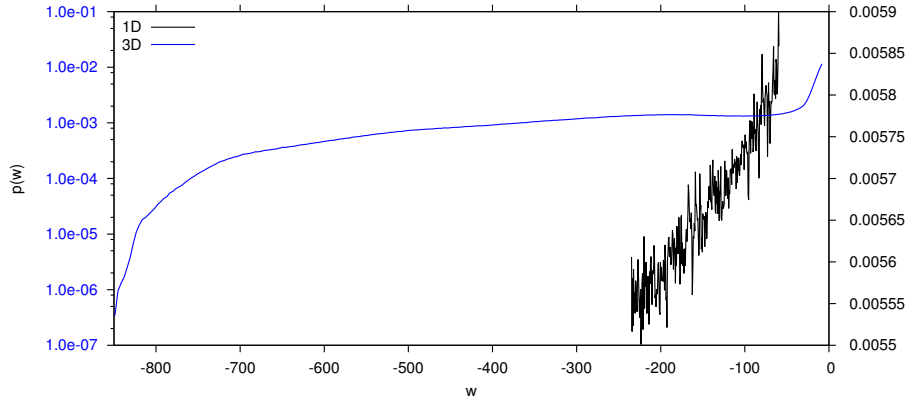


Figure 3.5.: PDF of the 9^{th} time eigenvalue with input relative uncertainties of $R = 0.01$ for 1 and 3 random variables.

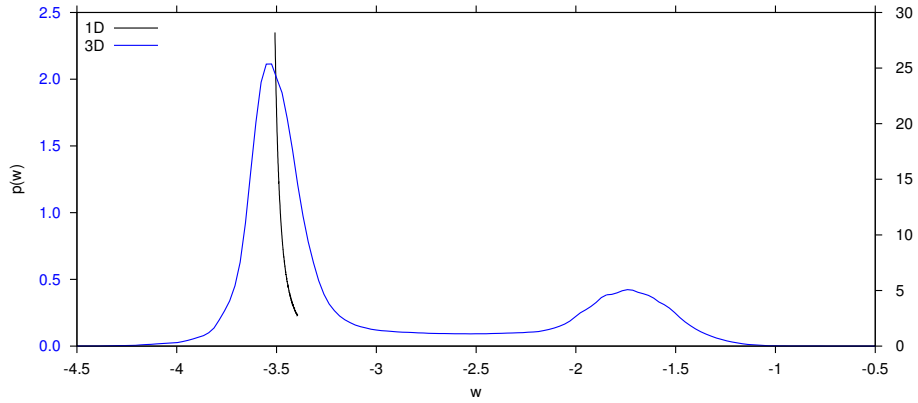


Figure 3.6.: PDF of the 8^{th} time eigenvalue with input relative uncertainties of $R = 0.01$ for 1 and 3 random variables.

many uniformly distributed random variables are combined to produce a single random variable (the reactivity in this case) which has a probability distribution which is converging to the Normal distribution.

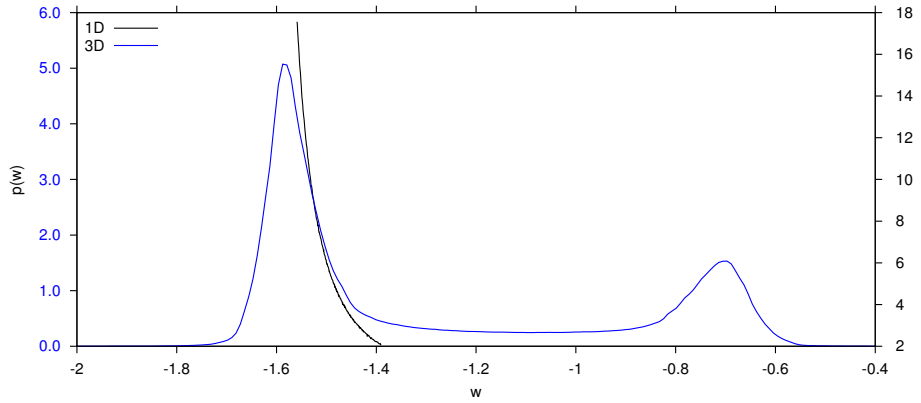


Figure 3.7.: PDF of the 7^{th} time eigenvalue with input relative uncertainties of $R = 0.01$ for 1 and 3 random variables.

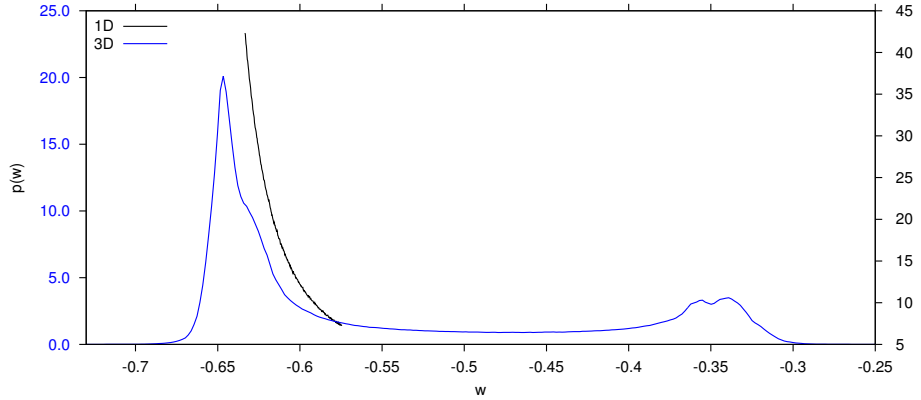


Figure 3.8.: PDF of the 6^{th} time eigenvalue with input relative uncertainties of $R = 0.01$ for 1 and 3 random variables.

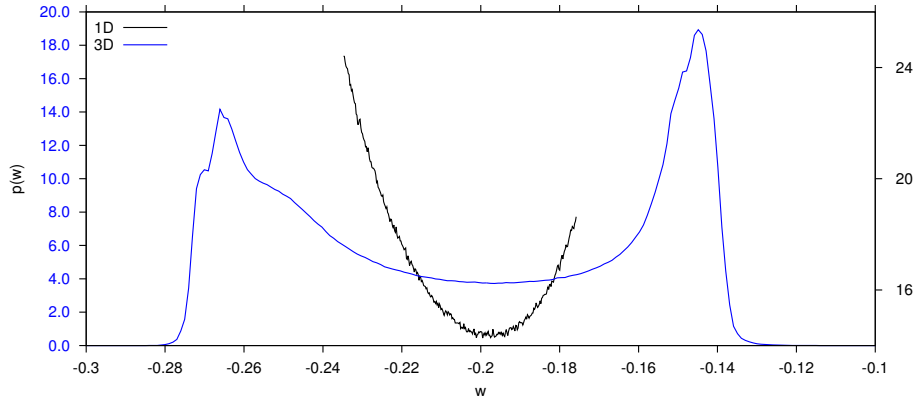


Figure 3.9.: PDF of the 5^{th} time eigenvalue with input relative uncertainties of $R = 0.01$ for 1 and 3 random variables.

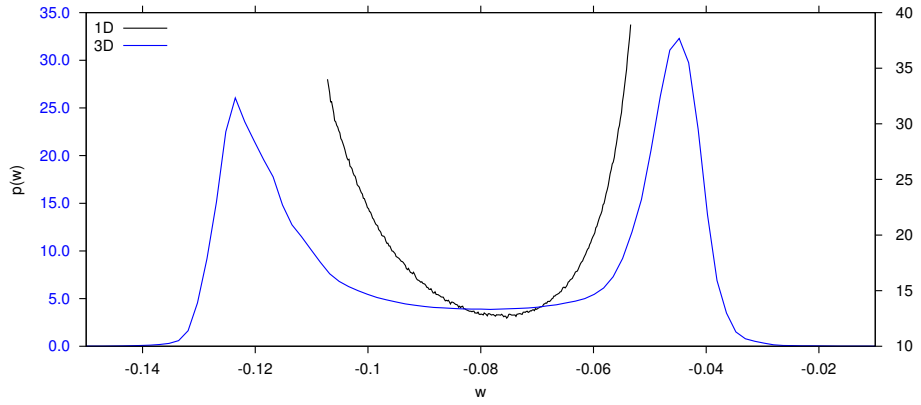


Figure 3.10.: PDF of the 4^{th} time eigenvalue with input relative uncertainties of $R = 0.01$ for 1 and 3 random variables.

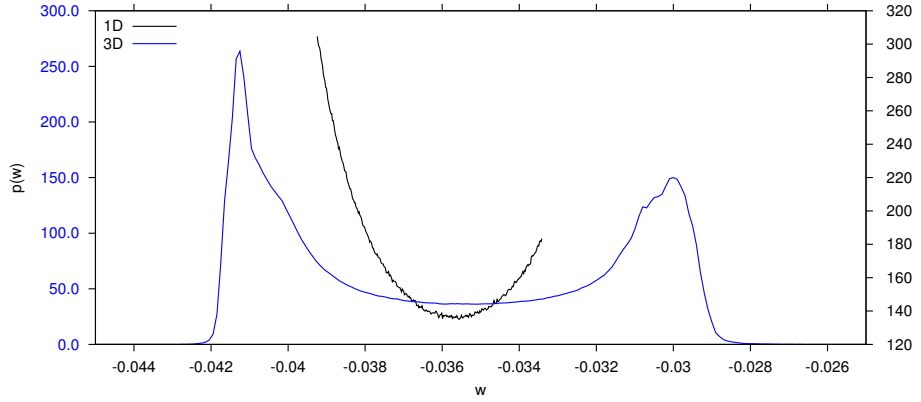


Figure 3.11.: PDF of the 3^{rd} time eigenvalue with input relative uncertainties of $R = 0.01$ for 1 and 3 random variables.

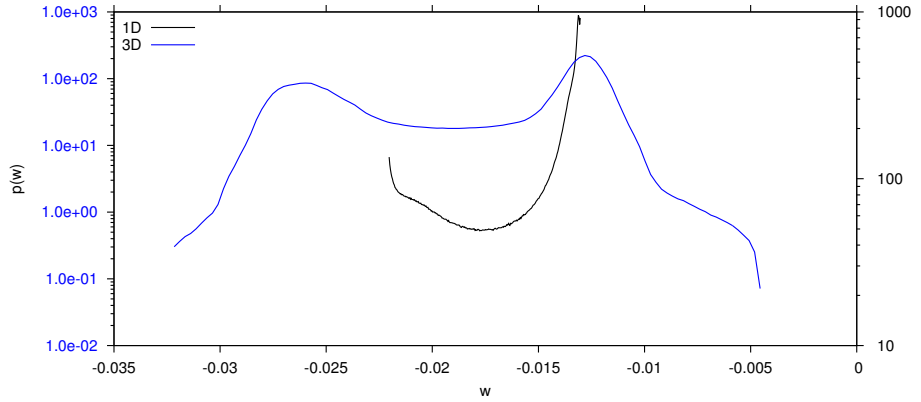


Figure 3.12.: PDF of the 2^{nd} time eigenvalue with input relative uncertainties of $R = 0.01$ for 1 and 3 random variables.

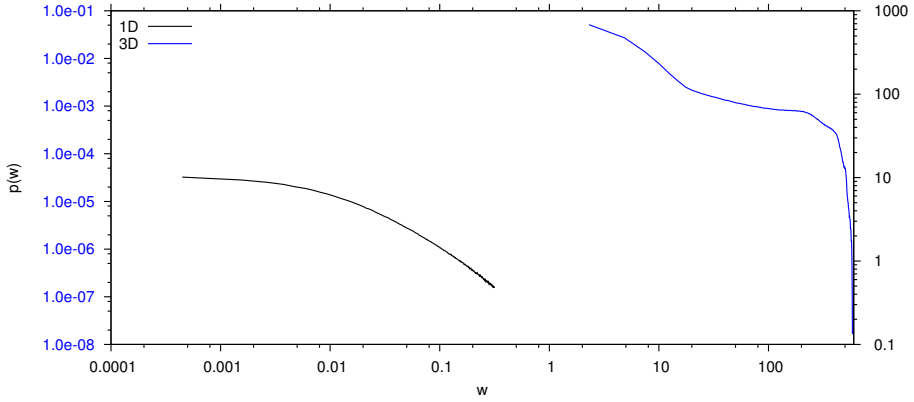
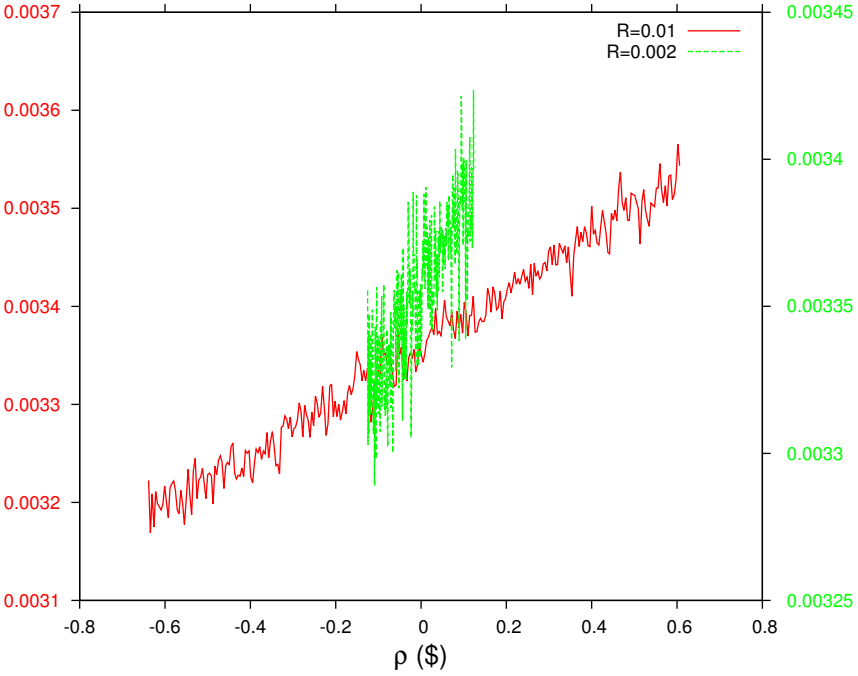
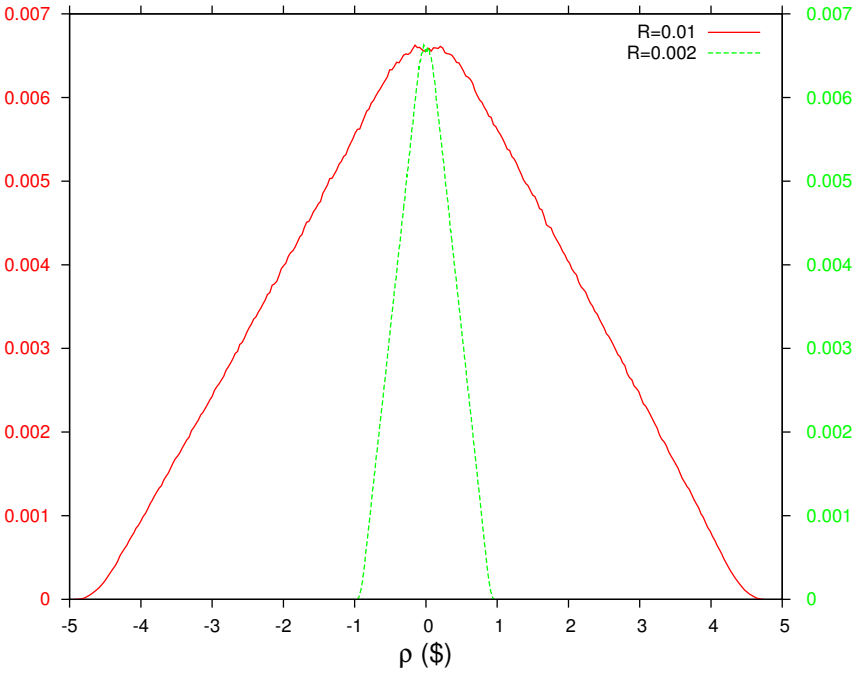


Figure 3.13.: PDF of fundamental time eigenvalue with input relative uncertainties of $R = 0.01$ for 1 and 3 random variables.



(a) 1D



(b) 3D

Figure 3.14.: Probability distribution function for the reactivity ρ.

3.6. Summary and Conclusions

In this chapter we have outlined the theory of polynomial chaos (PC) and shown how a polynomial chaos expansion (PCE) may be used to represent any second order random process. Optimal rates of convergence of the PCE are obtained with an appropriate choice of polynomial basis resulting in a generalised polynomial chaos expansion (gPCE); mixtures of polynomials may also be used, which has been demonstrated in Appendix (B). In section (3.4) the general approach to computing the statistics of stochastic eigenvalue problems using a PCE was outlined. This approach replaced the dependence of the response variables upon the random parameters $\boldsymbol{\xi}$ explicitly using a PCE. This approach is known as the intrusive method. Two examples of the use of an intrusive PCE, the w-eigenvalue and k-eigenvalue, were presented in section (3.5.3).

An important conclusion to be drawn from the examples in this chapter concerns the anomalous behaviour of the mean values of the reactivity, $< \rho >$ and the time constant $< w >$. We have seen that a value of $< \rho > \leq 0$ does not necessarily correspond to a value of the average time constant $< w > \leq 0$, a fact which leads us to suggest that some caution must be exercised when using any static calculation for reactivity safety margins. In actual physical terms, it is the time constant and not the reactivity that determines the behaviour of the system and hence the dynamic response to any uncertainty. One reason for the anomalous behaviour can be seen by reference to Figs. (3.13) and (3.14) which show the probability distributions of the time constant and the reactivity, respectively. The reactivity distribution is reasonably symmetrical about the mean value, whereas the

time constant distribution is highly weighted to positive values. This is due to the presence of delayed neutrons which do not enter the static calculation. However, although the mean values suggest that a negative value of reactivity may result in a positive time constant, w, when considering the uncertainties on $< w >$ (which are consistently above 100% relative to the mean) we cannot say with any certainty that the two methods will not give the same results. This is what we expect, in the deterministic case, when the system is at or near critical.

In their report [78], the authors show that the important differences between static and dynamic reactivity can be attributed to the very different energy spectra for the two cases, which is especially noticeable for reflected systems. When uncertainty is also applied to these energy-dependent problems the difference between static and dynamic results will become even more problematical. Our advice to those wishing to infer uncertainty in criticality, due to cross-section uncertainty, is to compare both methods so that a measure of model uncertainty can be obtained as well as data uncertainty.

A further outcome of this work is a numerical comparison between the NISP and NK/NKLS approaches to calculating stochastic eigenvalues. Both methods are capable of calculating the statistics of the fundamental eigenvalue as well as all other modes. The line search algorithm corrects some of the convergence issues of the basic NK algorithm but still fails to converge the 3 dimensional w eigenvalue problem for large relative uncertainties. From the results in Table (3.4), we have shown that the NISP approach is consistently faster than the intrusive NKLS method. The increase in exe-

cution time as the number of stochastic dimensions increases is significantly less for NISP. The execution time of k-eigenvalue calculations is less than w-eigenvalues due to the reduced complexity of the system of equations and the ability to calculate the elements of the Jacobian exactly without the use of differencing.

A more appropriate method for computing the stochastic time eigenvalues using a PCE and NK-type algorithm would be to use an orthogonal basis in the stochastic space which has a local support. This is motivated by the fact that the response of the time eigenvalue, w, to changes in the random variables $\boldsymbol{\xi}$ exhibits sharp local gradients as the reactivity approaches β, the delayed neutron fraction. A local method such as the Wiener-Harr [54] expansion or the multi-element generalised polynomial chaos expansion (MEgPCE) [57] would provide a much more accurate approximation to the random response with potentially much lower order basis functions. This processes could be optimised further with the implementation of adaptive strategies such as adaptive MEgPCE [56] where the splitting of the stochastic parameter space could be driven by some of the convergence characteristics of the NK and NKLS algorithms.

Finally, and most importantly, we note that the NISP is significantly faster than the intrusive Newton approaches. NISP also exhibits none of the convergence issues associated with gradient-based root finding procedures. In the example, a maximum of 3 random dimensions were used. Extrapolating from the execution times presented in Table (3.4), the execution for several hundred variables, which will readily be the case for industrial scale problems, would make the solution via intrusive methods intractable.

Chapter 4

Non-Intrusive Spectral Projection (NISP)

4.1. Introduction

From the results in Section (3.5) of Chapter (3) we saw that the intrusive polynomial chaos approach can be computationally expensive and difficult to implement; the execution time for both k and w eigenvalues increased rapidly with the number of dimensions. This was in contrast to the non-intrusive approach which required no modification to the deterministic code and showed a significant reduction in execution time, particularly for the w-eigenvalue. For realistic industrial problems, the number of dimensions may number in the hundreds or even thousands which is clearly an intractable amount for the intrusive approach. In this chapter we introduce the non-intrusive spectral projection (NISP) method which may be used to calculate the coefficients of a PCE. This approach projects the response of a model, which is subject to an uncertainty represented using a set of random variables $\boldsymbol{\xi}$, on to a polynomial basis spanning the space of the random variables $\boldsymbol{\xi}$. As we have seen, this projection or integration results in a set of independent evaluations of the physics code similar to a statistical sampling procedure.

In the first section of this chapter the theory of the NISP is introduced. The computational expense of the NISP approach is directly related to the number of quadrature points in the scheme which is a function of the number of random dimensions modelled in the problem. Minimising the number of quadrature points for a given accuracy is therefore key to an efficient NISP strategy; in the second section quadrature rules and adaptive and non-adaptive construction methods used to perform the projection are discussed. The ultimate goal is to build a polynomial chaos representation of the parameter space of the random variables $\boldsymbol{\xi}$. To this end, the third section of this chapter defines a method which uses information derived from the quadrature scheme to build a polynomial chaos surrogate. In the fourth section some analytic tests are used to illustrate the theory and verify the algorithms presented in the previous sections. The final section is dedicated to discussion and conclusions of this chapter.

4.2. Theory

The Non-Intrusive Spectral Projection (NISP) approach computes the coefficients in a PCE by minimising the mean square approximation error of the model response $R(\boldsymbol{x}, \boldsymbol{\xi})$ by the polynomial chaos surrogate. The vector $\boldsymbol{x}$ represents all of the dependent variables in the response such as volume, angle, time and energy. The parameter $\boldsymbol{\xi}$ is a vector of IID random variables representing the uncertainty in the input parameters or boundary conditions etc. To derive an expression for the coefficients in the PCE, we start with

the expansion from Eqn.(3.3.1), namely

$$R(\boldsymbol{x},\boldsymbol{\xi}) = \sum_{\boldsymbol{\alpha}\in\mathcal{A}^{M,p}} R_{\boldsymbol{\alpha}}(\boldsymbol{x})\Phi_{\boldsymbol{\alpha}}(\boldsymbol{\xi}) \tag{4.2.1}$$

where $\mathcal{A}^{M,p}$ is an arbitrary set of polynomial indices. Equation (4.2.1) may be re-written as

$$R(\boldsymbol{x},\boldsymbol{\xi}) = \vec{\boldsymbol{r}}^T(\boldsymbol{x})\vec{\boldsymbol{\Phi}}(\boldsymbol{\xi}) \tag{4.2.2}$$

where

$$\vec{\boldsymbol{r}}^T(\boldsymbol{x}) = \{R_0(\boldsymbol{x}),\cdots,R_{N_P}(\boldsymbol{x})\}^T$$
$$\vec{\boldsymbol{\Phi}}^T(\boldsymbol{\xi}) = \{\Phi_0(\boldsymbol{\xi}),\cdots,\Phi_{N_P}(\boldsymbol{\xi})\}^T$$

noting that N_P+1 is the cardinality of the set $|\mathcal{A}^{M,p}|$. The mean square minimisation problem may then be written as

$$\mathcal{J}(\vec{\boldsymbol{r}}(\boldsymbol{x})) \equiv \mathbb{E}\left[\left(\vec{\boldsymbol{r}}^T(\boldsymbol{x})\vec{\boldsymbol{\Phi}}(\boldsymbol{\xi}) - R(\boldsymbol{x},\boldsymbol{\xi})\right)^2\right]. \tag{4.2.3}$$

where $\mathbb{E}[\cdot]$ denotes the mathematical expectation and amounts to a multi-dimensional integral over the probability space of the random variables $\boldsymbol{\xi}$ with respect to their probability density functions, $p(\boldsymbol{\xi})$. Differentiating the functional, $\mathcal{J}$, with respect to $R_{\boldsymbol{\alpha}}$ gives

$$\frac{d\mathcal{J}}{dR_{\boldsymbol{\alpha}}} = 2R_{\boldsymbol{\alpha}}\mathbb{E}\left[\Phi^2_{\boldsymbol{\alpha}}(\boldsymbol{\xi})\right] - 2\mathbb{E}\left[\Phi_{\boldsymbol{\alpha}}(\boldsymbol{\xi})R(\boldsymbol{x},\boldsymbol{\xi})\right] \tag{4.2.4}$$

The minimality condition $\frac{d\mathcal{J}}{dR_{\boldsymbol{\alpha}}} = 0$ leads to:

$$R_{\boldsymbol{\alpha}} = \frac{\mathbb{E}[R(\boldsymbol{x}, \boldsymbol{\xi})\Phi_{\boldsymbol{\alpha}}(\boldsymbol{\xi})]}{\mathbb{E}[\Phi^2_{\boldsymbol{\alpha}}(\boldsymbol{\xi})]} \quad \forall\ \boldsymbol{\alpha} \in \mathcal{A}^{M,p}. \tag{4.2.5}$$

The denominator in Eqn.(4.2.5) is given by the normalisation constant for the particular polynomial basis and is defined by Eqn. (3.2.4). The numerator, however, must be calculated by an appropriate integration scheme. This multidimensional integral defined by the expectation, $\mathbb{E}$, may be written in the following general form:

$$\boldsymbol{I}f = \int_{\Theta} f(\boldsymbol{\xi}) d\boldsymbol{\xi}. \tag{4.2.6}$$

The integrals are approximated using a weighted sum of the function $f(\boldsymbol{\xi})$ evaluated at different points (nodes) in the parameter space. This approximation is written as follows:

$$\boldsymbol{I}f \approx \sum_i w_i f(\boldsymbol{\xi}_i) \tag{4.2.7}$$

The weighted sum given in Eqn.(4.2.7) is known as a quadrature scheme. The following section is dedicated to describing some of the quadrature techniques used to evaluate high dimensional integrals of the form in (4.2.6).

4.3. Quadrature Methods

The goal of this section is to define an integration strategy which optimally computes multidimensional integrals. To take full advantage of any smoothness present in the integrand, hence reducing the number of quadrature points, an adaptive strategy will ultimately be used. Initially, different

one dimensional quadrature rules are discussed in terms of their range of integration and method of construction. Once appropriate rules have been chosen, the construction of multivariate rules are discussed using tensor products and then sparse grids using Smolyak algorithm [3]. In section (4.3.4) an adaptive sparse grid algorithm is introduced from the work by Gerstner [4, 68] where an error measure based upon the variance of the integrand has been used to refine the quadrature points.

4.3.1. Uni-variate Rules

In this section we briefly describe some of the different types of interpolatory quadrature methods that are used for numerical integration and then outline in more detail some of the rules that will be used with this work. We now define a quadrature rule, with an order or level given by $\mathcal{L}$, as follows

$$U_{\mathcal{L}}(f) = \sum_{i=1}^{n_{\mathcal{L}}} w_i f(x_i) \tag{4.3.1}$$

where $n_{\mathcal{L}}$ is the number of points or nodes in the quadrature scheme corresponding to a level $\mathcal{L}$.

We now draw on two important distinctions when deciding between quadrature rules for this work; whether successive quadrature rules are nested and whether the nodes in each rule are constrained. A sequence of quadrature rules is nested if the nodes of $U_{\mathcal{L}_i}$ are a subset of the nodes of $U_{\mathcal{L}_j}$ for $j > i$. Nested schemes allow the re-use of existing function evaluations which is important for implementing efficient adaptive strategies.

As we have already mentioned, the accuracy of an integration scheme

is important. A quadrature rule is said to have a degree of polynomial exactness equal to d if it is exact for all polynomials of degree $\leq$ d (in one dimensions). The degree of polynomial exactness for constrained rules lies somewhere between $n \leq \deg(U_n) \leq 2n-1$ depending on the order of the interpolating polynomials [98]. Examples of constrained methods are Newton-Cotes type rules where the nodes are chosen to be equally spaced. The advantage of using a constrained rule is that it may be nested by construction. The optimal degree of accuracy, $2n-1$, is obtained with unconstrained, Gaussian-type rules.

Gaussian type rules are available for [0,1] (Gauss-Legendre) and $\mathbb{R}$ (Gauss-Hermite) but are not nested. For Gauss-Legendre rules, an n+1 point extension to an n-point rule is available [99](known as a Konrod extension or Gauss-Patterson rule). This produces a 2n+1 point rule that is nested by construction. This rule has a degree of accuracy $\deg(U_n) = \frac{1}{2}(3n+1)$ for odd n which is lower than the regular Gauss-Legendre rule but does have the advantage of being nested. An analogous procedure for the Gauss-Hermite rule on $\mathbb{R}$ has been proposed [100] and is known as the Genz-Keister rule. This method is available for rules with n=1,3,9,19 and 35 and has an accuracy of $\deg(U_n) \approx \frac{3}{2}n$.

Another important quantity for describing the accuracy of a quadrature rule is the level. The number of nodes corresponding to a given level, which we have denoted $\mathcal{L}$, depends on whether a quadrature rule is nested and whether it is open, closed or semi-open. For a closed rule, nodes are allowed on the boundary of the domain, whereas, open rules never have nodes on the boundary. Semi-open rules are a combination of both open and closed.

For a given level, in one dimension, the number of nodes, $n_{\mathcal{L}}$, is calculated using a growth rule. In this work, we have used the following exponential growth rules:

$$\begin{array}{ll} 2^{\mathcal{L}}+1 & \text{Closed rules} \\ 2^{\mathcal{L}+1}-1 & \text{Open rules} \end{array} \qquad \mathcal{L} \geq 1 \tag{4.3.2}$$

For $\mathcal{L}=0 \quad , n_{\mathcal{L}}=1$.

4.3.2. Tensor Product Quadrature Rules

Tensor product quadrature rules, as the name suggests, are built from tensor products of the weights and nodes of one dimensional quadrature rules. The M dimensional tensor product, which we denote $P_{\boldsymbol{\mathcal{L}}}(f)$, is given by the following

$$P_{\boldsymbol{\mathcal{L}}}(f) = \bigotimes_{i=1}^{M} U_{\mathcal{L}_i}(f) \tag{4.3.3}$$

which may be written explicitly in terms of the one dimension rules as

$$P_{\boldsymbol{\mathcal{L}}}(f) = \sum_{i_1=1}^{n_{\mathcal{L}_1}} \cdots \sum_{i_M=1}^{n_{\mathcal{L}_M}} w_{i_1} \cdots w_{i_m} f(x_{i_1} \cdots x_{i_M}). \tag{4.3.4}$$

In Eqns.(4.3.3) and (4.3.4) the bold type symbol $\boldsymbol{\mathcal{L}}$ is a vector of quadrature levels detailing the level of the one dimensional quadrature rule for each of the M dimensions, namely $\boldsymbol{\mathcal{L}} = \{\mathcal{L}_1, \cdots, \mathcal{L}_M\}$.

The number of terms in the quadrature rule is given by

$$N = \prod_{i=1}^{M} n_{\mathcal{L}_i} \tag{4.3.5}$$

4.3.3. Smolyak Sparse Grids

From Eqn.(4.3.5) we can see that the number of points in a tensor product quadrature rule increases exponentially with the number of dimensions M. Therefore, tensor product rules are only suitable for problems with a low number of dimensions. To reduce the number of points in a multivariate quadrature rule, without adversely affecting the accuracy, the sparse grid construction was proposed [3]. Sparse grids are built upon tensor products of hierarchical difference sets of one dimensional quadrature rules, U_k, as follows:

$$\Delta_k := U_k - U_{k-1} \quad \text{with} \quad U_0 = 0 \tag{4.3.6}$$

for $k \geq 1$. A univariate quadrature rule can then be built from a summation of these difference sets, namely

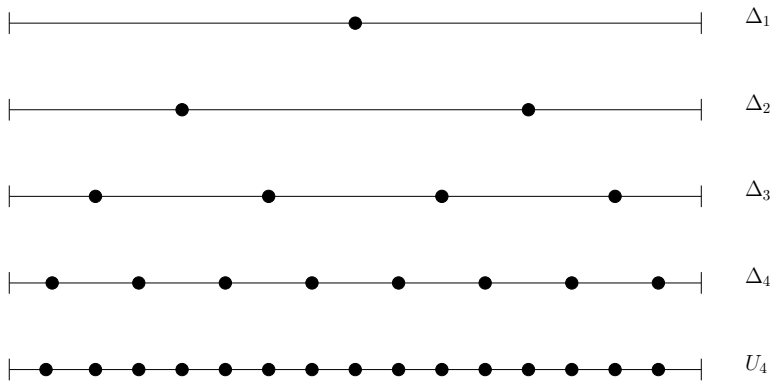


Figure 4.1.: Hierarchical difference spaces of a level $\mathcal{L}$=4 univariate Newton-Cotes quadrature rule.

$$U_{\mathcal{L}} = \sum_{m=1}^{\mathcal{L}} \Delta_m. \tag{4.3.7}$$

This is shown for a level $\mathcal{L} = 4$ Newton-Cotes type formula in Fig.(4.1). The Smolyak construction, which we denote $A(\mathcal{L}, M)$, for a M dimensional quadrature rule of total level $\mathcal{L}$ is written as

$$A(\mathcal{L}, M) = \sum_{|\boldsymbol{k}|_1 \leq M+\mathcal{L}-1} \bigotimes_{i=1}^{M} \Delta_{k_i} \tag{4.3.8}$$

here $|\boldsymbol{k}|_1 = \sum_{i=1}^{M} k_i$ is the L_1 norm. Thus, out of all the possible sets $\boldsymbol{k} \in \mathbb{N}$, only those are chosen whose 1-norm is smaller than a constant. If, instead, we use the $|\boldsymbol{k}|_\infty$ norm

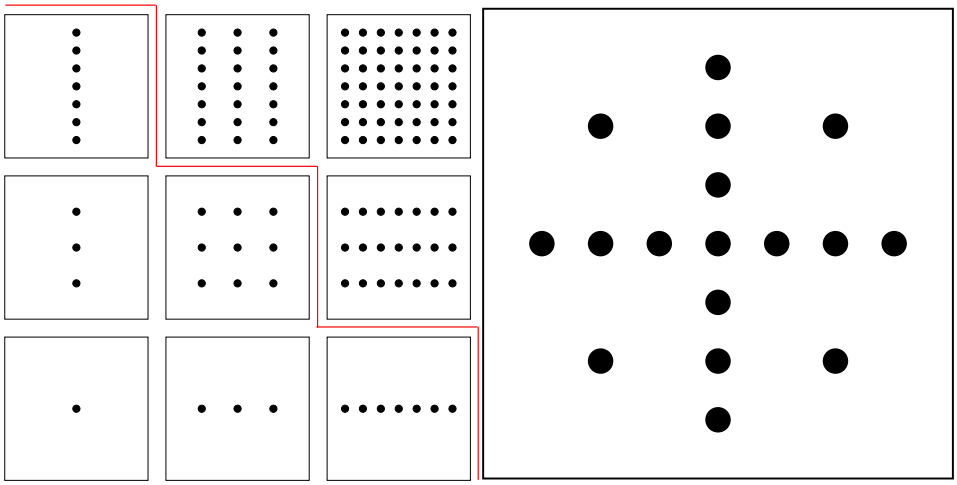
$$A(\mathcal{L}, M) = \sum_{k_1=1}^{\mathcal{L}} \cdots \sum_{k_M=1}^{\mathcal{L}} \Delta_{k_1} \otimes \cdots \otimes \Delta_{k_M} \tag{4.3.9}$$

and we recover the tensor product formula (4.3.4) where the level for each dimension is equal to $\mathcal{L}$. For numerical purposes it is more convenient to rewrite (4.3.8) in terms of the univariate rules U_k. The tensor product of the difference sets $\Delta_{\boldsymbol{k}}$ for an index set $\boldsymbol{k}$ is given by [101]

$$\bigotimes_{i=1}^{M} (U_{k_i} - U_{k_i-1}) = \sum_{\boldsymbol{\alpha} \in \{0,1\}^M} (-1)^{|\boldsymbol{\alpha}|_1} \bigotimes_{i=1}^{M} U_{k_i-\alpha_i}. \tag{4.3.10}$$

If we let $k_i = j_i + \alpha_i$, the right hand side of Eqn.(4.3.8) can be replaced with (4.3.10) provided the index set $\boldsymbol{\alpha}$ is subject to the following constraint: $|\alpha| \leq M + \mathcal{L} - 1 - |\boldsymbol{j}|$. Equation (4.3.8) is now written

$$A(\mathcal{L}, M) f = b(M + \mathcal{L} - 1 - |\boldsymbol{k}|, M) \left(\bigotimes_{i=1}^{M} U_{k_i} \right) f \tag{4.3.11}$$



(a) (b)

Figure 4.2.: Example of a Smolyak [3] sparse grid construction with a level $\mathcal{L} = 3$ Newton-Cotes quadrature. Allowed indices are below the red line.

where

$$\begin{aligned} b(a,b) &= \sum_{\boldsymbol{\alpha}\in\{0,1\},|\boldsymbol{\alpha}|\leq a} (-1)^{|\boldsymbol{\alpha}|} \\ &= \sum_{i=0}^{\min(a,b)} (-1)^i \sum_{\boldsymbol{\alpha}\in\{0,1\},|\boldsymbol{\alpha}|=i} 1 \\ &= \sum_{i=0}^{\min(a,b)} (-1)^i \binom{b}{i} \\ &= (-1)^a \binom{b-1}{a}. \end{aligned} \tag{4.3.12}$$

Using (4.3.12), (4.3.11) now has the form

$$A(l,M)f = \sum_{M \leq |\boldsymbol{k}|_1 \leq \mathcal{L}+M-1} (-1)^{M+\mathcal{L}-1-|\boldsymbol{k}|} \begin{pmatrix} M-1 \\ |\boldsymbol{k}|-\mathcal{L} \end{pmatrix} \left(\bigotimes_{i=1}^{M} U_{k_i} \right) f \tag{4.3.13}$$

The construction of a sparse grid using Eqn.(4.3.13) is illustrated in Fig.(4.2). Here we can see that only those indices on the simplex $|\boldsymbol{k}|_1 \leq M + \mathcal{L} - 1$ are used in the construction. Since $M = 2$ and $\mathcal{L} = 3$, the norm $|\boldsymbol{k}|_1 \leq 2$ thus only the following indices are allowed: $(1,1)$; $(1,2)$; $(1,3)$; $(2,2)$; $(2,1)$; $(3,1)$.

4.3.4. Adaptive Sparse Grids

For highly anisotropic multivariate integrands, the ability to use a different order quadrature scheme along different dimensions can improve both accuracy and efficiency. The fundamental idea behind adaptive sparse grids is to place different emphasis upon different dimensions. One approach is to replace the conventional sparse grid index set: $|\boldsymbol{k}|_1 = \mathcal{L} + M - 1$ with $a \cdot \boldsymbol{k} \leq \mathcal{L} + M - 1$ where a is a weight vector [69]. Here the weights were chosen based on the exponential convergence rate of the integral in each direction with respect to the number of quadrature nodes. This method was shown [69] to perform well (using Clenshaw-Curtis rules) for problems up to 121 dimension when compared with conventional Monte Carlo approaches. However, it may not be possible to estimate the vector a accurately *a-priori* and *a-posteriori* error estimates can be difficult to evaluate for practical problems. An alternative approach proposed in [4, 68] uses a self adaptive algorithm to iteratively build the optimum index set for the required integral. This construction leads to what is known as a generalised sparse grid.

To describe the theory behind the generation of a generalised sparse grid, it is useful to firstly define the admissibility condition on the index sets, viz

$$\boldsymbol{k} - \boldsymbol{e}_j \in \mathcal{I} \quad \text{for} \quad 1 \leq j \leq M, \quad k_j > 1 \tag{4.3.14}$$

where $\boldsymbol{e}_j$ is a unit vector in the direction j and $\mathcal{I}$ is the set of all chosen indices $\boldsymbol{k}$. Equation (4.3.14) says that, for a new index $\boldsymbol{k}$, the previous order along each direction in $\boldsymbol{k}$ must already exist for the new index to be allowed. As an example, we consider a graphical representation of a two dimensional adaptive integration in Figure (4.3). Here active and current indices are only placed in positions when their left and bottom faces are connected to a member of the old index set, i.e. a member of the old set is in the backward neighbourhood of the proposed index. Admissible forward neighbours are denoted with an arrow.

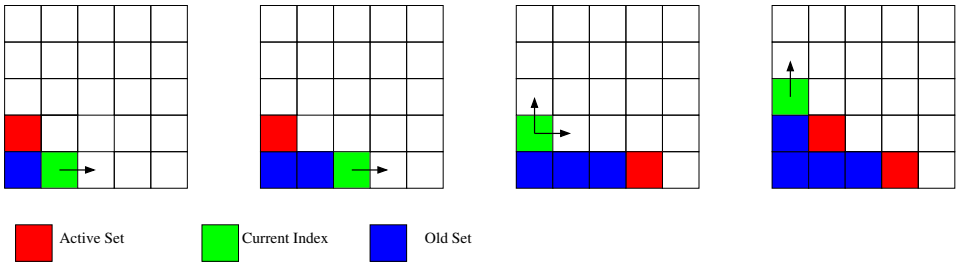


Figure 4.3.: Example of an adaptive sparse grid procedure showing the active and old index sets. The current index is also shown with the admissible forward neighbours denoted by a forward pointing arrow.

With the admissibility condition in (4.3.14), the generalised sparse grid is defined as

$$A(\mathcal{I}) = \sum_{\boldsymbol{k} \in \mathcal{I}} \bigotimes_{i=1}^{M} \Delta_{k_i}. \tag{4.3.15}$$

Equation (4.3.15) is not immediately useful in its current form, it is more practical to use Eqn.(4.3.10) and express $A(\mathcal{I})$ in terms of the univariate quadratures U_l, namely

$$A(\mathcal{I}) = \sum_{\boldsymbol{k}\in\mathcal{I}} \left(\sum_{\boldsymbol{\alpha}\in\{0,1\}^M} (-1)^{|\boldsymbol{\alpha}|_1} \chi_{\mathcal{I}}(\boldsymbol{k}+\boldsymbol{\alpha}) \right) \bigotimes_{i=1}^{M} U_{k_i} \tag{4.3.16}$$

where the indicator variable $\chi_{\mathcal{I}}$ is defined as

$$\chi_{\mathcal{I}}(\boldsymbol{k}) = \begin{cases} 1 & \text{if } \boldsymbol{k} \in \mathcal{I} \\ 0 & \text{else} \end{cases} . \tag{4.3.17}$$

What remains now is to define a measure which describes the importance of each of the indices in the set $\mathcal{I}$.

4.3.4.1. Error Measures

In order for the adaptive algorithm to be successful, there must be some way to predict the importance of an index $\boldsymbol{k}$. In essence, these importance or error measures control the adaptive refinement of the algorithm. If the error measure of an index $\boldsymbol{k}$ is below some threshold then there will be no more refinement in the forward direction of this index. This criteria assumes that the error associated with an index decreases monotonically in the forward direction.

The error indicator for index $\boldsymbol{k}$ is denoted by $g_{\boldsymbol{k}}$ and depends on the differential integral of the function we are integrating. The differential integral

is given by

$$\Delta_{\boldsymbol{k}} f = U_{\boldsymbol{k}} f - U_{\boldsymbol{k-1}} f \tag{4.3.18}$$

which is the value of the integral including the new index $\boldsymbol{k}$ less the previously calculated indices. In the majority of uncertainty studies, it is the variance of a function which is the quantity of interest and therefore the adaptive procedure must be tuned to calculate this quantity. As such, we also use the square of the differential integral, namely

$$\Delta^2_{\boldsymbol{k}} f = U_{\boldsymbol{k}} f^2 - U_{\boldsymbol{k-1}} f^2 \tag{4.3.19}$$

The quantity in (4.3.19) tells us by how much the square of the integral has changed when the newly calculated index $\boldsymbol{k}$ has been added. The final accuracy of the integral of this absolute measure is of course problem dependent and may result in large relative errors if the value of the integral is small. As such, we have chosen to use the square of the differential integral relative to the square of the integral, viz

$$g_{\boldsymbol{k}} = \frac{\Delta^2_{\boldsymbol{k}} f}{U_{\boldsymbol{k-1}} f^2} \tag{4.3.20}$$

In [4] the authors defined an adaptive generalised sparse grid algorithm for computing high dimensional integrals. We reproduce this algorithm in Algorithm(3) for convenience, the only fundamental difference being the use of a different error measure. In words, the algorithm proceeds as follows: Firstly, the active set, $\mathcal{A}$, is initialised with the index corresponding to the nominal value of the function which is assumed to have already been

calculated. The old index set, $\mathcal{O}$, is empty, the total error, r, is set to the error of the nominal index, and the integral value, I, is initialised with the contribution from the nominal index. The adaptive algorithm will proceed while the total error is less than a predefined threshold δ_{Quad}. To begin with, within the iterative loop, the index with the largest error, $g_{\boldsymbol{k}}$, is chosen from the active set. This index is then removed from the active set, appended to the old set and its associated error removed from the total error. The next part of the algorithm computes the admissible forward neighbours of the current index. Each allowed index is added to the active set, its contribution to the value of the integral is appended and its associated error added to the total.

Algorithm 3 Adaptive sparse grid algorithm proposed by Gerstner [4].

$\boldsymbol{k} = (0, 0, \cdots, 0)$
$\mathcal{O} = \emptyset$
$\mathcal{A} = \{\boldsymbol{k}\}$
$r = g_{\boldsymbol{k}}$
$I = \Delta_{\boldsymbol{k}} f$
while $r <\delta_{\text{Quad}}$ **do**
  Choose $\boldsymbol{k} \in \mathcal{A}$ with largest $g_{\boldsymbol{k}}$
  $\mathcal{O} = \mathcal{O} \cup \boldsymbol{k}$
  $\mathcal{A} = \mathcal{A} \setminus \boldsymbol{k}$
  $r = r - g_{\boldsymbol{k}}$
  for l=1 **to** M **do**
    $\boldsymbol{j} = \boldsymbol{i} + \boldsymbol{e}_l$
    if $\boldsymbol{j} - \boldsymbol{e}_q \in \mathcal{O}$ **for all** $q = 1, \cdots, M$ **then**
      $\mathcal{A} = \mathcal{A} \cup \{\boldsymbol{j}\}$
      $I = I + \Delta_{\boldsymbol{k}} f$
      $r = r + g_{\boldsymbol{j}}$
    end if
  end for
end while

4.4. Computing Polynomial Chaos Expansions Using Sparse Grid Quadratures

The conventional approach to constructing a polynomial chaos expansion is to define it *a-priori* using a formula such as Eqn.(3.2.7). A much more efficient approach would be to build it iteratively or to use some pre-existing information about the function we would like to represent. The quadrature levels in a sparse grid may provide such information. When the adaptive generalised sparse grid algorithm has finished successfully, it yields the integral of the function f using a sparse grid index set, $\mathcal{I}$, which is optimal with respect to the error measure $g_{\boldsymbol{k}}$. This set of indices may be used to infer information about the structure of the integrand in question. I.e. a larger number of quadrature points selected along one direction suggests a higher polynomial behaviour than a direction with fewer quadrature points.

In this section we propose a method of building a PCE directly from the sparse grid quadrature levels. From the level indices of the sparse grid quadrature rule we infer the orders of the polynomials in the PCE. To do this, we start with the polynomial exactness of the univariate quadrature methods from section (4.3.1), viz

$$\deg(U_n) = \frac{1}{2}(3n+1) \qquad \text{Gauss-Patterson} \tag{4.4.1}$$

$$\deg(U_n) = \frac{3}{2}n \qquad \text{Genz-Keister} \tag{4.4.2}$$

where n is the number of points in the quadrature rule. We now insert the expression for the open growth rules from Eqn.(4.3.2) into (4.4.1) and

(4.4.2) which yields

$$\deg(U_n) = 3\left(2^{\mathcal{L}} - \frac{1}{3}\right) \qquad \text{Gauss-Patterson} \tag{4.4.3}$$

$$\deg(U_n) = 3\left(2^{\mathcal{L}} - \frac{1}{2}\right) \qquad \text{Genz-Keister} \tag{4.4.4}$$

we now have an expression for the degree of exactness of the quadrature rule in terms of its level $\mathcal{L}$. Since the quadrature rules are being used to perform a projection of a random response on to a polynomial basis, the maximum polynomial order of the integrand will be twice that of the basis we are projecting onto. In other words, the maximum polynomial order of the basis is half the degree of polynomial exactness of the quadrature rule. We now have the following expressions

$$p = 3\left(2^{\mathcal{L}-1} - \frac{1}{6}\right) \qquad \text{Gauss-Patterson} \tag{4.4.5}$$

$$p = 3\left(2^{\mathcal{L}-1} - \frac{1}{4}\right) \qquad \text{Genz-Keister} \tag{4.4.6}$$

Equations (4.4.5) and (4.4.6) allow us to build a polynomial chaos expansion of a function based upon its structure inferred via its integration.

4.5. Numerical Examples

The following numerical examples have been performed to verify the theory outlined in the above sections. In particular, Test Set 1 comprises of a set of integrals associated with Gaussian probability spaces, uniform probability spaces and a mixture of both which are used to to verify the evaluation of integrals on these common probability spaces. Test Set 2 explores the use of the adaptive sparse grid quadrature scheme focusing on its ability to correctly identify any anisotropy that exists in the integrand. In the final test set, Test Set 3, a simple product of polynomials is used to verify the construction of a polynomial chaos expansion via the sparse grid index set.

4.5.1. Test Set 1

In this first example set we wish to verify that the sparse grid quadrature schemes are evaluating integrals correctly. To do this we define the following test integrands

$$f^{(1)}(\boldsymbol{\xi}) = \prod_{i=1}^{M} \frac{1}{2 + w_i \xi_i^2} = \prod_{i=1}^{M} f_i^{(1)}(\xi_i) \tag{4.5.1}$$

$$f^{(2)}(\boldsymbol{\eta}) = \prod_{i=1}^{M} \cos(\eta_i) = \prod_{i=1}^{M} f_i^{(2)}(\eta_i) \tag{4.5.2}$$

$$\begin{aligned} f^{(3)}(\boldsymbol{\xi}, \boldsymbol{\eta}) &= \left(\prod_{i=1}^{m_1} \frac{1}{2 + w_i \xi_i^2} \right) \left(\prod_{i=1}^{m_2} \cos(\eta_i) \right) \\ &= \left(\prod_{i=1}^{m_1} f_i^{(2)}(\eta_i) \right) \left(\prod_{i=1}^{m_2} f_i^{(1)}(\xi_i) \right) \qquad m_1 + m_2 = M \end{aligned} \tag{4.5.3}$$

where w_i are a set of parameters that control the anisotropy of the integrand and are not to be confused with the weights in the quadrature scheme. The

univariate integrals in the above equations can be evaluated exactly:

$$\int_{-1}^{1} p(\xi_i) f_i^{(1)}(\xi_i) d\xi_i = \frac{\sqrt{w_i}}{\sqrt{2}} \arctan\left(\frac{\sqrt{w_i}}{\sqrt{2}}\right) \tag{4.5.4}$$

$$\int_{-\infty}^{\infty} p(\eta_i) f_i^{(2)}(\eta_i) d\eta_i = e^{-\frac{1}{2}}. \tag{4.5.5}$$

where the weight functions are defined as

$$p(\xi_i) = \frac{1}{2} \tag{4.5.6}$$

$$p(\eta_i) = \frac{1}{\sqrt{2\pi}} e^{-\frac{\eta_i^2}{2}} \tag{4.5.7}$$

Therefore, in the M dimensional case, we have

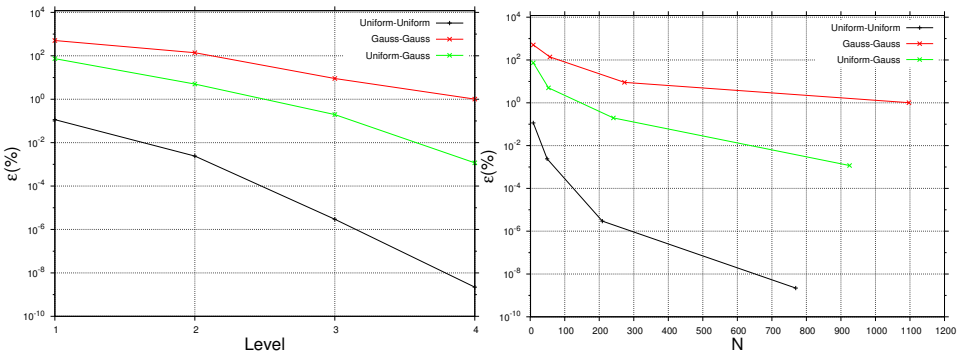
$$\int_{-1}^{1} \prod_{i=1}^{M} p(\xi_i) f_i^{(1)}(\xi_i) d\xi_i = 2^{-\frac{M}{2}} \arctan\left(\frac{\sqrt{w_i}}{\sqrt{2}}\right)^M \tag{4.5.8}$$

$$\int_{-\infty}^{\infty} \prod_{i=1}^{M} p(\eta_i) f_i^{(2)}(\eta_i) d\eta_i = e^{-\frac{M}{2}} \tag{4.5.9}$$

$$\int_{-1}^{1} \prod_{i=1}^{m_1} p(\xi_i) f_i^{(1)}(\xi_i) d\xi_i \int_{-\infty}^{\infty} \prod_{i=1}^{m_2} p(\eta_i) f_i^{(2)}(\eta_i) d\eta_i = w_i^{\frac{m_1}{2}} 2^{-\frac{m_1}{2}} \arctan\left(\frac{\sqrt{w_i}}{\sqrt{2}}\right)^{m_1} e^{-\frac{m_2}{2}}. \tag{4.5.10}$$

In the following example we let $M = 4$, $m_1 = m_2 = 2$ and the values of $w_i = 10^{-(i-1)}$. The values of the integrals in Eqns. (4.5.1) - (4.5.3) are calculated for sparse grid levels 1,2,3 and 4. The relative error is calculated and the results are plotted in Figure(4.4).

From Fig.(4.4) we can see that the convergence of the relative error decreases exponentially with the level of the quadrature rule. We also note that the Gauss-Patterson (uniform) rules are more accurate than the Genz-Keister (Gaussian) with the combination of the two lying somewhere in



(a) Relative error versus Level (b) Relative error versus number of points

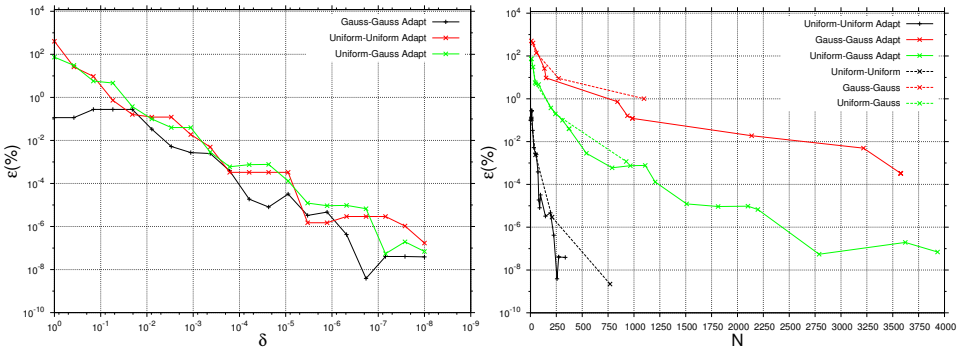
Figure 4.4.: Convergence of the test integrals using sparse grid quadrature schemes for increasing level.

between.

The next test explores the use of the adaptive sparse quadrature algorithm. The values of the integrals in Eqns. (4.5.1) - (4.5.3) are calculated for adaptive tolerances $\delta_{\text{Quad}} = 5 \times 10^{-1} \rightarrow \delta_{\text{Quad}} = 1 \times 10^{-8}$. The relative error is plotted in Fig.(4.5) versus δ_{Quad} and number of points N. In Fig.(4.8a) we can see that the relative error decreases exponentially with the adaptive tolerance. In Fig.(4.8b) the relative error is plotted against the number of points along with the results of the conventional sparse grid from Fig.(4.4b). Here we can see that the adaptive procedure is more efficient than the conventional sparse grid procedure.

4.5.2. Test Set 2

In the following tests we wish to verify that the adaptive sparse grid procedure is correctly capturing the anisotropy of a particular integrand. The following two dimensional integrands are defined as follows



(a) Error versus adaptive tolerance (b) Error versus number of points

Figure 4.5.: Convergence of the test integrals using adaptive sparse grid quadrature schemes for decreasing adaptive tolerance, δ_{Quad} .

$$I_1 = \int_{-1}^{1} dx \int_{-1}^{1} dy \left(\exp\{-x^2\} + \exp\{-y^2\}\right) \tag{4.5.11}$$

$$I_2 = \int_{-1}^{1} dx \int_{-1}^{1} dy \left(\exp\{x\} + \exp\{y\} + xy\right) \tag{4.5.12}$$

$$I_3 = \int_{-\infty}^{\infty} \exp\{-x^2\} dx \int_{-1}^{1} dy \exp\{-x^2 - y^2\} \tag{4.5.13}$$

$$I_4 = \int_{-\infty}^{\infty} \exp\{-x^2\} dx \int_{-\infty}^{\infty} \exp\{-y^2\} dy \left(\exp\{-x^2\} + y\right) \tag{4.5.14}$$

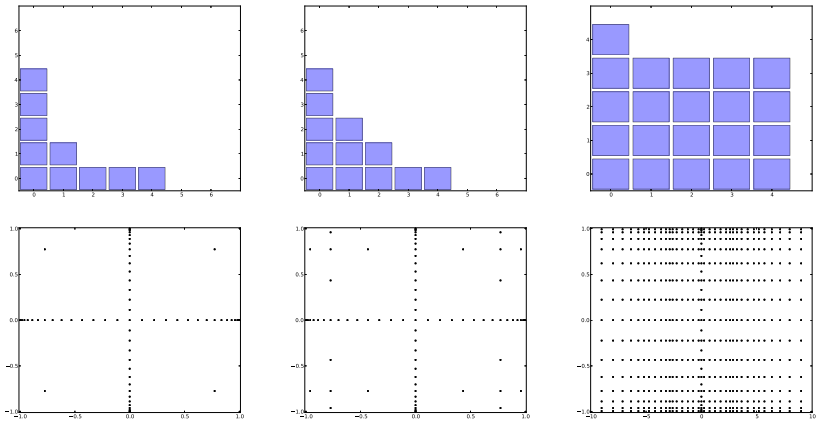
$$I_5 = \int_{-\infty}^{\infty} \exp\{-x^2\} dx \int_{-\infty}^{\infty} \exp\{-y^2\} dy \left(x^2 \exp\{-y^2\} + \exp\{-y^2\}\right) \tag{4.5.15}$$

$$I_6 = \int_{-\infty}^{\infty} \exp\{-x^2\} dx \int_{-1}^{1} dy \frac{1 + 0.1y}{1 + 0.1x} \tag{4.5.16}$$

Integrands $I_1 \to I_3$ are isotropic. I_1 and I_2 are defined on the domain $[-1:1]^2$ whereas I_3 is defined on the mixed domain $[-1:1] \times [-\infty:\infty]$. Integrands $I_4 \to I_6$ are anisotropic where I_4 and I_5 are defined on the domain $[-\infty:\infty]^2$ and I_6 is defined on $[-1:1] \times [-\infty:\infty]$.

In the following examples a tolerance of $\delta_{\text{Quad}} = 1 \times 10^{-12}$ is used for

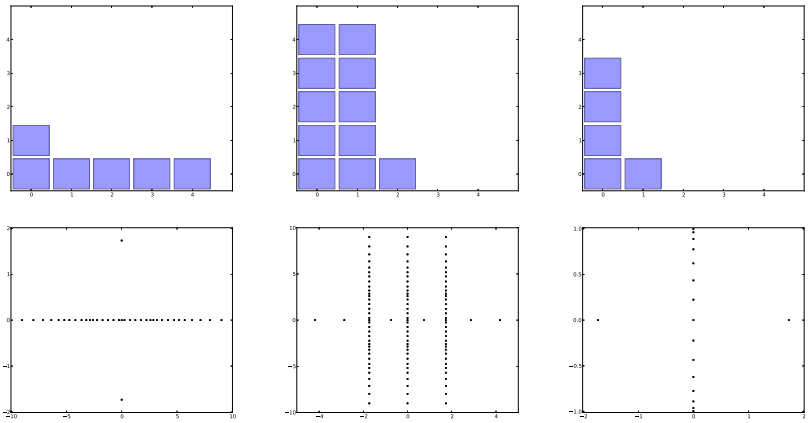
the adaptive procedure. Results of the isotropic integrands are given in Fig.(4.6) and the anisotropic results are given in Fig.(4.7). For all of the following results, each sub-figure is split into a diagram representing the sparse grid indices and also the points associated with the grid. In Fig.(4.6a) the algorithm has only selected the univariate terms; this is because the integrand I_1 is the sum of independent functions of x and y. In Fig.(4.6b) some resolution has been prescribed to the cross terms which is due to the inclusion of the term xy in the integrand I_2. In Fig.(4.6c) the algorithm has selected almost the full tensor product of quadrature points; the indices are not symmetric since the integrand is defined over a mixed domain.



(a) I_1 (b) I_2 (c) I_3

Figure 4.6.: Example of a generalised sparse grid construction for isotropic integrands using Gauss-Patterson and combined Gauss-Patterson and Genz-Keister quadratures.

In all of the anisotropic examples in Fig.(4.7) the algorithm correctly selects the direction which has the most variation or structure admitting quadrature points along directions where there is no dependency.



(a) I_4 (b) I_5 (c) I_6

Figure 4.7.: Example of a generalised sparse grid construction for anisotropic integrands using Gauss-Patterson and combined Gauss-Patterson and Genz-Keister quadratures.

4.5.3. Test Set 3

In the next test we wish to verify the construction of a PCE using the sparse grid level indices as described in Section(4.4). In particular we will calculate the variance using the PCE and compare it to exact results. The variance of a function with respect to the probability measure $p(\xi)$ is calculated using

$$\mathrm{Var}[f] = \int f(\boldsymbol{\xi})^2 p(\boldsymbol{\xi}) d\boldsymbol{\xi} - \int f(\boldsymbol{\xi}) p(\boldsymbol{\xi}) d\boldsymbol{\xi}. \tag{4.5.17}$$

The function that we have chosen is the following:

$$f(\boldsymbol{\xi}) = \prod_{i=1}^{M} (1 + \xi_i) \tag{4.5.18}$$

which is a tensor product of linear polynomials in each dimension. Analytic expressions for the variance of the function in Eqn.(4.5.18) with respect

to the Normal probability weight, the uniform probability weight and a mixture of the two are given as follows:

$$\begin{aligned}
\mathrm{Var}[f_{\mathrm{uni}}] &= \int \prod_{i=1}^{M}(1+\xi_i)^2 p(\xi_i)d\xi_i - \int \prod_{i=1}^{M}(1+\xi_i)p(\xi_i)d\xi_i \\
&= \left(\frac{4}{3}\right)^M - 1 \qquad (4.5.19) \\
\mathrm{Var}[f_{\mathrm{norm}}] &= \int \prod_{i=1}^{M}(1+\eta_i)^2 p(\eta_i)d\eta_i - \int \prod_{i=1}^{M}(1+\eta_i)p(\eta_i)d\eta_i \\
&= 2^M - 1 \qquad (4.5.20) \\
\mathrm{Var}[f_{\mathrm{mix}}] &= \int \left(\prod_{i=1}^{m_1}(1+\eta_i)^2 p(\eta_i)\right)\left(\prod_{i=1}^{m_2}(1+\xi_i)^2 p(\xi_i)\right) d\xi_i d\eta_i \\
&\quad - \int \left(\prod_{i=1}^{m_1}(1+\eta_i)p(\eta_i)\right)\left(\prod_{i=1}^{m_2}(1+\xi_i)p(\xi_i)\right) d\xi_i d\eta_i \\
&= 2^{m_1}\left(\frac{4}{3}\right)^{m_2} - 1 \qquad (4.5.21)
\end{aligned}$$

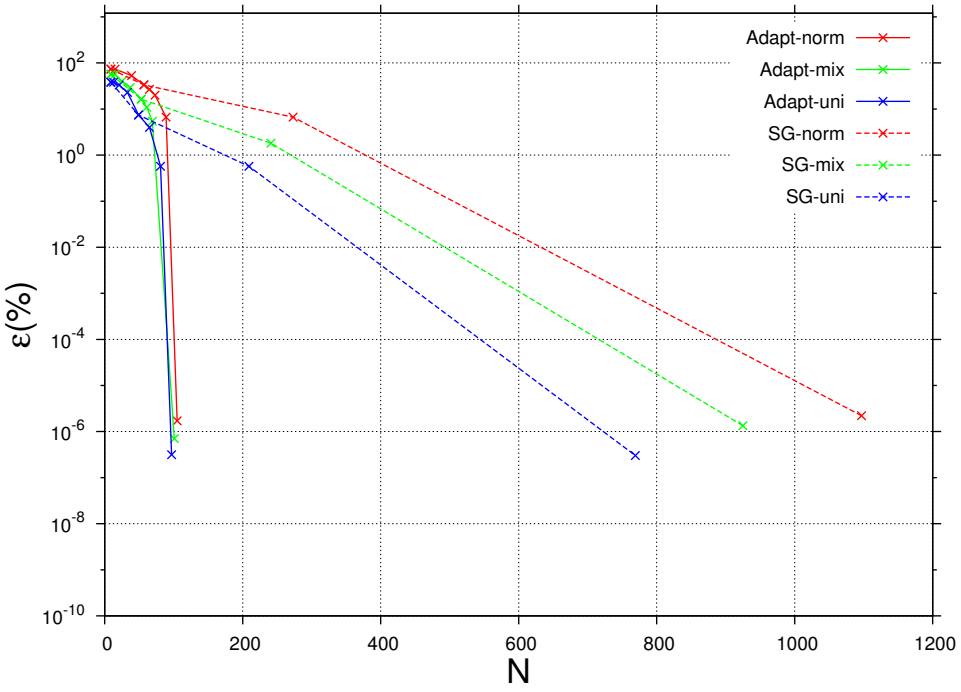
where the probability density functions $p(\xi_i)$ and $p(\eta_i)$ are given by Eqns.(4.5.6) and (4.5.7) respectively.

We now calculate a PCE for Eqn.(4.5.18) using the three different probability weights. For the numerical calculations we choose $M = 4$ and $m_1 = m_2 = 2$. The coefficients of the PCE are calculated using the non-intrusive approach defined in Eqn.(4.2.5). The orders of the polynomials in the expansion, which make up the set $\mathcal{A}$ in Eqn.(4.2.5), are calculated using Eqn.(4.4.5) or (4.4.6) (depending on the rule) for both the generalised and conventional sparse grid integration schemes. The results of these simulations are presented in Figure(4.8) where we can see that the adaptive construction significantly out-performs the conventional approach for this particular function. The reason for this is that the adaptive procedure al-

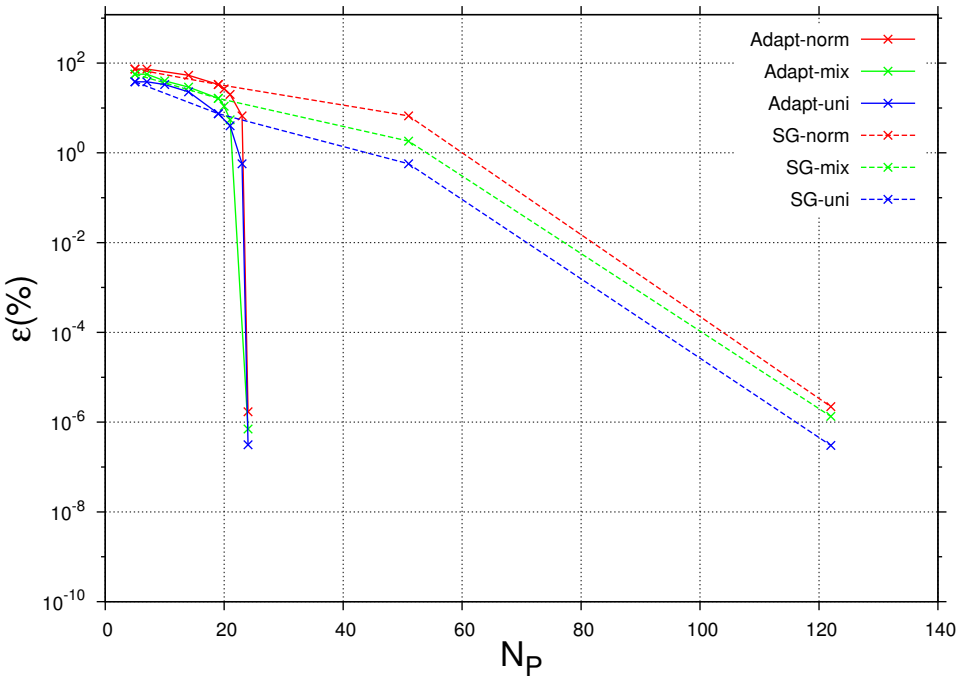
lows all indices in the tensor product of one dimensional indices and quickly captures the high monomial order cross terms in Eqn.(4.5.17) viz. $\prod_{i=1}^{M} \xi_i$.

4.6. Discussion and Conclusions

In this chapter we have outlined a non-intrusive method for building a polynomial chaos expansion which treats the physics code as a "black box". The approach, known as non-intrusive spectral projection or NISP, calculates the coefficients by projecting the stochastic space of the model response (in our case k_{eff}) onto each polynomial individually. To minimise the number of polynomials we have adopted an approach where the polynomials in the basis are chosen based upon the structure of the integrand. The structure of the integrand is inferred from the quadrature scheme which in this instance is the generalised sparse grid method proposed in [4, 68]. Verification tests were performed which showed the adaptive procedure was more efficient that its non-adaptive counterpart. A further set of tests showed that the adaptive algorithm correctly identified anisotropy in the integrands which ultimately leads to a more efficient placement of quadrature points. The final test set showed how the adaptive procedure allows a sparse PCE to be built which, for the example given, was significantly more accurate than using the conventional method of constructing a polynomial basis via Eqn.(3.2.7).



(a) Error versus N



(b) Error versus N_P

Figure 4.8.: Convergence of the variance calculated using a polynomial chaos expansion built with conventional sparse grid and adaptive sparse grid indices.

Chapter 5

High Dimensional Model Representation (HDMR)

5.1. Introduction

In Chapter (4) we outlined the NISP method which uses adaptive quadrature to perform the projection of the stochastic response on to the polynomial chaos basis. The NISP approach, combined with an adaptive quadrature scheme, has been used by previous authors [66] to compute the statistics of an elliptic partial differential equation with 121 random dimensions. This is a substantial number but may not be sufficient for realistic criticality problems. An alternative method used to represent the stochastic space of a model response, known as the high dimensional model representation or HDMR, can be used to further reduce the number of quadrature points required to integrate the stochastic response surface and hence build a polynomial chaos expansion. Previous authors [5] have used the HDMR technique to directly integrate stochastic fluid flow problems with up to 500 random dimensions.

In this chapter we introduce the basic properties of the HDMR expansion and show how it may be used in conjunction with a quadrature scheme

(adaptive or otherwise) to build a sparse polynomial chaos expansion of the response surface $R(\boldsymbol{\xi})$. In the first section the theory of the HDMR expansion is given and in the proceeding section adaptive algorithms are defined to appropriately truncate the expansion. In Section (5.4) a method for building a sparse polynomial chaos expansion from the combined HDMR and quadrature scheme is outlined. Section (5.5) gives some verification problems for the HDMR algorithms as well as a comparison with Latin Hypercube sampling (LHS) for a range of pin cell problems.

5.2. Theory

To begin, let $R(\boldsymbol{\xi}) : \mathbb{R}^M \rightarrow \mathbb{R}$ be a real valued smooth multivariate stochastic function where $\boldsymbol{\xi} = \{\xi_1, \cdots, \xi_M\}$ are a set of IID random variables with M being the number of stochastic dimensions. The stochastic function $R(\boldsymbol{\xi})$ may also be a function of some other, deterministic parameter space, i.e. $R(\boldsymbol{x}, \boldsymbol{\xi})$, but we omit the dependence on $\boldsymbol{x}$ for now to simplify the notation. $R(\boldsymbol{\xi})$ may also be multivariate, i.e. $R(\boldsymbol{\xi}) = \{R_1(\boldsymbol{\xi}), \cdots, R_I(\boldsymbol{\xi})\}$, but since the focus of this work is on criticality calculations we need only consider a univariate response.

The influence of input variables on the response can be independent and/or cooperative. Therefore, in some situations, it is more convenient to express the multivariate response function in terms of a hierarchical correlated function expansion in terms of the input variables. This type of expansion is known as a Sobol expansion or HDMR expansion and is written [70, 71, 72, 73, 74, 75] as:

$$R(\boldsymbol{\xi}) = R_0 + \sum_{i=1}^{M} R_i(\xi_i) + \sum_{1 \le i_1 < i_2 \le M} R_{i_1 i_2}(\xi_{i_1}, \xi_{i_2}) + \cdots + R_{i_1,\cdots,i_M}(\xi_{i_1}, \xi_{i_2}, \cdots, \xi_{i_M}). \tag{5.2.1}$$

The term $R_i(\xi_i)$ is a first order term representing the effect of the variable ξ_i acting independently, and in general, non-linearly upon the response $R(\boldsymbol{\xi})$. The function $R_{i_1 i_2}(\xi_{i_1}, \xi_{i_2})$ is a second order term that describes the cooperative effects of the variables ξ_{i_1} and ξ_{i_2} on the response. Higher order terms represent the effects of an increasing number of variables with the last function describing the cooperative effect between all M parameters. Usually the higher order terms in Eqn.(5.2.1) are negligible [74] so that typically HDMR with only a few low order terms is adequate to describe the output behaviour. Inclusion of only the first and the second order terms results in fast convergence of the expansion. However, the importance of higher order terms is of course problem dependent since it is ultimately the physics model which determines the interactions between the variables $\boldsymbol{\xi}$.

From now the derivation will follow the notation given in [5] where Eqn.(5.2.1) is written using a more compact notation as follows

$$R(\boldsymbol{\xi}) = \sum_{\boldsymbol{u} \subseteq \mathcal{D}} R_{\boldsymbol{u}}(\boldsymbol{\xi}_{\boldsymbol{u}}) \tag{5.2.2}$$

for a given set $\boldsymbol{u} \subseteq \mathcal{D}$, where $\mathcal{D} := \{1, \cdots, M\}$ denotes the set of coordinate indices and $R_{\emptyset}(\boldsymbol{\xi}_{\emptyset}) = r_0$. The cardinality of the set $\boldsymbol{u}$ is defined as ν and $\boldsymbol{\xi}_{\boldsymbol{u}}$ denotes the ν dimensional vector containing those components

of $\boldsymbol{\xi}$ that belong to the set $\boldsymbol{u}$, i.e. $\boldsymbol{\xi}_{\boldsymbol{u}} = (\xi_i)_{i\in\boldsymbol{u}}$. The cardinality ν is also referred to as the order of the HDMR component function and should not be confused with the average number of neutrons produced per fission $\overline{\nu}$.

Now let us define the following

$$d\mu(\boldsymbol{\xi}) = \prod_{i=1}^{M} d\mu(\xi_i) \tag{5.2.3}$$

which is an M dimensional product measure defined on Borel subsets of Θ^M. Here Θ^M is the multidimensional stochastic space defined in Section (2.3) with the superscript, M, used to emphasise the number of dimensions in the space. The measure $d\mu$ determines the particular form of the component functions and induces the projection operator $P_{\boldsymbol{u}} : \Theta^M \to \Theta^\nu$, namely

$$P_{\boldsymbol{u}}R(\boldsymbol{\xi}_{\boldsymbol{u}}) = \int_{\Omega^{M-\nu}} R(\boldsymbol{\xi}) p_{\mathcal{D}/\boldsymbol{u}}(\boldsymbol{\xi}) d\mu_{\mathcal{D}/\boldsymbol{u}}(\boldsymbol{\xi}) \tag{5.2.4}$$

where $d\mu_{\mathcal{D}/\boldsymbol{u}}(\boldsymbol{\xi}) := \prod_{i\in\mathcal{D}, i\notin\boldsymbol{u}} d\mu_i(\xi_i)$ and $p_{\mathcal{D}/\boldsymbol{u}}(\boldsymbol{\xi}) := \prod_{i\in\mathcal{D}, i\notin\boldsymbol{u}} p_i(\xi_i)$. Here $p(\xi_i)$ is the probability density function of the random variable ξ_i. The terms $R_{\boldsymbol{u}}(\boldsymbol{\xi}_{\boldsymbol{u}})$ in (5.2.2) can also be defined recursively by

$$R_{\boldsymbol{u}}(\boldsymbol{\xi}_{\boldsymbol{u}}) = P_{\boldsymbol{u}}R(\boldsymbol{\xi}_{\boldsymbol{u}}) - \sum_{\boldsymbol{v}\subset\boldsymbol{u}} R_{\boldsymbol{v}}(\boldsymbol{\xi}_{\boldsymbol{v}}). \tag{5.2.5}$$

At this point we note that there are several forms of HDMR associated with different measures. In [73] the Lebesgue measure $d\mu(\boldsymbol{\xi}) = d(\boldsymbol{\xi}) = \prod_{i=1}^{M} d\xi_i$ is used. With this choice of measure the decomposition in Eqn.(5.2.1)

is known as the ANOVA-HDMR where ANOVA stands for the ANAlysis Of VAraince. A significant drawback of ANOVA-HDMR is the need to compute high dimensional integrals, for example, the computation of the zero order term r_0 takes the form

$$r_0 = \int_{\Omega^M} R(\xi_1, \cdots, \xi_M) p(\boldsymbol{\xi}) d\boldsymbol{\xi} \tag{5.2.6}$$

which is an M dimensional integral. The ANOVA method is usually computed using sampling or the Fourier amplitude sensitivity test [102] but more recently has been computed using the coefficients of the polynomial chaos expansion [103]. To avoid the large number of multidimensional integrals involved in ANOVA-HDMR, a more computationally efficient method known as the cut-HDMR method was developed [73, 74]. In this method the measure is chosen as the Dirac measure located at a reference point $\boldsymbol{c} \in \Theta^M$, i.e.

$$d\mu(\boldsymbol{\xi}) = \prod_{i=1}^{M} \delta(\xi_i - c_i) \tag{5.2.7}$$

which, from (5.2.4), induces the following projections

$$P_{\boldsymbol{u}} R(\boldsymbol{\xi}_{\boldsymbol{u}}) = R(\boldsymbol{\xi})|_{\boldsymbol{\xi}=\boldsymbol{c}/\boldsymbol{\xi}_{\boldsymbol{u}}} \tag{5.2.8}$$

where we use the notation $R(\boldsymbol{\xi})|_{\boldsymbol{\xi}=\boldsymbol{c}/\boldsymbol{\xi}_i} = R(c_1, \cdots, \xi_i, \cdots, c_M)$. The terms of the cut-HDMR decomposition are thus related to the terms of the classical ANOVA decomposition in the sense that all integrals are replaced by point evaluations at a fixed anchor point $\boldsymbol{c} \in \Theta^M$. This approach is also referred to as anchored-ANOVA. This decomposition represents $R(\boldsymbol{\xi})$ as a superposition of its values on lines, faces and hyperplanes, etc, which intersect the

cut point $\boldsymbol{c}$ and are parallel to the coordinate axes. In the convergence limit, where all the correlated functions in Eqn.(5.2.1) are considered, cut-HDMR is invariant to the choice of the reference point $\boldsymbol{c}$. However, in practice, the choice of reference point $\boldsymbol{c}$ is very important for cut-HDMR especially if only low order interactions are considered. In [104] the authors show the optimality of different reference points (also called anchor points) using numerical simulation. Other authors [71, 105] suggest that the cut-HDMR expansion usually leads to a satisfactory approximation within a desired accuracy if the reference point is chosen as the mean vector.

The component functions in the HDMR expansion are orthogonal with respect to the inner product induced by the measure μ, namely

$$\int \mathrm{X}_{\boldsymbol{u}}(\boldsymbol{\xi}_{\boldsymbol{u}})\mathrm{X}_{\boldsymbol{v}}(\boldsymbol{\xi}_{\boldsymbol{v}})d\mu(\boldsymbol{\xi}) \quad \text{for} \quad \boldsymbol{u} \neq \boldsymbol{v}. \tag{5.2.9}$$

Computing the expectation of the cut-HDMR expansion only requires multidimensional integration equal to the order of the component function, namely, the mean value of the response function can be computed using

$$\begin{aligned} \mathbb{E}[R(\boldsymbol{\xi})] &= \sum_{\boldsymbol{u}\subseteq\mathcal{D}} \mathbb{E}[R_{\boldsymbol{u}}(\boldsymbol{\xi}_{\boldsymbol{u}})] \\ &= \sum_{\boldsymbol{u}\subseteq\mathcal{D}} \overline{R}_{\boldsymbol{u}} \end{aligned} \tag{5.2.10}$$

where

$$\overline{R}_{\boldsymbol{u}} = \mathbb{E}[R(\boldsymbol{\xi})|_{\boldsymbol{\xi}=\boldsymbol{c}/\boldsymbol{\xi}_{\boldsymbol{u}}}] - \sum_{\boldsymbol{v}\subset\boldsymbol{u}} \overline{R}_{\boldsymbol{v}} \tag{5.2.11}$$

In other words, a third order cut-HDMR component will require a three

dimensional integration. The variance of the response function $\mathrm{X}(\boldsymbol{\xi})$ may also be represented using a hierarchical expansion, to derive this we start with the familiar expression for the variance:

$$\mathrm{Var}[\mathrm{X}(\boldsymbol{\xi})] = \mathbb{E}[\mathrm{X}^2(\boldsymbol{\xi})] - \mathbb{E}[\mathrm{X}^2(\boldsymbol{\xi})]^2. \tag{5.2.12}$$

Inserting (5.2.2) into (5.2.12) we have

$$\mathrm{Var}[\mathrm{X}(\boldsymbol{\xi})] = \mathbb{E}\left[\left(\sum_{\boldsymbol{u}\subseteq\mathcal{D}} \mathrm{x}_{\boldsymbol{u}}(\boldsymbol{\xi}_{\boldsymbol{u}})\right)^2\right] - \mathbb{E}\left[\left(\sum_{\boldsymbol{u}\subseteq\mathcal{D}} \mathrm{x}_{\boldsymbol{u}}(\boldsymbol{\xi}_{\boldsymbol{u}})\right)\right]^2 \tag{5.2.13}$$

Using the recurrence relation from Eqn. (5.2.5) and the Dirac measure for the cut HDMR expansion from (5.2.7) we have

$$\begin{aligned}\mathrm{Var}[\mathrm{X}(\boldsymbol{\xi})] = \mathbb{E}&\left[\left(\sum_{\boldsymbol{u}\subseteq\mathcal{D}} \left(\mathrm{X}(\boldsymbol{\xi})|_{\boldsymbol{\xi}=\boldsymbol{c}/\boldsymbol{\xi}_{\boldsymbol{u}}} - \sum_{\boldsymbol{v}\subset\boldsymbol{u}} \mathrm{x}_{\boldsymbol{v}}(\boldsymbol{\xi}_{\boldsymbol{v}})\right)\right)^2\right] \\ &- \mathbb{E}\left[\sum_{\boldsymbol{u}\subseteq\mathcal{D}} \left(\mathrm{X}(\boldsymbol{\xi})|_{\boldsymbol{\xi}=\boldsymbol{c}/\boldsymbol{\xi}_{\boldsymbol{u}}} - \sum_{\boldsymbol{v}\subset\boldsymbol{u}} \mathrm{x}_{\boldsymbol{v}}(\boldsymbol{\xi}_{\boldsymbol{v}})\right)\right]^2.\end{aligned} \tag{5.2.14}$$

Expanding the squares in (5.2.14) and using the orthogonality relation from Eqn.(5.2.9), we have

$$\begin{aligned}\mathrm{Var}[\mathrm{X}(\boldsymbol{\xi})] = &\sum_{\boldsymbol{u}\subseteq\mathcal{D}} \left(\mathbb{E}\left[\mathrm{X}^2(\boldsymbol{\xi})|_{\boldsymbol{\xi}=\boldsymbol{c}/\boldsymbol{\xi}_{\boldsymbol{u}}}\right] - \mathbb{E}\left[\mathrm{X}^2(\boldsymbol{\xi})|_{\boldsymbol{\xi}=\boldsymbol{c}/\boldsymbol{\xi}_{\boldsymbol{u}}}\right]\right) \\ &- \sum_{\boldsymbol{u}\subseteq\mathcal{D}} \left(\mathbb{E}\left[\sum_{\boldsymbol{v}\subset\boldsymbol{u}} \mathrm{x}_{\boldsymbol{v}}^2(\boldsymbol{\xi}_{\boldsymbol{v}})\right] - \mathbb{E}\left[\sum_{\boldsymbol{v}\subset\boldsymbol{u}} \mathrm{x}_{\boldsymbol{v}}(\boldsymbol{\xi}_{\boldsymbol{v}})\right]^2\right)\end{aligned} \tag{5.2.15}$$

which may be written as

$$\mathrm{Var}[\mathrm{X}(\boldsymbol{\xi})] = \sum_{\boldsymbol{u}\subseteq\mathcal{D}} \sigma_{\boldsymbol{u}}^2 \tag{5.2.16}$$

where

$$\sigma_{\boldsymbol{u}}^2 = \mathrm{Var}[\mathrm{X}(\boldsymbol{\xi})|_{\boldsymbol{\xi}=\boldsymbol{c}/\boldsymbol{\xi}_{\boldsymbol{u}}}] - \sum_{\boldsymbol{v}\subset\boldsymbol{u}} \sigma_{\boldsymbol{v}}^2 \tag{5.2.17}$$

and

$$\mathrm{Var}[\mathrm{X}(\boldsymbol{\xi})|_{\boldsymbol{\xi}=\boldsymbol{c}/\boldsymbol{\xi}_{\boldsymbol{u}}}] = \mathbb{E}[\mathrm{X}^2(\boldsymbol{\xi})|_{\boldsymbol{\xi}=\boldsymbol{c}/\boldsymbol{\xi}_{\boldsymbol{u}}}] - \mathbb{E}[\mathrm{X}(\boldsymbol{\xi})|_{\boldsymbol{\xi}=\boldsymbol{c}/\boldsymbol{\xi}_{\boldsymbol{u}}}]^2 \tag{5.2.18}$$

$$\sigma_{\boldsymbol{v}} = \mathbb{E}\left[\mathrm{x}_{\boldsymbol{v}}^2(\boldsymbol{\xi}_{\boldsymbol{v}})\right] - \mathbb{E}\left[\mathrm{x}_{\boldsymbol{v}}(\boldsymbol{\xi}_{\boldsymbol{v}})\right]^2. \tag{5.2.19}$$

The notion of order when referring to the cut-HDMR expansion should not be confused with the order of a Taylor series expansion. It has been shown [70], however, that a first order cut-HDMR component function of a single input parameter is equal to the sum of all Taylor series terms involving that parameter only. Likewise, in the general case of M input parameters, the cut-HDMR component function is equal to the sum of all Taylor series terms involving all M parameters [71]. Unlike a Taylor expansion of a given order, the cut-HDMR expansion does not limit the non-linearity of the response function. Thus, any truncated cut-HDMR expansion provides a better representation of the response than any truncated Taylor expansion of the same order.

5.3. Adaptive HDMR

The total number of terms in the full cut-HDMR expansion is 2^M. To be computationally feasible for large M, this expansion must be truncated. There are two ways to do this: limit the number of variables in each component function and limit the number of component functions for a given number of variables. The first restriction defines the truncation dimension N_t and the second defines the superposition dimension N_{s_i} for a number of dimensions i. These numbers describe roughly the number of important dimensions and the order of important interactions respectively. The total number of terms can now be calculated by

$$N_{\mathrm{HDMR}} = 1 + \sum_{i=1}^{N_t} N_{s_i}$$

In practice the truncation and superposition dimensions are not known *a priori* and in order to calculate them all 2^M terms in the full cut-HDMR expansion would be required. This would be impractical since it would require more computational effort than integrating the response function $R(\boldsymbol{\xi})$ directly. In this work we would like to minimise the total number of terms in the HDMR expansion and hence minimise the total number of quadrature points needed to compute the integral in Eqns.(5.2.11) and (5.2.17). Therefore, we would like to look at adaptive strategies that automatically detect the truncation and superposition dimensions. The adapted cut-HDMR expansion is written as follows:

$$R(\boldsymbol{\xi}) = r_0 + \sum_{i\in\mathcal{F}_1} R_i(\xi_i) + \sum_{(i_1,i_2)\in\mathcal{F}_2} R_{i_1 i_2}(\xi_{i_1},\xi_{i_2}) + \sum_{(i_1,i_2,i_3)\in\mathcal{F}_3} R_{i_1 i_2 i_3}(\xi_{i_1},\xi_{i_2},\xi_{i_3}) + \cdots + \sum_{(i_1,\cdots,i_{N_t})\in\mathcal{F}_{N_t}} R_{i_1\cdots i_3}(\xi_{i_1},\cdots,\xi_{i_{N_t}}) \tag{5.3.1}$$

which can be written in a more compact form

$$R(\boldsymbol{\xi}) = \sum_{u\in\mathcal{F}} R_{\boldsymbol{u}}(\boldsymbol{\xi}_{\boldsymbol{u}}) \tag{5.3.2}$$

where $\mathcal{F}$ is the union of all the sparse index sets $\mathcal{F}_i$, namely

$$\mathcal{F} = \bigcup_{i=0}^{N_t} \mathcal{F}_i.$$

Each of the sparse index sets $\mathcal{F}_i$ are calculated adaptively with the cardinality of each equalling the superposition dimension for that truncation dimension, viz. $|\mathcal{F}_i| = N_{s_i}$. Every component $R_{\boldsymbol{u}}$ in Eqn.(5.3.2) has an associated weight $\eta_{\boldsymbol{u}} \geq 0$ which describes the contribution of $R_{\boldsymbol{u}}$ to the full expansion. The adaptive strategy consists of computing the superposition dimension N_{s_k} for each set $\mathcal{F}_k$ successively for increasing expansion order until the relative change in expansion approximation, according to a predefined measure, falls below some threshold. To this end, the zeroth and first order expansions must be constructed. This is the minimal amount of computational effort that is required to start the adaptive procedure and it scales linearly with the number of dimensions M. The weights, η_i, for all of the first order terms are calculated and the sparse set $\mathcal{F}_1$ is formed. There are several alternatives in the literature [6, 5] for calculating the weight η. Since we are mainly concerned with the convergence of the second order

statistics, we have chosen the weight based upon the variance contribution of each first order component relative to the variance attributed by all first order components, namely

$$\eta_i = \frac{\mathrm{Var}(R_i)}{\sum_{j=1}^{M} \mathrm{Var}(R_j)}. \tag{5.3.3}$$

Each first order function describes the sole interaction of that dimension upon the output when it is acting independently of all other dimensions. This quantity can be thought of as a sensitivity measure for the ith dimension. The importance of any given dimension can then be defined when the weight η_i is above some threshold δ_{HDMR}. A similar weight is defined for the higher order interactions $\eta_{\boldsymbol{u}}$ as follows:

$$\eta_{\boldsymbol{u}} = \frac{|\mathrm{Var}(R_{\boldsymbol{u}})|}{\left|\sum_{\boldsymbol{v}\in\mathcal{F}_{|\boldsymbol{v}|},|\boldsymbol{v}|\leq\nu-1} \mathrm{Var}(R_{\boldsymbol{v}})\right|}. \tag{5.3.4}$$

The weights, η, can be used to determine the superposition dimensions $\{N_{s_k}; k = 1, \cdots, N_t\}$. The truncation dimension N_t is determined when $\rho_t < \delta_{\mathrm{HDMR}}$ where the weight ρ is determined using the following:

$$\rho_p = \frac{\left|\sum_{\nu\leq p} \mathrm{Var}(R_{\boldsymbol{u}}) - \sum_{\nu\leq p-1} \mathrm{Var}(R_{\boldsymbol{u}})\right|}{\left|\sum_{\nu\leq p-1} \mathrm{Var}(R_{\boldsymbol{u}})\right|}. \tag{5.3.5}$$

The approach taken in [6, 5] for calculating the weights η and ρ is defined in Algorithm (4). The computation is as follows: To begin, the sparse set of first order interactions $\mathcal{F}_1$ is formed from all of the first order interactions that have a weight greater than the threshold value δ_{HDMR}. An intermediate second-order set $\mathcal{R}$ is now formed from all of the allowed subsets of the

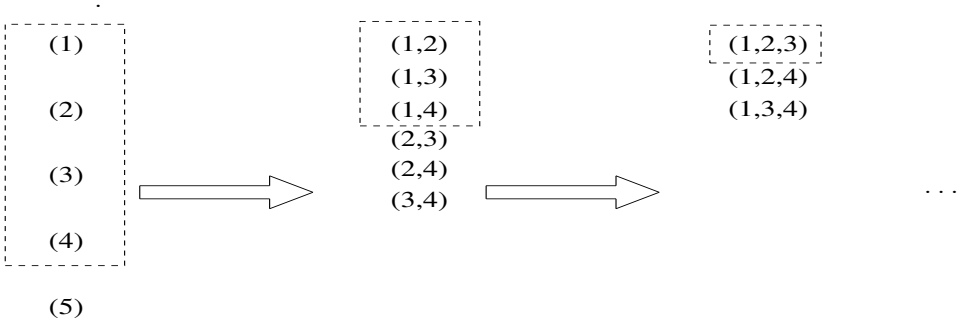
Cartesian product $\mathcal{F}_1 \times \mathcal{F}_1$. All computations associated with $\mathcal{R}$ are now performed and associated weights are calculated. The sparse set of interactions $\mathcal{F}_2$ is formed from all of the second order interactions that have a weight greater than the threshold value δ_{HDMR}. The weight ρ_2 is calculated using the set $\mathcal{F}_2$. This process repeats until $\rho_n < \delta_{\text{HDMR}}$.

Algorithm 4 Conventional adaptive HDMR as outlined by Ma [5] and Yang [6].

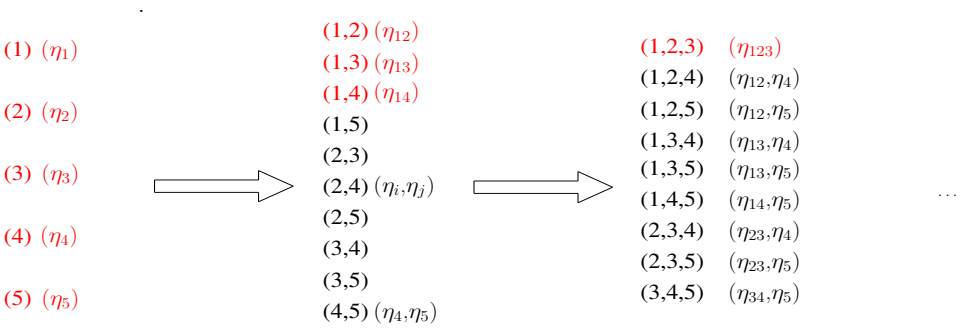
Calculate R_0, $R_i \; \forall \, i \in \{1, \cdots, M\}$
$\mathcal{F}_1 = \{i; \eta_i > \delta_{\text{HDMR}}\}$
$i = 2$
while $\rho_i > \delta_{\text{HDMR}}$ **do**
  $\mathcal{R} = \{\boldsymbol{v} \in \mathcal{F}_{i-1} \times \mathcal{F}_1; \boldsymbol{v} \in \mathcal{D}\}$
  Compute all functions corresponding to the set $\mathcal{R}$
  $\mathcal{F}_i = \{\boldsymbol{u} \in \mathcal{R}; \eta_{\boldsymbol{u}} > \delta_{\text{HDMR}}\}$
  Calculate ρ_i
  $i = i + 1$
end while

In other words, Algorithm (4) is forming the set of important interactions, f_i, whose cardinality, $|f_i|$, is equal to the superposition dimension, N_{s_i}, from a set of pre computed values, R. This approach is inefficient if $|R| >> |f_i|$. As an example we consider a case where $M = 5$ with the adaptive process illustrated in Fig.(5.1a). Here the set $\mathcal{R}$ is shown for each order with the sparse set $\mathcal{F}_i$ enclosed within the dashed line. From this illustration we can see that the algorithm may result in the cardinality of the set $\mathcal{R}$ being greater than the set $\mathcal{F}_i$, i.e. $|\mathcal{R}| > |\mathcal{F}_i|$.

The potential inefficiencies of Algorithm (4) could become impractical for large values of M, the number of stochastic dimensions. Consider the case where 100 one dimensional terms were deemed to be important by the



(a) Conventional approach



(b) Modified approach

Figure 5.1.: Graphical examples of the adaptive HDMR strategies.

algorithm, this would result in the calculation of 10,000 two dimensional terms. If only 1000 two dimensional terms are deemed to be important, then this is a huge waste of computational resources. An alternative approach is proposed in Algorithm (5). The computation proceeds as follows: As before, the zeroth and first order terms are calculated. This time the first order sparse set $\mathcal{F}_1$ is a tuple of the index i and associated weight η_i. The indexes of the intermediate second order set $\mathcal{R}$ (also a tuple) is now formed from all of the allowed index subsets of the Cartesian product $\mathcal{F}_1 \times \mathcal{F}_1$. An associated weight $\tilde{\eta}$ is calculated for each of the index subsets of $\mathcal{R}$ based upon the weights of $\mathcal{F}_1$. For example:

$$(1,2) \rightarrow \tilde{\eta}_{12} = \eta_1 \eta_2$$

The weights $\tilde{\eta}$ provide a prediction of the importance of the second order terms based upon the calculated importance of the first order terms. The set $\mathcal{R}$ is now sorted in ascending order according to the predicted importance $\tilde{\eta}$. Each member of $\mathcal{R}$ is computed until its calculated weight η falls below the threshold δ_{HDMR}. The sparse set $\mathcal{F}_2$ is now formed from all those members of $\mathcal{R}$ whose calculated weights η are above the threshold δ_{HDMR}. The above process is repeated for all of the higher order interactions until the weight $\rho_n < \delta_{\text{HDMR}}$. For the case of $M = 5$, the modified adaptive procedure is illustrated in Fig.(5.1b).

Both of the adaptive procedures defined in Algorithms (4) and (5) assume that the importance of higher order terms can be predicted based upon the importance of lower order interactions. The proposed algorithm assumes that the actual importance η decreases monotonically with the predicted importance $\tilde{\eta}$. Therefore, the accuracy of the adaptive procedure is dependent upon the quality of the predicted importance. The accuracy is also dependent upon the rate of decay. If the multivariate terms decay very quickly, Algorithm (5) will be very efficient. If, however, the contribution of these terms is isotropic, then the algorithm may finish before enough of the terms have been computed.

5.4. Combining Polynomial Chaos with HDMR

The computation of the expectation of the response surface using HDMR defined in Eqn.(5.3.2) consists of a series of integrations along cuts and hyperplanes in the stochastic space. This procedure can easily be extended to produce a surrogate model of the response function $R(\boldsymbol{\xi})$ by projecting each

Algorithm 5 Modified adaptive HDMR algorithm.

Calculate R_0, $R_i \, \forall \, i \in \{1, \cdots, M\}$
$\mathcal{F}_1 = \{(i, \tilde{\eta}_i); i = 1, \cdots, M\}$
$i = 2$
while $\rho > \delta_{\text{HDMR}}$ **do**
  $\mathcal{R} = \{(\boldsymbol{v}, \eta) \in \mathcal{F}_{i-1} \times \mathcal{F}_1; \boldsymbol{v} \in \mathcal{D}\}$
  Re-order the set $\mathcal{R}$ in ascending order according to $\tilde{\eta}$
  $\mathcal{F}_i = \emptyset$
  while $\boldsymbol{u} \in \mathcal{R}$ **and** $\eta_{\boldsymbol{u}} > \delta_{\text{HDMR}}$ **do**
    Calculate $\overline{R}_{\boldsymbol{u}}$, $\sigma^2_{\boldsymbol{u}}$ and weight $\eta_{\boldsymbol{u}}$ associated with set $\boldsymbol{u}$
    $\mathcal{F}_i += (\boldsymbol{u}, \eta_{\boldsymbol{u}})$
  end while
  Calculate ρ
  $i = i + 1$
end while

of the HDMR component functions $R_{\boldsymbol{u}}$ onto its own candidate polynomial basis. Combining the adaptive HDMR and PCE approaches in this manner allows a sparse PC representation to be built which optimally represents the response function.

Starting with the expression for the PC coefficients using the non-intrusive approach

$$r_{\boldsymbol{\alpha}} = \frac{\mathbb{E}\left[\Phi_{\boldsymbol{\alpha}}(\boldsymbol{\xi}) R(\boldsymbol{\xi})\right]}{N^2_{\boldsymbol{\alpha}}} \qquad \boldsymbol{\alpha} \in \mathcal{A} \tag{5.4.1}$$

where $\mathcal{A}$ is the set of all polynomial chaos indexes. We may now insert the expression for the adapted HDMR expansion from Eqn.(5.3.2) into (5.4.1) to yield

$$r_{\boldsymbol{\alpha}} = \frac{\mathbb{E}\left[\Phi_{\boldsymbol{\alpha}}(\boldsymbol{\xi}) \sum\limits_{\boldsymbol{u} \in \mathcal{F}} R_{\boldsymbol{u}}(\boldsymbol{\xi}_{\boldsymbol{u}})\right]}{N^2_{\boldsymbol{\alpha}}}. \tag{5.4.2}$$

Using the recurrence relations in (5.2.5) we may replace the integration over

the component $R_{\boldsymbol{u}}(\boldsymbol{\xi}_{\boldsymbol{u}})$ with one involving the response surface $R(\boldsymbol{\xi})$

$$r_{\boldsymbol{\alpha}} = \frac{1}{N_{\boldsymbol{\alpha}}^2}\mathbb{E}\left[\Phi_{\boldsymbol{\alpha}}(\boldsymbol{\xi})\sum_{\boldsymbol{u}\in\mathcal{F}}\left(R(\boldsymbol{\xi}_{\boldsymbol{u}}) - \sum_{\boldsymbol{v}\subset\boldsymbol{u}} R_{\boldsymbol{v}}(\boldsymbol{\xi}_{\boldsymbol{v}})\right)\right]$$
$$= \frac{1}{N_{\boldsymbol{\alpha}}^2}\sum_{\boldsymbol{u}\in\mathcal{F}}\left(\mathbb{E}\left[\Phi_{\boldsymbol{\alpha}}(\boldsymbol{\xi}_{\boldsymbol{u}})R(\boldsymbol{\xi}_{\boldsymbol{u}})\right] - \sum_{\boldsymbol{v}\subset\boldsymbol{u}}\mathbb{E}\left[\Phi_{\boldsymbol{\alpha}}(\boldsymbol{\xi}_{\boldsymbol{u}})R_{\boldsymbol{v}}(\boldsymbol{\xi}_{\boldsymbol{v}})\right]\right). \qquad (5.4.3)$$

From Eqn.(5.4.3) we can see that each ν dimensional quadrature over the response function requires the subtraction of all ν dimensional projections onto all subsets of $\boldsymbol{u}$. For example, consider the bi-variate polynomial basis spanning the two dimensional surface described by the variables ξ_1 and ξ_2. The surrogate model for this surface is then defined by the coefficients $r_{\boldsymbol{\alpha}}$ where $\boldsymbol{\alpha} = (1,0),(2,0),(1,1),(0,1),(0,2)$. The first coefficient $r_{(1,0)}$ can be calculated as follows:

$$N_1^2 N_0^2\, r_{(1,0)} = \int \Phi_{(1,0)}(\xi_1)R(\xi_1)p(\xi_1)d\xi_1$$
$$+ \left(\int\int \Phi_{(1,0)}(\xi_1)R(\xi_1,\xi_2)p(\xi_1,\xi_2)d\xi_1 d\xi_2 - \int \Phi_{(1,0)}(\xi_1)R_1(\xi_1)p(\xi_1)d\xi_1\right)$$
$$+ \text{ higher order projections.}$$

The coefficient for the one dimensional polynomial spanning dimension 1 has contributions from the univariate term in the HDMR expansion, $R_1(\xi_1)$, a contribution from the two dimensional term $R(\xi_1,\xi_2)$ and all other higher dimensional terms involving dimension 1.

5.5. Numerical Examples

In the following section two sets of numerical simulations are presented which were conducted to illustrate the use of the HDMR method. The

first set of tests were performed to verify the HDMR method, check that the coupling with the quadrature methods is performing correctly and to show how the HDMR method can be used to build a sparse polynomial chaos expansion. The second set of test problems uses the HDMR method to calculate the uncertainty on k_{eff} for a realistic pin cell problem using evaluated covariance data.

5.5.1. Verification Tests

To investigate the numerical properties of the HDMR expansion we define the following function

$$R(\boldsymbol{\xi}) = \frac{1}{1 + \sigma\sqrt{3}\sum_{k=1}^{M} \alpha_k \xi_k} \quad \xi_k \in [-1, 1] \tag{5.5.1}$$

with

$$\alpha_k = \exp\{-|k|/l\} \tag{5.5.2}$$

The terms α_k control the contribution of each random dimension through the parameter l. The parameter l is referred to as the structure parameter for the remainder of this example. The larger the value of l the slower the set $\{\alpha\}$ decays and the more dimensions contribute to the non-linear function $R(\boldsymbol{\xi})$. The parameter σ is the standard deviation which controls the magnitude of the variation in the random input. The random variables ξ_k vary uniformly between $[-1, 1]$. The number of dimensions $M = 10$ for all problems in this section and the standard deviation is initially set to $\sigma = 0.1$. For the following examples we use the relative error which is

defined as

$$\epsilon = \frac{||R(\boldsymbol{\xi}) - \tilde{R}(\boldsymbol{\xi})||_2}{||R(\boldsymbol{\xi})||_2}$$

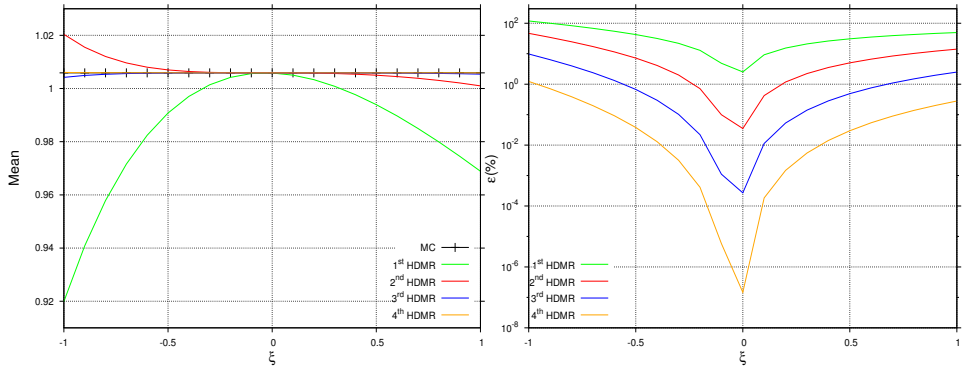
where $\tilde{R}$ is the approximate solution calculated using the HDMR expansion. The reference solution is calculated using the LHS method with 10^8 samples.

5.5.1.1. Choice of Cut Point

When using the cut-HDMR expansion the choice of the cut point or anchor point $\boldsymbol{c}$ is very important. In Figs.(5.2) and (5.3) the mean and variance, and their respective errors, are plotted as all values of the vector $\boldsymbol{c}$ are varied between $[-1, 1]$. These figures show that the HDMR is convergent with respect to increasing order but the optimum results are gained when the cut point is equal to the mean of the input parameters ($\boldsymbol{\xi} = 0$). This is consistent with the results published in [71, 105]. In all of the remaining examples we always take the cut point as the mean value.

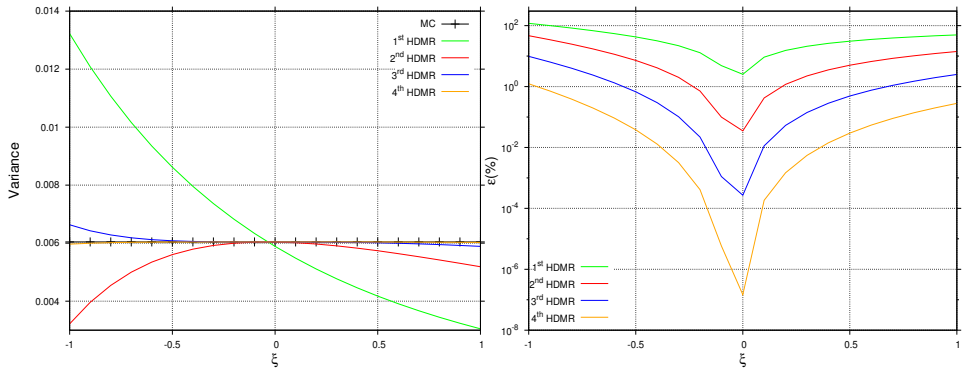
5.5.1.2. Structure of Response Function

Another important feature of the response function, which will affect the convergence of the HDMR expansion, is its structure. Depending on the problem under investigation, the amount of of interaction between variables and the number of multivariate effects may vary considerably. To investigate the structure effects, the relative error, ϵ, in the mean and variance of the response function are plotted in Fig.(5.4) for values of the structure parameter $l = 0.5, 1, 2$ and 5. We can see that for low values of l the expansion converges rapidly but the rate slows as l is increased. The reason for



(a) Mean values (b) Mean error

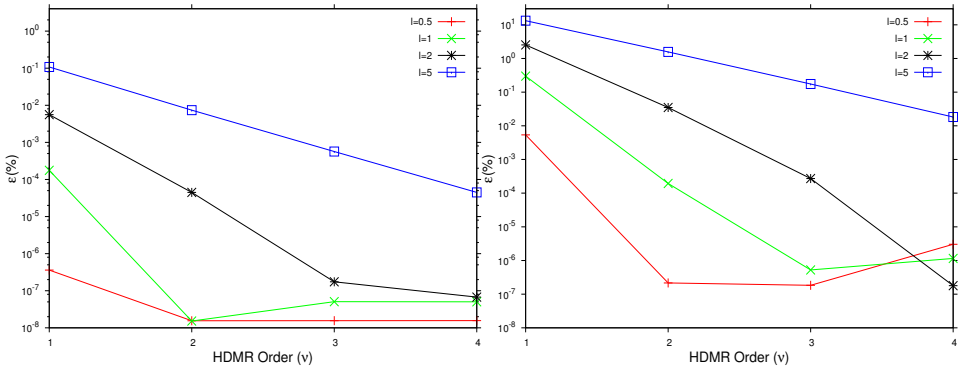
Figure 5.2.: Mean value and relative, ϵ, error in the mean versus the cut point c for the first four HDMR orders. A level 5 Gauss-Legendre sparse grid has been used to calculate integrals and a value of $l = 2$ has been used for the structure parameter.



(a) Variance values (b) Variance error

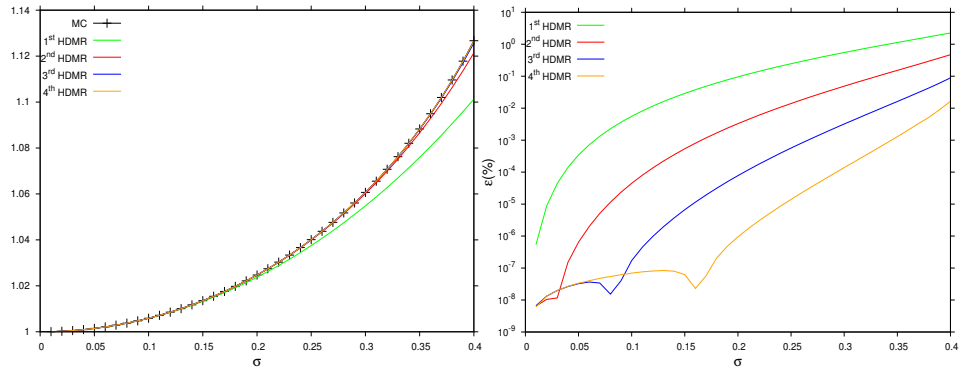
Figure 5.3.: Variance and relative error, ϵ, in the variance versus the cut point c for the first four HDMR orders. A level 5 Gauss-Legendre sparse grid has been used to calculate integrals and a value of $l = 2$ has been used for the structure parameter.

this is that as l increases the set $\{\alpha\}$ becomes more isotropic; more of the input variables become important and more high dimensional terms in the HDMR expansion become important.



(a) Mean (b) Variance

Figure 5.4.: Relative error versus HDMR order for various values of structure parameter l. A level 5 Gauss-Legendre sparse grid has been used to calculate integrals.

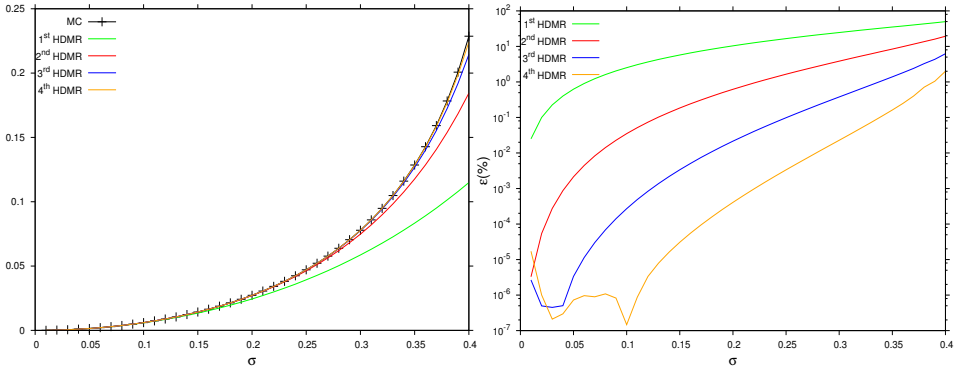


(a) Mean values (b) Mean error

Figure 5.5.: Mean value and relative error in the mean versus the relative standard deviation (σ) of the input parameters for the first four HDMR orders. A level 5 Gauss-Legendre sparse grid has been used to calculate integrals.

5.5.1.3. Magnitude of the Uncertainty

In this work the HDMR expansion is being used for the propagation of uncertainty. As such, the convergence of the HDMR expansion with respect to the relative uncertainty of the input parameters must also be examined. One such study for a test function similar to the one we have chosen has



(a) Variance values (b) Variance error

Figure 5.6.: Variance and relative error in the variance versus the relative standard deviation (σ) of the input parameters for the first four HDMR orders. A level 5 Gauss-Legendre sparse grid has been used to calculate integrals.

been reported in [5]. Results for a structure parameter of $l = 2$ are computed (using a level 5 Guass-Legendre sparse grid) as a function of the relative standard deviation of the input parameters in Figs.(5.5) and (5.6). From these we can see that as σ increases higher order terms in the HDMR expansion increase in importance. The poor asymptotic behaviour of the higher order terms as $\sigma \to 0$ is due to the accuracy of the HDMR solution exceeding the accuracy of the LHS reference solution.

5.5.1.4. Adaptive HDMR

In the next part of this subsection we compare the performance of the two adaptive algorithms defined in the previous section namely Algorithms (4) and (5). It is important to know which of the algorithms is more efficient in terms of the error calculated for a given number of function evaluations N. Obviously the smaller the error for a given number of function evaluations the more efficient the algorithm. We also wish to assess the efficiency of

each algorithm with respect to the structure of the response function. To these ends, the relative error is plotted versus the number of realisations in Fig. (5.7) for three different structure parameters: $l = (0.1, 1.0, 2.0)$. A non-adaptive sparse grid quadrature scheme is used with a level of L=4 to compute the integrals in the HDMR expansion. For all of the values of l in this figure, Algorithm (2) is consistently more efficient. This can be explained by considering the variation of the error with respect to the HDMR threshold δ_{HDMR} which is plotted in Fig(5.8). For Algorithm (1) the change in error is very abrupt, whereas the change in error with δ_{HDMR} for Algorithm (2) is more incremental. In other words, Algorithm (2) computes just enough terms in the expansion to satisfy the adaptivity criterion.

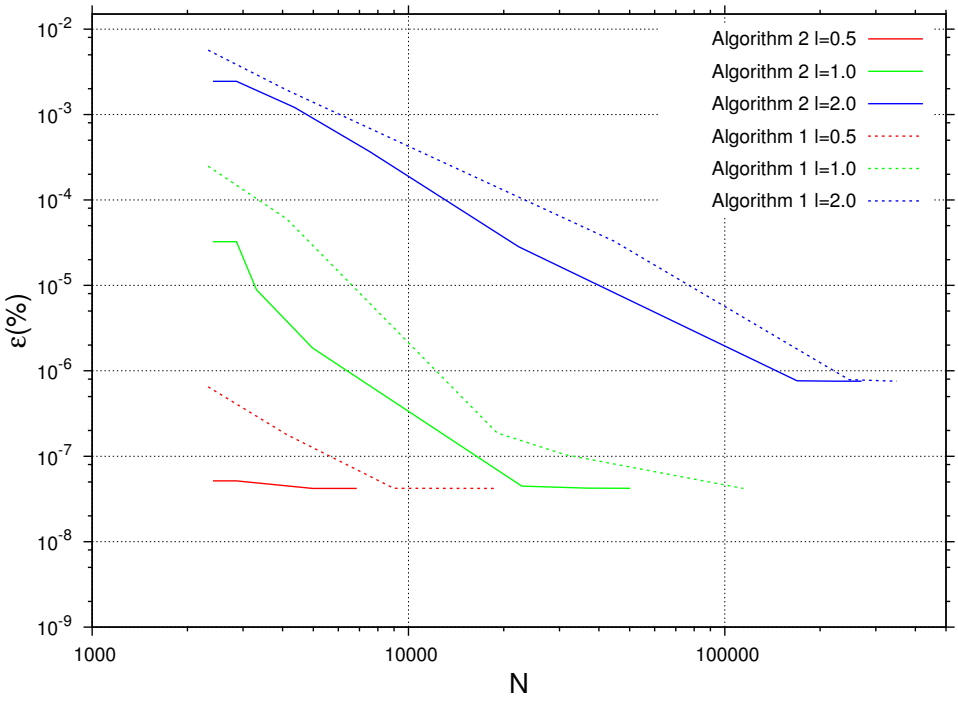


Figure 5.7.: Convergence of the relative error versus the number of realisations, N.

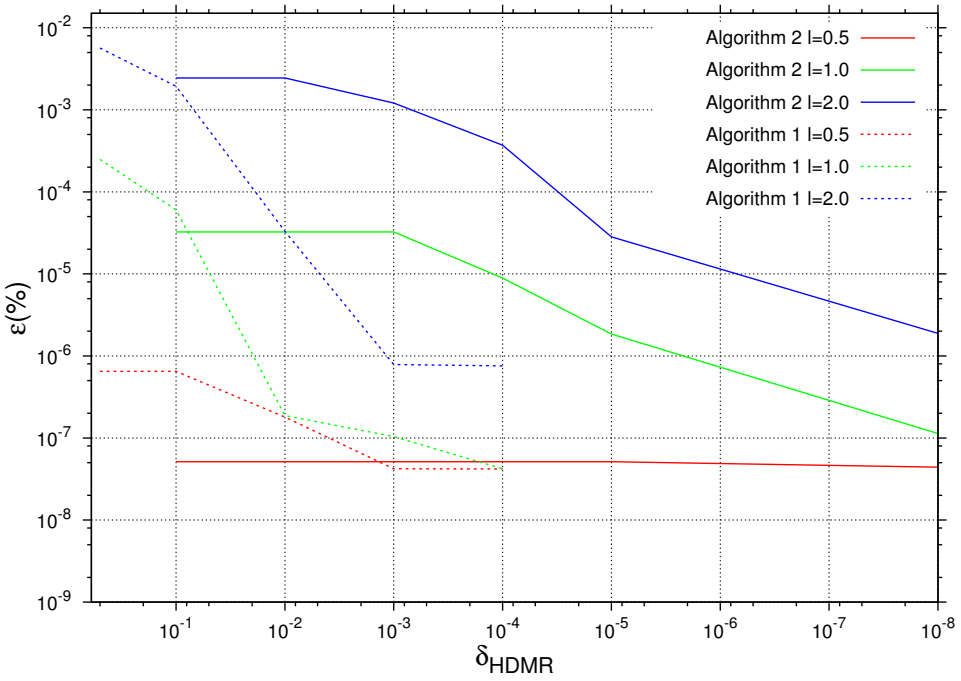


Figure 5.8.: Convergence of the relative error versus the adaptive HDMR threshold, δ_{HDMR}.

5.5.1.5. Combination with Adaptive Quadrature

For all of the calculations performed so far, the integrals of the HDMR component functions in Eqn.(5.2.5) have been performed using a fixed level Gauss-Legendre sparse grid quadrature scheme. For a given sparse grid level, the number of quadrature points may be unnecessarily large for some HDMR component functions or contrastingly, it may be too few. In this section we investigate the use of the adaptive sparse grid algorithm for calculating the HDMR components which comprise the variance of the function in Eqn.(5.5.1). For this investigation the number of dimensions is 10, the standard deviation $\sigma = 0.1$ and the structure parameter $l = 2.0$. We also use the nested Gauss-Patterson quadrature rule for both the adaptive and non adaptive sparse grids. The relative error in the standard deviation of the function in Eqn.(5.5.1) is plotted against the number of quadrature

points / function evaluations (N) in Fig.(5.9) and the adaptive HDMR tolerance (δ_{HDMR}) in Fig.(5.10). These results are from a number of sparse grid quadrature levels and adaptive integration tolerances, δ_{Quad} .

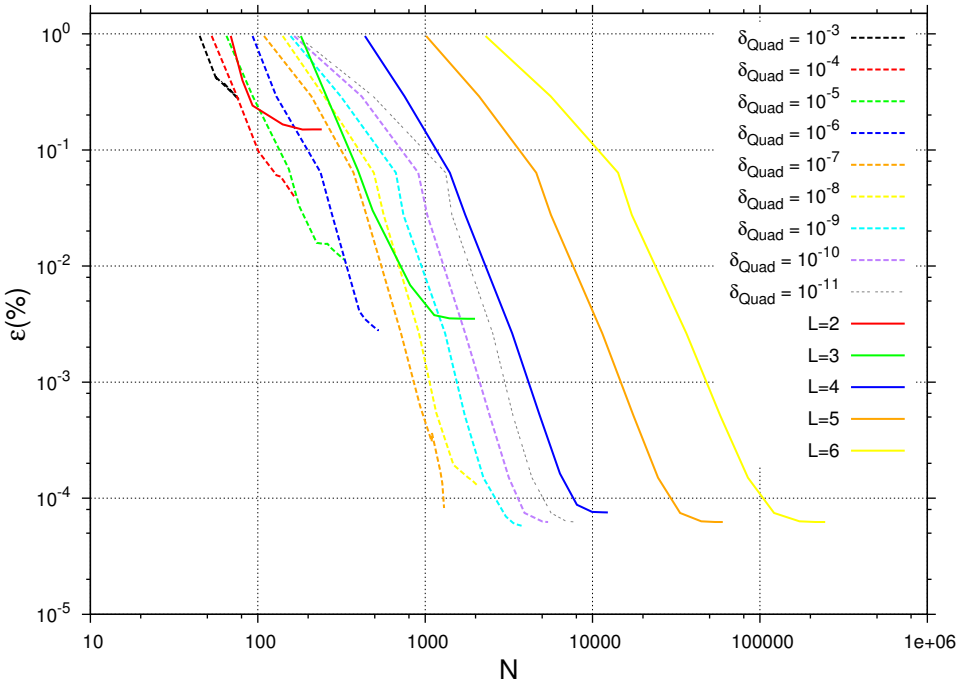


Figure 5.9.: Relative error, ϵ, versus the number of realisations, N. Values of $\sigma = 0.1$ and $l = 2.0$ have been used whilst integration has been performed with Gauss-Patterson rules.

In Fig.(5.9) we can clearly see that the use of the level L=5 and L=6 non-adaptive sparse grid quadrature rules are far less efficient than any of the adaptive procedures; the efficiencies of the adaptive quadrature results appear to be bounded by the L=4 non-adaptive results. This was found to be because the adaptive quadrature scheme produced no componenets of the L=5 or L=6 quadrature schemes for the error tolerances tested. In this context we have taken the efficiency as the accuracy of the result relative to the number of function evaluations - the number of function evaluations

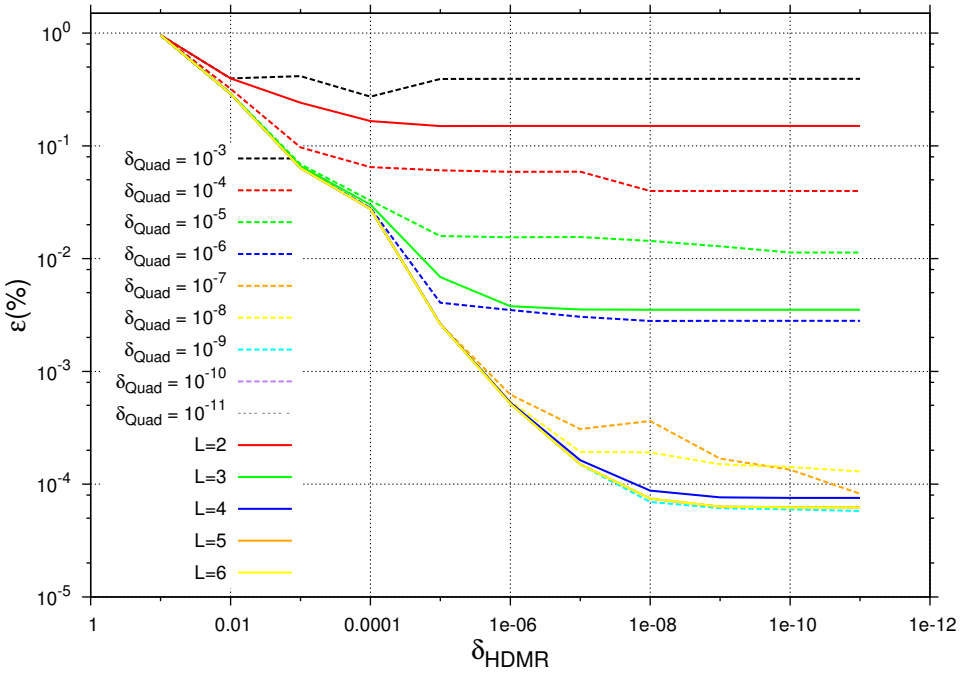


Figure 5.10.: Relative error, ϵ, versus the adaptive HDMR tolerance, δ_{HDMR}. Values of $\sigma = 0.1$ and $l = 2.0$ have been used whilst integration has been performed with Gauss-Patterson rules.

being proportional to the computational effort. From Fig.(5.10) we can see that the reduction in the relative error versus adaptive HDMR tolerance, δ_{HDMR}, is very similar for the adaptive integration tolerances $\delta_{\text{Quad}} = 10^{-7}$ and 10^{-8} and the Level L=4 regular sparse grid. However from Fig.(5.9), the adaptive quadratures are more efficient than the non-adaptive ones; in fact, the $\delta_{\text{Quad}} = 10^{-7}$ results are about an order of magnitude more efficient than the L=4 quadratures. The results in both Figures (5.9) and (5.10) show that in order to improve the accuracy of the HDMR solution both the adaptive HDMR tolerance (δ_{HDMR}) and the adaptive quadrature tolerance (δ_{Quad}) must be decreased simultaneously. If the correct combination of δ_{HDMR} and δ_{Quad} are chosen, HDMR with adaptive quadrature is far more efficient than its non-adaptive counterpart.

5.5.1.6. Building a Sparse Polynomial Chaos Expansion

In this section we show how the adaptive/non-adaptive quadrature rules combined with the adaptive HDMR procedure can be used to build a sparse polynomial chaos expansion (PCE). The number of coefficients in the PCE is increased by decreasing either the adaptive HDMR tolerance or the adaptive quadrature tolerance. The variance in the PCE of the response parameter is calculated using Eqn.(3.3.3) which we have repeated below for convenience:

$$\mathrm{Var}(\boldsymbol{x}) = \sum_{\boldsymbol{\alpha} \in \mathcal{A}^{M,p}} R^2_{\boldsymbol{\alpha}}(\boldsymbol{x}) N^2_{\boldsymbol{\alpha}}.$$

The relative error in the standard deviation is then plotted against the number of quadrature points, N, in Figure (5.11) and against the number of polynomials in the PCE, N_P, in Figure (5.12); these results are for HDMR with adaptive and non-adaptive quadrature and also for the non-intrusive spectral projection (NISP) methods with adaptive and non-adaptive quadrature.

The results in both Figure (5.11) and (5.12) give an indication of the relative efficiency of each approach. The results show that NISP with adaptive quadrature is consistently the most efficient although, with the appropriate choice of δ_{HDMR} and δ_{Quad}, the HDMR approach with adaptive quadrature is still competitive in terms of accuracy per realisation/polynomial. We also note that HDMR using the conventional sparse grid of level L converges to the non-adaptive NISP with the same level as the adaptive HDMR tolerance $\delta_{\mathrm{HDMR}} \to 0$. A more decisive factor in the choice of HDMR with adaptive quadrature over the use of the NISP with adaptive quadrature, is the execution time of the algorithms. The relative error in the calculated variance is plotted versus execution time for both HDMR and NISP with adaptive

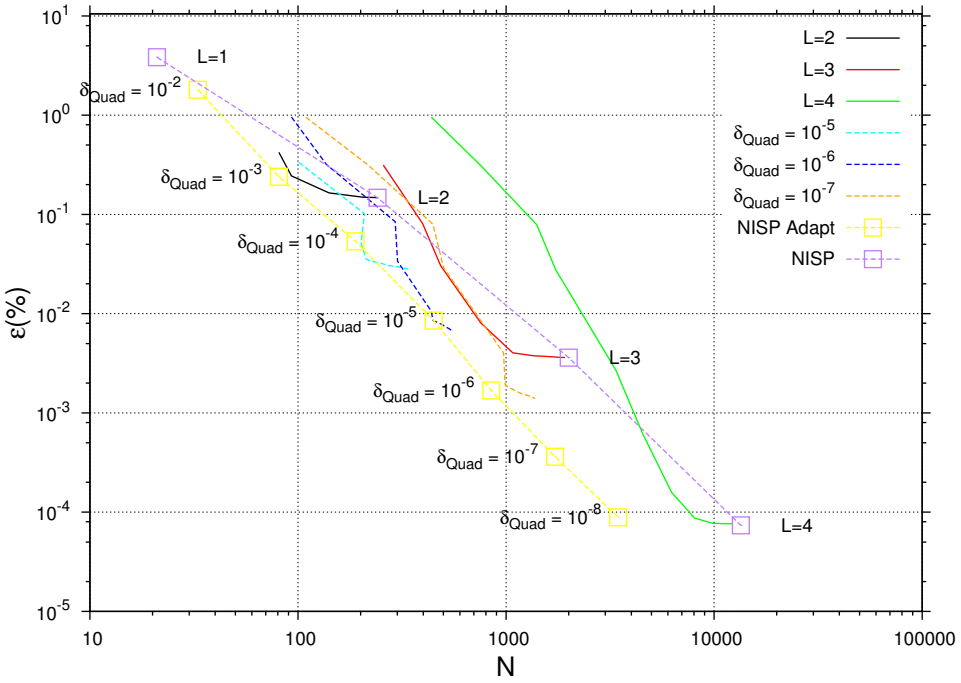


Figure 5.11.: Relative error in the variance versus the number of realisations (N).

quadrature for 10 and 20 stochastic dimensions, M, in Figure (5.13). Here we can see that increasing the number of dimensions from 10 to 20 results in greater than an order of magnitude increase in the execution time of the adaptive NISP whereas, the adaptive HDMR is comparatively insensitive to this change. However, the implementation of the adaptive quadrature scheme may not be the most efficient due to the high level programming methods that were used. Efficient data structures for the adaptive quadrature algorithm have been proposed in [68] and may go some way in reducing the execution time.

5.5.2. Rowlands' Pin Cell Problems

The Light Water Reactor (LWR) Rowlands' pin-cell benchmarks are a set of pin-cell problems described in an OECD report by J.L. Rowlands [106] for

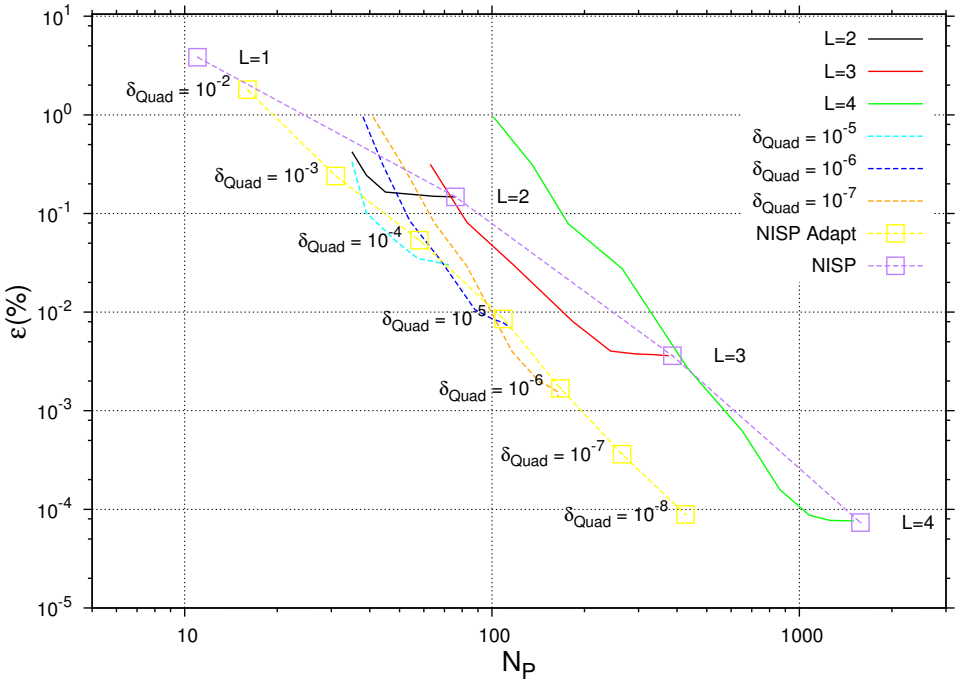


Figure 5.12.: Relative error in the variance versus the number of polynomials in the PCE (N_P).

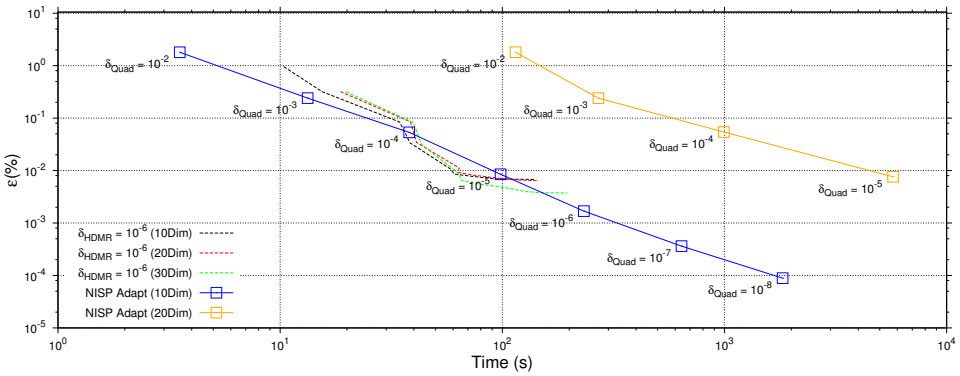


Figure 5.13.: Relative error in the variance versus execution time for HDMR and NISP using adaptive quadrature.

benchmarking LWR lattice physics codes. There are two pin-cells described in the report, the first is a simple PWR square Uranium Oxide (UO_2) pin-cell problem without leakage and the second is a geometrically similar Mixed Oxide (MOX) pin-cell. They are both three region cells consisting of

a central fuel region, a zirconium clad region and water coolant region. The outer radii of the fuel and clad regions are denoted r_1 and r_2 respectively and the size of the square coolant region denoted by (x_d, y_d) which are widths of the x and y dimensions respectively. The geometries of the problems are specified by the following values:

$$\text{UOX:} \quad r_1 = 0.40\text{cm} \quad r_2 = 0.450\text{cm} \quad x_d = y_d = 1.20\text{cm}$$

$$\text{MOX:} \quad r_1 = 0.41\text{cm} \quad r_2 = 0.475\text{cm} \quad x_d = y_d = 1.26\text{cm}$$

The temperature of each pin-cell is assumed to be a homogeneous value of 293.16K. A schematic of the problems is shown in Figure (5.14) and the material compositions are given in Table (5.1). The clad region of the Rowlands' pin cell problem is composed of zirconium which is formed from 5 naturally occurring isotopes according to Table (5.2).

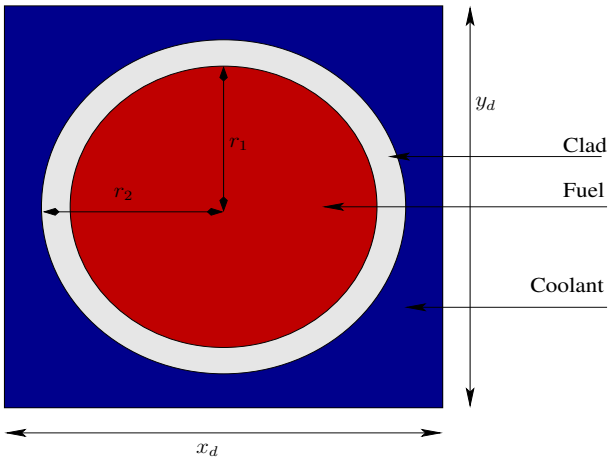


Figure 5.14.: Two-dimensional xy geometry of the LWR Rowlands pin-cell problem.

All k_{eff} calculations for the uncertainty analysis have been performed using the even parity transport code EVENT [26]. The energy discretisation

Material	Composition		Number density (atoms.barn^{-1}.cm^{-1})	
	UOX	MOX	UOX	MOX
Fuel	^{235}U	^{235}U	7.0803×10^{-4}	5.1050×10^{-5}
	^{238}U	^{238}U	2.2604×10^{-2}	2.0370×10^{-2}
	^{16}O	^{16}O	4.6624×10^{-2}	4.5880×10^{-2}
		^{238}Pu		4.6690×10^{-5}
		^{239}Pu		1.4650×10^{-3}
		^{240}Pu		5.6910×10^{-4}
		^{241}Pu		2.7130×10^{-4}
		^{242}Pu		1.4130×10^{-4}
		^{241}Am		3.0280×10^{-5}
Clad	Zr	Zr	4.3241×10^{-2}	3.8800×10^{-2}
Coolant	H	H	6.6988×10^{-2}	4.7440×10^{-2}
	^{16}O	^{16}O	3.3414×10^{-2}	2.3720×10^{-2}

Table 5.1.: Material compositions for the fuel, clad and coolant regions of the Rowlands' PWR square pin-cell problem.

Isotope	Abundance (%)
^{90}Zr	51.45
^{91}Zr	11.22
^{92}Zr	17.15
^{94}Zr	17.38
^{96}Zr	2.80

Table 5.2.: Isotopic abundance of natural Zirconium.

used 3, 9 and 26 energy groups. The angular variation in the neutron flux was modelled using a P_3 spherical harmonic expansion and the scattering was assumed to be isotropic. The low angular discretisation and the assumption of isotropic scattering were prescribed in order to minimise the execution time of the simulations. The pin cell is modelled in xy geometry using one eighth symmetry to reduce the number of unknowns in the problem. The geometry of the pin cells was discretised using the finite element method using 100 linear triangles in the fuel region, 100 bilinear quadrilaterals in the clad region and 100 bi-linear quadrilaterals in the coolant

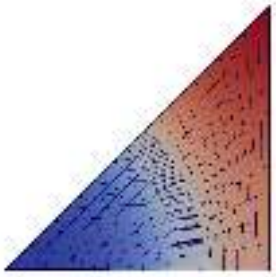


Figure 5.15.: Discretised geometry of the Rowlands' pin-cell problems for EVENT calculations.

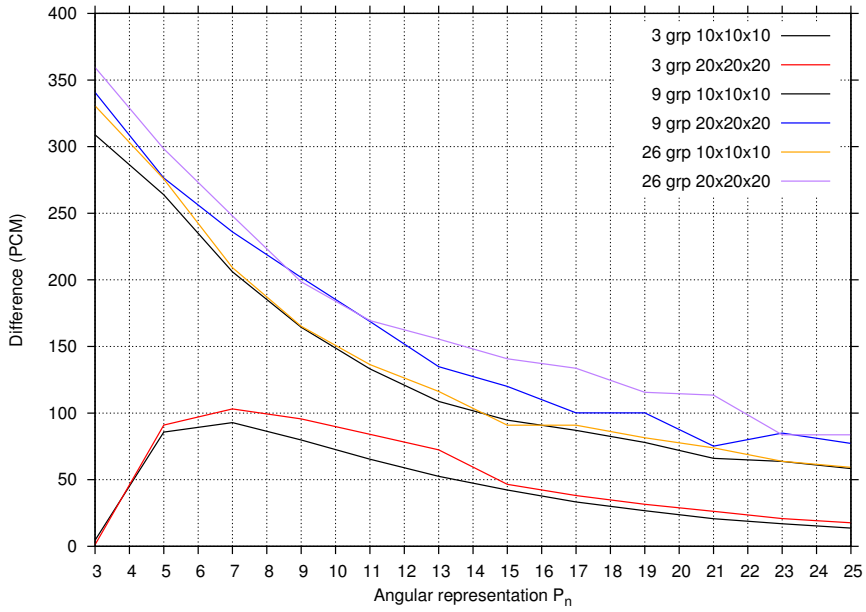
region as shown in Fig.(5.15). As a consequence of using linear triangles and quadrilaterals, the mesh is a polygonal approximation to the exact circular geometry of the fuel and clad regions in the pin cell. Therefore, in order to preserve the fissile, clad and coolant areas, the radii need to be modified. The relationship used to modify the radii of the two-dimensional finite element approximation of the sector of the circle is given by:

$$R' = \left(\sqrt{\frac{\theta}{N_\Delta \sin(\frac{\theta}{N_\Delta})}} \right) R. \tag{5.5.3}$$

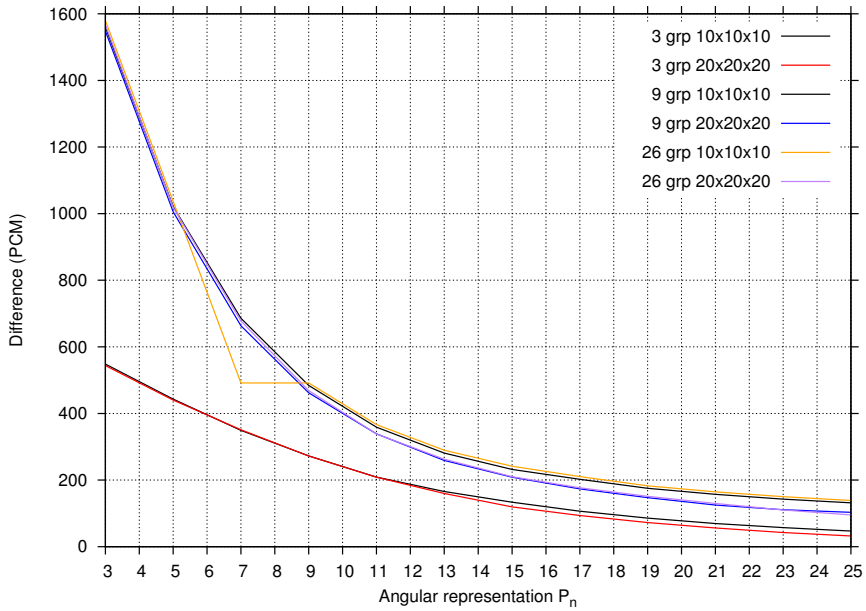
The symbol R' is the new radius, R is the old radius, N_Δ is the number of divisions on the arc and θ is the angle of the arc of the circle being meshed in radians.

The convergence of EVENT k_{eff} calculations with respect to reference solutions are given in Fig.(5.16). The reference solutions were calculated using the method of characteristic code CACTUS [107] which is part of the WIMS [28] modular code suite. The CACTUS calculations used 11 azimuthal angles and 7 polar angles with a track spacing of 0.005. The spatial domain was split 30x30 in the x-y directions. The problem has also

been modelled using diagonal symmetry.



(a) UOX Pin Cell



(b) MOX Pin Cell

Figure 5.16.: Convergence of EVENT calculations for the UOX and MOX Rowlands' pin-cell problems with space and angle.

From Fig.(5.16) we can see that both UOX and MOX problems converge

to the CACTUS solution as the angular representation of the flux is increased. The justification for using the lowest, P_3 representation was to minimise the execution time making many hundreds of thousands of realisations for Monte Carlo sampling feasible. The P_3 solution with a 10x10x10 mesh, a splitting of 10 along each line of each region in Fig.(5.15), takes fractions of a second to compute whereas the higher spatial and angular representations take in the order of 5 minutes. As a result of the low fidelity representation, a systematic error will be present in each EVENT calculation. We do not expect this systematic error to have any significance on the quantification of the uncertainty on the nuclear data when comparisons are made between Monte Carlo sampling and the polynomial chaos methods. We also note that the convergence characteristics are different for the 3 group problems compared to the 9 and 26 group problems for the UOX pin cell in Fig. (5.16a). We can offer no explaination for these observed trends but are confident that it will have no bearing on the final uncertainty results.

For all of the following problems, the input random processes (the correlated uncertain nuclear data) are represented using a Karhunen Loéve expansion. The number of terms in the Karhunen Loéve expansion is truncated when the cumulative sum of the eigenvalues in the decomposition = 1 - see Section (2.3.1). Truncating the expansion in this way represents all of the random information contained in the random process whilst removing any degeneracy.

5.5.2.1. Nuclear Data Covariances

The uncertainties in the nuclear data are tabulated in an evaluated nuclear data library in the form of covariance matrices. For these data to be com-

patible with a reactor physics or criticality code, the file must be processed using a nuclear data processing code such as NJOY [20]. For the case of a deterministic criticality code, which uses the multi-group scheme, NJOY performs the necessary tasks to produce group condensed uncertainties in the form of covariance matrices. The covariance library used in this work was very much a "test" library compiled from various different nuclear data evaluations such as: ENDF/B-VI.8, ENDF/B-VII.0, JEF-2.2, JEFF-3.1, JENDL-3.3 and TENDL-2008. The library was produced with three group schemes: 3, 9 and 26 energy groups.

The covariance matrices available in the library were produced for each available nuclide (MAT number in ENDF format) and for every available reaction for that nuclide (MT number). NJOY also produces covariance matrices for the mutual covariances between reactions. However, no data is present for any potential correlations between nuclides which are therefore assumed to be independent.

The covariances are produced at infinite dilution, which means that the weighting spectrum does not include any effects of resonance absorption. Not considering these effects in the calculation of the covariances means that the uncertainties are overestimated. This is due to the damping effect that the resulting flux depressions from resonance absorption have on the multi-group constants. In an attempt to account for this, we made the assumption that the shielded and un-shielded covariances have the same relative uncertainties. In other words, the relative covariances produced by NJOY (see equation (2.3.7)) are used and re-normalised using mean values which have been corrected for resonance absorption.

The mean values of the multi-group nuclear data were generated using the reactor physics code WIMS [28]. The Method of Characteristics code CACTUS [107], which is a part of the WIMS code suite, was used to condense the 172 group WIMS data library to the 3,9 and 26 groups required for the EVENT calculations. The subgroup method was used to calculate the effect of the resonance absorption for ^{235}U , ^{238}U and ^{239}Pu; for all other nuclides equivalence theory was used [108].

As we have mentioned, the covariances are produced per reaction per nuclide; this may not, however, correspond directly with the reaction cross sections used in a criticality code such as EVENT or CACTUS. Thus we must define the relationships between the reactions output by NJOY to those used in the reactor physics code and process the covariance data accordingly. The microscopic absorption and scattering cross sections for a given nuclide are defined in CACTUS and EVENT as

$$\sigma_a = \sigma_f + \sigma_c \tag{5.5.4}$$

$$\sigma_s = \sigma_e + \sigma_{in} + 2\sigma_{2n} + 3\sigma_{3n} \tag{5.5.5}$$

where we have defined the total capture cross sections σ_c as

$$\sigma_c = \sum_i \sigma_{c_i} - \sigma_{2n} - 2\sigma_{3n} \tag{5.5.6}$$

From the definition in (5.5.6) we can see that the total capture cross

section is equal to the sum over many capture reactions such as (n,p), (n,d), (n,t) etc but not including fission. For the sake of simplicity, and to minimise the amount of data that needs to be processed, we only consider the following MT numbers:

(n,n) : Elastic scattering σ_e (MT=2)

(n,n') : Inelastic scattering σ_{in} (MT=4)

$(n,2n)$: Production of two neutrons σ_{2n} (MT=16)

$(n,3n)$: Production of three neutrons σ_{3n} (MT=17)

(n,γ) : Radiative capture σ_g (MT=102)

(n,f) : Total fission σ_f (MT=18)

$\overline{\nu}$: Average total number of neutrons per fission $\overline{\nu}$ (MT=452)

The total capture cross section is now reduced to the following:

$$\sigma_c = \sigma_g - \sigma_{2n} - 2\sigma_{3n} \tag{5.5.7}$$

We may now use Eqns.(5.5.4), (5.5.5) and (5.5.7) to produce appropriate covariances for use in calculations. If two random processes, say Σ and Σ', are comprised of a sum of other random processes, for example

$$\Sigma = \sum_i \alpha_i a_i \quad \Sigma' = \sum_j \beta_j b_j \tag{5.5.8}$$

where the sets $\{a_i\}$ and $\{b_j\}$ are random process and α_i and β_j are deterministic coefficients, then the covariance between Σ and Σ' is written as

follows:

$$\mathrm{Cov}_{\Sigma\Sigma'}(E_g, E_h) = \sum_i \sum_j \alpha_i \beta_j \mathrm{Cov}_{a_i b_j}(E_g, E_h). \tag{5.5.9}$$

As an example, the covariance between σ_c and σ_f may be written as

$$\mathrm{Cov}_{\sigma_c\sigma_f}(E_g, E_h) = \mathrm{Cov}_{\sigma_g\sigma_f}(E_g, E_h) - \mathrm{Cov}_{\sigma_{2n}\sigma_f}(E_g, E_h) - 2\mathrm{Cov}_{\sigma_{3n},\sigma_f}(E_g, E_h) \tag{5.5.10}$$

A final covariance matrix for each nuclide, which we denote C, is produced detailing the covariances of each reaction and the cross covariance between reactions. The symmetric matrix C has the following form:

$$C = \begin{pmatrix} \mathrm{Cov}[\sigma_c, \sigma_c] & \mathrm{Cov}[\sigma_c, \sigma_s] & \mathrm{Cov}[\sigma_c, \sigma_f] & \mathrm{Cov}[\sigma_c, \overline{\nu}] \\ \mathrm{Cov}[\sigma_s, \sigma_c] & \mathrm{Cov}[\sigma_s, \sigma_s] & \mathrm{Cov}[\sigma_s, \sigma_f] & \mathrm{Cov}[\sigma_s, \overline{\nu}] \\ \mathrm{Cov}[\sigma_f, \sigma_c] & \mathrm{Cov}[\sigma_f, \sigma_s] & \mathrm{Cov}[\sigma_f, \sigma_f] & \mathrm{Cov}[\sigma_f, \overline{\nu}] \\ \mathrm{Cov}[\overline{\nu}, \sigma_c] & \mathrm{Cov}[\overline{\nu}, \sigma_s] & \mathrm{Cov}[\overline{\nu}, \sigma_f] & \mathrm{Cov}[\overline{\nu}, \overline{\nu}] \end{pmatrix} \tag{5.5.11}$$

Examples of matrix C, normalised to give correlations, are given in Fig.(5.17) for ^{235}U for the microscopic unmodified NJOY data. Here we can see that the $\overline{\nu}$ data is completely independent of all the reaction cross sections.

The eigenspectrum of the covariance matrix C defined above has been computed for hydrogen, ^{239}Pu, ^{240}Pu, ^{235}U and ^{238}U. These eigenspectra have been normalised and are plotted in cumulative form in Fig. (5.18). From this figure we can see that the eigenspectrum of hydrogen, H, decays very quickly and the majority of the variation may be expressed with the first eigenvalue. This is in contrast to ^{235}U, for example, whose eigenspectrum has a much lower rate of decay with a much lower proportion of the

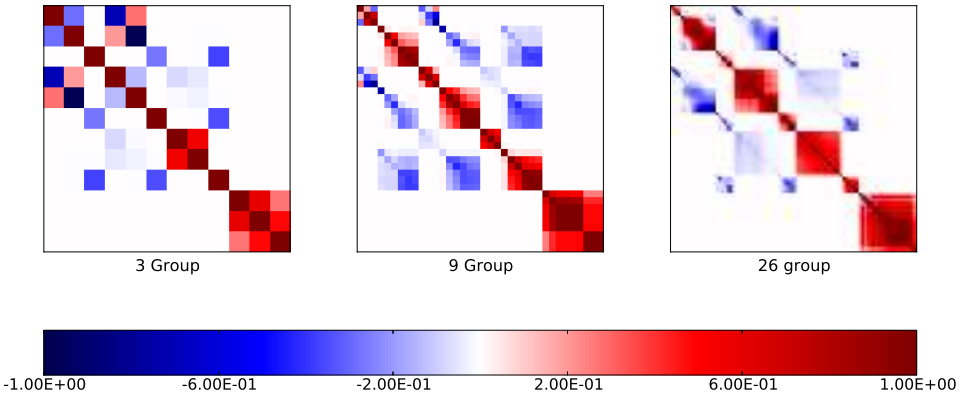


Figure 5.17.: Correlation matrix C from Eqn.(6.1.2) of ^{235}U for 3, 9 and 26 groups.

variation contained within the first eigenmode.

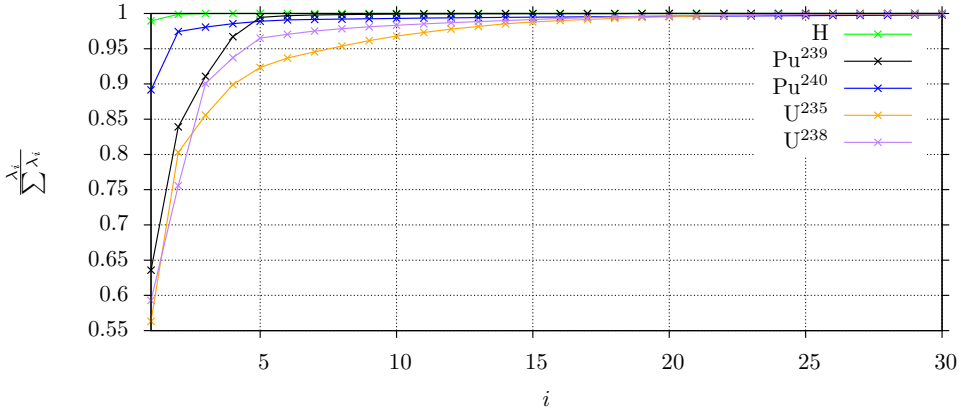


Figure 5.18.: Cumulative graph of the eigenspectra of H, ^{239}Pu, ^{240}Pu, ^{235}U and ^{238}U for the covariance matrix defined by Eqn.(6.1.2). There are 26 energy groups for each reaction and $\overline{\nu}$. Only the first 30 eigenvalues have been plotted.

5.5.2.2. HDMR Versus Latin Hypercube Sampling (LHS)

The purpose of the following numerical experiments was to look at the efficiency of the HDMR method compared to LHS. To this end, a set of test cases was devised using the Rowlands' pin cell problems which had an increasing number of uncertain input parameters which is denoted by M. This

hierarchy of test cases is detailed in Table(5.3).

Groups	UOX			MOX		
	Name	Covariance Data	M	Name	Covariance Data	M
3	UOX_{12}	^{235}U	12			
	UOX_{42}	U + H + O + Zr	42	MOX_{114}	U + Pu + ^{241}Am + H + O + Zr	114
9	UOX_{36}	^{235}U	36			
				MOX_{288}	U + Pu + ^{241}Am	288
	UOX_{136}	U + H + O + Zr	136	MOX_{342}	U + Pu + ^{241}Am + H + O + Zr	342
26	UOX_{104}	^{235}U	104	MOX_{416}	^{235}U + ^{238}U + ^{239}Pu + ^{240}Pu	416
				MOX_{832}	U + Pu + ^{241}Am	832
	UOX_{364}	U + H + O + Zr	364	MOX_{988}	U + Pu + ^{241}Am + H + O + Zr	988

Table 5.3.: Hierarchy of Rowlands' pin-cell problems with differing numbers of stochastic dimensions, M. We define: U=^{235}U + ^{238}U, Pu=^{238}Pu + ^{239}Pu + ^{240}Pu + ^{241}Pu + ^{242}Pu.

The number of random dimensions in each problem is varied by assuming different nuclides are uncertain. For example; the UOX_{12} problem in Table(5.3) only considers uncertainties on U^{235} and all other nuclides are deterministic. This set of test problems provides a spread in the number of dimensions from 12 - 988. The number of uncertain parameters is given as a subscript in the problem name. All of the input uncertainties are assumed to have a Gaussian distribution which is a standard assumption.

To investigate the efficiency of both the LHS and HDMR approaches, the relative error is plotted against the number of realisations. The number of realisations was determined during run time of the HDMR method; once found, this number of Latin Hypercube samples was performed for three different random number seeds. An error was computed for each of the seeded LHS computations. The average error for each of these calculations was also computed. The relative error requires a reference solution, this was

computed using 10^6 Latin Hypercube samples. The results of the reference solutions are given in Table (5.4) below:

Groups	UOX				MOX			
	Name	Mean	Variance	R(%)	Name	Mean	Variance	R(%)
3	UOX_{12}	1.3876	2.2277E-4	1.0757				
	UOX_{42}	1.3876	2.7559E-4	1.1964	MOX_{114}	1.2157	1.5015E-4	1.0079
9	UOX_{36}	1.3831	8.8523E-5	0.6802				
					MOX_{288}	1.2003	3.6955E-5	0.5064
	UOX_{136}	1.3831	1.1482E-4	0.7747	MOX_{342}	1.2003	3.8520E-5	0.5170
26	UOX_{104}	1.3829	8.7052E-5	0.6746	MOX_{416}	1.2001	3.2026E-5	0.4715
					MOX_{832}	1.2001	3.5750E-5	0.4982
	UOX_{364}	1.3829	1.1300E-4	0.7686	MOX_{988}	1.2001	3.7203E-5	0.5082

Table 5.4.: Mean, variance and relative standard deviation R of k_{eff} for the problems defined in Table (5.3). These are the reference values calculated using 10^6 Latin hypercube samples.

The HDMR results were computed using an adaptive HDMR tolerance of $\delta_{\text{HDMR}} = 10^{-5}$ and an adaptive quadrature tolerance of $\delta_{\text{Quad}} = 10^{-5}$. The relative error has been computed for the mean and the variance of k_{eff} for each problem and the results are plotted in Figures (5.19) and (5.20) respectively. The number of realisations, denoted by N, used in each of the HDMR and LHS results are given in Table (5.5). The results for the mean show that the HDMR error remains largely constant whilst the LHS error steadily decreases. The error in the HDMR calculation of the mean is consistently lower than the average LHS error for all values of M. The HDMR calculation of the variance is about an order of magnitude more accurate than the average LHS calculation for all of the problems up to 988 dimensions.

To assess the effectiveness of the adaptive HDMR procedure, the relative contribution of the variance from each HDMR order, ν, (not to be confused with $\overline{\nu}$, the average number of neutrons produced per fission) has also been

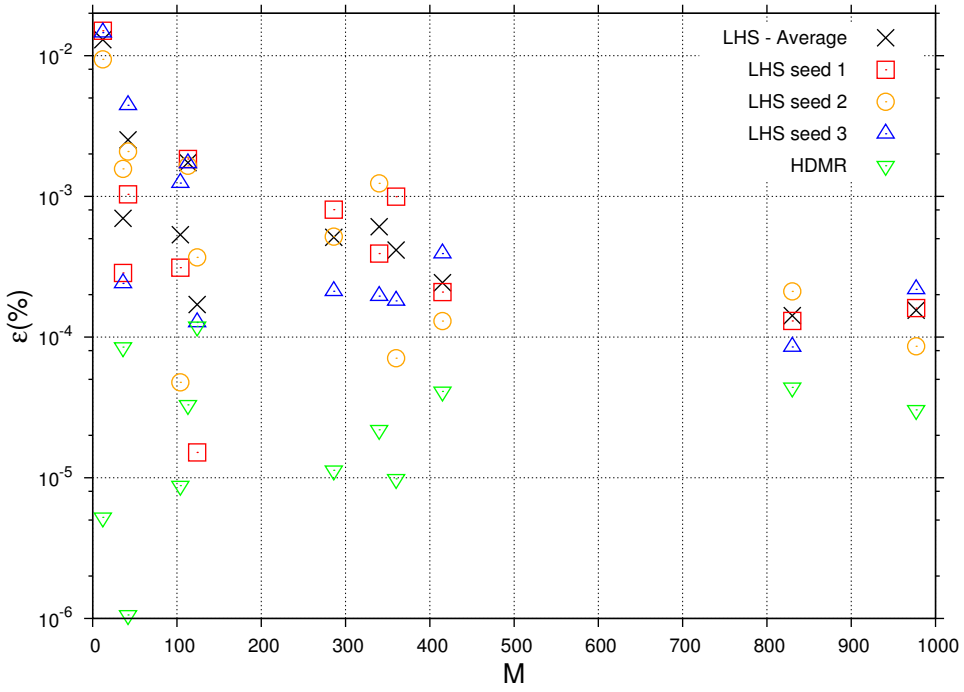


Figure 5.19.: Relative error in the mean versus number of stochastic dimensions M for the problems in Table(5.3) calculated using both HDMR and LHS.

Groups	UOX			MOX		
	Name	M	N	Name	M	N
3	UOX_{12}	12	55	MOX_{114}	114	279
	UOX_{42}	42	149			
9	UOX_{36}	36	89	MOX_{288}	288	603
	UOX_{136}	136	297	MOX_{342}	342	711
26	UOX_{104}	104	215	MOX_{416}	416	855
				MOX_{832}	832	1691
	UOX_{364}	364	739	MOX_{988}	988	1985

Table 5.5.: The number of realisations used in the HDMR and LHS calculations presented in Figs. (5.19) and (5.20) for the Rowlands' pin cell problems.

calculated. This relative variance is defined as follows:

$$\mathrm{Var}_\nu = \frac{\sum_{|\boldsymbol{u}|=\nu} \sigma_{\boldsymbol{u}}}{\mathrm{Var}_T} \tag{5.5.12}$$

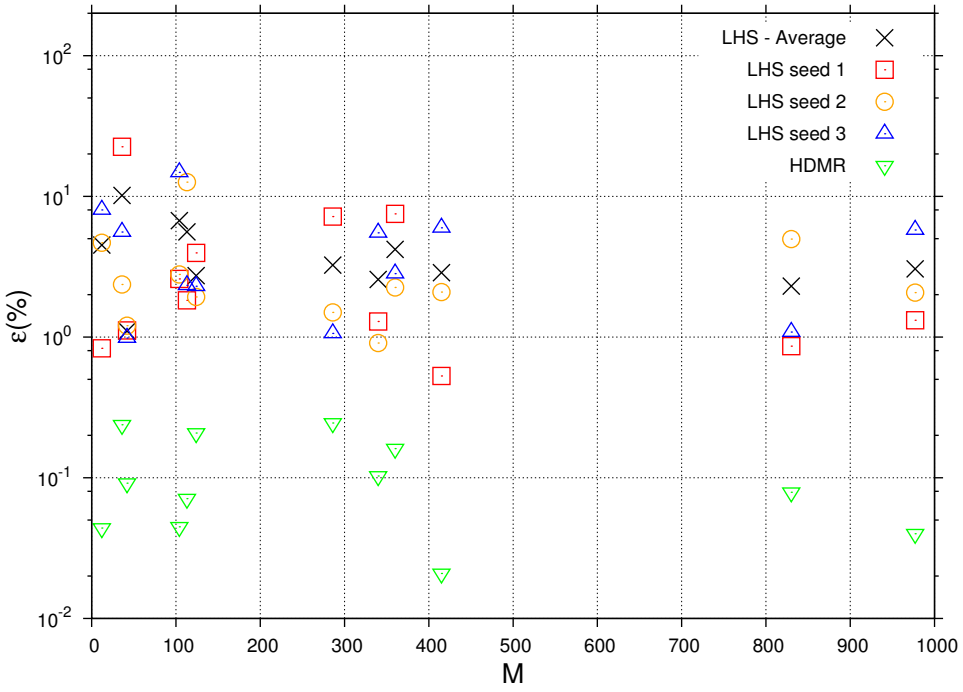


Figure 5.20.: Relative error in the variance versus number of stochastic dimensions M for the problems in Table(5.3) calculated using both HDMR and LHS.

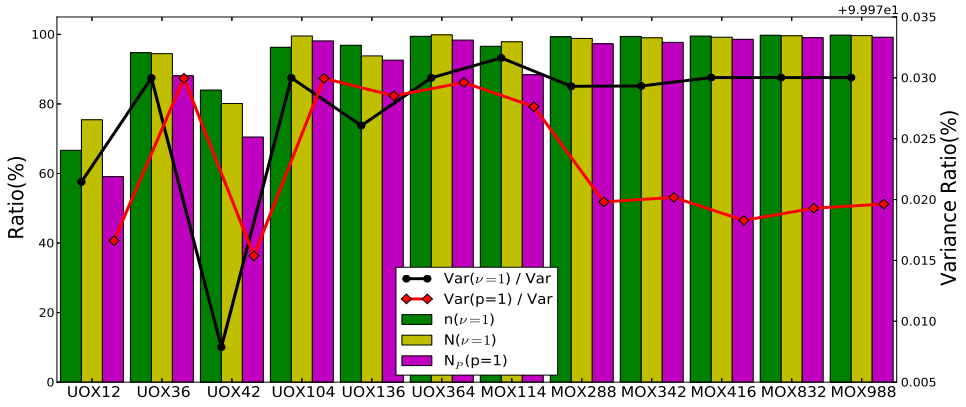
where Var_T is the total variance represented by the HDMR expansion and $\sigma_{\boldsymbol{u}}$ is the variance of the HDMR component for dimensions $\boldsymbol{u}$. The variance ratio defined by $\mathrm{Var}_{\boldsymbol{\nu}}$ in Eqn.(5.5.12) gives the variance attributed by all HDMR components with a number of dimensions equal to ν. The variance ratio for all of the problems in Table (5.3) are plotted in Fig.(5.21) along with the relative number of HDMR components, which is denoted $n(\nu = 1, 2, \mathrm{etc})$, and the relative number of realisations which is denoted $N(\nu = 1, 2, \mathrm{etc})$. In other words $n(\nu = 1)$ is the ratio of one dimensional HDMR components to the total number in the expansion, and $N(\nu = 1)$ is the ratio of the number of samples required to calculate the one dimensional terms to the total number of samples. We have also plotted the relative contributions to the polynomial chaos variance for each polynomial order p which we denote

Var_p. The set of polynomial chaos indexes $\mathcal{A}$ was computed iteratively using the adaptive HDMR and quadrature methods. The variance ratio for polynomial order p is defined as

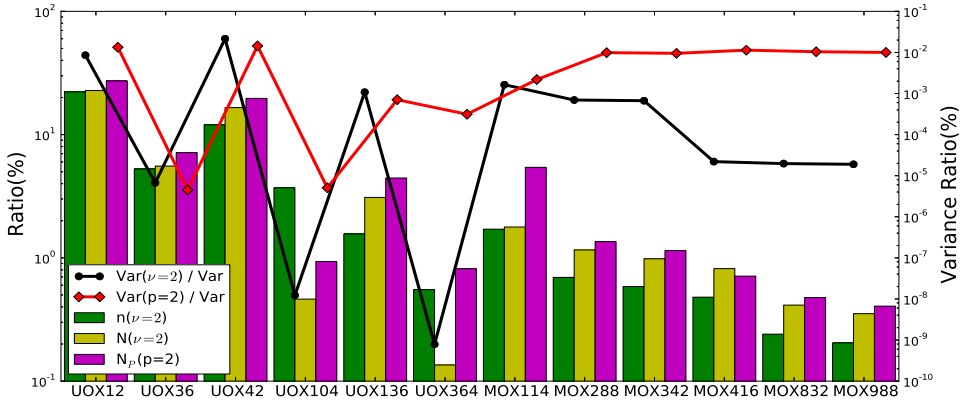
$$\mathrm{Var}_p = \frac{\sum\limits_{\boldsymbol{\alpha}\in\mathcal{A};|\boldsymbol{\alpha}|=p} N_{\boldsymbol{\alpha}}^2 R_{\boldsymbol{\alpha}}^2}{\sum\limits_{\boldsymbol{\alpha}\in\mathcal{A}} N_{\boldsymbol{\alpha}}^2 R_{\boldsymbol{\alpha}}^2} \tag{5.5.13}$$

The relative number of polynomial coefficients which is denoted $N_P(p = 1, 2, \text{etc})$ has also been calculated where $N_P(p = 1)$ is the ratio of linear polynomials to the total number in the polynomial expansion and $N_P(p = 2)$ is the ratio of quadratic polynomials etc. In Fig.(5.21a) results of variance ratio and number ratio for $\nu = 1$ and $p = 1$ are plotted. Here we can see that the first order ($\nu = 1$) HDMR components contribute at least 60% of the total components and contribute greater than 99.97% of the calculated, total variance. The same is also true for the PCE variance ratio. In Fig.(5.21b) results are plotted for $\nu = 2$ and $p = 2$. Here we can see that the relative number of components and realisations are in the range of $0.1\% \rightarrow 10\%$ for all problems but the variance ratio of the HDMR components is of the order of $10^{-2}\% \rightarrow 10^{-3}\%$. This means that, in the best case scenario, 0.1% of the work results in a $10^{-2}\%$ contribution to the variance and in the worst case, 10% of the work results in a $10^{-3}\%$ contribution. Even in the best case, the utilisation of the computational effort results in a small contribution to the final result. A similar trend is observed in the results for the PCE variance ratio. In Fig.(5.21c) results are plotted for $\nu = 3$ and $p = 3$. Again, as with the results for $\nu = 2$, the relative number of components and realisations are in the range of $0.1\% \rightarrow 10\%$ for all problems but in this instance the variance ratio of the HDMR components is as low as $10^{-9}\%$. We note that only four problems computed the third order HDMR components resulting

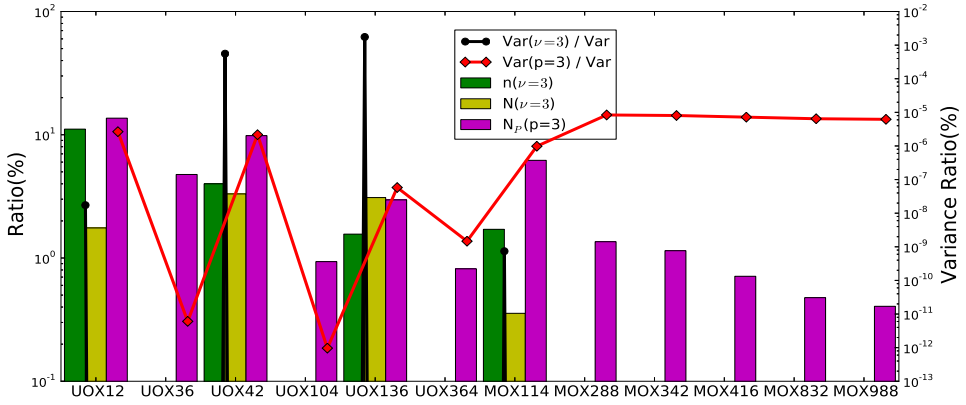
in the discontinuities in the HDMR variance ratio. For all other problems, the algorithm decided three variable terms were unimportant. Values of the PCE variance ratio for $p = 3$ do exist for all problems since it is the adaptive quadrature algorithm that determines these values and sufficient non-linear behaviour may exist in any of the HDMR terms. Although no restriction was placed on the maximum order ν, no fourth order ($\nu = 4$) components were calculated by the algorithm for any of the problems.



(a) $\nu = 1$ / p=1

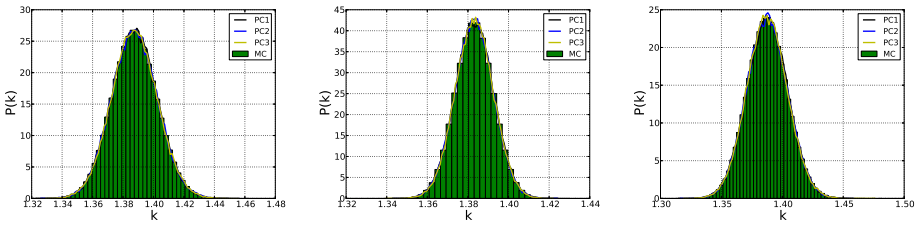


(b) $\nu = 2$ / p=2

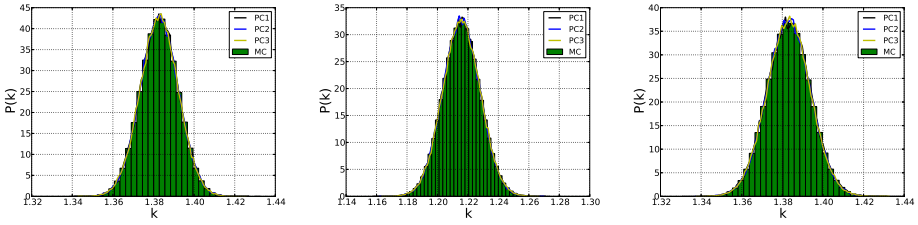


(c) $\nu = 3$ / p=3

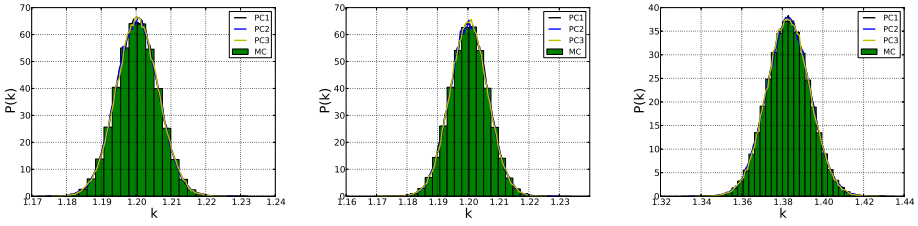
Figure 5.21.: Relative contributions of the variance of each HDMR order ν, the variance of each polynomial order p, the relative number of HDMR terms, the relative number of quadrature points and the relative number of polynomials.



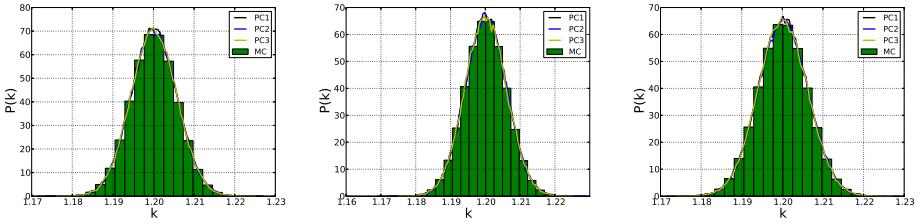
(a) UOX_{12} (b) UOX_{36} (c) UOX_{42}



(d) UOX_{104} (e) MOX_{114} (f) UOX_{136}



(g) MOX_{288} (h) MOX_{342} (i) UOX_{364}



(j) MOX_{416} (k) MOX_{832} (l) MOX_{988}

Figure 5.22.: Probability density functions for the problems in Table (5.3) calculated using polynomial chaos and LHS. Adaptive HDMR threshold $\delta_{\text{HDMR}} = 10^{-5}$ and adaptive quadrature threshold, $\delta_{\text{Quad}} = 10^{-5}$.

For all of the problems in Table (5.3), each component in the HDMR expansion of the k_{eff} response surface was projected onto its own polynomial chaos basis using Eqn.(5.4.3). The resulting sparse PCEs were then used to calculate a PDF; one PDF was calculated for each polynomial order p. These PDFs are plotted in Figure (5.22) alongside the PDF calculated using the reference Latin Hypercube solution. Here we can see that there is no visible difference between PDFs for different values of p. Since the PCE variance ratios for $p = 2$ and $p = 3$ in Fig.(5.21) are insignificant, very little difference between the PDFs was expected. We also note that the $p = 1$ PDF, i.e. linear polynomials only, provides a sufficient representation of the reference solution.

5.5.2.3. Log-Normal Versus Gaussian Distributed Uncertainties

For all of the pin cell problems studied in section (5.5.2.2), the uncertainties in the nuclear data were modelled using a Gaussian distribution. This distribution supports negative numbers and as such, it allows negative values of the nuclear data to be realised when sampling; this is obviously un-physical. An alternative distribution, which is closely related to the Gaussian distribution, is the Log-Normal distribution. This distribution is sometimes preferable to the Gaussian as it removes any possibility of generating negative valued samples.

In this section a comparison is made between Log-Normal and Gaussian distributions for one of the Rowlands' pin cell problems, namely UOX_{12}. The covariance data is again sourced from evaluated data and processed in the same way as in the previous section. There is however, an additional processing step which is required before the correlated nuclear data may

be sampled according to the Log-Normal distribution. The covariance matrices must be transformed from a Log-Normal to a Gaussian space using Eqn.(2.4.9). The resulting Gaussian covariances were then decomposed using the Karhunen Loéve method; correlated samples were generated in the usual way and transformed back to the Log-Normal space using Eqn.(2.4.8).

To look at the efficiency of the HDMR method when using Log-Normal and Gaussian uncertainties, the relative error is plotted versus the number of realisations in Fig.(5.23). The reference solution is calculated using LHS with 10^6 samples. The accuracy and hence number of function evaluations required in the HDMR expansion was varied by decreasing the values of δ_{HDMR} from $10^{-1} \rightarrow 10^{-10}$. The adaptive quadrature method was used with a value of $\delta_{\text{Quad}} = 10^{-5}$. The results in Fig.(5.23) show that the HDMR method is more efficient when using Gaussian distributed uncertainties when compared to Log-Normally distributed uncertainties for this problem. The results for the Gaussian uncertainties have fewer points since the number of terms which contribute a proportion of the variance above the threshold δ_{HDMR} is small hence the algorithm only calculates a small number of components. We also note the strange behaviour in the convergence rate of the LogNormal problem. One possible explanation for this is that; since the HDMR expansion is a superposition of many terms, incrementally adding more terms may take the computed solution further away from the true solution. Ultimately, when all of the important interactions are considered,the computed solution will converge which is what we observe.

To explain the differences in computational expense for the two different probability distributions, the variance ratio from Eqn.(5.5.12) is plotted for

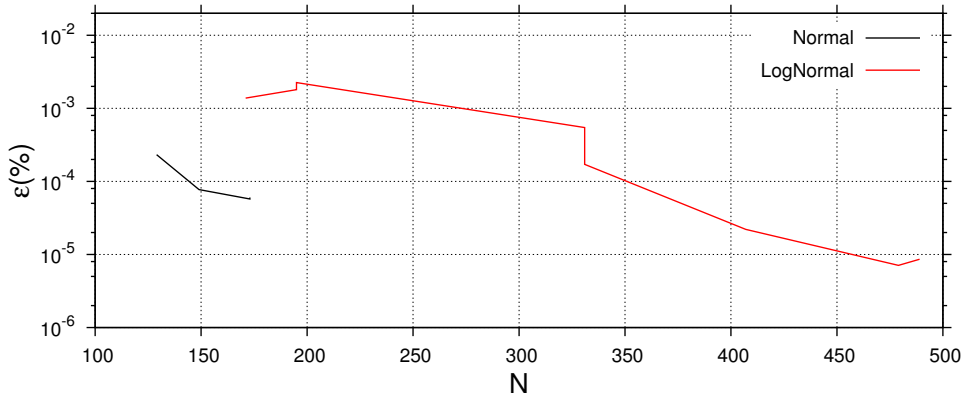
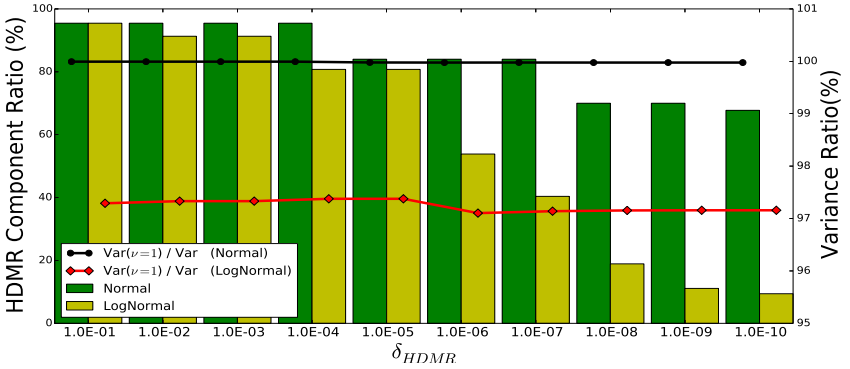


Figure 5.23.: Relative error versus number of realisations for the UOX_{42} Rowlands' pin-cell problem using Log-Normal and Gaussian distributed uncertainties.

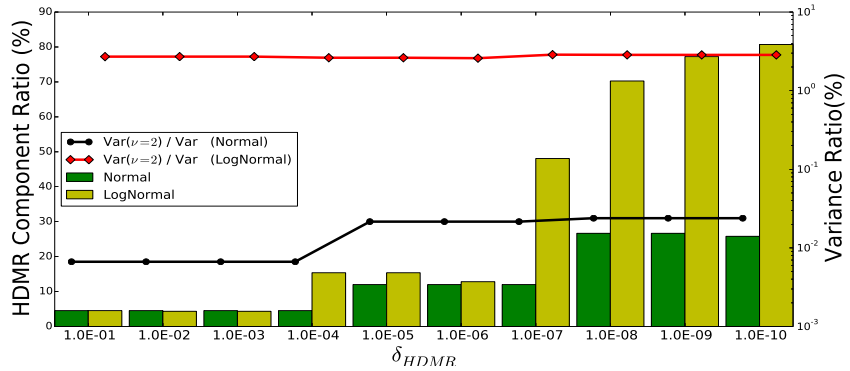
each distribution and the first three HDMR orders ($\nu = 1, 2, 3$) in Fig.(5.24). In Fig.(5.24a) we can see that as the adaptive HDMR threshold, δ_{HDMR}, decreases, the variance contribution of the first order terms for Gaussian uncertainties remains constant at a value of approximately 100%. This is compared to a value of approximately 97% for the LogNormal uncertainties. We also note that the number of components for the Gaussian case does not depreciate substantially with δ_{HDMR}, whereas, the number of components for the Log-Normal case drops to around 10%. In Fig.(5.24b) the variance ratios and the component ratios for the second order HDMR components are plotted. Here we can see that the second order components contribute approximately 3% when using LogNormally distributed uncertainties whereas the contribution when assuming a Gaussian distribution is 10^{-2}%. We also note the increase in the relative number of second order components of the Log-Normal case which corresponds to this decrease in the first order terms. In Fig.(5.24c) the third order components are plotted. The variance contributions are of the order of 0.1% and 10^{-4} for Log-Normal and Gaussian uncertainties respectively. We also note that the threshold δ_{HDMR} for the

inclusion of third order Gaussian components is a lot lower than Log-Normal since the contribution of the Gaussian components to the total variance is much smaller.

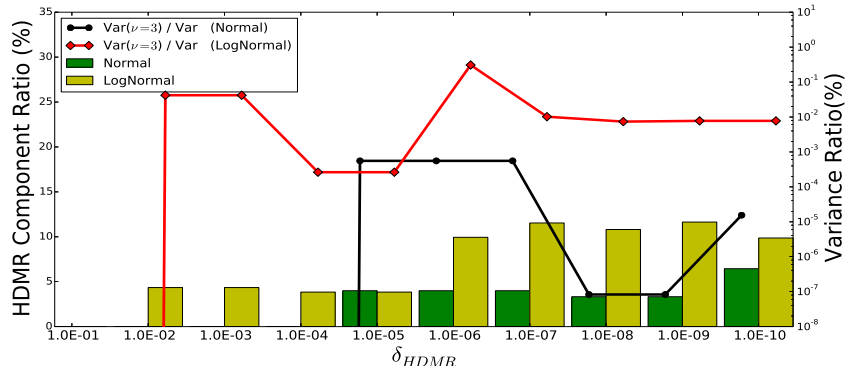
The reason for the increased contribution of the second and third order terms is probably due to the additional processing of the covariance data and the additional non-linearities which are introduced when sampling from a Log-Normal distribution.



(a) $\nu = 1$



(b) $\nu = 2$



(c) $\nu = 3$

Figure 5.24.: HDMR component and variance ratios for the Rowlands' UOX_{12} problem using Gaussian and Log-Normal nuclear data uncertainties.

5.6. Discussion and Conclusions

In this chapter an adaptive HDMR method has been combined with an adaptive sparse grid quadrature scheme to iteratively compute the coefficients in a polynomial chaos expansion via projection.

In Section (5.5.1.5) the adaptive sparse grid quadrature rules were used to calculate the components in the adaptive HDMR. The variance of a test response function was calculated in this way for a range of adaptive HDMR thresholds θ and also using a range of adaptive quadrature tolerances δ and non-adaptive quadrature levels L. The results showed that HDMR with adaptive quadrature is more efficient than with non-adaptive quadrature and as the tolerance θ is decreased, so must the adaptive quadrature tolerance δ.

In Section (5.5.1.6) the adaptive HDMR method was compared to the adaptive quadrature algorithm by computing the variance of a test response function. The results showed that the adaptive quadrature is slightly more efficient than adaptive HDMR with adaptive quadrature. However, when the number of random variables used in the problem increased from 10 to 20, the adaptive quadrature algorithm took 10 times longer to compute the solution whereas, the HDMR method was comparatively insensitive to this change.

In Section (5.5.2.2), the adaptive HDMR method was used to compute the variance in k_{eff} due to evaluated nuclear data covariances for 12 Rowlands' pin cell problems. The number of uncertain parameters in these

problems ranged from 12 to 988. HDMR solutions were compared to those computed using LHS with an equivalent number of samples. The results showed that the HDMR method was an order of magnitude more accurate than LHS when computing the variance for all problems up to 988 random dimensions. For all of these problems, where the uncertain nuclear data are described by a Gaussian distribution, the vast majority ($\geq$ 99.7%) of the calculated variance is due to the first order (uni-variate) HDMR components. The computation of the second and third order terms are inefficient for the Rowlands' problems when considering the contribution they provide to the final result and the number of calculations they require.

In Section (5.5.2.3) the variance in k_{eff} is calculated for one of the Rowlands' pin cell problems as in Section (5.5.2.2) but with the assumption that the uncertainties are described by a Log-Normal distribution. The results showed that the contribution to the variance of the second and third order terms were larger than those calculated for the case of Gaussian uncertainties. The second order terms contributed around 3% of the total variance for Log-Normal uncertainties and therefore should not be ignored.

In further work, we wish to investigate differential parameters such as reaction rates and leakages which may be subject to uncertainties other than nuclear data covariances. The purpose of this further work is to ascertain if response parameters other than k_{eff} exhibit non-linear dependencies that require high order HDMR terms for the accurate determination of response statistics. The inclusion of higher order terms in the HDMR expansion increases the computational cost prompting re-investigation of the efficiency of adaptive HDMR versus Latin Hypercube. We expect, with the inclusion

of high order HDMR terms, that the efficiency of the HDMR approach will decrease making LHS more competitive. The exact number of dimensions, where the HDMR is still more efficient than LHS, will depend upon the number of non-linear HDMR terms and will hence be problem dependent.

Chapter 6

Uncertainty Quantification in Nuclear Criticality Assessment of Americium-241 Spheres

6.1. Introduction

The aim of this investigation is to apply the polynomial chaos methods described in previous chapters to a real problem. This aim can be split into two objectives. Firstly, we compare the uncertainty method used in the Monte Carlo code MONK to the polynomial chaos method via the computation of first order sensitivities and uncertainties. This concerns assessing the response of the criticality coefficient, k_{eff} , to nuclear data uncertainty for americium-241, uranium and plutonium systems which are represented by reference spherical geometries. Secondly, we investigate the use of the k_{eff} =0.95 sub-critical limit for americium-241 systems when nuclear data uncertainties are propagated explicitly. Using the uncertainties calculated for the americium-241 systems, we then suggest alternative sub-critical lim-

its based upon comparisons with well-understood uranium and plutonium systems.

The nuclide americium-241, or ^{241}Am, has been identified as a viable isotope for use in radioisotope thermoelectric generators (RTGs). The most commonly used isotope for space battery applications has been ^{238}Pu but, due to short supply, research has focused on the use of ^{241}Am. ^{241}Am is produced via the beta decay of ^{241}Pu and is therefore present, in considerable quantities, in plutonium stock piles. The separation of large quantities of ^{241}Am is unprecedented and presents a number of new challenges, not least to criticality safety. ^{241}Am is a fissionable species and will theoretically support criticality; therefore safe critical mass limits must be understood for safe packaging and transportation.

The criticality safety criterion used in applied criticality safety assessment in the UK is specified as follows:

$$k_{\text{eff}} + 3\sigma \leq X - E_{\text{PD}} - E_{\text{SM}} - E_{\text{R}} \tag{6.1.1}$$

where σ is the standard deviation associated with a Monte Carlo simulation and

- X is the sub-critical limit. This limit is justified in various technical papers/guidance for systems of interest as required. The criterion adopted in the UK is that k_{eff} must not exceed 0.95 $+3\sigma$, except for uranium systems having an enrichment of less than 5% ^{235}U where a limit of 0.98 is applied [109].

- E_{SM} is the allowance for error due to specification and modelling of the system being addressed. When using a conservative modelling

estimate, a value of $E_{\mathrm{SM}} = 0$ is normally applied.

- E_{R} is the allowance for the susceptibility of the system to increase in reactivity. Because the systems we have chosen are spherical and are the most reactive / bounding configurations, a value of $E_{\mathrm{R}} = 0$ is applied.

- E_{PD} is the allowance for error due to the MONK program and the nuclear data used - E_{PD} is a measure of how well the code and, particularly, the nuclear data is representing the system being assessed. This is identified through validation of the code / nuclear data combination. This provides an estimate of the under- or over-estimation (or bias) of the code for this type of system. This aspect is discussed further below. For americium-241 systems E_{PD} is unknown.

There are currently no integral experimental measurements of critical americium systems which could be used to validate the evaluated nuclear data or to establish bias in simulated results. Therefore, we are unable to calculate a value for E_{PD}. There exist, however, approximations to the critical mass of some americium systems which were calculated using the equivalent mass method [110]. This technique replaces a small quantity of material in a known critical assembly with a small sample of material; a measurement of the change in reactivity is used to calculate the worth of the introduced sample. The reactivity worth is inferred through the period of the multiplying system via the Inhour equation. The critical masses of bare, water reflected and steel reflected ^{241}Am systems have been inferred from reactivity coefficient measurements [111, 112] of fast critical assemblies such as FLATTOP and BIG TEN. These masses are summarised in Table (6.1) along with the corresponding critical radii. The lack of integral experimen-

tal data for ^{241}Am systems means a different approach to criticality safety may be required, or may require additional supporting evidence, when considering nuclear data and nuclear data uncertainties.

Problem	Inferred Critical Mass (kg)	Inferred critical radius (cm)
Bare sphere	58	10.0428
Water reflected	51	9.6214
Steel reflected	34	8.4051

Table 6.1.: Inferred critical masses for ^{241}Am spheres quoted from [2]. The density of ^{241}Am is taken to be 13.67g/cc.

In this work we have studied four simple ^{241}Am spheres with different reflector materials. Uncertainty calculations for k_{eff} have been performed on these configurations and, to put the results into context, they have been compared to more familiar uranium and plutonium systems. The uranium and plutonium systems used as reference cases were chosen to be geometrically and spectrally similar to the americium problems, i.e. they are spherical configurations with fast neutron spectra. The reference cases chosen are known as the FLATTOP problems and are described in more detail in Section (6.2).

Two approaches have been used to assess the uncertainty or variation in k_{eff} due to nuclear data. The first involves the computation of k_{eff} using a range of nuclear data evaluations. Here we assume that there is an underlying probability distribution describing the spread in k_{eff} result calculated using different nuclear data evaluations. The statistics of this distribution gives an indication of the uncertainty in the nuclear data - uncertainties calculated in this way are referred to as evaluation uncertainties. Since

the number of nuclear data evaluations is finite, the accuracy of the statistics due to the limited sample size will be low. Each evaluation is treated with equal weight. Consistent values of k_{eff} for different evaluations shows that the nuclear data is more consistent across evaluations and suggests the uncertainty in the data is small. The second approach involves a single evaluation with corresponding covariance data where the uncertainties are propagated explicitly using methods such as polynomial chaos or the MONK sensitivity method. A comparison of the uncertainties calculated using both techniques, multiple evaluations versus single evaluation plus covariance, have been conducted for both the FLATTOP and americium problems. These have then been compared to the margin associated with a typical 0.95 sub-critical limit to provide one possible approach for determining a criterion for criticality assessments for americium-241 systems.

This chapter is structured as follows: Subsection (6.1.1) describes the methods and codes used to compute k_{eff} , Subsection (6.1.2) describes how the nuclear covariances are processed and modelled and Subsection (6.1.3) defines some expressions used to calculate uncertainties and sensitivities from the polynomial chaos expansion and the MONK sensitivities. Section (6.2) is dedicated to the FLATTOP problems. The first part of this section gives results of MONK and WIMS calculations of k_{eff} for the FLATTOP problems using a range of nuclear data evaluations. The convergence of EVENT to the WIMS k_{eff} is also studied to ensure any additional modelling errors are minimised. The second part of Section (6.2) calculates the uncertainties on k_{eff} due to ENDF/B-VII.1 and JENDL 4.0 nuclear covariance data using the polynomial chaos and MONK sensitivity methods. First order sensitivities of k_{eff} with respect to different reactions are calculated and

compared for both polynomial chaos and MONK sensitivity methods using ENDF/B-VII.1 and JENDL 4.0 covariances. The statistics of k_{eff} are represented using probability density functions, means, variances and relative standard deviations. These are then used to investigate the consistency of the evaluation uncertainties along with their size relative to the sub-critical limit. Section (6.3) gives results of the americium-241 calculations. In the first part of this section the critical mass for each of four americium spheres is calculated, using both MONK and WIMS, with a variety of nuclear data evaluations. The MONK critical mass results are compared to results by another author. Again, the convergence of EVENT to the WIMS k_{eff} is studied to ensure the modelling error is sufficiently reduced. In the second part of Section (6.3) the sensitivities and statistics of k_{eff} are computed using polynomial chaos and MONK sensitivity methods and the results of both are compared. The uncertainties are then considered in the context of a sub-critical limit.

6.1.1. Computing k_{eff}

The industry standard code for the calculation of k_{eff} for criticality safety applications in the UK is MONK [33]. This is a Monte Carlo code and each time the code is executed under the same physical conditions a different answer is produced due to the statistical nature of the computation. An initial investigation showed that the polynomial chaos method attempts to represent the unwanted statistical variations present in Monte Carlo simulations. When k_{eff} is calculated for various perturbations in nuclear data, each result includes an uncorrelated statistical uncertainty. These statistical uncertainties add additional highly non-linear structure to the k_{eff} response which the polynomial expansion attempts to capture. To overcome this

effect would have required impractically long MONK run times to reduce the statistical variation sufficiently or considerable extra development to extract the underlying variation from the statistical noise. An explanation for this, and an example of the anomalous behaviour, is given in Appendix (C). Since we are unable to use MONK, or any other Monte Carlo code, for the uncertainty calculations with polynomial chaos, we must use a deterministic method. The polynomial chaos methods had been developed initially for use with the deterministic, Imperial College code, EVENT [26] and so it was decided to use this for the uncertainty quantification. EVENT uses the even parity form of the spherical harmonics method to represent the angular variation of the neutron flux, it uses the finite element method to represent the spatial variation of the neutron flux and it uses the multi-group method to represent the energy dependence of neutron flux and the input nuclear data.

In order to produce multi-group nuclear data for EVENT, which accounts for all of the resonance shielding and group condensation effects introduced by the multi-group discretisation, we must use a reactor physics code such as WIMS. Using WIMS, which is a light water reactor physics code with a library group scheme which has been optimised for a thermal spectrum, will not be as accurate as the continuous energy MONK calculations for the fast spectrum systems which we are investigating. The WIMS-ECCO capability in WIMS is more suited to fast systems due to its much finer energy representation (1968 energy groups), however it does not include a spherical geometries option and would require additional sets of data libraries. Therefore, the following WIMS route was used to calculate multi-group cross sections for use with EVENT: **HEAD** $\rightarrow$ **FLURIG** $\rightarrow$ **PIP** $\rightarrow$ **COND** $\rightarrow$ **FLURIG** $\rightarrow$ **PIP**. The **HEAD** module defines the materials and geome-

try of the problem and performs simple resonance self-shielding calculations based upon equivalence relations. The **FLURIG** module calculates collision probabilities in spherical geometry and the **PIP** module calculates the eigenvalue (k_{eff}) of the transport equation from the collision probabilities produced by **FLURIG**. The **COND** module was used to condense the data from the WIMS 172 group scheme to a 26 group scheme which is used for all of the problems in this work. The 26 group scheme will be described in more detail in Section (6.1.2).

Although the polynomial chaos methods will exclusively use the EVENT code to compute k_{eff} , MONK will still be used to compare results and to compute sensitivities and uncertainties. Due to the statistical nature of the Monte Carlo procedure, the statistical error associated with MONK results must be considered when making comparisons. We must also be sure, since we are using a power method to compute k_{eff} , that the fission source has sufficiently converged. For all of the calculations in this chapter, 100 stages were used to settle the fission source, 3000 neutrons were used in each super-history and the final value of k_{eff} was converged to a statistical tolerance of 5×10^{-4} (50pcm). The super-history powering method in MONK tracks the entire neutron progeny through to capture for up to 10 generations which reduces the correlation between successive scoring stages.

6.1.2. Modelling and Processing Covariance Data

Modern nuclear data evaluations contain covariance data for many reaction cross sections (FILE 32 in ENDF format) and also resonance parameters (FILE 33 in ENDF format). The two most recent evaluations, which have

covariance data for the majority of the nuclides and reactions used in this work, are the ENDF/B-VII.1 and JENDL 4.0 evaluations. The covariance data from each of these evaluations were processed into a broad 26 energy group format library at infinite dilution of resonance absorption using the NJOY [20] data processing code. The weighting spectrum used to condense the point wise nuclear data into group format used a thermal Maxwellian in the low energy regions, a $1/E$ spectrum in the intermediate energies and a fission Maxwellian at fission energies. The energy boundaries and parameters used for the Maxwellian distributions can be found in the nuclear data section of the WIMS manual [113].

The 26 group scheme used for the covariance libraries is a standard energy scheme for shielding applications. This group format contains 3 groups in the thermal energy range (0.0 $\rightarrow$ 0.2 eV), 3 groups in the intermediate energy range (0.2 eV $\rightarrow$ 820.85 keV) and 20 groups in the fast energy range (820.85 keV $\rightarrow$ 20 MeV). Because the majority of the energy groups are in the fast energy range and the systems being studied have fast spectra, this group scheme is considered to be acceptible, although possibly not optimal, for our applications. The group boundaries for these data generally do not align with group boundaries in the WIMS library scheme. To enable like-for-like comparisons between MONK and WIMS/EVENT sensitivities, the MONK sensitivities were scored in the WIMS group scheme. The mismatch between the covariance energy scheme and the WIMS library scheme meant there would be a bias in the sensitivity calculations. The 26 group scheme used for the sensitivity calculations was chosen to match the covariance scheme as closely as possible. This bias is expected to be small since the mismatch between group boundaries is less than 1% in all cases and even

smaller at high energies where we expect the problems being investigated to be most sensitive.

In this work, the microscopic capture and fission cross sections are assumed to be uncertain along with the average number of neutrons produced per fission, nu-bar. The scattering cross sections are assumed to be deterministic. The omission of scattering uncertainty was done due to lack of data; the computation of group-to-group scattering covariances from the NJOY covariances requires the probabilities of scattering between energy groups which were unavailable for the current study. The data produced by NJOY are per nuclide per reaction. For the problems presented in this study, some nuclides are represented in elemental form and reactions such as the total capture are defined as the combination of many capture reactions. This necessitates the need to further process covariances of individual reactions and nuclides using Eqn.(5.5.9). There may also exist covariances between reactions so the final covariance matrix is written as

$$C = \begin{pmatrix} \mathrm{Cov}[\sigma_c, \sigma_c] & \mathrm{Cov}[\sigma_c, \sigma_f] \\ \mathrm{Cov}[\sigma_f, \sigma_c] & \mathrm{Cov}[\sigma_f, \sigma_f] \end{pmatrix} \tag{6.1.2}$$

where σ_c is the microscopic capture cross section and σ_f is the microscopic fission cross section. No correlations exist between the reaction cross sections and the average number of neutrons emitted per fission, nu-bar, in the evaluated data used. Therefore, nu-bar covariances are represented independently of the reaction cross sections. There are also no correlations between different nuclides which we assume are statistically independent.

Reaction cross sections and nu-bar are condensed from the 172 energy

group WIMS library using problem specific fluxes using the modules of the WIMS code. The group condensed data may then be output for use in third party codes such as EVENT. Only transport, absorption, scatter and fission cross sections are written to the WIMS output. The relations between these cross sections are written below:

$$\sigma_t = \sigma_a + \sigma_s \tag{6.1.3}$$

$$\sigma_a = \sigma_f + \sigma_c \tag{6.1.4}$$

$$\sigma_s = \sigma_e + \sigma_{in} + 2\sigma_{2n} + 3\sigma_{3n} \tag{6.1.5}$$

where σ_t, σ_a, σ_e, σ_{in}, σ_{2n}, σ_{3n} are the total, absorption, elastic, inelastic, double neutron emission, $(n, 2n)$, and triple neutron emission, $(n, 3n)$, microscopic cross sections respectively. We may also define the total capture cross section σ_c as

$$\sigma_c = \sum_i \sigma_{c_i} - \sigma_{2n} - 2\sigma_{3n} \tag{6.1.6}$$

where the σ_{c_i} represent all of the capture-type reactions such as radiative capture (n, γ), proton emission (n, p), alpha emission (n, α) etc. To avoid excessive and unnecessary processing, the minor reactions that contribute little to the neutron balance are not included. We only consider the following

quantities (or MT numbers in ENDF format [114]):

$(n, 2n)$: Production of two neutrons σ_{2n} (MT=16)

$(n, 3n)$: Production of three neutrons σ_{3n} (MT=17)

(n, γ) : Radiative capture σ_g (MT=102)

(n, f) : Total fission σ_f (MT=18)

nu-bar : Average total number of neutrons per fission $\overline{\nu}$ (MT=452)

The total capture cross section is now reduced to the following:

$$\sigma_c = \sigma_g - \sigma_{2n} - 2\sigma_{3n} \tag{6.1.7}$$

where we have denoted the microscopic radiative capture cross section as σ_g.

The EVENT code requires the specification of total, absorption, the product of nu-bar and fission and scattering cross sections as input. Each of these quantities can readily be formed from realisations of the sampled parameters, namely σ_c, σ_f and nu-bar, using Eqns. (6.1.3)-(6.1.6). To account for transport effects, the EVENT scattering cross section may be modified as follows:

$$\sigma_{s,g\to g} = \sigma_{tr,g} - \sigma_{a,g} - \sum_{g' \neq g} \sigma_{s,g'\to g} \tag{6.1.8}$$

where g and g' represent the energy group dependence of the microscopic multi-group cross sections and σ_{tr} is the transport cross section - the transport cross section is calculated by WIMS. With this modification to the within-group scattering cross section, realisations of the transport cross sec-

tion may be generated as follows

$$\sigma_{tr,g} = \sigma_{c,g} + \sigma_{f,g} + \sum_{g'} \sigma_{s,g' \to g}. \tag{6.1.9}$$

The uncertainty methods used in this chapter require a parametric representation of the nuclear data uncertainties. This is achieved using a set of standard Gaussian-distributed random variables (zero mean and unit standard deviation) which are then shifted according to the mean values of the nuclear data and scaled according to the covariances between the data uncertainties. All of the correlated nuclear data uncertainties are described using the Karhunen Loéve expansion. The Karhunen Loéve or KL expansion represents correlated random variables in terms of a spectral expansion of their covariance matrix producing an optimal expansion in the mean square sense. The theory of the KL expansion is discussed in Section(2.3.1). The parameter N_{KL}, which determines the number of terms in the KL expansion, has been chosen such that all of the variation in the nuclear data is modelled whilst removing any degeneracy from the representation. All nuclear data uncertainties considered in the following work are described using a Gaussian (or Normal) distribution. For all of the simulations performed in this chapter it was found that using a Gaussian probability distribution gave positive realisations of the nuclear data for the covariances used so there was no need to use a physically bounding distribution such as log-Normal.

6.1.3. Calculating k_{eff} Sensitivities and Uncertainties

In this chapter two different approaches for calculating k_{eff} sensitivities and uncertainties have been used. The first is the polynomial chaos method and the second is the first-order sensitivity method. The first-order sensitiv-

ity method calculates the first-order differentials of k_{eff} with respect to the uncertain input parameters. Uncertainties in k_{eff} are approximated using the relation from Eqn.(1.3.8) which we have re-written below to remind the reader

$$\text{Var}[k_{\text{eff}}] = S\ \text{rCov}(\boldsymbol{D}, \boldsymbol{D})\ S^T. \tag{6.1.10}$$

In Eqn.(6.1.10), S are the relative sensitivities which are defined by Eqn.(1.3.9) and $\text{rCov}(\boldsymbol{D}, \boldsymbol{D})$ is the relative covariance matrix of the input nuclear data $\boldsymbol{D}$. The sensitivities in MONK are calculated using the differential operator sampling method which is described in Section (1.3.2.3).

Polynomial chaos is a global method, in other words it approximates the effect of parameter variation on k_{eff} over the entire probability space. The theory of the polynomial chaos (PC) method is described in Chapter (3) and we may write the polynomial chaos expansion (PCE) of k_{eff} as follows:

$$k_{\text{eff}}(\boldsymbol{\xi}) = \sum_{\alpha \in \mathcal{A}} k_\alpha \Phi_\alpha(\boldsymbol{\xi}) \tag{6.1.11}$$

where $\boldsymbol{\xi}$ are a set of IID random variables, Φ are the orthogonal polynomial basis and $\mathcal{A}$ are the set of polynomial indexes. The index set, $\mathcal{A}$, is calculated using combined adaptive HDMR and adaptive quadrature methods with adaptive tolerances of $\delta_{\text{HDMR}} = 1 \times 10^{-7}$. $\delta_{\text{Quad}} = 1 \times 10^{-7}$. These low tolerances have been chosen to ensure the polynomial expansion has sufficiently converged.

Unlike polynomial chaos, the first order sensitivity method is inherently local and only accounts for small changes in k_{eff} around the mean values

where the response of k_{eff} to data variations is approximately linear. In order to compare these two approaches, the PCE may be differentiated yielding the sensitivity of the response variable with respect to the input quantity of interest. The first order sensitivities are computed from a PCE using Eqn.(3.3.8) which yields a PCE approximation to the sensitivity matrix S. The sensitivities calculated from the PCE for k_{eff} may then be compared to the ones produced with MONK and the uncertainties may also be compared using Eqn.(6.1.10).

Since each nuclide is statistically independent, it is straight forward to calculate their individual contributions to the total uncertainty. The individual contributions, or partial uncertainties, may be calculated using the first-order sensitivities using the following

$$\text{Var}[k_{\text{eff},n}] = S_n \, \text{rCov}(\boldsymbol{D}_n, \boldsymbol{D}_n) \, S_n^T. \tag{6.1.12}$$

where the subscript "n" relates to the specific nuclide e.g. ^{235}U. A similar expression is also available for the partial uncertainties using PC, namely

$$\text{Var}[k_{\text{eff},n}] = \sum_{\alpha \in \mathcal{A}_n, \alpha \neq \mathbf{0}} \frac{k_\alpha^2 \left\langle \Phi_\alpha^2(\boldsymbol{\xi}) \right\rangle}{N_\alpha} \tag{6.1.13}$$

where N_α is a normalisation constant and the index set $\mathcal{A}_n$ contains the PC indexes relating to nuclide n. The partial uncertainties calculated using Eqn.(6.1.13) are global and describe the effect of input uncertainties across the full range of their variation.

6.2. The FLATTOP Experiments

In this section we analyse two critical benchmark systems which were performed experimentally using the FLATTOP critical assembly machine. The first has an enriched uranium core which is enclosed by a natural uranium reflector, the second has a plutonium core enclosed in a natural uranium reflector [115]. Both configurations are composed of spherical shells with the radii defined in Table (6.2). For full details of these FLATTOP benchmarks see the following specifications [116, 117].

Benchmark	Core Radius (cm)	Reflector Radius (cm)
FLATTOP U	6.1156	24.1242
FLATTOP Pu	4.5332	24.1420

Table 6.2.: Geometrical description of the uranium core FLATTOP benchmark, FLATTOP U, and the plutonium core FLATTOP benchmark, FLATTOP Pu.

A first consideration in assessing the uncertainty on k_{eff} is to review the effect of using different nuclear data evaluations for its computation. For each of the FLATTOP systems, the MONK Monte Carlo criticality code has been used to evaluate k_{eff} for a range of nuclear data evaluations. In Table (6.3) the final value of k_{eff} , or K(Three) - the statistical estimator of k_{eff} produced by MONK, is quoted along with the pcm difference and the number of standard deviations, SD=50pcm, between the critical value of 1. We can see that for some evaluations, namely JEF 2.2 (DICE and BINGO) and JENDL 3.3, there are very large (around 1000pcm) differences between the benchmark results - these are highlighted in red in Table (6.3). None of the evaluations give results within one standard deviation (50pcm) of critical except for JENDL 4.0 (BINGO) and JEFF 3.2 (BINGO) for the plutonium problem and UKNDL (DICE) for the uranium problem - these

are highlighted in greed in Table (6.3).

The unweighted average, standard deviation and relative standard deviation in percent, R(%), for the range of data evaluations in Table (6.3) are given in Table (6.4). We can see that the average values for the uranium and plutonium FLATTOP problems are 106 and 200 pcm away from critical respectively which is not unreasonable. However both averages have an associated standard deviation of at least 500 pcm which illustrates there is significant variation between evaluations.

In Section (6.1) and Appendix (C) we noted that Monte Carlo methods are difficult to use with projection-based uncertainty methods such as polynomial chaos. As such, the EVENT code was chosen as the eigenvalue solver for calculating k_{eff} .

The first step toward using EVENT for quantifying the effect of nuclear data uncertainties in k_{eff} is to produce cross section data in a 26 energy-group scheme which represents that of the covariance library. As was explained in Section (6.1.1), problem specific cross section data is produced using WIMS. The FLURIG module of WIMS, which computes mesh-to-mesh collision probabilities in spherical geometries, assumes a flat source over each computational mesh. The term mesh in WIMS would be analogous to an element in finite element terminology. Due to the constant source approximation, the geometry specified in HEAD was split into 1cm regions and further split into 25 meshes. The relative change in k_{eff} when increasing the spatial discretisation was approximately 1 pcm in all cases at which point we assumed k_{eff} was converged. To compare with the MONK results, k_{eff} for both FLATTOP problems was computed for all of the available data

Evaluation	uranium			plutonium		
	K(Three)	Diff (pcm)	Diff (SD)	K(Three)	Diff (pcm)	Diff (SD)
UKNDL (DICE)	0.99950	-50	-1	1.00090	90	1.8
JEF 2.2 (DICE)	0.99410	-590	-11.8	0.99070	-970	-19.4
JEF 2.2 (BINGO)	0.99230	-770	-15.4	0.98840	-1160	-23.2
JEFF 3.1 (BINGO)	1.00240	240	4.8	1.00300	300	6.0
JEFF 3.2 (BINGO)	1.00120	120	2.4	0.99950	-50	-1
ENDF/B-VI.6 (DICE)	1.00540	540	10.8	1.00420	420	8.4
ENDF/B-VII.0 (BINGO)	1.00300	300	6.0	1.00080	80	1.6
ENDF/B-VII.1 (BINGO)	1.00230	230	4.6	1.00120	120	2.4
JENDL 3.3 (DICE)	1.01160	1160	23.2	0.99140	-860	-17.2
JENDL 4.0 (BINGO)	0.99880	-120	-2.4	0.99990	-10	-0.2

Table 6.3.: FLATTOP criticality benchmarks calculated using MONK10A. The differences from critical are quoted in pcm and MONK standard deviations (SD).

Problem	Mean	Standard deviation	R(%)
FLATTOP U	1.00106	5.5×10^{-3}	0.55
FLATTOP Pu	0.99800	5.6×10^{-3}	0.56

Table 6.4.: Statistics of k_{eff} from the range of MONK calculations for different evaluations in Table (6.3).

libraries and the results are reproduced in Table (6.5).

There are significant discrepancies, of the order 1000 pcm, between the WIMS k_{eff} and the benchmark result of k_{eff} =1. A possible explanation is that the WIMS methods and data libraries are optimised for thermal energy systems whereas the FLATTOP problems have a fast spectrum. We also encountered issues when using the WIMS sub-group treatment of the resonant nuclides. When using the sub-group treatment for the spherical FLATTOP problems the data (corrected for resonance shielding effects) produced large negative collision probabilities which are un-physical resulting in the k_{eff} calculation to fail. Therefore, the WIMS resonance sub-group methods have not been used for these problems. The lack of a detailed resonance treatment may account for some of the difference between WIMS and MONK calculations. The mean and standard deviation of the 172 group results in Table (6.5) were calculated and are given in Table (6.6). From Table (6.6) we can see that the WIMS results for the uranium and plutonium FLATTOP problems are 662 and 800 pcm away respectively from critical which is a considerable bias. The standard deviations are again around 500 pcm which are consistent with the spread in the MONK results from Table (6.4). We must note, however, that the WIMS results are only calculated using a sub-set of the evaluations used in the MONK calculations.

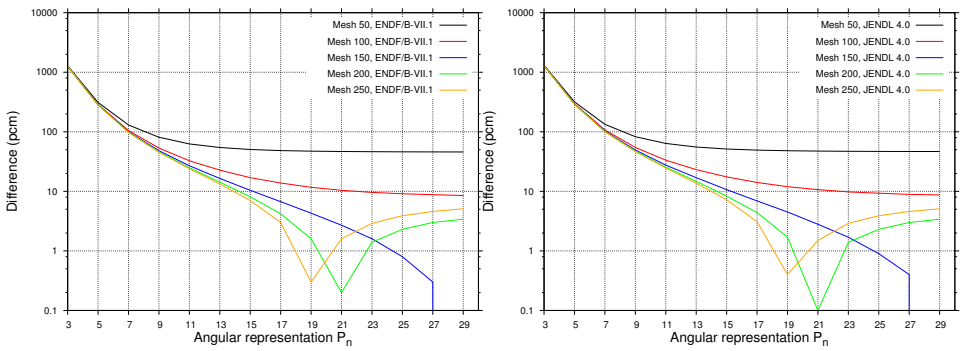
Evaluation	uranium			
	k_{eff} (172 groups)	Diff (pcm)	k_{eff} (26 groups)	Diff (pcm)
JEF 2.2	0.99887	-113	0.99947	-53
JEFF 3.1	1.00879	879	1.00936	936
ENDF/BVII.0	1.01034	1034	1.01094	1094
ENDF/BVII.1	1.01029	1029	1.01088	1088
JENDL 4.0	1.00480	480	1.00543	543
Evaluation	plutonium			
	k_{eff} (172 groups)	Diff (pcm)	k_{eff} (26 groups)	Diff (pcm)
JEF 2.2	0.99793	-207	0.99834	-166
JEFF 3.1	1.01245	1245	1.01288	1288
ENDF/BVII.0	1.01091	1091	1.01130	1130
ENDF/BVII.1	1.01082	1082	1.01121	1121
JENDL 4.0	1.00788	788	1.00835	835

Table 6.5.: FLATTOP k_{eff} calculations using WIMS with 172 and 26 group WIMS nuclear data. The route **HEAD** - **FLURIG** - **PIP** has been used.

Problem	Mean	Standard deviation	R(%)
FLATTOP U	1.00662	4.9×10^{-3}	0.48
FLATTOP Pu	1.00800	5.8×10^{-3}	0.58

Table 6.6.: Statistics of the WIMS k_{eff} calculations given in Table (6.5).

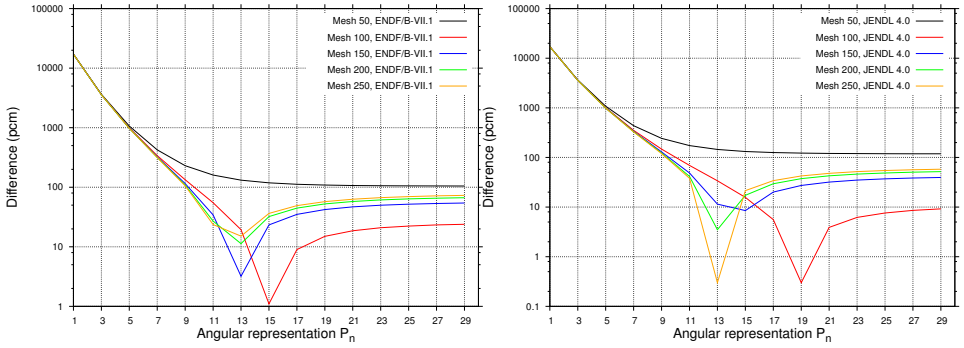
Next, we studied the convergence of the EVENT code with respect to the 26 group WIMS results to ensure that no extra modelling error was introduced in the EVENT calculations. The FLATTOP problems are modelled in one-dimensional spherical geometry in EVENT. Both the core and reflector regions are split into a number of finite elements which we denote N_e. To make sure EVENT has properly converged, the angular resolution or spherical harmonic order, P_N, is increased from $P_N = 1, \cdots, 29$ for an increasing number of spatial elements, $N_e = \{50, 100, 150, 200, 250\}$. The difference between EVENT results and the 26 group WIMS results from Table (6.5) are plotted in Figs.(6.1) and (6.2).



(a) ENDF/B-VII.1 (b) JENDL 4.0

Figure 6.1.: Convergence of EVENT-k_{eff} with spatial and angular discretisation for the uranium FLATTOP problems.

Figure (6.1) gives results for the uranium problem and (6.2) gives results for the plutonium problem. Convergence studies were only performed for



(a) ENDF/B-VII.1 (b) JENDL 4.0

Figure 6.2.: Convergence of EVENT-k_{eff} with spatial and angular discretisation for the plutonium FLATTOP problems.

JENDL 4.0 and ENDF/B-VII.1 which correspond to the covariance data available. For all of the convergence plots, we can see that as both the space and angle discretisations are refined the difference from the WIMS k_{eff} reduces. The dips in the convergence plots show that the final value of EVENT k_{eff} approaches the WIMS k_{eff} and finally converges to a slightly different result; this is not important when assessing if the EVENT solution has converged. This artefact in the convergence is also responsible for the discontinuous jumps in the "Mesh 150" results for the uranium problem where the difference falls to zero. With an angular resolution of P_{25} or greater and a spatial discretisation of 200 finite elements, any increases in space or angle resolution results in about 2pcm change in k_{eff} . At this point the EVENT solution is sufficiently converged. The differences between the WIMS and EVENT results will be due to the different computational approaches used in the codes, the final differences are 5pcm for the uranium problem and 50 pcm for the plutonium problem using 250 finite elements in each material region and a P_{25} angular discretisation. These differences were judged to be acceptable for the purposes of using EVENT in assess-

ing uncertainties; the main contribution to the error between MONK and EVENT is due to the approximations made in the WIMS calculations.

6.2.1. Sensitivity Studies and Uncertainty Quantification

In this section the uncertainty in k_{eff} is calculated using the method of polynomial chaos and the first order sensitivity approach available in MONK. The k_{eff} values corresponding to each realisation of the nuclear data were determined using EVENT with spherical geometry and angular representation of P_{25} and 250 finite elements. The sensitivity coefficients in MONK are calculated with respect to the infinitely dilute cross sections so we may use the infinitely dilute covariance data when propagating the uncertainties using Eqn.(6.1.10). The EVENT sensitivities, on the other hand, are calculated with respect to the shielded cross sections and so we must use resonance shielded covariance data when calculating the uncertainties with Eqn. (6.1.10). Since the effect of resonance absorption is problem dependent the corresponding covariance data requires a separate uncertainty calculation before the main calculation may begin. Instead, we have approximated the covariance data by assuming that the relative uncertainties are the same for both shielded and un-shielded covariance data. The self-shielded covariances are then calculated using the mean values of the self-shielded, multigroup cross sections and the relative covariance data.

For the plutonium FLATTOP problems covariance data for ^{239}Pu, ^{240}Pu, ^{241}Pu, ^{234}U, ^{235}U and ^{238}U was used and for the uranium FLATTOP problems ^{234}U, ^{235}U and ^{238}U covariance data was used. These covariance data were taken from the ENDF/B-VII.1 and JENDL 4.0 evaluations since they were the most modern evaluations which contained the majority of the data

required. For the reasons discussed previously in Section (6.1.2), only fission, radiative capture and nu-bar uncertainties were considered for each nuclide. The uncertainty in k_{eff} due to the covariance data of these nuclides was calculated using the first order sensitivity method in MONK and the first order sensitivities derived from the polynomial chaos expansion of k_{eff} - see Section (6.1.3) for an explanation of the methods used.

The results of the MONK and EVENT-PCE uncertainty calculations are given in Table (6.7). These results are the partial uncertainties and are tabulated as percentages of the standard deviation relative to the mean value denoted $R(\%)$. The statistical errors of the MONK partial uncertainties were determined to be less than $1 \times 10^{-6}\%$, which is less than the precision of the results in Table (6.7), and have therefore not been included. Values of R were calculated using Eqn. (6.1.11) for both MONK and PCE sensitivities as well as the global PCE uncertainties using Eqn. (6.1.13). We can see that the comparison with the MONK and PCE uncertainty (PCE (FOS) in Table (6.7)) methods are in very good agreement - here FOS stands for first order sensitivity. The largest discrepancy between the two approaches is for the total uncertainty in the FLATTOP uranium problem using ENDF/B-VII.1 where the values differ by 0.093% (i.e. around 7% of the uncertainty). We also note that there is very little difference between the PCE (FOS) results and the PCE results. This shows that no extra information is derived from the full PCE expansion and the uncertainty may be calculated sufficiently using the first order sensitivity method for these problems.

A summary of the statistics of the FLATTOP problems calculated using polynomial chaos using ENDF/B-VII.1 and JENDL 4.0 covariance data is

JENDL 4.0	uranium			plutonium		
	MONK	PCE (FOS)	PCE	MONK	PCE (FOS)	PCE
^{234}U	2.647×10^{-2}	2.714×10^{-2}	2.714×10^{-2}	1.523×10^{-4}	1.677×10^{-4}	1.677×10^{-4}
^{235}U	4.107×10^{-1}	4.152×10^{-1}	4.152×10^{-1}	5.384×10^{-3}	4.609×10^{-3}	4.609×10^{-3}
^{238}U	5.409×10^{-2}	1.056×10^{-1}	1.059×10^{-1}	8.888×10^{-2}	1.043×10^{-1}	1.048×10^{-1}
^{239}Pu	-	-	-	4.264×10^{-1}	4.250×10^{-1}	4.250×10^{-1}
^{240}Pu	-	-	-	1.536×10^{-2}	1.552×10^{-2}	1.552×10^{-2}
^{241}Pu	-	-	-	1.807×10^{-3}	2.242×10^{-3}	2.242×10^{-3}
Total	$\mathbf{4.151 \times 10^{-1}}$	$\mathbf{4.292 \times 10^{-1}}$	$\mathbf{4.291 \times 10^{-1}}$	$\mathbf{4.358 \times 10^{-1}}$	$\mathbf{4.379 \times 10^{-1}}$	$\mathbf{4.380 \times 10^{-1}}$
ENDF/B-VII.1	uranium			plutonium		
	MONK	PCE (FOS)	PCE	MONK	PCE (FOS)	PCE
^{234}U	9.699×10^{-2}	9.563×10^{-2}	9.563×10^{-2}	6.466×10^{-4}	5.401×10^{-4}	5.401×10^{-4}
^{235}U	1.251	1.344	1.348	1.660×10^{-2}	1.585×10^{-2}	1.585×10^{-2}
^{238}U	1.092×10^{-1}	1.068×10^{-1}	1.068×10^{-1}	1.172×10^{-1}	1.180×10^{-1}	1.181×10^{-1}
^{239}Pu	-	-	-	3.138×10^{-1}	3.134×10^{-1}	3.134×10^{-1}
^{240}Pu	-	-	-	2.308×10^{-2}	2.037×10^{-2}	2.037×10^{-2}
^{241}Pu	-	-	-	3.771×10^{-3}	3.105×10^{-3}	3.105×10^{-3}
Total	**1.259**	**1.352**	**1.355**	$\mathbf{3.362 \times 10^{-1}}$	$\mathbf{3.359 \times 10^{-1}}$	$\mathbf{3.358 \times 10^{-1}}$

Table 6.7.: Relative uncertainties R(%) in the results of k_{eff} due to ENDF/B-VII.1 and JENDL 4.0 covariance data for the FLATTOP problems. Results are calculated using the MONK sensitivity method, the PCE and its derived first order sensitivities (FOS) are calculated using EVENT.

given in Table (6.8). The statistics gathered from the k_{eff} values calculated from different evaluations are given in Table (6.6) which we refer to as the "evaluation statistics" (evaluation averages etc.) in the following paragraph to avoid confusion. Comparing the evaluation statistics with the results in Table (6.8) we note the following: Firstly, the mean values of k_{eff} calculated using the JENDL 4.0 data are lower, by approximately 180 pcm, than the evaluation averages and the ENDF/B-VII.1 mean values are higher, by approximately 100 pcm, than the evaluation averages. Secondly, apart from the ENDF/B-VII.1 uranium statistics, all of the standard deviations (SDs) agree well with the evaluations SDs; the polynomial chaos SDs are approximately 400 pcm whereas the evaluation SDs are approximately 500 pcm. The ENDF/B-VII.1 uranium SD is of the order of 1400 pcm which is considerably higher than the evaluation SD and the JENDL 4.0 SD from Table (6.8). This fact alone is not enough to say that the ENDF/B-VII.1 uranium covariance data are an overestimate since all evaluators may have settled on close central estimates of the data while recognising that there are large uncertainties. Comparing the SDs in Table (6.8) we can see that all values are approximately 400 pcm apart from the ENDF/B-VII.1 uranium result which is roughly 3.5 times larger. These comparisons suggests that the ENDF/B-VII.1 uranium covariance data leads to an overall excessive uncertainty.

Problem	ENDF/B-VII.1			JENDL 4.0		
	Mean	SD	R(%)	Mean	SD	R(%)
FLATTOP U	1.00787	1.37×10^{-2}	1.355	1.00465	4.31×10^{-3}	0.429
FLATTOP Pu	1.00904	3.39×10^{-3}	0.336	1.00619	4.40×10^{-3}	0.438

Table 6.8.: Statistics of k_{eff} using ENDF/B-VII.1 and JENDL 4.0 covariance data calculated using polynomial chaos.

A closer examination of the uncertainties in the FLATTOP uranium problem was performed and the contributions to the total relative uncertainty are tabulated in Table (6.9) for both ENDF/B-VII.1 and JENDL 4.0 covariances. The quoted values were calculated using MONK which has the facility to calculate the contributions for each nuclide and reaction. For these uncertainty calculations the contributions from the within-group elastic scattering, (n,n), covariances have also been included. From Table (6.9) we can see that the relative uncertainties are consistent for all of the nuclides and reactions apart from the radiative capture, (n,γ), reaction of ^{235}U. We also note that the absolute contribution from scattering to the total relative uncertainty is of the order 0.1% which is the least significant of all the reactions. Thus the inclusion of scattering in the uncertainty results would only make small differences.

Nuclide and Reaction	ENDF/B-VII.1	JENDL 4.0
^{234}U nu-bar	9.510×10^{-3}	1.282×10^{-2}
^{234}U (n,f)	9.605×10^{-2}	7.674×10^{-3}
^{234}U (n,γ)	9.496×10^{-3}	2.185×10^{-2}
^{234}U (n,n)	2.068×10^{-3}	3.072×10^{-3}
^{235}U nu-bar	5.126×10^{-1}	2.383×10^{-1}
^{235}U (n,f)	2.329×10^{-1}	2.776×10^{-1}
^{235}U (n,γ)	1.117	1.866×10^{-1}
^{235}U (n,n)	1.091×10^{-1}	1.287×10^{-1}
^{238}U nu-bar	1.091×10^{-1}	5.387×10^{-2}
^{238}U (n,f)	2.700×10^{-3}	2.957×10^{-3}
^{238}U (n,γ)	1.908×10^{-3}	3.811×10^{-3}
^{238}U (n,n)	1.067×10^{-2}	5.854×10^{-3}

Table 6.9.: Contribution of each reaction and nuclide to the total relative uncertainty for the FLATTOP uranium problem using ENDF/B-VII.1 and JENDL 4.0 covariance data.

From Table (6.9) the large difference between the ENDF/B-VII.1 and JENDL 4.0 uncertainties for the FLATTOP uranium problem was attributed

to the uncertainty contribution from the ^{235}U (n,γ) reaction. This large difference can stem from either the calculation of the sensitivities or from the covariance data (or both). In the following, comparisons are made between the absolute values of the first order sensitivities for each problem, data evaluation and computational method. Only the sensitivities for the nuclide which make the largest contribution to the total uncertainty is examined; for the FLATTOP uranium problem this is ^{235}U and for the FLATTOP plutonium problem this is ^{239}Pu. For both ENDF/B-VII.1 and JENDL 4.0 covariances and the MONK and PCE sensitivity approaches, sensitivities are plotted against incident neutron energy for ^{235}U in Fig.(6.3); the analogeous results are plotted for ^{239}Pu in Fig.(6.4). Each of the MONK sensitivities has an associated standard deviation which is plotted as an error bar. From these figures we can see that there is largely good agreement between the PCE and MONK sensitivities for both data evaluations, particularly at intermediate energies. For the fission and nu-bar sensitivities there are slight differences at fast and thermal energies which is most likely due to the weighting spectrum used in the WIMS multi-group data. For both capture reactions there are considerable differences at fast energies. A likely explanation for this is due to the definition of the WIMS capture cross section. The capture cross section used in the WIMS/EVENT studies was computed using Eqn.(6.1.4) from the fission and absorption cross sections listed in the WIMS output. As such, the computed capture cross section contains contributions from several capture-type reactions as defined by Eqn.(6.1.6). The MONK k_{eff} sensitivities are calculated with respect to radiative capture only; the differences at fast energies between MONK and WIMS/EVENT sensitivities is most likely due to the inclusion of other capture reactions in the WIMS capture cross section, particularly threshold

reactions, which increases the calculated sensitivities. Although there are differences between the MONK and PCE results for the capture reaction at fast energies, the MONK results for both data evaluations give consistent values. Considering this, and the fact that the magnitude of the absolute capture sensitivities are smaller than the fission and nu-bar ones, it indicates that the large difference between the evaluations for the ^{235}U (n,γ) reaction in Table (6.9) is due to the covariance data.

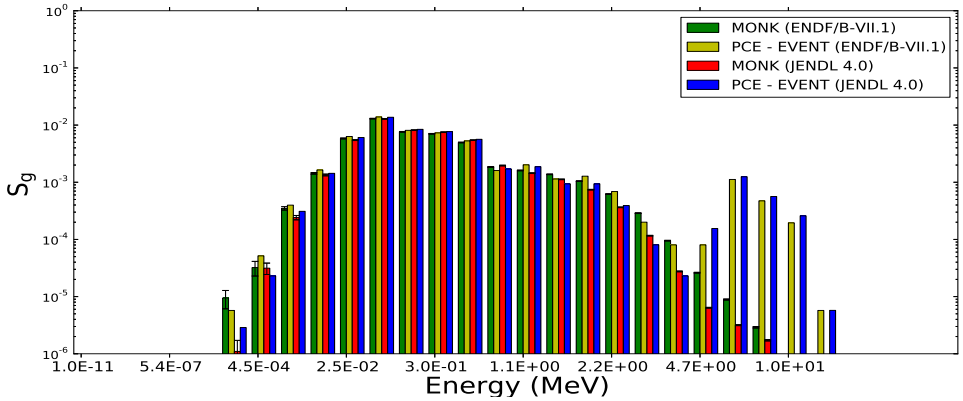
To look at the impact of threshold reactions on the capture sensitivities, the MONK sensitivities of k_{eff} to the $(n, 2n)$ and $(n, 3n)$ reactions have also been calculated. These may be combined into a total capture sensitivity using the chain rule for differentiation, namely:

$$\frac{\partial k_{\text{eff}}}{\partial \sigma_c} = \frac{\partial k_{\text{eff}}}{\partial \sigma_g}\frac{\partial \sigma_g}{\partial \sigma_c} + \frac{\partial k_{\text{eff}}}{\partial \sigma_{2n}}\frac{\partial \sigma_{2n}}{\partial \sigma_c} + \frac{\partial k_{\text{eff}}}{\partial \sigma_{3n}}\frac{\partial \sigma_{3n}}{\partial \sigma_c}. \tag{6.2.1}$$

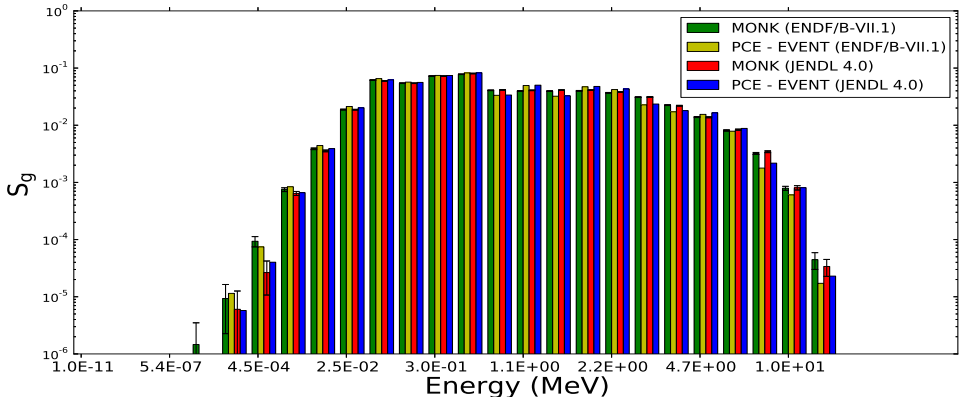
The partial differentials involving the capture cross sections may be calculated using the relationship in Eqn. (6.1.7) which yields the following equation for the sensitivity of k_{eff} due to σ_c:

$$\frac{\partial k_{\text{eff}}}{\partial \sigma_c} = \frac{\partial k_{\text{eff}}}{\partial \sigma_g} - \frac{\partial k_{\text{eff}}}{\partial \sigma_{2n}} - \frac{1}{2}\frac{\partial k_{\text{eff}}}{\partial \sigma_{3n}}. \tag{6.2.2}$$

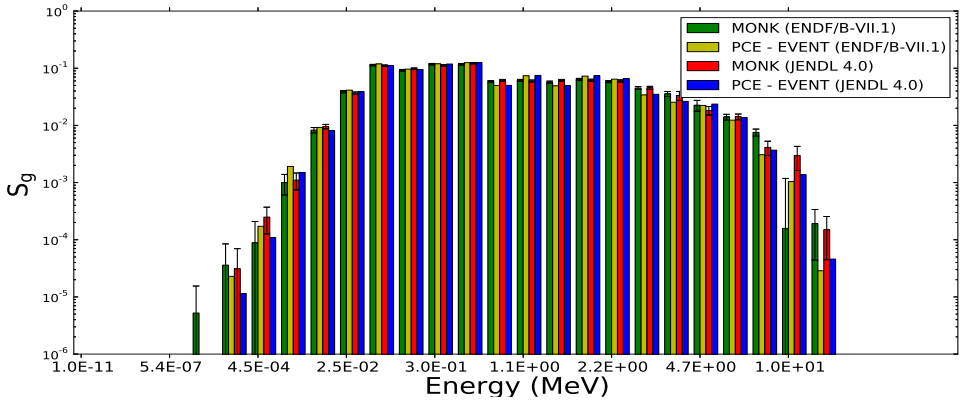
Equation (6.2.2) can be used to combine reaction sensitivities into a total capture sensitivity. The MONK sensitivities have been combined in this fashion and are compared to the EVENT-PCE sensitivities in Figure (6.5) for ^{235}U in the uranium FLATTOP problem and ^{239}Pu in the plutonium FLATTOP problem. Here we can see that there is much better agreement in the capture cross sections at high energies. To be consistent with the



(a) U235 Radiative Capture

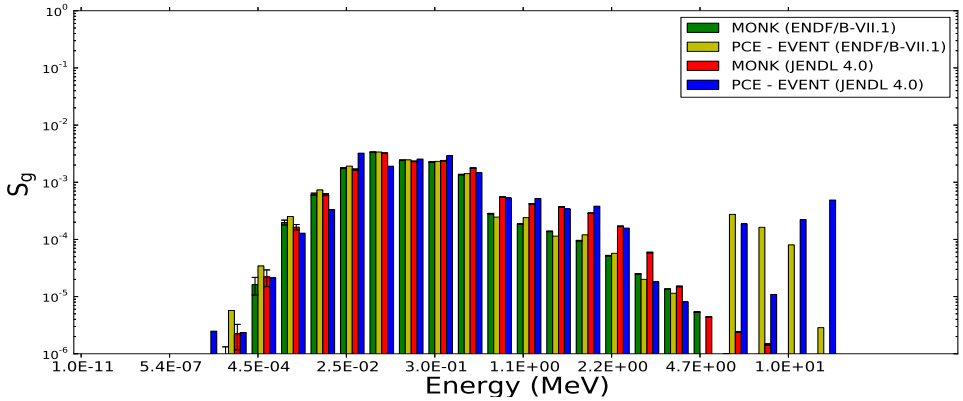


(b) U235 Fission

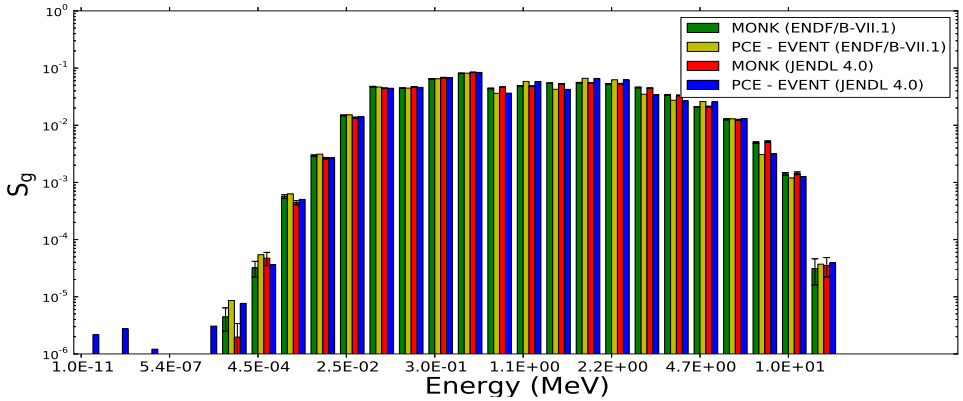


(c) U235 nu-bar

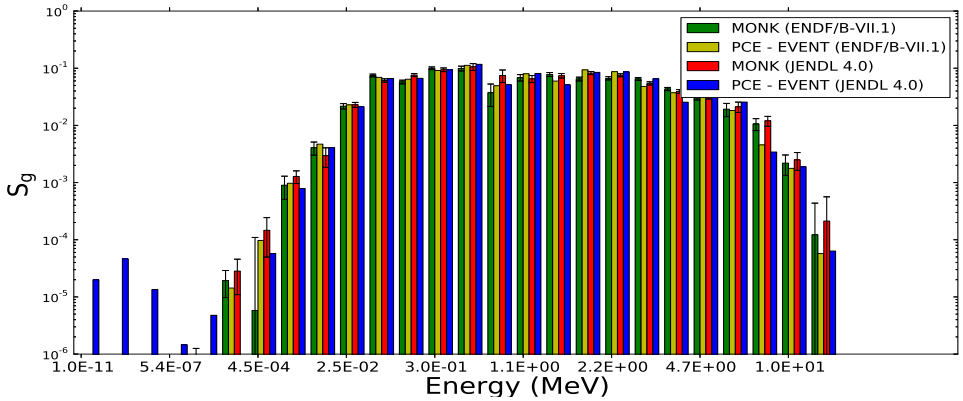
Figure 6.3.: First order sensitivities of k_{eff} to ^{235}U fission and nu-bar for the FLATTOP uranium problem.



(a) Pu239 Radiative Capture



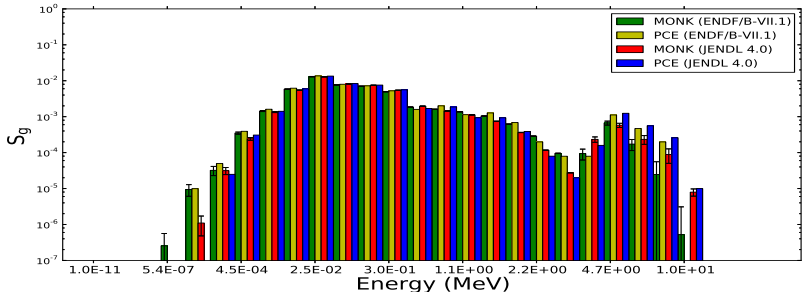
(b) Pu239 Fission



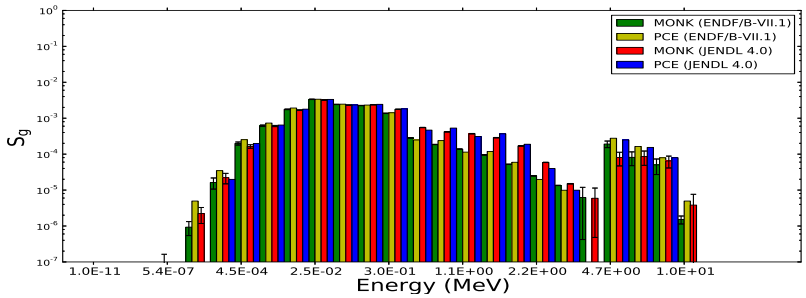
(c) Pu239 nu-bar

Figure 6.4.: First order sensitivities of k_{eff} to ^{239}Pu fission and nu-bar for the FLATTOP plutonium problem.

covariance data, the MONK capture sensitivities will only be calculated with respect to radiative capture. These will be different to the EVENT capture sensitivities at high energies which will include effects from reactions other than radiative capture.



(a) U235 Capture



(b) Pu239 Capture

Figure 6.5.: First order sensitivities of k_{eff} to capture reactions for ^{235}U in the uranium FLATTOP problem and ^{239}Pu in the plutonium FLATTOP problem.

Comparing the results from Tables (6.3) and (6.5) highlights the large differences between k_{eff} calculated using MONK and WIMS. However, aside from the modelling inconsistency associated with the MONK capture sensitivities, the results in Figs. (6.3) and (6.4) show that the MONK and WIMS (EVENT) sensitivities are sufficiently close that the uncertainty studies using EVENT are perfectly valid and would not have been significantly different if MONK had been used throughout.

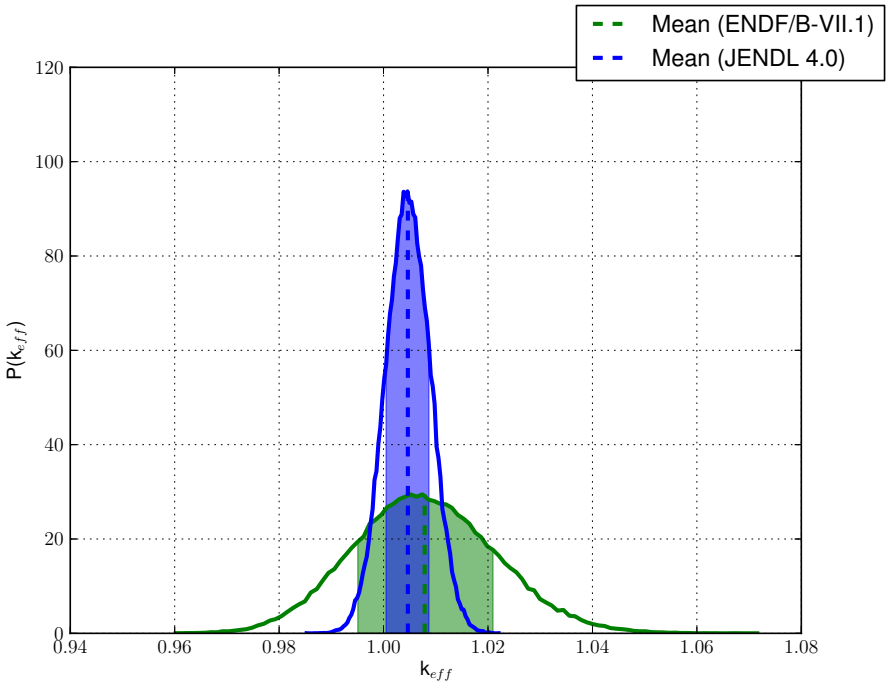
6.2.2. Relationship of Uncertainties to the Sub-Critical Limit

The PCE can also be used to calculate a PDF of the response quantity. This is achieved by randomly sampling the PCE and producing a histogram - see Section (3.3.3). For both of the FLATTOP problems and both evaluations, a PDF has been calculated from the PCE and plotted in Figs.(6.6a) and (6.6b). From these probability density functions the probability, P, of the two evaluations giving a value which is consistent within the uncertainties may be calculated as follows:

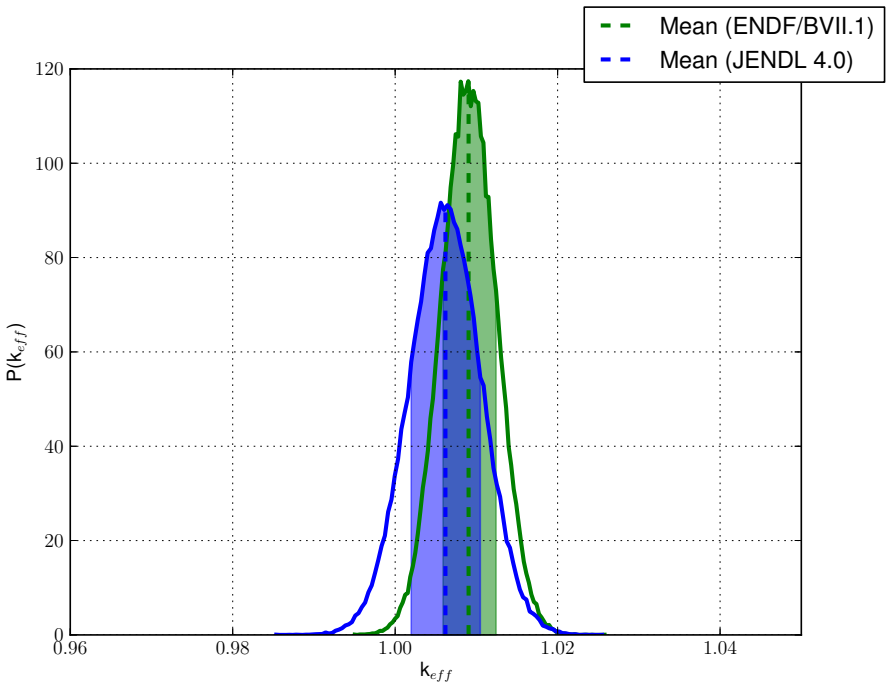
$$P = \int_{\mathcal{O}} p(k)^{\text{ENDF/BVII.1}} dk \int_{\mathcal{O}} p(k)^{\text{JENDL 4.0}} dk \tag{6.2.3}$$

where $\mathcal{O}$ is the region in which the two probability density functions overlap. Due to the infinite support of Gaussian distributions, the overlap region of any two Gaussian distributions is, itself, infinite. Therefore, the region of overlap has been calculated directly from the histogram of PCE samples; probability bins with zero counts is interpreted as zero probability which provides bounds for the distributions. We may also calculate the probability that k_{eff} is below the sub-critical limit, 0.95, which we denote by $P(k_{\text{eff}} \leq 0.95)$, as follows:

$$P(k_{\text{eff}} \leq x) = \int_{-\infty}^{0.95} P(k) dk. \tag{6.2.4}$$



(a) FLATTOP U



(b) FLATTOP Pu

Figure 6.6.: Probability density functions for k_{eff} for the plutonium and uranium FLATTOP experiments calculated using ENDF/B-VII.1 and JENDL 4.0 covariance data. The shaded regions correspond to $\overline{k}_{\text{eff}} \pm$ 1 standard deviation.

The PDFs for the two FLATTOP problems using both evaluations are given in Fig. (6.6). The two pairs of distributions show considerable overlap. In Fig. (6.6a) the results for the uranium ENDF/B-VII.1 calculations have a considerably larger standard deviation compared to the JENDL 4.0 results which is consistent with the results in Table (6.7). From Eqn. (6.2.3) the probability that both evaluations give results in the same range of "k_{eff} - space" has been calculated for ENDF/B-VII.1 and JENDL 4.0 from the results in Fig. (6.6) and are as follows: uranium - 79.43%, plutonium - 99.49%. From these probabilities we can see that the FLATTOP uranium simulations are likely to give the same range of results in the presence of the nuclear data uncertainties, the plutonium overlap probability shows that simulations are almost certain to give the same range of results within the bounds of the nuclear data uncertainties.

The probability of being below the sub-critical mass limit was calculated

Evaluation	uranium	plutonium
JENDL 4.0	0.0000	0.0000
ENDF/B-VII.1	0.0000	0.0000

Table 6.10.: Probabilities of k_{eff} being below the sub-critical limit,0.95, for the FLATTOP problems using ENDF/B-VII.1 and JENDL 4.0 evaluations.

for each problem and data evaluation and is given in Table (6.10). From these results we can see that there is zero probability of k_{eff} being below the threshold k_{eff} =0.95 for all of the problems except the uranium problem using ENDF/B-VII.1 data. The probabilities have been rounded to four decimal places; when using Gaussian statistics the distribution will never be exactly zero since its support is infinite.

Problem	Number of standard deviations	
	ENDF/B-VII.1	JENDL 4.0
FLATTOP U	3.65	11.60
FLATTOP Pu	14.75	11.36

Table 6.11.: Difference between the mean value and sub-critical limit of k_{eff} =0.95 in standard deviations for the FLATTOP problems.

Alternatively, we may express the sub-critical limit in terms of the number of standard deviations below the mean value. The differences between the sub-critical limit, k_{eff} =0.95, and the mean values of k_{eff} have been calculated in terms of the standard deviations determined using the ENDF/B-VII.1 and JENDL 4.0 covariance data. The differences are given in Table (6.11) and are consistent for both FLATTOP problems with the JENDL 4.0 data but are significantly different for the ENDF/B-VII.1 - this discrepancy is due to the erroneous fission spectrum in the ENDF BINGO library and has been discussed previously. The large number of standard deviations support the vanishingly small probabilities (essentially zero) of k_{eff} being below 0.95 given in Table (6.10). Even for the ENDF/B-VII.1 uranium data, the 3.65 standard deviations corresponds to a probability of less than 1.1×10^{-3}%.

6.3. Americium 241

In this section we calculate critical masses using a range of nuclear data evaluations for four spherical americium-241 systems and calculate uncertainties in the critical system using ENDF/B-VII.1 and JENDL 4.0 covariance data. The first model is a simple bare sphere with no reflector, the second is a sphere surrounded by a water reflector, the third is a sphere with a graphite reflector and the fourth is a sphere with a 304-steel reflector. The reflector width is 30cm for each of the three configurations which surrounds the

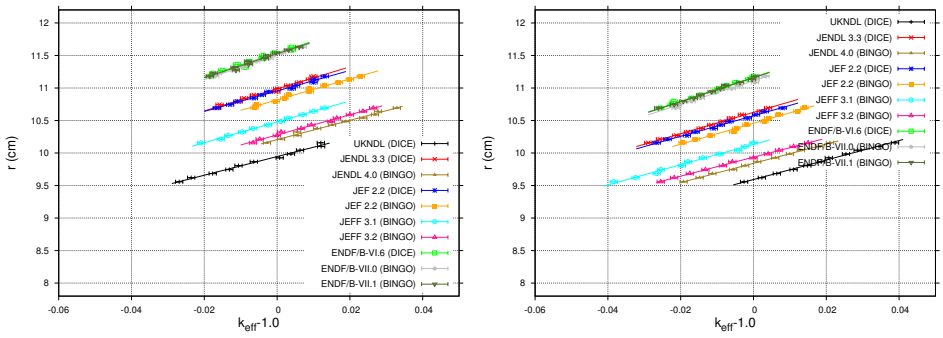
central fissionable region. The fissionable material in all of the configurations is composed entirely of ^{241}Am at a density of 13.67 g/cc. The water is modelled as atom fractions of hydrogen and oxygen, O: 0.033414 and H: 0.066988, and graphite is represented as purely carbon 12 with a density of 2.1 g/cc. The composition of 304-steel is 71% Fe, 19% Cr and 10% Ni and has a density of 7.85 g/cc.

The first task is to calculate the critical mass of these four configurations for different nuclear data evaluations. This can be be compared to previous work by another author [2]. As discussed in the introduction, there are currently no integral experimental data for americium critical masses but these may be inferred using a technique known as the equivalent-mass method. This has been done for a selection of americium-241 systems [111, 112] which may provide some degree of validation for the calculated critical masses.

Once the critical dimensions of the spherical systems have been determined they are modelled using WIMS to produce multi-group cross section data for use with EVENT. This data, produced for the EVENT code, is then used in the subsequent uncertainty calculations.

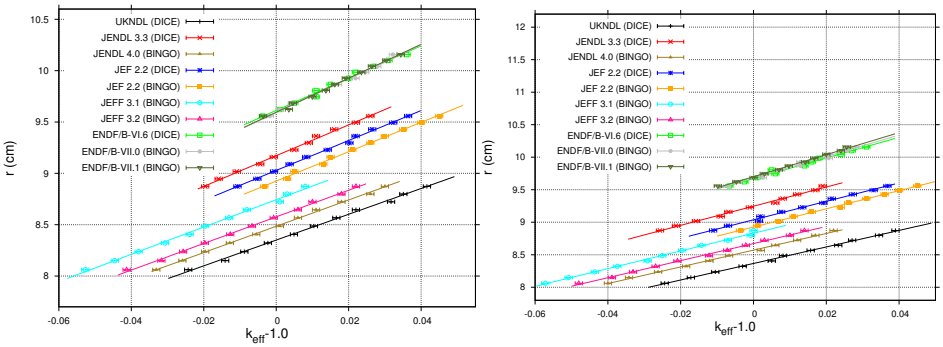
6.3.1. Critical Mass Calculations

In this section, critical masses and radii are determined for the four simple spherical systems described above. To calculate the critical mass, calculations are performed using MONK at radii corresponding to a broad range of masses from 10kg $\rightarrow$ 100kg in 10kg increments. Once the mass region has been narrowed down by this "broad sweep", a fine sweep is conducted in increments of 1kg.



(a) Bare Sphere (b) Water Reflector

Figure 6.7.: Radius versus k_{eff} -1.0 for the un-reflected and water reflected ^{241}Am spheres.



(a) Graphite Reflector (b) Steel Reflector

Figure 6.8.: Radius versus -1.0 for the Graphite reflected and Steel reflected ^{241}Am spheres.

In Fig. (6.7) K(Three)-1.0, where K(Three) is the statistical estimator of k_{eff} produced by MONK, is plotted versus the radius of the bare sphere and the water reflected sphere. The values of k_{eff} -1.0 versus radius are plotted for the graphite and steel reflected spheres in Fig.(6.8). The results shown are taken at 1kg mass separations in the broad region identified to contain the critical mass. A value of 1.0 is subtracted from k_{eff} so that the y-intercept of the best-fit line yields the critical radius. The intercept is

determined via a least squares fit of a linear function to the data. The statistical error associated with each MONK k_{eff} calculation is used to weight the importance of each point during the fitting process. Values of the critical radius, critical mass and their errors for a range of nuclear data evaluations are given in Table (6.12) below. The errors in the critical radius were determined from the least-squares fitting procedure.

The results for the bare, water reflected and steel reflected critical masses in Tables (6.12) and (6.13) agree with the published results in [2] to 3 standard deviations. In their work [2], the authors highlighted an issue with the ^{241}Am fission spectrum for MONK DICE calculations with the ENDF/B-VI.6 evaluation which gave anomalously high results for the critical mass. From Tables (6.12) and (6.13) we can see that the ENDF/B-VII.0 and ENDF/B-VII.1 results are largely unchanged from the ENDF/B-VI.6 results suggesting that the problem remains. The average value, standard deviation and relative standard deviation of the critical radii were calculated from the MONK spread of results in Tables (6.12) and (6.13) and are given in Table (6.14). The statistics have been calculated with and without the ENDF evaluations which have been judged to be suspect based on the findings by another author. From the results in Table (6.14) we can see that the relative standard deviations, R(%), are fairly consistent for all of the problems. The exclusion of the ENDF evaluations reduces R by around 1.5%.

As before, with the FLATTOP problems, WIMS calculations are performed so that multi-group cross section data can be produced for use with the EVENT code. The critical radii have been used from Tables (6.12)

Evaluation	Bare Sphere		Water Reflector	
	Radius (cm)	Mass (kg)	Radius (cm)	Mass (kg)
UKNDL (DICE)	9.94554 ± 0.0071	56.330 ± 0.120	9.59357 ± 0.0072	50.559 ± 0.114
JENDL 3.3 (DICE)	10.9859 ± 0.0064	75.921 ± 0.133	10.6248 ± 0.0051	68.678 ± 0.099
JENDL 4.0 (BINGO)	10.2056 ± 0.0094	60.865 ± 0.167	9.84170 ± 0.0024	54.585 ± 0.040
JEF 2.2 (DICE)	10.9555 ± 0.0057	75.292 ± 0.118	10.5734 ± 0.0056	67.686 ± 0.107
JEF 2.2 (BINGO)	10.8166 ± 0.0075	72.465 ± 0.151	10.4571 ± 0.0060	65.477 ± 0.113
JEFF 3.1 (BINGO)	10.4793 ± 0.0029	65.895 ± 0.056	10.1329 ± 0.0107	59.574 ± 0.189
JEFF 3.2 (BINGO)	10.2784 ± 0.0060	62.177 ± 0.108	9.93630 ± 0.0026	56.173 ± 0.043
ENDF/B-VI.6 (DICE)	11.5385 ± 0.0118	87.964 ± 0.270	11.1654 ± 0.0086	79.703 ± 0.185
ENDF/B-VII.0 (BINGO)	11.5094 ± 0.0061	87.300 ± 0.139	11.1108 ± 0.0105	78.540 ± 0.223
ENDF/B-VII.1 (BINGO)	11.5267 ± 0.0094	87.694 ± 0.214	11.1572 ± 0.0074	79.528 ± 0.158

Table 6.12.: Critical radius and critical mass values for bare and water reflected ^{241}Am spheres.

Evaluation	Graphite Reflector		Steel Reflector	
	Radius (cm)	Mass (kg)	Radius (cm)	Mass (kg)
UKNDL (DICE)	8.3502 ± 0.0050	33.338 ± 0.060	8.3717 ± 0.0029	33.596 ± 0.034
JENDL 3.3 (DICE)	9.1721 ± 0.0047	44.183 ± 0.069	9.2416 ± 0.0052	45.195 ± 0.076
JENDL 4.0 (BINGO)	8.4846 ± 0.0033	34.975 ± 0.040	8.5707 ± 0.0048	36.050 ± 0.060
JEF 2.2 (DICE)	9.0283 ± 0.0051	42.137 ± 0.160	9.0444 ± 0.0044	42.364 ± 0.061
JEF 2.2 (BINGO)	8.9243 ± 0.0077	40.699 ± 0.106	8.9306 ± 0.0065	40.785 ± 0.088
JEFF 3.1 (BINGO)	8.7431 ± 0.0079	39.270 ± 0.104	8.8274 ± 0.0093	39.387 ± 0.124
JEFF 3.2 (BINGO)	8.5762 ± 0.0039	36.119 ± 0.050	8.6725 ± 0.0053	37.350 ± 0.068
ENDF/B-VI.6 (DICE)	9.6127 ± 0.0101	50.861 ± 0.071	9.6558 ± 0.0112	51.549 ± 0.180
ENDF/B-VII.0 (BINGO)	9.5912 ± 0.0098	50.521 ± 0.155	9.6791 ± 0.0109	51.924 ± 0.174
ENDF/B-VII.1 (BINGO)	9.5948 ± 0.0087	50.579 ± 0.138	9.7001 ± 0.0057	52.263 ± 0.091

Table 6.13.: Critical radius and critical mass values for graphite and steel reflected ^{241}Am spheres.

Problem	With ENDF			Without ENDF		
	Mean (cm)	SD (cm)	R(%)	Mean (cm)	SD (cm)	R(%)
Bare	10.82414	0.58578	5.41	10.52383	0.40486	3.85
Water	10.45931	0.57363	5.48	10.16568	0.39747	3.91
Graphite	9.00775	0.47700	5.29	8.75411	0.30178	3.45
Steel	9.06939	0.48471	5.34	8.80841	0.29561	3.36

Table 6.14.: Statistics of the MONK americium-241 critical radius calculations for a range of data evaluations.

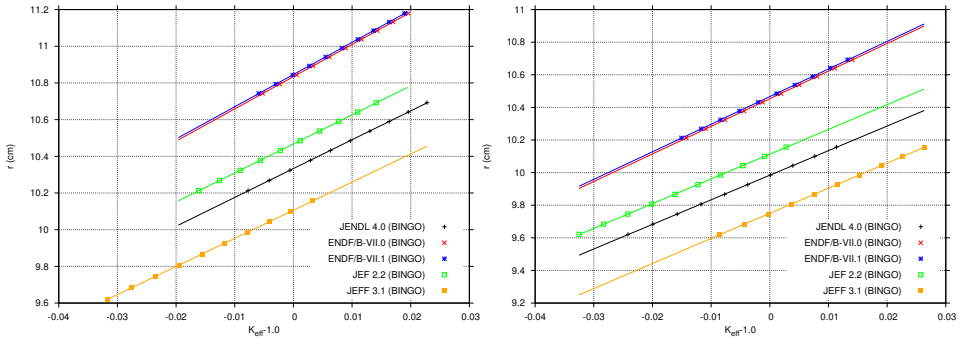
and (6.13) and the problem geometries have been split into 1cm spherical shells and the number of WIMS meshes has been refined until the relative change in the value of k_{eff} is of the order 1pcm. Results of the WIMS k_{eff} calculations are presented in Table (6.15) for ENDF/B-VII.1 and JENDL 4.0 nuclear data. The JENDL 4.0 solutions give much better agreement to the critical value of 1 than the ENDF/B-VII.1 results which are up to 4600 pcm different. The large differences in the ENDF data support the calculation of critical mass from the MONK calculations being erroneous due to a problem with the representation of the fission spectrum.

Problem	WIMS-172 ENDF/B-VII.1	WIMS-172 JENDL 4.0
Bare	1.03800	0.99170
Water	1.04680	0.99990
Graphite	1.03560	0.98940
Steel	1.04440	1.00030

Table 6.15.: WIMS k_{eff} calculations using MONK-calculated critical radii.

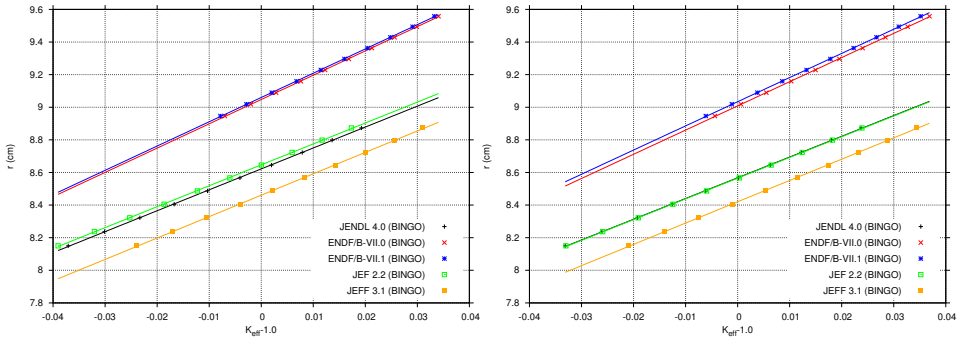
To avoid this problem, the critical mass calculations have been performed using WIMS. Although the fission spectrum data may now be more accurate, additional systematic errors will be present due to the discrete energy representation and the weighting spectrum in the WIMS data library. The critical mass calculations using WIMS proceed in the same manner as the

MONK calculations; a broad mass sweep in increments of 10kg is performed first followed by a fine mass sweep in increments of 1kg. The WIMS geometry is split into 1cm spherical shells which are each split into 25 meshes to ensure a good representation of the neutron flux and a converged value of k_{eff} . The value of radius is plotted versus k_{eff} -1.0; the value of the zero intercept of the linear fit to the data then yields the value of critical mass. The plots of radius versus k_{eff} -1.0 are given in Figs.(6.9) and (6.10).



(a) Bare sphere (b) Water reflector

Figure 6.9.: Critical mass calculations for the Bare and Water reflected americium-241 spheres using WIMS.



(a) Graphite sphere (b) Steel reflector

Figure 6.10.: Critical mass calculations for the steel and graphite reflected americium-241 spheres using WIMS.

The equations for the linear fits to the data in Figs.(6.9) and (6.10) are

given in Table (6.16). These data describe the following linear relationship between the radius and k_{eff} :

$$r = a(k_{\text{eff}} - 1) + r_c. \tag{6.3.1}$$

The mean value of the radius in terms of the k_{eff} mean is given as

$$\overline{r} = r_c + a(\overline{k}_{\text{eff}} - 1) \tag{6.3.2}$$

and the variance of the radius in terms of the k_{eff} variance is given as

$$\text{Var}[r] = a^2 \text{Var}[k_{\text{eff}}] \tag{6.3.3}$$

The expressions in Eqns. (6.3.2) and (6.3.3) relate the mean and variance of k_{eff} to the mean and variance of the radius when the nuclear data are constant (at their mean values). We wish to relate the variation in k_{eff} , when the nuclear data is varied according to its covariance data, to the variation in critical radius for different data evaluations. Therefore we must understand how k_{eff} relates to radius for all of the possible variations in nuclear data defined by its covariances. From Eqn. (6.3.3) we can see that the variances of k_{eff} and radius are related by a^2, the changes in a (the gradient) across evaluations are due to changes in the nuclear data. Therefore, any changes in the gradient between evaluations will suggest that the gradient will also change if the nuclear data are varied for a single evaluation. From Figures (6.9) and (6.10) and Table (6.16) we can see that the changes in the gradients are not insignificant which indicates the expressions in (6.3.2) and (6.3.3) are unlikely to hold for all realisations of the nuclear data. To properly account for the changes in nuclear data we must know the expressions relating a

and r_c to the nuclear data. This would require many calculations similar to those in Figures (6.9) and (6.10) for different perturbations in the nuclear data. Instead, we will make pessimistic assumptions about the gradients using the variations given in Table (6.16). Only values of a are changed since $\overline{k}_{\text{eff}} \approx 1$ and $\overline{r} \approx r_c$. The expression for the variance from Eqn. (6.3.3) is modified as follows

$$\text{Var}[r] = \left(a + 3\sqrt{\text{Var}[a]}\right)^2 \text{Var}[k_{\text{eff}}] \tag{6.3.4}$$

in other words, the gradient is increased by 3 standard deviations.

Results of the WIMS critical mass calculations are given in Table (6.17). When these results are compared to the MONK critical mass results in Tables (6.12) and (6.13) we can see that the WIMS results are approximately 0.5-7 kilograms lower for JEF/JEFF and JENDL data (the latter being in fairly good agreement). Mass differences of these magnitudes are much greater than the quoted uncertainties and cannot, therefore, be accounted by the statistical errors in the MONK calculations or due to the errors introduced by the linear fitting of the results. These differences must be due to the discrete multi-group representation of the WIMS nuclear data and the weighting spectrum (which is optimised for light water reactors) used to condense the evaluated data into the WIMS 172 group format. Comparison of the results for the ENDF data show mass differences of $\approx 8 - 15$ kg. This extra discrepancy is due to the incorrect fission spectrum as discussed above, a problem that does not seem to occur with WIMS.

The different evaluations used for the critical mass calculations produce a range of values for critical mass and critical radius. From the results in

Problem	Bare		Water		Graphite		Steel	
	a (cm)	r_c (cm)	a (cm)	r_c (cm)	a (cm)	r_c (cm)	a (cm)	r_c (cm)
ENDF/B-VII.0	17.5637	10.8341	16.9321	10.4533	14.9020	9.0474	14.8313	9.0081
ENDF/B-VII.1	17.5510	10.8457	16.9178	10.4662	14.8874	9.0599	14.8211	9.0338
JEF 2.2	15.8305	10.4675	15.1747	10.1131	12.8271	8.6468	12.7063	8.5653
JEFF 3.1	15.3297	10.1060	15.3879	9.7503	13.1301	8.4606	13.0618	8.4203
JENDL 4.0	15.7234	10.3331	15.0748	9.9840	12.8282	8.6219	12.7166	8.5673
Mean	16.3997	10.5173	15.8975	10.1534	13.7150	8.7672	13.6274	8.7189
Standard deviation	1.0732	0.3216	0.9448	0.3085	1.0840	0.2710	1.1037	0.2822

Table 6.16.: Coefficients of the linear fit $r = a(k_{\text{eff}}\text{-}1)+r_c$ where r is the radius, a is the gradient and r_c is the critical radius.

Evaluation	Bare Sphere		Water Reflector	
	Radius (cm)	Mass (kg)	Radius (cm)	Mass (kg)
JEF 2.2	10.4675 ± 0.0003	65.673 ± 0.005	10.1131 ± 0.0006	59.226 ± 0.011
JEFF 3.1	10.1060 ± 0.0006	59.101 ± 0.011	9.7503 ± 0.0005	53.078 ± 0.009
JENDL 4.0	10.3331 ± 0.0004	63.176 ± 0.007	9.9840 ± 0.0004	56.986 ± 0.007
ENDF/B-VII.0	10.8341 ± 0.0003	72.817 ± 0.007	10.4533 ± 0.0003	65.406 ± 0.006
ENDF/B-VII.1	10.8457 ± 0.0003	73.052 ± 0.007	10.4662 ± 0.0003	65.648 ± 0.006
Evaluation	Graphite Reflector		Steel Reflector	
	Radius (cm)	Mass (kg)	Radius (cm)	Mass (kg)
JEF 2.2	8.6468 ± 0.0010	37.018 ± 0.013	8.5653 ± 0.0009	35.981 ± 0.011
JEFF 3.1	8.4605 ± 0.0010	34.678 ± 0.012	8.4202 ± 0.0010	34.185 ± 0.012
JENDL 4.0	8.6219 ± 0.0010	36.700 ± 0.012	8.5673 ± 0.0009	36.007 ± 0.011
ENDF/B-VII.0	9.0474 ± 0.0010	42.406 ± 0.014	9.0081 ± 0.0011	41.856 ± 0.015
ENDF/B-VII.1	9.0598 ± 0.0009	42.581 ± 0.013	9.0338 ± 0.0010	42.215 ± 0.014

Table 6.17.: Critical radius and critical mass values for graphite and steel reflected ^{241}Am spheres calculated using WIMS.

Problem	Mean (cm)	Standard deviation (cm)	R(%)
Bare	10.51728	0.32163	3.06
Water	10.15338	0.30846	3.04
Graphite	8.76728	0.27102	3.09
Steel	8.71894	0.28222	3.24

Table 6.18.: Statistics of the WIMS americium-241 critical radius calculations for a range of data evaluations.

Table (6.17) the mean, standard deviation and relative standard deviation have been calculated and are presented in Table (6.18). The relative standard deviations, which include the ENDF evaluations, are all of the order 3% which compare well with the MONK results from Table (6.14) which exclude the ENDF evaluations. The mean values of the WIMS results closely match the MONK results which exclude the ENDF evaluations from Table (6.14).

A further comparison of the WIMS and MONK critical mass results can be made by normalising the results to experimental data. In this instance, because no experimental information is available, we have used the inferred critical masses given in Table (6.1). In this case the results must be interpreted with caution since the reference result may contain significant error. We must also note that critical masses have only been inferred for the bare, water reflected and steel reflected systems. The ratio of calculated to experimental results, "C/E", shows how close a calculation, (C), is to the experimental, (E), results. Values of C/E < 1.0 tell us the simulation is under predicting whilst values of C/E > 1.0 mean that the simulation is over predicting. In Figure (6.11) C/E values have been plotted for all of the available data evaluations. The results show that both MONK and WIMS results for JENDL 4.0 give the most similar results whereas the ENDF re-

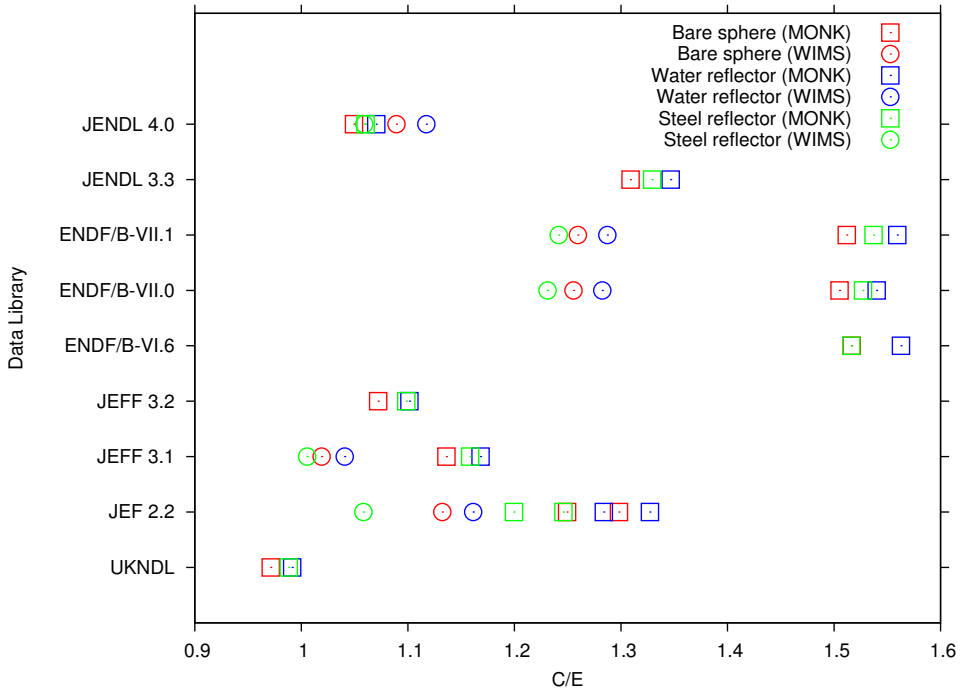
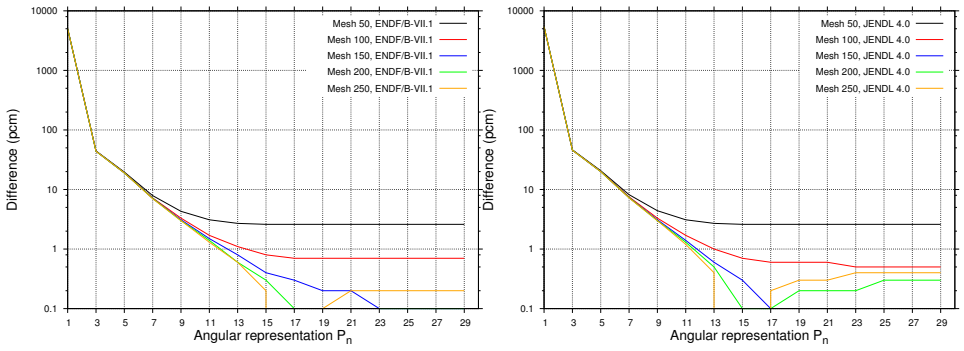


Figure 6.11.: Calculated versus experimental values for WIMS and MONK critical mass calculations.

sults show the largest differences. These large differences for MONK are again due to the error in the BINGO fission spectrum.

For the rest of the uncertainty analysis, values of critical mass calculated using the WIMS code will be used. As previously discussed, the polynomial chaos methods need to use a deterministic flux solution. Also, the WIMS ENDF results do not appear to be subject to the errors in the fission spectrum that appear in the MONK results or appear to be less pronounced. The WIMS calculations will instead be subject to systematic errors due to the multi-group data, but we do not expect the systematic errors to have a significant impact on the calculated uncertainties which has been discussed previously in Section (6.2.1) .

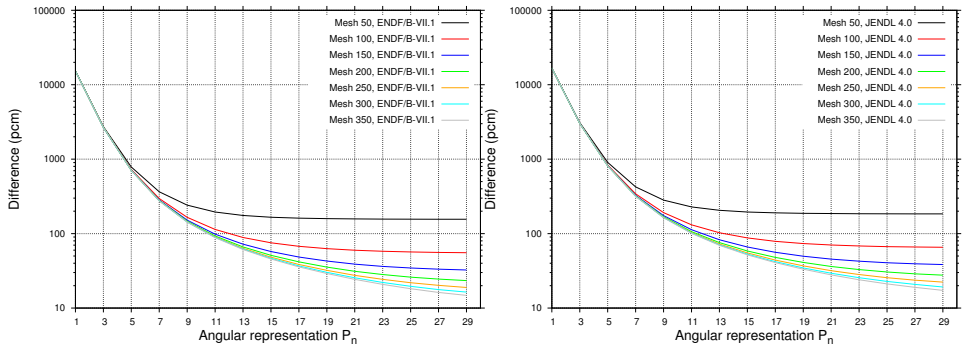
Before we may proceed to the evaluation of the uncertainties due to the nuclear covariance data, cross sections must be produced for the code EVENT. The WIMS code is executed using the critical radii defined above using 1cm spherical shells with 25 meshes per shell. Once the cross section data had been produced, a convergence analysis of the spatial and angular discretisation for the EVENT code was performed. Analogous to the FLAT-TOP problems, the americium problems were modelled in one dimensional spherical geometry. The angular resolution or spherical harmonic order, P_N, was increased from $P_N = 1, \cdots, 29$ for incremental increases in spatial resolution of $\{50, 100, 150, 200, 250\}$. The differences between the WIMS and EVENT k_{eff} results are plotted in Figures (6.12) - (6.15).



(a) ENDF/B-VII.1 (b) JENDL 4.0

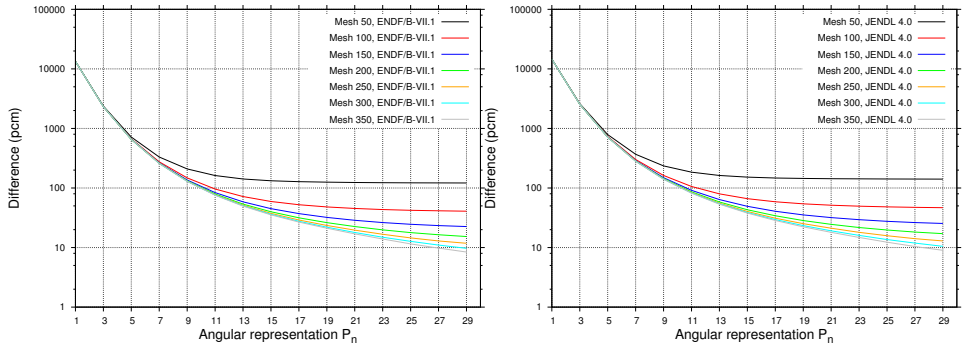
Figure 6.12.: Convergence of EVENT calculations for the bare americium-241 sphere.

The spatial and angular resolutions were chosen such that the difference between WIMS and EVENT calculations were $\leq$ 10pcm. The P_N order and number of finite elements used in both the americium-241 core and reflector regions are listed in Table (6.19).



(a) ENDF/B-VII.1 (b) JENDL 4.0

Figure 6.13.: Convergence of EVENT calculations for the americium-241 sphere with a water reflector.

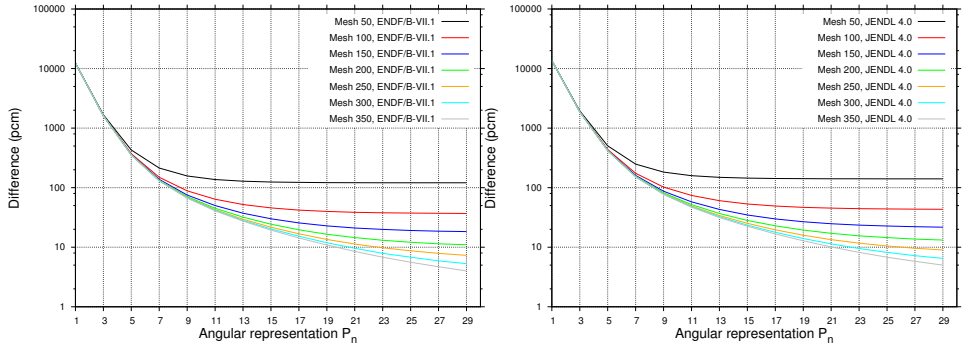


(a) ENDF/B-VII.1 (b) JENDL 4.0

Figure 6.14.: Convergence of EVENT calculations for the americium-241 sphere with a graphite reflector.

Problem	P_N	Elements
Bare	17	100
Water	27	350
Graphite	27	350
Steel	21	350

Table 6.19.: Spatial and angular discretisation parameters for the EVENT americium-241 problems.



(a) ENDF/B-VII.1 (b) JENDL 4.0

Figure 6.15.: Convergence of EVENT calculations for the americium-241 sphere with a steel reflector.

6.3.2. Sensitivity Studies and Uncertainty Quantification

In this section, the adaptive HDMR and quadrature methods defined in previous chapters are used to build a polynomial chaos expansion of the k_{eff} response surface. The EVENT code is used to compute values of k_{eff} for points in the probability space which is defined by the uncertainty in the nuclear data. As we have seen in the previous section, the WIMS and subsequent EVENT calculations are inconsistent with the MONK results, i.e. they are not within the bounds of the MONK statistical error. Therefore, there is a systematic difference between the EVENT and MONK results, which will be referred to below as modelling error (although this term presumes that the MONK result is correct given the nuclear data). The uncertainties of the input nuclear data are defined by 26 energy-group covariance matrices described in section (6.1.2). Only covariances for the ENDF/B-VII.1 and JENDL 4.0 evaluations are considered.

In Table (6.20) the mean, standard deviation and relative standard deviations of the four americium-241 problems are given. From these results we can see that the standard deviation appears insensitive to the inclusion of a reflector and also to the reflector material. These statistics can be mapped from uncertainties in k_{eff} to uncertainties in radius which we can compare to the variation in the critical radii produced from different data evaluations. The standard deviation of the radius can be calculated using Eqn. (6.3.3) where it is assumed that the relationship between radius and k_{eff} is insensitive to nuclear data perturbations. The relationship may also be expressed using Eqn. (6.3.4) which assumes a pessimistic assumption (plus 3 standard deviations) about the effect of nuclear data perturbations. This pessimistic assumption is based on the variation between these relationships for a range

of data evaluations. The standard deviation and relative standard deviation of the radius are given in Table (6.21) which we may compare to the results calculated using multiple data evaluations in Table (6.18). The statistics calculated using multiple data evaluations are referred to as the evaluation statistics for the rest of this discussion.

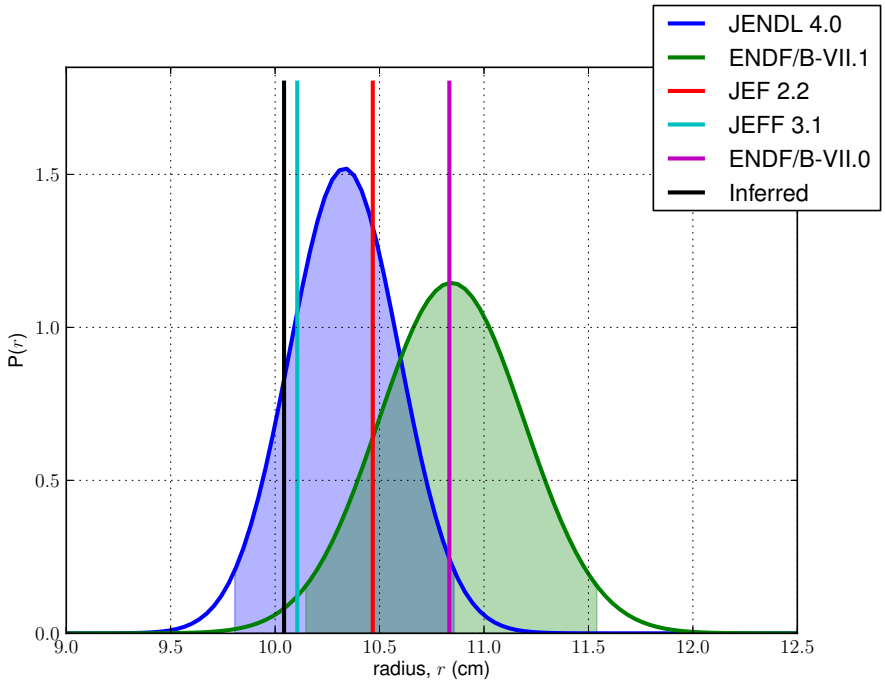
Problem	Deterministic		Mean	
	ENDF/B-VII.1	JENDL 4.0	ENDF/B-VII.1	JENDL 4.0
Bare	0.99991	0.99993	0.99989	0.99989
Water	0.99964	0.99957	0.99962	0.99957
Graphite	0.99934	0.99944	0.99932	0.99945
Steel	0.99898	0.99904	0.99896	0.99905
Problem	Standard deviation		R(%)	
	ENDF/B-VII.1	JENDL 4.0	ENDF/B-VII.1	JENDL 4.0
Bare	1.678×10^{-2}	1.387×10^{-2}	1.678	1.387
Water	1.671×10^{-2}	1.386×10^{-2}	1.671	1.386
Graphite	1.653×10^{-2}	1.393×10^{-2}	1.654	1.394
Steel	1.656×10^{-2}	1.410×10^{-2}	1.657	1.411

Table 6.20.: Statistics of k_{eff} for the americium-241 problems based on the use of covariance data.

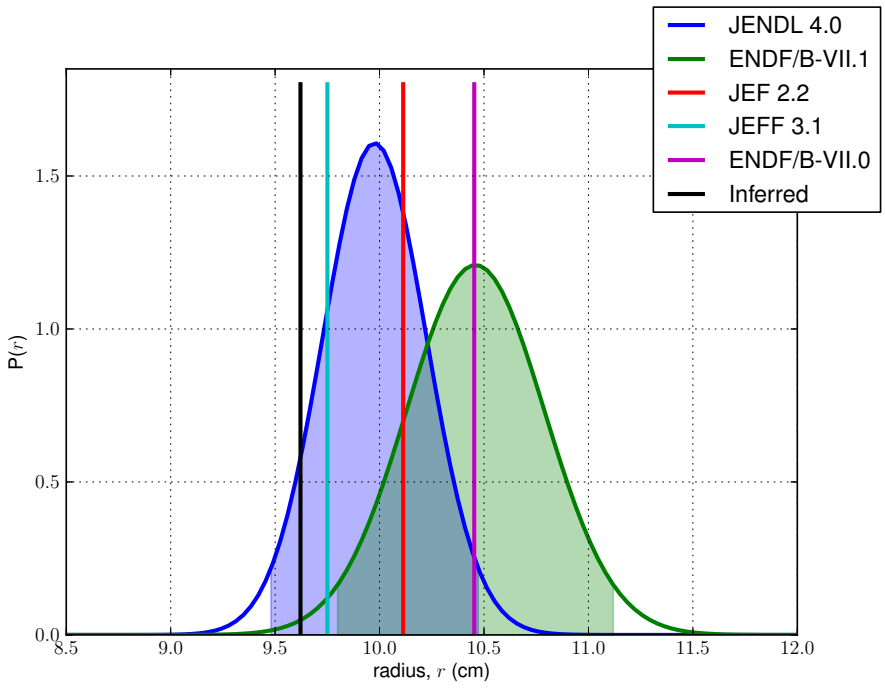
The standard deviations (SDs) of the evaluation statistics for all of the problems in Table (6.18) are approximately 0.3 cm and the relative standard deviations (RSDs) are approximately 3%. The SDs and RSDs calculated using the ENDF/B-VII.1 covariances with the pessimistic assumption described above are larger than the evaluation statistics whereas the JENDL 4.0 results are lower. The set of results in Table (6.21), which assume that the relationship between k_{eff} and radius is insensitive to nuclear data perturbations, are smaller than the evaluation statistics; the JENDL 4.0 results more so than the ENDF/B-VII.1. The true uncertainties based on the covariance data probably lie somewhere between the two sets of results in Table (6.21). The ENDF/B-VII.1 covariances are therefore consistent with the variation due to different evaluations. The JENDL 4.0 covariances ap-

pear to be slightly smaller.

A further comparison of the uncertainties due to covariance data and the spread in values of critical radius from different evaluations can be made if we compare the uncertainties in Table (6.21) to the radius values in Table (6.17). The uncertainties due to the covariances are plotted assuming a Gaussian distribution using the mean and standard deviations; the values of critical radius are plotted as vertical lines. These results are plotted in Figs (6.16a), (6.16b), (6.17a) and (6.17b) for the bare, water, graphite and steel reflected spheres respectively where two standard deviations either side of the mean have been shaded. The inferred critical radii have also been plotted from Table (6.1). For all of the spheres, the results for JEF 2.2, JEFF 3.1, ENDF/B-VII.0 and the inferred value (where available) are all within 2 standard deviations of the JENDL 4.0 result. The ENDF/B-VII.1 uncertainties bound all of the other deterministic results except the JEFF 3.1 and the inferred critical radius which tend to be greater than 2 standard deviations below the ENDF/B-VII.1 mean value.

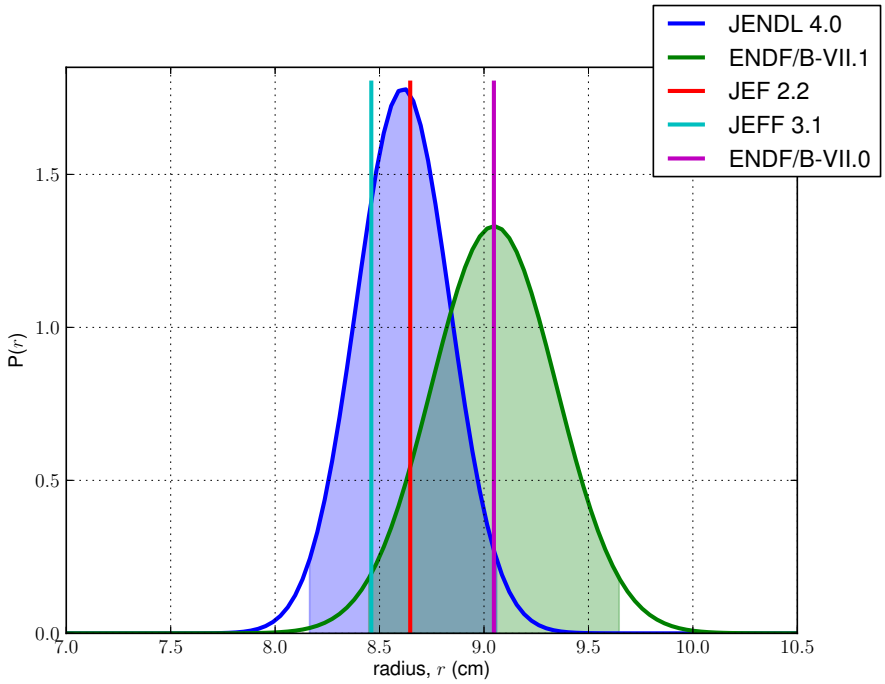


(a) Bare sphere

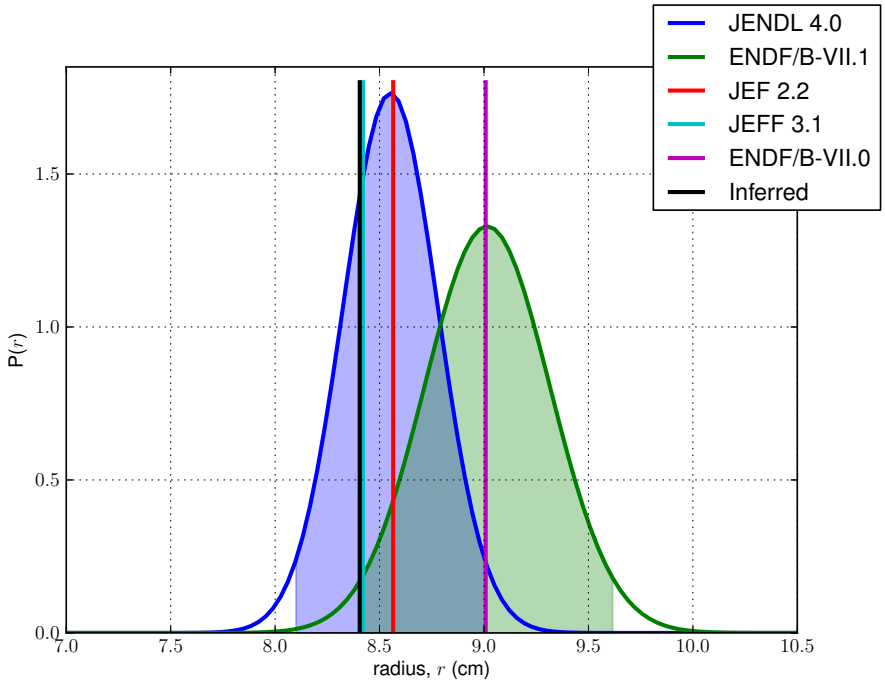


(b) Water reflector

Figure 6.16.: Probability density functions of the radius for the bare and water reflected ^{241}Am spheres for ENDF/B-VII.1 and JENDL 4.0 data evaluations. A region of $\overline{r} \pm$ 2 standard deviation have been shaded.



(a) Graphite reflector



(b) Steel reflector

Figure 6.17.: Probability density functions of radius for the graphite and steel reflected ^{241}Am spheres for ENDF/B-VII.1 and JENDL 4.0 data evaluations. A region of $\overline{r} \pm$ 2 standard deviation have been shaded.

$\mathrm{Var}[r] = a^2\,\mathrm{Var}[k_{\mathrm{eff}}]$				
Problem	Standard deviation (cm)		R(%)	
	ENDF/B-VII.1	JENDL 4.0	ENDF/B-VII.1	JENDL 4.0
Bare	0.2942	0.2179	2.71	1.38
Water	0.2826	0.2089	2.70	1.38
Graphite	0.2459	0.1787	2.72	1.39
Steel	0.2453	0.1794	2.72	1.41
$\mathrm{Var}[r] = \left(a + 3\sqrt{\mathrm{Var}[a]}\right)^2 \mathrm{Var}[k_{\mathrm{eff}}]$				
Problem	Standard deviation (cm)		R(%)	
	ENDF/B-VII.1	JENDL 4.0	ENDF/B-VII.1	JENDL 4.0
Bare	0.3482	0.2625	3.21	2.54
Water	0.3299	0.2482	3.15	2.49
Graphite	0.2997	0.2240	3.31	2.60
Steel	0.3001	0.2261	3.33	2.64

Table 6.21.: Statistics of the critical radius for the americium-241 problems.

In Tables (6.22) and (6.23) the partial uncertainties are calculated from the polynomial expansion of k_{eff} using Eqn.(6.1.11). The partial sensitivities calculated using the MONK sensitivity method are also listed and are used as a comparison with the PCE results. The statistical uncertainty for each of the MONK results were below $1 \times 10^{-6}\%$, which is below the precision of the values quoted in Tables (6.22) and (6.23), so they were not included. Covariance data for some nuclides are missing from the evaluations, for example, there are no covariance data for hydrogen in the JENDL 4.0 evaluation. In these cases the entries are left blank in Tables (6.22) and (6.23). For the JENDL 4.0 results in Table (6.22) and the ENDF/B-VI.1 results in Table (6.23) we can see that there is good agreement between the partial sensitivities of ^{241}Am. The MONK sensitivities to non-^{241}Am nuclides are generally a lot smaller than the PCE ones. This is because these nuclides are non-fissile and the only reaction considered, in these cases, was radiative capture (MT=102). Referring to the discussion in Section (6.2.1), the increase in the PCE sensitivities of the capture reactions is most likely due to

the presence of reactions other than radiative capture in the WIMS capture cross section. We can also see that, in all cases, the majority contribution to the total uncertainty is from ^{241}Am.

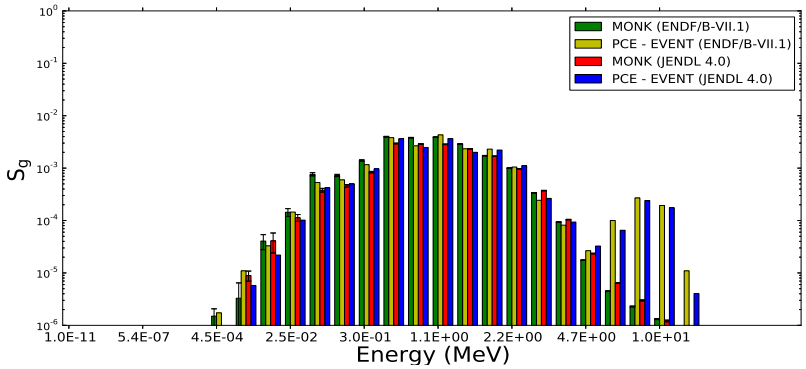
The sensitivity of k_{eff} to fission, capture and nu-bar, as a function of incident neutron energy, has been calculated for ^{241}Am for each of the four systems. The sensitivity results are plotted versus incident neutron energy for the bare system in Figure (6.18), the water reflected system in Figure (6.19), the graphite reflected system in Figure (6.20) and the steel reflected system in Figure (6.21). For all cases the fission and nu-bar sensitivities for MONK and EVENT-PCE are in good agreement. The capture sensitivities exhibit differences at fast energies for the same reasons discussed in Section (6.2.1).

JENDL 4.0	Bare Sphere			Water Reflector		
	MONK	PCE (FOS)	PCE	MONK	PCE (FOS)	PCE
^{241}Am	1.380	1.3869	1.3870	1.375	1.3861	1.386
H	-	-	-	-	-	-
O	-	-	-	1.080×10^{-5}	1.777×10^{-3}	1.777×10^{-3}
Total	**1.380**	**1.3869**	**1.3870**	**1.375**	**1.386**	**1.386**
JENDL 4.0	Graphite Reflector			Steel Reflector		
	MONK	PCE (FOS)	PCE	MONK	PCE (FOS)	PCE
^{241}Am	1.385	1.394	1.394	1.404	1.411	1.411
C	-	-	-	-	-	-
Ni	-	-	-	3.896×10^{-4}	5.082×10^{-3}	5.082×10^{-3}
Fe	-	-	-	2.296×10^{-3}	7.329×10^{-3}	7.330×10^{-3}
Total	**1.385**	**1.394**	**1.394**	**1.404**	**1.411**	**1.411**

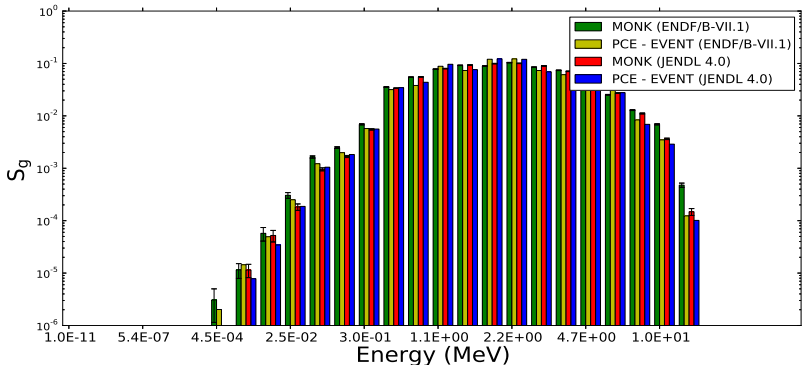
Table 6.22.: Relative uncertainties R(%) in the results of k_{eff} due to JENDL 4.0 covariance data for the ^{241}Am problems. Results are calculated using the MONK sensitivity method, the PCE and its derived first order sensitivities (FOS) are calculated using EVENT.

ENDF/B-VII.1	Bare Sphere			Water Reflector		
	MONK	PCE (FOS)	PCE	MONK	PCE (FOS)	PCE
^{241}Am	1.667	1.678	1.678	1.636	1.671	1.672
H	-	-	-	3.829×10^{-4}	5.229×10^{-4}	5.232×10^{-4}
O	-	-	-	1.720×10^{-5}	3.871×10^{-3}	3.871×10^{-3}
Total	**1.667**	**1.678**	**1.678**	**1.636**	**1.671**	**1.672**
ENDF/B-VII.1	Graphite Reflector			Steel Reflector		
	MONK	PCE (FOS)	PCE	MONK	PCE (FOS)	PCE
^{241}Am	1.661	1.654	1.654	1.686	1.657	1.657
C	-	-	-	-	-	-
Ni	-	-	-	2.898×10^{-4}	5.161×10^{-3}	5.161×10^{-3}
Fe	-	-	-	2.767×10^{-3}	6.956×10^{-3}	6.957×10^{-3}
Cr	-	-	-	1.975×10^{-4}	1.644×10^{-3}	1.644×10^{-3}
Total	**1.661**	**1.654**	**1.654**	**1.686**	**1.657**	**1.657**

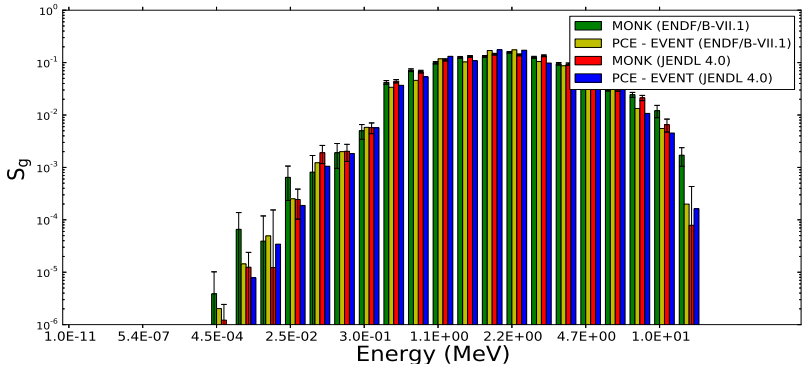
Table 6.23.: Relative uncertainties R(%) in the results of k_{eff} due to ENDF/B-VII.1 covariance data for the ^{241}Am problems. Results are calculated using the MONK sensitivity method, the PCE and its derived first order sensitivities (FOS) are calculated using EVENT.



(a) ^{241}Am Capture

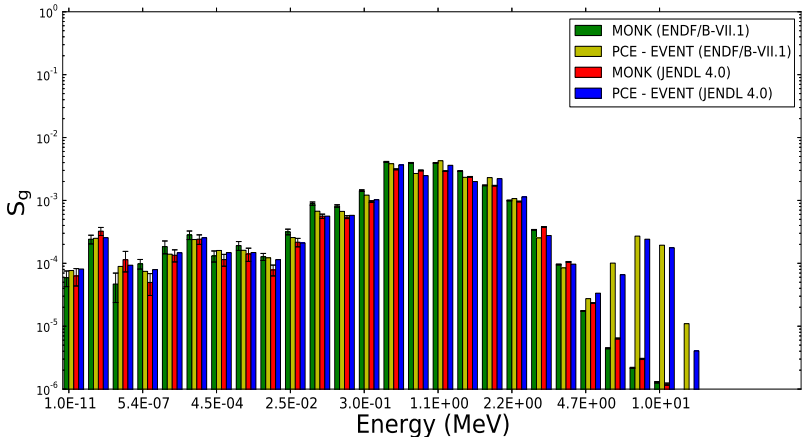


(b) ^{241}Am Fission

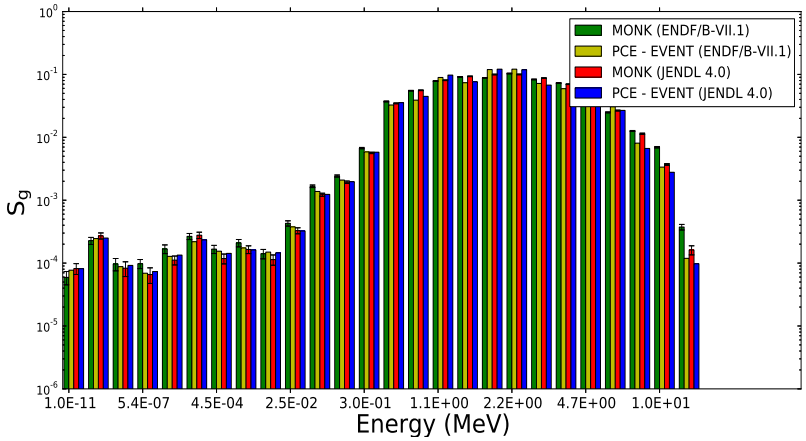


(c) ^{241}Am nu-bar

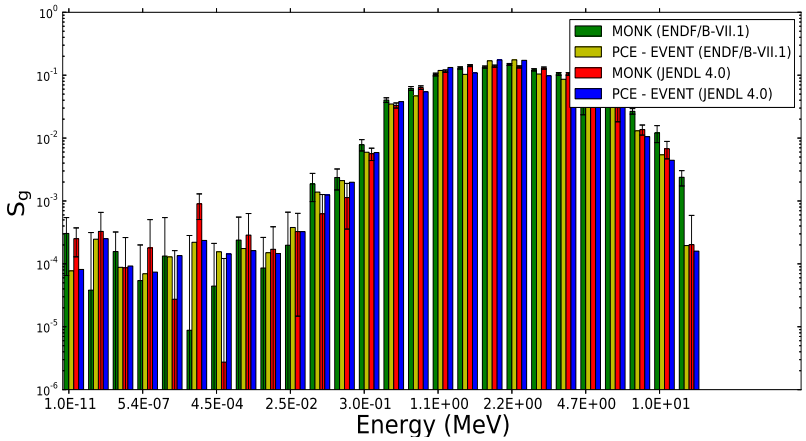
Figure 6.18.: First order sensitivities of k_{eff} to ^{241}Am capture, fission and nu-bar for the bare americium-241 sphere.



(a) ^{241}Am Capture

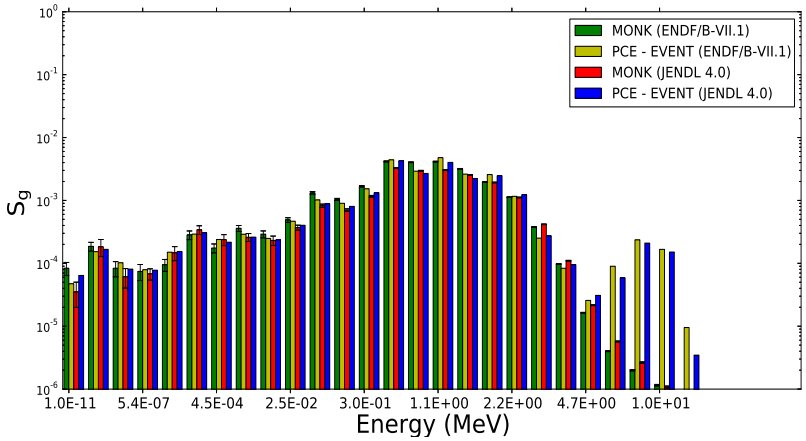


(b) ^{241}Am Fission

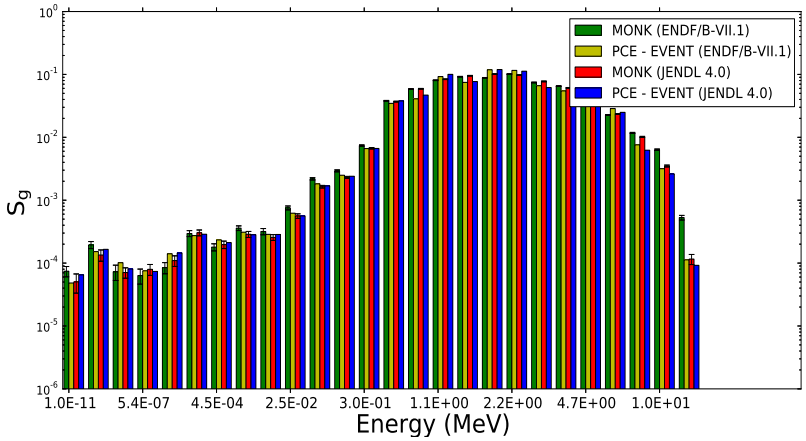


(c) ^{241}Am nu-bar

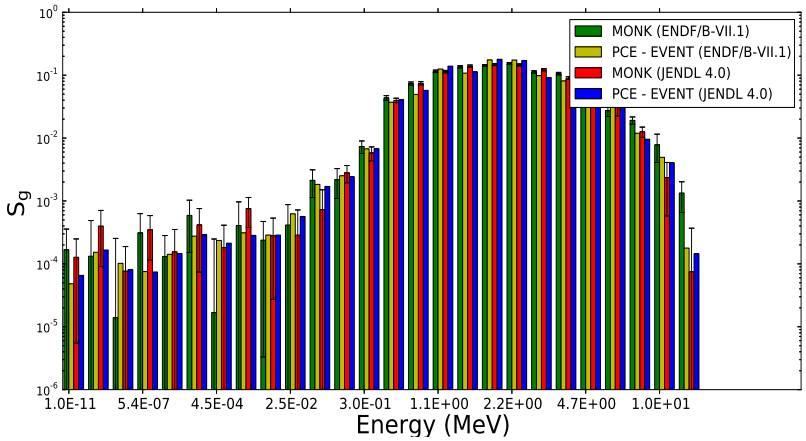
Figure 6.19.: First order sensitivities of k_{eff} to ^{241}Am capture, fission and nu-bar for the water reflected americium-241 sphere.



(a) ^{241}Am Capture

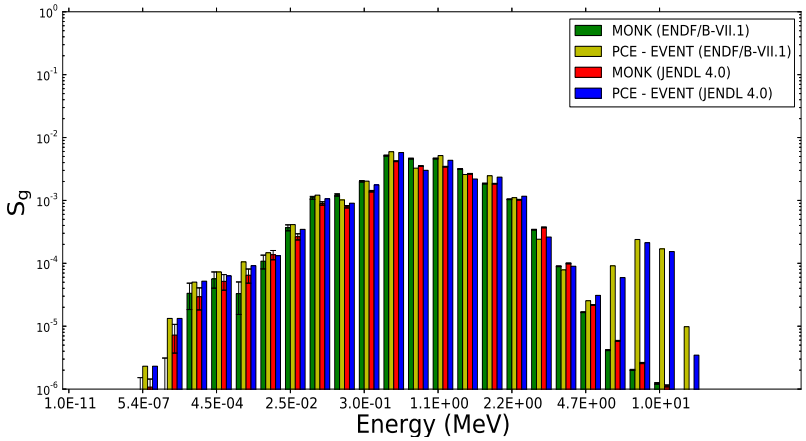


(b) ^{241}Am Fission

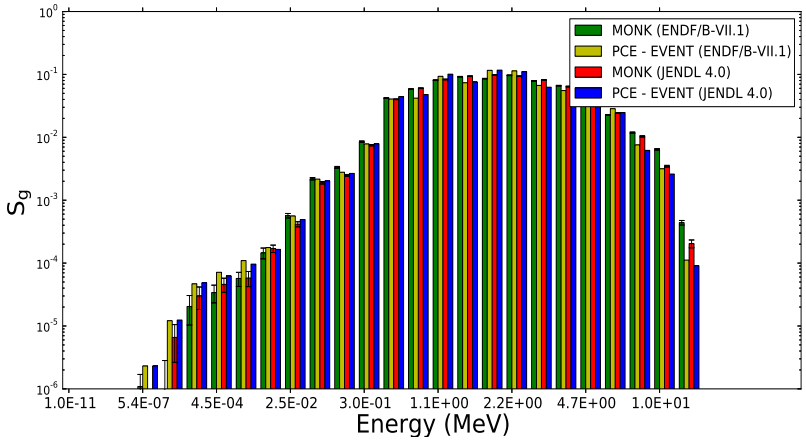


(c) ^{241}Am nu-bar

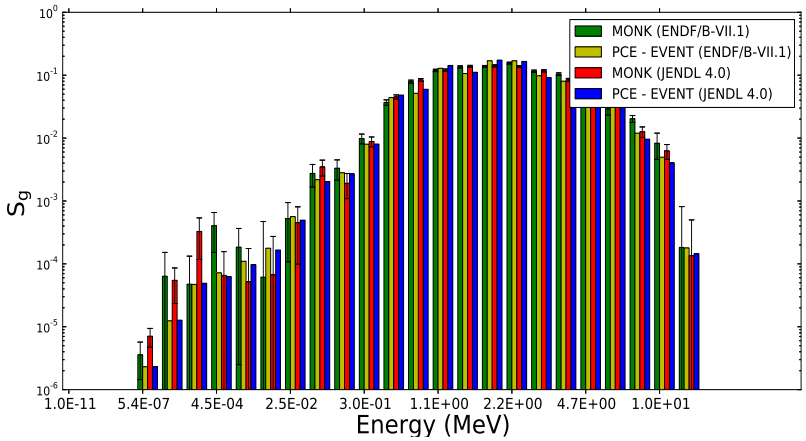
Figure 6.20.: First order sensitivities of k_{eff} to ^{241}Am capture, fission and nu-bar for the graphite reflected americium-241 sphere.



(a) ^{241}Am Capture

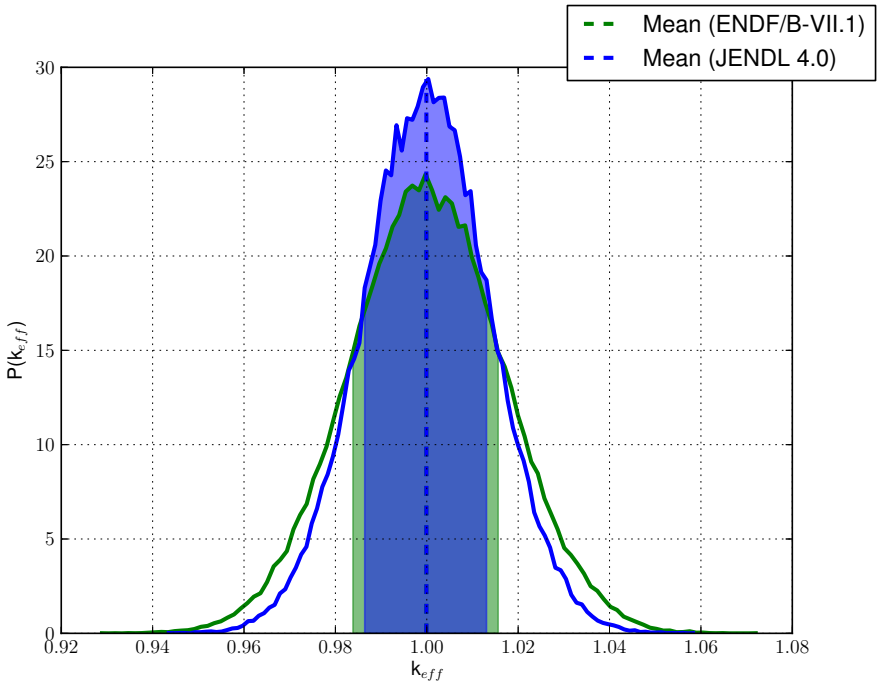


(b) ^{241}Am Fission

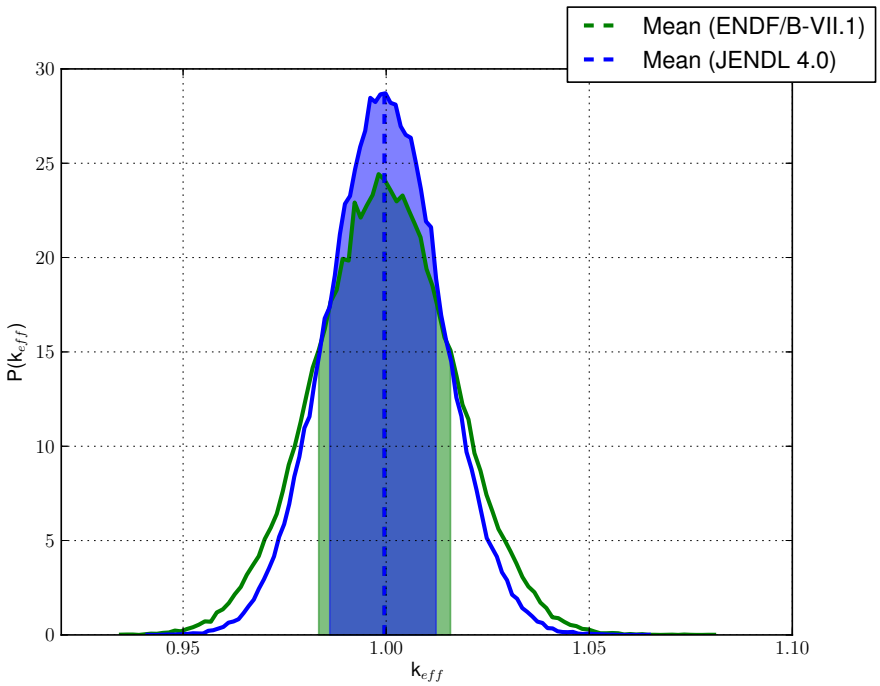


(c) ^{241}Am nu-bar

Figure 6.21.: First order sensitivities of k_{eff} to ^{241}Am capture, fission and nu-bar for the steel reflected americium-241 sphere.

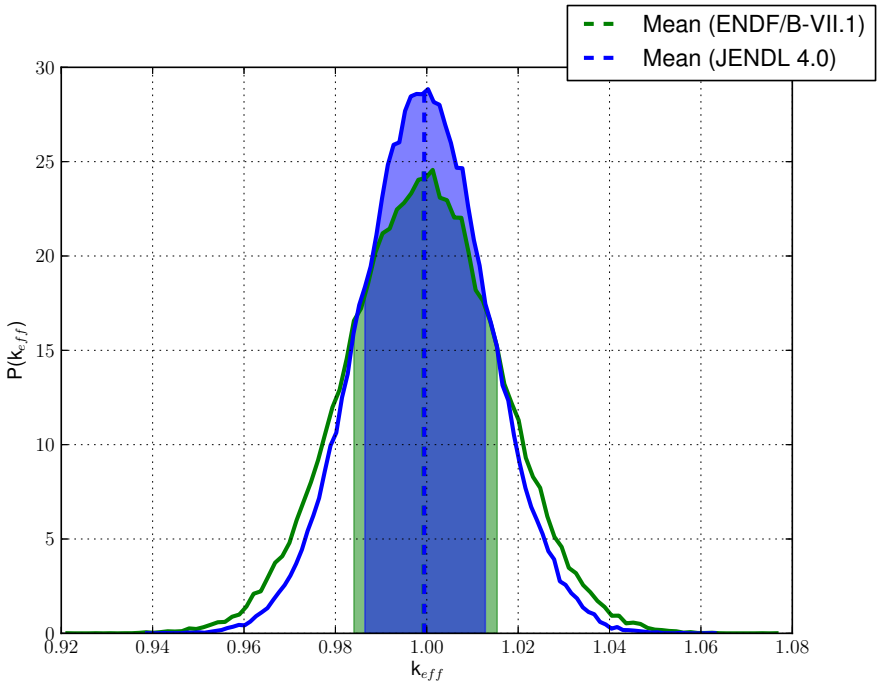


(a) Bare sphere

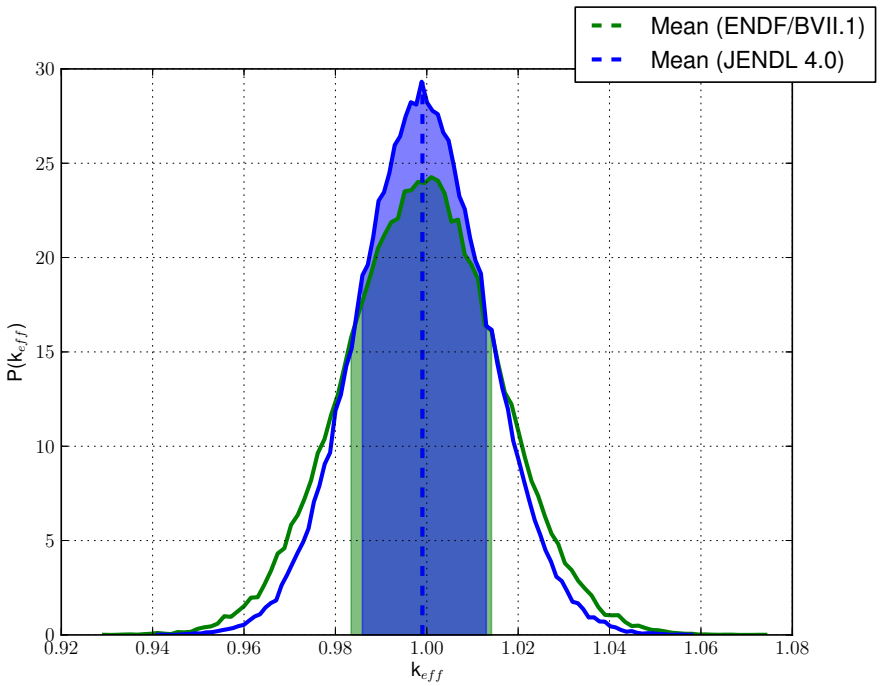


(b) Water reflector

Figure 6.22.: Probability density functions of k_{eff} for the bare and water reflected ^{241}Am spheres for ENDF/B-VII.1 and JENDL 4.0 data evaluations. The mean k_{eff} is high-lighted using a dashed line and the regions defined by $\overline{k}_{\text{eff}} \pm 1$ standard deviation have been shaded.



(a) Graphite reflector



(b) Steel reflector

Figure 6.23.: Probability density functions of k_{eff} for the graphite and steel reflected ^{241}Am spheres for ENDF/B-VII.1 and JENDL 4.0 data evaluations. The mean k_{eff} is high-lighted using a dashed line and the regions defined by $\overline{k}_{\text{eff}} \pm 1$ standard deviation have been shaded.

In the next part of this section the PCE is used to calculate PDFs of k_{eff} for each problem and nuclear data evaluation. The PDFs for the bare and water reflected spheres are given in Fig.(6.22) and the PDFs for the graphite and steel reflected spheres are given in Fig.(6.23). In both figures one standard deviation either side of the mean value has been shaded. The probability that a realisation of any of these distributions lies below the sub-critical limit, 0.95, can be calculated using the following

$$P(k_{\text{eff}} \leq 0.95) = \int_{-\infty}^{0.95} P(k)dk. \tag{6.3.5}$$

The values of the probabilities defined by Eqn.(6.3.5) for the sub-critical limit are tabulated in Table (6.24). From Table (6.24) we can see that the probabilities, $P(k_{\text{eff}} \leq 0.95)$, are all non-zero; the ENDF/B-VII.1 probabilities are approximately an order of magnitude large than the JENDL 4.0 probabilities.

Problem	ENDF/B-VII.1	JENDL 4.0
Bare	0.2130%	0.0250%
Water	0.1510%	0.0190%
Graphite	0.1850%	0.0245%
Steel	0.1990%	0.0425%

Table 6.24.: Probabilities of k_{eff} being below the sub-critical limit, k_{eff} =0.95, for the americium-241 problems using ENDF/B-VII.1 and JENDL 4.0 data evaluations.

Alternatively, as with the FLATTOP results from Table (6.11), we may express the 0.95 sub-critical limit in terms of the number of standard deviations below the mean value. These differences have been calculated using the standard deviations determined using the ENDF/B-VII.1 and JENDL 4.0 covariance data and are tabulated in Table (6.25). All of the values are

consistent, the ENDF/B-VII.1 results are slightly smaller than the JENDL 4.0 results reflecting the slightly larger standard deviations given in Table (6.20).

Problem	Number of standard deviations	
	ENDF/B-VII.1	JENDL 4.0
Bare	2.98	3.61
Water	2.99	3.61
Graphite	3.02	3.55
Steel	3.02	3.59

Table 6.25.: Difference between the mean value and sub-critical limit of k_{eff} =0.95 in standard deviations for the americium-241 problems.

6.4. Comparison of Americium-241 and FLATTOP Problems

Both of the americium-241 and FLATTOP problems are spherical systems with a central core region surrounded by a reflector. The main difference, apart from the fissile materials used, is that the FLATTOP problems have a fissile reflector. Computations of the criticality coefficient, k_{eff} , for the FLATTOP problems and critical radius for the americium-241 problems were performed using the Monte Carlo code MONK and the deterministic code WIMS. We note that there were considerable differences between the MONK and WIMS results for all of the problems. These differences are due to the modelling approximations in WIMS, e.g. the multi-group representation of the energy variable, and, in the case of the ENDF data, due to the erroneous representation of the ^{241}Am fission spectrum identified in [2].

For both the FLATTOP uranium and plutonium problems the value of

k_{eff} was calculated for a range of nuclear data evaluations. This range of data evaluations produced a spread in the value of k_{eff} and it was found that this spread produced a relative standard deviation of approximately 0.5%. The relative uncertainties calculated using ENDF/B-VII.1 or JENDL 4.0 with their respective covariance data agreed with these results with the exception of the ENDF/B-VII.1 result for the uranium core problem. This gave 1.37% which is around double that of the other predictions. This suggested that ENDF/B-VII.1 covariance data for ^{235}U data gives an over estimate of the nuclear data uncertainty.

For the americium problems a range of nuclear data evaluations were used to calculate the critical radius of each spherical system. The spread in results for different evaluations resulted in a RSD of approximately 3% in all cases. The RSDs calculated using a single evaluation plus covariance for k_{eff} were approximately 1.7% for ENDF/B-VII.1 data and 1.4% JENDL 4.0 data. These k_{eff} uncertainties were then translated to uncertainties in radius to compare with the results of multiple evaluations. The mapping produced uncertainties of approximately 3.2% for ENDF/B-VII.1 data and 2.5% for JENDL 4.0 data; the ENDF/B-VII.1 results were slightly larger, and the JENDL 4.0 results were slightly smaller than the spread from the calculations with multiple evaluations. Further comparisons of the spread from different evaluations with the uncertainties due to data covariances in Figures (6.16) and (6.17) showed that the JENDL 4.0 data is more bounding, the ENDF/B-VII.1 data has a bias towards larger values.

Comparing the uncertainty results from both FLATTOP and americium-241 problems showed that the uncertainty in k_{eff} is much higher for the

americium-241 problems than the FLATTOP problems. This is supported by both the explicit propagation of the covariance data and by analysing the spread in values from multiple data evaluations.

The polynomial chaos expansion (PCE) may be differentiated to yield approximations of the first order sensitivities (FOS) and may then be compared to faster FOS methods (like the MONK sensitivity option). Such comparisons were performed for both the FLATTOP and americium-241 problems. The PCE FOS were calculated using WIMS/EVENT and the conventional FOS were calculated using the MONK sensitivity option. The fission and nu-bar sensitivities were in good agreement but the capture sensitivities exhibited large differences at high energies. These differences were due to the different representations of the capture sensitivities in each code, more specifically, the MONK values account for radiative capture whereas the WIMS values include other threshold reactions and this accounts for the additional contributions at high energies. The total uncertainties were calculated from the FOS using Eqn. (6.1.10) and were in good agreement using both PCE FOS and MONK FOS indicating little error was introduced from the missing capture sensitivities. As discussed previously, there were large differences between the WIMS and MONK calculations. However, the good agreement between the MONK and WIMS/EVENT (calculated using PCE) sensitivities suggest this study is perfectly valid and would not have yielded significantly different uncertainty results if MONK had been used throughout.

Probability density functions (PDFs) of k_{eff} were calculated for both sets of problems using the ENDF/B-VII.1 and JENDL 4.0 covariance data.

From these PDFs the probability that a realisation of k_{eff} was below the sub-critical limit, k_{eff} =0.95, were calculated. The FLATTOP results gave a 0% probability (to four decimal places) that k_{eff} could be below 0.95. This is not surprising when considering the number of standard deviations between the mean value and the sub-critical limit from Table (6.11); these were approximately 12 for JENDL 4.0 (both uranium and plutonium problems) and 4 and 15 for ENDF/B-VII.1 (uranium and plutonium problems respectively) noting that the ENDF/B-VII.1 uranium covariances appear to be larger than might be expected. Conversely, the results for the americium-241 problems gave non zero probabilities of being below the sub-critical limit. The results for the ENDF/B-VII.1 covariances gave probabilities of $P(k_{\text{eff}} \leq 0.95) \approx 0.2\%$ whereas the JENDL 4.0 covariances gave probabilities of $P(k_{\text{eff}} \leq 0.95) \approx 0.02\%$. The number of standard deviations between the mean value and the sub-critical limit 0.95 were calculated for the americium-241 problems and are listed in Table (6.25). The results show that the number of SDs is consistent between problems using the same covariance evaluation and that all values are approximately bounded between 3 and 4 SDs.

Noting the results from Tables (6.11) and (6.25), estimates of the sub-critical limit can be made by subtracting a number of standard deviations from the mean value. The results for the americium-241 problems in Table (6.25) are approximately bounded by 3 and 4 standard deviations, the results for the FLATTOP problems are greater than 10 SDs from the mean (apart from the ENDF/B-V11.1 uranium result). When the sub-critical limit is three SDs below the mean, the total probability of a critical system being below this value, $P(k \leq \text{SCL})$ where SCL denotes sub-critical limit,

is $P(k \leq \text{SCL}) = 1.35 \times 10^{-3}$. For four SDs, $P(k \leq \text{SCL}) = 3.17 \times 10^{-5}$ and for 10 SDs $P(k \leq \text{SCL}) = 7.62 \times 10^{-24}$. In Table (6.26) the values of k_{eff} at 3,4 and 10 standard deviations below the mean value have been calculated. These may be used as estimates for the sub-critical mass limit. The relative percentage of the critical mass has also been calculated.

Problem	ENDF/B-VII.1					
	3 SD		4 SD		10 SD	
	SCL	Mass (%)	SCL	Mass (%)	SCL	Mass (%)
Bare	0.9497	77.50	0.9329	70.83	0.8322	38.66
Water	0.9499	77.60	0.9332	70.81	0.8329	38.63
Graphite	0.9504	77.48	0.9339	70.81	0.8347	38.64
Steel	0.9503	77.49	0.9338	70.96	0.8344	38.88
Problem	JENDL 4.0					
	3 SD		4 SD		10 SD	
	SCL	Mass (%)	SCL	Mass (%)	SCL	Mass (%)
Bare	0.9584	82.18	0.9445	76.75	0.8613	49.10
Water	0.9582	82.47	0.9443	76.93	0.8614	49.45
Graphite	0.9577	82.32	0.9436	77.12	0.8607	49.80
Steel	0.9584	82.32	0.9446	76.93	0.8590	49.44

Table 6.26.: Sub-critical limits and masses estimated using k_{eff} uncertainties calculated using ENDF/B-VII.1 and JENDL 4.0 covariance data for the americium-241 problems.

6.5. Conclusions

We have shown that the polynomial chaos method provides a valuable benchmark with which to test other uncertainty quantification techniques such as the MONK sensitivity method. The polynomial expansion, which has a global support in the uncertainty parameter space, was differentiated to yield first-order sensitivities which were compared directly to MONK sensitivities. The first-order sensitivities computed with both methods com-

pared well. The uncertainties computed using the first-order sensitivities and the full polynomial chaos expansion were very similar - to 3 or 4 significant figures, indicating very little extra information is derived from computation of the full PCE, i.e. first-order sensitivity analysis is sufficient for the applications investigated.

Comparing the results for the FLATTOP and americium-241 cases, the probabilities $P(k_{\text{eff}} \leq 0.95)$ suggest that the limit $k_{\text{eff}} \leq 0.95$ for the FLATTOP is safe when nuclear data covariances are considered; the number of standard deviations between the mean k_{eff} and the sub-critical limit are such that the probabilities $P(k_{\text{eff}} \leq 0.95)$ are vanishingly small. The probabilities $P(k_{\text{eff}} \leq 0.95)$ for the americium-241 problems are non-zero for all four configurations considered. Instead of the 0.95 sub-critical limit we have calculated the value of k_{eff} and the corresponding percentage of the critical mass corresponding to 3,4 and 10 standard deviations below the mean. Three and four SDs are bounding values of the 0.95 sub-critical limit for the ^{241}Am problems and 10 SDs is representative of the sub-critical limit for the FLATTOP problems. We have suggested that interpretation of the uncertainties of the ^{241}Am systems whilst considering well understood uranium and plutonium systems could provide one possible approach for determining appropriate sub-critical limits. Further work to support such an approach could be conducted by performing the analysis in Section (6.2) on other fast critical systems, potentially with other nuclides such as ^{233}U and also for the mass replacement experiments used to infer the ^{241}Am critical masses described in [111, 112]. It may also be necessary to perform more ^{241}Am systems other than the ones we have investigated here.

The computation of uncertainty is only as good as the covariance data which is used. For example, it was shown for the FLATTOP uranium problem that the uncertainties in k_{eff} were much larger using ENDF/B-VII.1 covariances compared to using JENDL 4.0 covariances. Contrasting these uncertainties with the uncertainties from multiple evaluations, which were comparable to the JENDL 4.0 uncertainties, raises some doubts as to the credibility of the ENDF/B-VII.1 covariance data of ^{235}U. There may also be several sources of uncertainty other than covariances when comparing calculated results to reality. The issue with the fission spectrum in the ^{241}Am ENDF MONK data illustrates this and highlights the need to compare computational methods as well as data when considering an unfamiliar system for which there is as yet no body of validation data.

Chapter 7

Summary and Conclusions

In the introductory chapter, Chapter (1), a brief description of the origin of nuclear data and it's uncertainties was given along with two methods for calculating the criticality coefficient k_{eff} ; the Monte Carlo and deterministic methods. A description and literature review of some existing uncertainty quantification techniques and the contemporary polynomial chaos methods was given.

In Chapter (2), multi-group diffusion equations were derived from the time dependent transport equation using both w-eigenvalue and k_{eff} -eigenvalue methods. The multi-group method averages the transport/diffusion equation over discrete energy regions resulting in a piece-wise continuous energy representation of the input nuclear data. In section (2.3) the uncertainties in the nuclear data were described using the concept of a random field provided that a) the random variables describing the nuclear data had finite variances and b) the energy dependence of the nuclear data was bounded and had a finite L_2 norm. In Section (2.3.1) the Karhunen Loéve expansion (KLE), which is an expansion in terms of IID Gaussian random variables, was derived for a discrete energy random field. In the final section of Chapter (2), the mappings for correlated Log-Normally distributed random

variables to Gaussian distributed random variables were defined. The Log-Normal distribution is bounded by zero and will therefore never support negative values. This was useful when sampling nuclear cross section data which physically cannot be less than zero.

In Chapter (3) the theory of polynomial chaos (PC) was outlined and it was shown how a polynomial chaos expansion (PCE) may be used to represent any second order random process. Optimal rates of convergence of the PCE are obtained with an appropriate choice of polynomial basis resulting in a generalised polynomial chaos expansion (gPCE); mixtures of polynomials may also be used, which was demonstrated in Appendix (B). In section (3.4) the general approach to computing the statistics of stochastic eigenvalue problems using a PCE was outlined. This approach replaced the dependence of the response variables upon the random parameters $\boldsymbol{\xi}$ explicitly using a PCE. This approach is known as the intrusive method. Two examples of the use of an intrusive PCE, the w-eigenvalue and k-eigenvalue, were presented in section (3.5.3). The intrusive method, when compared to the non-intrusive approach, required significantly longer execution times. The maximum number of dimensions used in the examples was 3; extrapolating to the many hundreds which may be present in realistic criticality problems strongly suggested that solving uncertainty problems with the intrusive technique would be intractable.

Chapter (4) outlined the use of an adaptive quadrature technique developed by Gerstner et al [4, 68] for building a sparse polynomial chaos expansion. Application of this procedure to simple test functions highlighted the potential for increased efficiency of the calculation of response statistics

with respect to the number of polynomials in the expansion and the number of model evaluations required to build it.

Chapter (5) used a technique known as high dimensional model representation (HDMR) to represent the k_{eff} response as a superposition of low dimensional functions. This facilitated the integration of the response which was performed using the adaptive quadrature methods defined in Chapter (4). The HDMR expansion was built adaptively using an algorithm of our own design but derived from work by another author [5]. The combination of the adaptive quadrature and HDMR methods allowed the construction of a sparse polynomial expansion for high-dimensional stochastic variables. This method of construction was tested on Rowlands' pin cell problems which had variable numbers of uncertain input parameters (cross sections and nu-bar). Results of comparisons between the polynomial chaos and Latin Hypercube estimations of the k_{eff} statistics showed that the PCE approach was an order of magnitude more accurate when calculating the mean and variance. Further analysis of these results showed that the majority of the variation could be represented using the univariate or first-order HDMR terms only and the second order and higher terms were largely superfluous to the calculation when using Gaussian statistics. We showed that this may not be the case when using Log-Normal statistics where the second-order HDMR terms contribute a larger proportion of the total variance.

Chapter (6) applied the polynomial chaos methods defined in previous chapters to a real problem. The problem was proposed by the National Nuclear Laboratory and involved investigating the safe sub-critical mass limits of americium-241 spheres in the presence of nuclear data uncertainties.

Evaluation of the uncertainty in k_{eff} was performed on four americium-241 systems and, to put the results into context, they were compared to more familiar uranium and plutonium systems. The uranium and plutonium systems used as reference cases were chosen to be geometrically and spectrally similar to the americium problems, i.e. they were spherical configurations with fast neutron spectra. The chosen reference cases are known as the FLATTOP problems. The uncertainties in k_{eff} were calculated explicitly from JENDL 4.0 and ENDF/B-VII.1 nuclear covariance data using the sensitivity method in the MONK Monte Carlo code and using the polynomial chaos method coupled with the deterministic code EVENT. The first-order sensitivities computed with both methods compared well. The uncertainties computed using the first-order sensitivities and the full polynomial chaos expansion were very similar - to 3 or 4 significant figures, indicating very little extra information is derived from computation of the full PCE, i.e. first-order sensitivity analysis is sufficient for the applications investigated. Instead of the 0.95 sub-critical limit we have calculated the value of k_{eff} and the corresponding percentage of the critical mass corresponding to 3,4 and 10 standard deviations below the mean. Three and four SDs are bounding values of the 0.95 sub-critical limit for the ^{241}Am problems and 10 SDs is representative of the sub-critical limit for the FLATTOP problems. We have suggested that interpretation of the uncertainties of the ^{241}Am systems whilst considering well understood uranium and plutonium systems could provide one possible approach for determining appropriate sub-critical limits. Further work to support such an approach could be conducted by performing the analysis in Section (6.2) on other fast critical systems, potentially with other nuclides such as ^{233}U and also for the mass replacement experiments used to infer the ^{241}Am critical masses described in [111, 112].

It may also be necessary to perform more ^{241}Am systems other than the ones we have investigated here.

The PCE (with FOS option) provided a valuable benchmark method to test whether the faster FOS methods (like the MONK sensitivity method) are adequate for calculating uncertainties; this was illustrated in the uncertainty results of the FLATTOP and americium-241 problems in Chapter (6). The HDMR additions have made the PCE method more practical allowing problems with many more random dimensions to be modelled; this was shown in the results of the Rowlands' pin cell problems in Chapter (5) where the adaptive HDMR method out-performed Latin hypercube sampling for problems up to, and including, 988 dimensions. Unlike random sampling, the HDMR/PCE approach gives the sensitivity breakdown as well as the total uncertainty and so allows a fuller comparison with FOS than simply comparing total uncertainties between FOS and sampling (which could mask competing differences). For the problems we have considered in this work, i.e. criticality calculations, the PCE FOS is little different from the full PCE and so there is little gain in using the full PCE. However, for other problems, such as burn-up calculations where the uncertainties at each burn-up step are compounded or other problems where the response parameters are highly non-linear, this may not be the case. This was partially illustrated in Chapter (5) where the Log-Normally distributed cross sections introduced additional non-linearity to the problem which increased the computational expense of the HDMR algorithm.

Bibliography

[1] Erin D. Fichtl. *Stochastic Methods for Uncertainty Quantification in Radiation Transport*. PhD thesis, University of New Mexico, 2009.

[2] H. Dias, N. Tancock, and A. Clayton. Critical mass calculations for ^{241}Am, ^{242m}Am and ^{243}Am. In *The 7th International Conference on Nuclear Criticality Safety (ICNC2003)*, 2003.

[3] S.A. Smolyak. Quadrature and interpolation formulas for tensor products of certain classes of functions. *Doklady Akademii Nauk SSSR*, 4:240–243, 1963.

[4] Thomas Gerstner and Michael Griebel. Numerical integration using sparse grids. *Numerical Algorithms*, 18:209–232, 1998.

[5] Xiang Ma and Nicholas Zabaras. An adaptive high-dimensional stochastic model representation technique for the solution of stochastic partial differential equations. *Journal of Computational Physics*, 229(10):3884 – 3915, 2010.

[6] Xiu Yang, Minseok Choi, Guang Lin, and George Em Karniadakis. Adaptive anova decomposition of stochastic incompressible and compressible flows. *Journal of Computational Physics*, 231(4):1587 – 1614, 2012.

[7] N.Otuka, S.Dunaeva, E.Dupont, O.Schwerer, and A.Blokhin. The role of the nuclear reaction data centres in experimental nuclear data knowledge sharing. In *Proceedings of the International Conference on Nuclear Data for Science and Technology (ND2010)*, page 1292, April 2010.

[8] M.B. Chadwick et al. ENDF/B-VII.0: Next generation evaluated nuclear data library for nuclear science and technology. *Nuclear Data Sheets*, 107:29313060, 2006.

[9] A.J. Koning et al. Status of the JEFF nuclear data library. In *Proceedings of the International Conference on Nuclear Data for Science and Technology*, page 1057, Jeju Island, Korea, 2010.

[10] Keiichi Shibata, Osamu IWAMOTO, Tsuneo NAKAGAWA, Nobuyuki IWAMOTO, Akira ICHIHARA, Satoshi KUNIEDA, Satoshi CHIBA, Kazuyoshi FURUTAKA, Naohiko OTUKA, Takaaki OHASAWA, Toru MURATA, Hiroyuki MATSUNOBU, Atsushi ZUKERAN, So KAMADA, and Jun-ichi KATAKURA. Jendl-4.0: A new library for nuclear science and engineering. *Journal of Nuclear Science and Technology*, 48(1):1–30, 2011.

[11] N. M. Larson. Updated users' guide for SAMMY: Multilevel R-matrix fits to neutron data using Bayes' equations. Technical Report ORNL/TM-9179/7, Oak Ridge National Laboratory, Oak Ridge, TN, USA, 2006.

[12] M. C. Moxon, T. C. Ware, and C. J. Dean. REFIT-2009 a least-square fitting program for resonance analysis of neutron transmission,

capture, fission and scattering data; users guide for REFIT-2009-10. Technical Report UKNSF(2010)P243, Harwell laboratory, 2010.

[13] Dan Gabriel Cacuci, editor. *Handbook of Nuclear Engineering*, volume 2. Springer, 2010.

[14] F.H.Fröhner. Evaluation and analysis of nuclear resonance data. Technical Report JEFF Report 18, Nuclear Energy Agency, 2000.

[15] L.C. Leal, N.M. Larson, H. Derrien, T. Kawano, and M.B. Chadwick. A new approach for nuclear data covariance and sensitivity generation. In *International conference on nuclear data for science and technology*, Santa Fe, NM (United States), 2004.

[16] G. Noguere, C. De Saint Jean, B. Iooss, P. Schilleebeeckx, and P. Siegler. Production of multigroup data covariance in the resonance range by monte-carlo calculations. In *PHYSOR 2006, ANS Topical Meeting on Reactor Physics*, 2006.

[17] A.J. Koning, S. Hilaire, and M.C. Duijvestijn. Talys- 1.0. In O. Bersillon, F. Gunsing, E. Bauge, R. Jacqmin, and S. Leray, editors, *Proceedings of the International Conference on Nuclear Data for Science and Technology*, April 22-27 2007.

[18] M. Herman, R. Capote, B.V. Carlson, P. Obložinský, M. Sin, A. Trkov, H. Wienke, and V. Zerkin. Empire: Nuclear reaction model code system for data evaluation. *Nuclear Data Sheets*, 108(12):2655 – 2715, 2007. Special Issue on Evaluations of Neutron Cross Sections.

[19] A.J. Koning and D. Rochman. Modern nuclear data evaluation with the {TALYS} code system. *Nuclear Data Sheets*, 113(12):2841 – 2934, 2012. Special Issue on Nuclear Reaction Data.

[20] R.E. MacFarlane and A.C. Kahler. Methods for processing ENDF/B-VII with NJOY. *Nuclear Data Sheets*, 111(12):2739 – 2890, 2010.

[21] J-Ch Sublet, P Ribon, and M Coste-Delclaux. CALENDF-2010 : User manual. Technical Report CEA-R-6277, ISSN 0429-3460, 2011.

[22] D. E. Cullen. Prepro 2007: ENDF/B processing codes. Technical Report IAEA-NDS-39 Rev. 13, International Atomic Energy Agency, 2007.

[23] E.E.Lewis. *Computational Methods of Neutron Transport*. American Nuclear Society, 1993.

[24] R.T. Ackroyd. *Finite Element Method for Particle Transport*. Research Studies Press, London, 1997.

[25] J. E. Morel, Todd A. Wareing, and Kenneth Smith. A linear-discontinuous spatial differencing scheme for SN radiative transfer calculations. *Journal of Computational Physics*, 128(2):445–462, 1996.

[26] C.R.E. de Oliveira. An arbitrary geometry finite element method for multigroup neutron transport with anisotropic scattering. *Progress in Nuclear Energy*, 18(12):227 – 236, 1986.

[27] Mark A. Goffin, Christopher M.J. Baker, Andrew G. Buchan, Christopher C. Pain, Matthew D. Eaton, and Paul N. Smith. Minimising the error in eigenvalue calculations involving the Boltzmann transport equation using goal-based adaptivity on unstructured meshes. *Journal of Computational Physics*, 242(0):726 – 752, 2013.

[28] T.D. Newton and L.J. Hutton. The next generation WIMS lattice code: WIMS9. In *PHYSOR*, 2002.

[29] Stephen A. Dupree and Stanley K. Fraley. *A Monte Carlo Primer. A Practical Approach to Radiation Transport*. Plenum Publishers, 2002.

[30] Jerome Spanier and Ely M. Gelbard. *Monte Carlo Principles and Neutron Transport Problems*. Dover, 2008.

[31] S. M. Bowman. SCALE 6: Comprehensive nuclear safety analysis code system. *Nuclear Technology*, 174:126–148.

[32] X-5 Monte Carlo Team. MCNP^{TM} a general Monte Carlo n-particle transport. Technical Report LA-UR-03-1987, Los Alamos National Laboratory, 2004.

[33] M.J. Armishaw et al. MONK 9a. In *Proc. 8th Int. Conf. Nuclear Criticality Safety*, St Petersburg, Russia, 2007.

[34] C.M. Diop, O. Petit, E. Dumonteil, F.X. Hugot, Y.K. Lee, and A. Mazzolo. TRIPOLI-4: A 3d continuous-energy Monte Carlo transport code. In *PHYTRA1: First International Conference on Physics and Technology of Reactors and Applications*, Marrakech (Morocco), March 14-16, 2007.

[35] Malvin H. Kalos and Paula A. Whitlock. *Monte Carlo Methods*. Wiley-Blackwell, 2008.

[36] M. D. McKay, R. J. Beckman, and W. J. Conover. Comparison of three methods for selecting values of input variables in the analysis of output from a computer code. *Technometrics*, 21(2):239–245, 1979.

[37] J.C. Helton and F.J. Davis. Latin hypercube sampling and the propagation of uncertainty in analyses of complex systems. *Reliability Engineering &; System Safety*, 81(1):23–69, 2003.

[38] Yousry Azmy and Enrico Sartori. *Nuclear Computational Science: A Century in Review*. Springer, 2010.

[39] Dan G. Cacuci. *Sensitivity and Uncertainty Analysis: Theory, Volume I*. CRC Press, 2007.

[40] Dan G. Cacuci. *Sensitivity and Uncertainty Analysis: Volume II: Applications to Large-Scale Systems*. CRC Press, 2007.

[41] ORNL. SCALE: Modular code system for performing standardized computer analyses for licensing evaluations. Technical Report ORNL/TM-2005/39, ORNL, April 2005.

[42] Y. Ronen, A. Galperin, and D.G. Cacuci. Derivation and application of second-order uncertainty analysis for normally distributed parameters. *Annals of Nuclear Energy*, 9(7):351 – 358, 1982.

[43] A. Gandini. A generalized perturbation method for bi-linear functionals of the real and adjoint neutron fluxes. *Journal of Nuclear Energy*, 21(10):755 – 765, 1967.

[44] W. Wieselquist, A. Vasiliev, and H. Ferroukhi. Towards an uncertainty quantification methodology with CASMO-5. In *International Conference on Mathematics and Computational Methods Applied to Nuclear Science and Engineering (M&C 2011)*, Rio de Janeiro, RJ, Brazil, May 2011.

[45] M. C. G. Hall. Cross-section adjustment with Monte Carlo sensitivities: Application to the Winfrith iron benchmark. *Nuclear Science and Engineering*, 81:423–431, 1082.

[46] P. Spanos and R. Ghanem. Stochastic finite element expansion for random media. *Journal of Engineering Mechanics*, 115(5):1035–1053, 1989.

[47] R.G. Ghanem and P.D. Spanos. *Stochastic Finite Elements: A Spectral Approach*. New York : Springer, 1991.

[48] Roger Ghanem. Ingredients for a general purpose stochastic finite elements implementation. *Computer Methods in Applied Mechanics and Engineering*, 168(1-4):19–34, 1999.

[49] M. M. R. Williams. Polynomial chaos functions and neutron diffusion. *Nuclear Science and Engineering*, 155:109–118, 2007.

[50] M. M. R. Williams and Matthew Eaton. A probabilistic study of the influence of parameter uncertainty on solutions of the neutron transport equation. *Progress in Nuclear Energy*, 52(6):580–588, 2010.

[51] D.A.F. Ayres, M.D. Eaton, A.W. Hagues, and M.M.R. Williams. Uncertainty quantification in neutron transport with generalized polynomial chaos using the method of characteristics. *Annals of Nuclear Energy*, 45:14–28, 2012.

[52] M. M. R. Williams. A method for solving a stochastic eigenvalue problem applied to criticality. *Annals of Nuclear Energy*, 37(6):894–897, 2010.

[53] M. M. R. Williams. A method for solving stochastic eigenvalue problems. *Applied Mathematics and Computation*, 215(11):3906–3928, 2010.

[54] O.P. Le Maître, O.M. Knio, H.N. Najm, and R.G. Ghanem. Uncertainty propagation using Wiener-haar expansions. *Journal of Computational Physics*, 197(1):28 – 57, 2004.

[55] O.P. Le Maître, H.N. Najm, R.G. Ghanem, and O.M. Knio. Multi-resolution analysis of Wiener-type uncertainty propagation schemes. *Journal of Computational Physics*, 197(2):502 – 531, 2004.

[56] Xiaoliang Wan and George Em Karniadakis. An adaptive multi-element generalized polynomial chaos method for stochastic differential equations. *Journal of Computational Physics*, 209(2):617–642, 2005.

[57] Jasmine Foo, Xiaoliang Wan, and George Em Karniadakis. The multi-element probabilistic collocation method (ME-PCM): Error analysis and applications. *Journal of Computational Physics*, 227(22):9572 – 9595, 2008.

[58] D. Xiu and J. Hesthaven. High-order collocation methods for differential equations with random inputs. *SIAM Journal on Scientific Computing*, 27(3):1118–1139, 2005.

[59] G. Lin, A.M. Tartakovsky, and D.M. Tartakovsky. Uncertainty quantification via random domain decomposition and probabilistic collocation on sparse grids. *Journal of Computational Physics*, 229:6995–7012, 2010.

[60] Erin D. Fichtl and Anil K. Prinja. The stochastic collocation method for radiation transport in random media. *Journal of Quantitative Spectroscopy and Radiative Transfer*, 112(4):646–659, 2011.

[61] Baskar Ganapathysubramanian and Nicholas Zabaras. Sparse grid collocation schemes for stochastic natural convection problems. *Journal of Computational Physics*, 225(1):652–685, 2007.

[62] Graud Blatman and Bruno Sudret. Sparse polynomial chaos expansions and adaptive stochastic finite elements using a regression approach. *Comptes Rendus Mcanique*, 336(6):518–523, 2008.

[63] Graud Blatman and Bruno Sudret. Efficient computation of global sensitivity indices using sparse polynomial chaos expansions. *Reliability Engineering & System Safety*, 95(11):1216–1229, 2010.

[64] Graud Blatman and Bruno Sudret. Adaptive sparse polynomial chaos expansion based on least angle regression. *Journal of Computational Physics*, 230(6):2345–2367, March 2011.

[65] P.J. Dossantos-Uzarralde and A. Guittet. A polynomial chaos approach for nuclear data uncertainties evaluations. *Nuclear Data Sheets*, 109(12):2894–2899, 2008.

[66] I. Babuska, F. Nobile, and R. Tempone. A stochastic collocation method for elliptic partial differential equations with random input data. *SIAM J. Numer. Anal.*, 45(3):1005–1034, 2007.

[67] F. Nobile, R. Tempone, and C. G. Webster. A sparse grid stochastic collocation method for partial differential equations with random input data. *SIAM Journal on Numerical Analysis*, 46(5):2309–2345, 2008.

[68] Thomas Gerstner and Michael Griebel. Dimension-adaptive tensor-product quadrature. *Computing*, 71:2003, 2003.

[69] F. Nobile, R. Tempone, and C. Webster. An anisotropic sparse grid stochastic collocation method for partial differential equations with random input data. *SIAM Journal on Numerical Analysis*, 46(5):2411–2442, 2008.

[70] S. Rahman and H. Xu. A univariate dimension-reduction method for multi-dimensional integration in stochastic mechanics. *Probabilistic Engineering Mechanics*, 19(4):393 – 408, 2004.

[71] H. Xu and S. Rahman. A generalized dimension-reduction method for multidimensional integration in stochastic mechanics. *Int. J. Numer. Meth. Engng.*, 61(12):1992–2019, 2004.

[72] H. Xu and S. Rahman. Decomposition methods for structural reliability analysis. *Probabilistic Engineering Mechanics*, 20(3):239 – 250, 2005.

[73] Herschel Rabitz, Ömer F. Aliş, Jeffrey Shorter, and Kyurhee Shim. Efficient input-output model representations. *Computer Physics Communications*, 117(2):11 – 20, 1999.

[74] Herschel Rabitz and Ömer F. Aliş. General foundations of high dimensional model representations. *Journal of Mathematical Chemistry*, 25:197–233, 1999.

[75] Rajib Chowdhury, B. N. Rao, and A. Meher Prasad. High-dimensional model representation for structural reliability analysis. *Commun. Numer. Meth. Engng.*, 25(4):301–337, 2009.

[76] Alain Hebért. *Applied Reactor Physics*. Presses Internationales Polytechnique, 2009.

[77] Robert V. Meghreblian and David K. Holmes. *Reactor Analysis*. Mcgraw Hill, 1960.

[78] D.F. Cullen, C.J Clouse, R. Procassini, and R.C. Little. Static and dynamic criticality; are they different? Technical Report UCRL-TR-201506, Lawrence Livermore National Laboratory, 2003.

[79] Philip Holmes, John L. Lumley, and Gal Berkooz. *Turbulence, Coherent Structures, Dynamical Systems and Symmetry*. Cambridge University Press, 1996.

[80] Geoffrey Grimmett and David Stirzaker. *Probability and Random Processes*. Oxford University Press, 2009.

[81] M. Rosenblatt. Remarks on a multivariate transformation. *Annals of Mathematical Statistics*, 23(3):470472, 1952.

[82] A. Der Kiureghian and P. L. Liu. Structural reliability under incomplete information. *J. Eng. Mech*, page 85104, 1986.

[83] G. E. P. Box and D. R. Cox. An analysis of transformations. *Journal of the Royal Statistical Society. Series B (Methodological)*, 26(2):211–252, 1964.

[84] N. Wiener. The homogeneous chaos. *American Journal of Mathematics*, 60:897–936, 1938.

[85] Dongbin Xiu and George Em Karniadakis. The Wiener–Askey polynomial chaos for stochastic differential equations. *SIAM Journal on Scientific Computing*, 24(2):619–644, 2002.

[86] Radu Alexandru Todor and Christoph Schwab. Convergence rates for sparse chaos approximations of elliptic problems with stochastic

coefficients. *IMA Journal of Numerical Analysis*, 27(2):232–261, April 2007.

[87] R. Cameron and W. Martin. The orthogonal development of non-linear functionals in series of fourier-hermite functionals. *Annals of Mathematics*, 48(2):385–392, 1947.

[88] D. Ayres, S. Park, and M.D. Eaton. Propagation of input model uncertainties with different marginal distributions using a hybrid polynomial chaos expansion. *Annals of Nuclear Energy*, 66(0):1 – 4, 2014.

[89] O.P.Le Maitre and O.M.Knio. *Spectral Methods for Uncertainty Quantification*. Springer, 2010.

[90] Sharif Rahman. A solution of the random eigenvalue problem by a dimensional decomposition method. *International Journal for Numerical Methods in Engineering*, 67(9):1318–1340, 2006.

[91] C. V. Verhoosel, M. A. Gutirrez, and S. J. Hulshoff. Iterative solution of the random eigenvalue problem with application to spectral stochastic finite element systems. *Int. J. Numer. Meth. Engng.*, 68(4):401–424, 2006.

[92] Anthony Nouy. A generalized spectral decomposition technique to solve a class of linear stochastic partial differential equations. *Computer Methods in Applied Mechanics and Engineering*, 196(4548):4521 – 4537, 2007.

[93] M.M.R. Williams. A method for solving stochastic eigenvalue problems. *Applied Mathematics and Computation*, 215(11):3906–3928, feb 2010.

[94] Roger Ghanem and Debraj Ghosh. Efficient characterization of the random eigenvalue problem in a polynomial chaos decomposition. *International Journal for Numerical Methods in Engineering*, 72(4):486–504, 2007.

[95] Debraj Ghosh. *On the Characterization and Analysis of the Random Eigenvalue Poblem*. PhD thesis, The Johns Hopkins University, 2007.

[96] J. E. Dennis and Robert B. Schnabel. *Numerical Methods for Unconstrained Optimization and Nonlinear Equations*. Prentice Hall, 1983.

[97] Stanley C. Eisenstat and Homer F. Walker. Globally convergent inexact newton methods. *SIAM Journal on Optimization*, 4(2):393–422, 1994.

[98] Philip J. Davis and Phillip Rabinowitz. *Methods of Numerical Integration*. Dover, 2007.

[99] T.N.L Patterson. The optimum addition of points to quadrature formulae. *Mathematics of Computation*, 22:847–856, 1968.

[100] Alan Genz and B.D Keister. Fully symmetric interpolatory rules for multiple integrals over infinite regions with gaussian weight. *Journal of Computational and Appied Mathematics*, 71:299–309, 1996.

[101] Grzegorz W. Wasilkowski and Henryk Wozniakowski. Explicit cost bounds of algorithms for multivariate tensor product problems. *Journal of Complexity*, 11:1–56, 1995.

[102] Andrea Saltelli. *Sensitivity Analysis*. Wiley, 2000.

[103] Sudret Bruno. Global sensitivity analysis using polynomial chaos expansions. *Reliability Engineering & System Safety*, 93(7):964–979, July 2008.

[104] Z. Zhang, M. Choi, and G. Karniadakis. Error estimates for the anova method with polynomial chaos interpolation: Tensor product functions. *SIAM Journal on Scientific Computing*, 34(2):A1165–A1186, 2012.

[105] I.M. Sobol. Theorems and examples on high dimensional model representation. *Reliability Engineering & System Safety*, 79(2):187 – 193, 2003.

[106] J.L. Rowlands. The pincell benchmarks and other calculational benchmarks. Technical Report JEF/DOC-494, OECD/NEA Paris, 1994.

[107] M J Halsall. Cactus, a characteristics solution to the neutron transport equations in complicated geometries. Technical report, United Kingdom Atomic Energy Establishment, 1980.

[108] D.J. Powney and T.D. Newton. Overview of the WIMS 9 resonance treatment. Technical Report ANSWERS/WIMS/TR.26, Serco Assurance, 2004.

[109] J. Venner, R.M. Haley, and R.L. Bowden. k-effective as a measure of criticality safety. In *The 7th International Conference on Nuclear Criticality Safety (ICNC2003)*, 2003.

[110] Adolf Garcia and R. Michael Westfall. Technical bases for ANS-8 standards. Technical report, American Nuclear Society, 2004.

[111] C. C. Byers, G. E. Hansen, J. J. Koelling, E. A.Plassmann, and D. R. Smith. Reactivity coefficients of heavy isotopes in LASL's fast critical assemblies. *Trans Am. Nucl. Soc.*, 28:295, 1978.

[112] R. G. Sanchez. Proposal for experiments with actinide elements. Technical Report LA-UR-1627, Los Alamos Scientific Laboratory, 1994.

[113] Answers Software. WIMS: A modular scheme for neutronics calculations. User guide for version 10. Technical Report ANSWERS/WIMS/REPORT/014, Answers, 2014.

[114] M. Herman and A. Trkov. *ENDF-6 Formats Manual*.

[115] G. E. Hansen and H. C. Paxton. Reevaluated critical specifications of some Los Alamos fast-neutron systems. Technical Report LA-4208, Los Alamos Scientific Laboratory, 1969.

[116] R. W. Brewer, T. P. McLaughlin, and Virginia Dean. Plutonium sphere reflected by normal uranium using FLATTOP. Technical Report PU-MET-FAST-006, Nuclear Energy Agency, 2014.

[117] R. W. Brewer, T. P. McLaughlin, and Virginia Dean. Uranium-235 sphere reflected by normal uranium using FLATTOP. Technical Report HEU-MET-FAST-028, Nuclear Energy Agency, 2014.

Appendices

Appendix A

Transformations between Log-Normal and Normal Distributions

A realisation of the discrete energy nuclear data is represented as $\{\mathcal{D}_g; g = 1, \cdots N_G\}$ where $\mathcal{D}_g \equiv \boldsymbol{\mathcal{D}}(E_g, \boldsymbol{\xi})$ is a random variable representing the uncertainty in the nuclear data in energy group g. The total number of energy groups is given as N_G. When the marginal distributions of a correlated random field are non-Gaussian it is necessary to transform the random field to a field with Gaussian marginals before it may be represented in terms of a set of IID random variables. In this Appendix we derive the expressions which transform the means and covariance of a Log-Normally distributed random field into their Gaussian-distributed equilvalents.

In Section (2.3.1) we have shown how a random field with Gaussian marginal distributions may be represented in terms of a set of IID random variables, $\boldsymbol{\xi}$, using the Karhunen Loéve expansion as follows:

$$\mathcal{D}(E_g, \boldsymbol{\xi}) = \overline{\mathcal{D}}(E_g) + \sum_{h=1}^{N_G} L_{gh}\varphi_h(E_g). \tag{A.0.1}$$

We now assume that the random variables $\mathcal{D}_g$ are descirbed by a Log-Normal distribution with mean and variance given by

$$\overline{\mathcal{D}}_g^{(\mathrm{LN})} \equiv \mathbb{E}[\mathcal{D}_g] \tag{A.0.2}$$

$$\mathrm{Var}_{\boldsymbol{\mathcal{D}}}^{(\mathrm{LN})}(E_g) \equiv v_g^{(\mathrm{LN})} \equiv \mathbb{E}[\mathcal{D}_g^2] - \overline{\mathcal{D}}_g^{(\mathrm{LN})}\overline{\mathcal{D}}_g^{(\mathrm{LN})} \tag{A.0.3}$$

here the superscript, "(LN)", refers to the Log-Normal distribution. Likewise, for a parameter described by the Normal distribution, we use the superscript "(N)". We may transform the random variable $\mathcal{D}_g^{(\mathrm{LN})}$ back to the space of normal variables by taking logarithms. Using this fact and Eqn.(A.0.1) we may now write

$$\ln\left(\mathcal{D}_g^{(\mathrm{LN})}\right) = \overline{\mathcal{D}}_g^{(\mathrm{N})} + \sum_{k=1}^{N} L_{ik}^{(\mathrm{N})} \ln(\xi_k) \tag{A.0.4}$$

or alternatively

$$\mathcal{D}_g^{(\mathrm{LN})} = \exp\left(\overline{\mathcal{D}}_g^{(\mathrm{N})} + \sum_{k=1}^{N} L_{ik}^{(\mathrm{N})} \ln(\xi_k)\right) \tag{A.0.5}$$

$$= \exp(\overline{\mathcal{D}}_g^{(\mathrm{N})}) \prod_{k=1}^{M} \xi_k^{L_{ik}^{(\mathrm{N})}} \tag{A.0.6}$$

where the variables ξ_k are now defined by the following PDF

$$p(\xi) = \frac{1}{\sqrt{2\pi}\xi} \exp\left(\frac{\ln(\xi)^2}{2}\right) \quad \xi \in [0, \infty] \tag{A.0.7}$$

To proceed with the derivation we define the following expression:

$$\int_0^\infty \xi^j p(\xi) d\xi = \exp\left(\frac{j^2}{2}\right). \tag{A.0.8}$$

Using Eqns.(A.0.6) and (A.0.8) the mean may be calculated as follows

$$\begin{aligned}\overline{\mathcal{D}}_g^{(\mathrm{LN})} &= \int_0^\infty \exp(\overline{\mathcal{D}}_g^{(\mathrm{N})}) \prod_{k=1}^{M} \xi_k^{L_{ik}^{(\mathrm{N})}} p(\xi) d\xi \\ &= \exp(\overline{\mathcal{D}}_g^{(\mathrm{N})}) \prod_{k=1}^{M} \exp\left(\frac{L_{ik}^{(\mathrm{N})} L_{ik}^{(\mathrm{N})}}{2}\right) \end{aligned} \tag{A.0.9}$$

The covariance between X_i and X_j is computed using Eqn.(2.3.6)

$$\begin{aligned}\mathrm{Cov}_{\boldsymbol{\mathcal{D}}\boldsymbol{\mathcal{D}}}^{(\mathrm{LN})}(E_g, E_h) &= \int_0^\infty \boldsymbol{\mathcal{D}}^{(\mathrm{LN})}(E_g;\boldsymbol{\xi}) \boldsymbol{\mathcal{D}}^{(\mathrm{LN})}(E_h;\boldsymbol{\xi}) p(\boldsymbol{\xi}) d\boldsymbol{\xi} - \overline{\mathcal{D}}_g^{(\mathrm{LN})} \overline{\mathcal{D}}_h^{(\mathrm{LN})} \\ &= \mathbb{E}[\mathcal{D}_g^{(\mathrm{LN})} \mathcal{D}_h^{(\mathrm{LN})}] - \overline{\mathcal{D}}_g^{(\mathrm{LN})} \overline{\mathcal{D}}_h^{(\mathrm{LN})} \end{aligned} \tag{A.0.10}$$

In the above, the second order term is calculated as follows

$$\begin{aligned}\mathbb{E}[\mathcal{D}_g^{(\mathrm{LN})} \mathcal{D}_h^{(\mathrm{LN})}] &= \int_0^\infty \exp(\overline{\mathcal{D}}_g^{(\mathrm{N})} + \overline{\mathcal{D}}_h^{(\mathrm{N})}) \prod_{k=1}^{M} \xi_k^{L_{ik}^{(\mathrm{N})} + L_{jk}^{(\mathrm{N})}} p(\xi) d\xi \\ &= \exp(\overline{\mathcal{D}}_g^{(\mathrm{N})}) \exp(\overline{\mathcal{D}}_h^{(\mathrm{N})}) \prod_{k=1}^{M} \exp\left(\frac{[L_{ik}^{(\mathrm{N})} + L_{jk}^{(\mathrm{N})}]^2}{2}\right) \\ &= \exp(\overline{\mathcal{D}}_g^{(\mathrm{N})}) \exp(\overline{\mathcal{D}}_h^{(\mathrm{N})}) \prod_{k=1}^{M} \exp\left(\frac{L_{ik}^{(\mathrm{N})} L_{ik}^{(\mathrm{N})}}{2}\right) \exp\left(\frac{L_{jk}^{(\mathrm{N})} L_{jk}^{(\mathrm{N})}}{2}\right) \exp(L_{ik}^{(\mathrm{N})} L_{jk}^{(\mathrm{N})}) \\ &= \overline{\mathcal{D}}_g^{(\mathrm{LN})} \overline{\mathcal{D}}_h^{(\mathrm{LN})} \exp\left(\sum_{k=1}^{M} L_{ik}^{(\mathrm{N})} L_{jk}^{(\mathrm{N})}\right) \end{aligned} \tag{A.0.11}$$

Therefore,

$$\mathrm{Cov}_{\boldsymbol{\mathcal{D}}\boldsymbol{\mathcal{D}}}^{(\mathrm{N})}(E_g, E_h) = \ln\left[\frac{\mathrm{Cov}_{\boldsymbol{\mathcal{D}}\boldsymbol{\mathcal{D}}}^{(\mathrm{LN})}(E_g, E_h)}{\overline{\mathcal{D}}_g^{(\mathrm{LN})} \overline{\mathcal{D}}_h^{(\mathrm{LN})}} + 1\right] \tag{A.0.12}$$

and

$$\overline{\mathcal{D}}_g^{(\mathrm{N})} = \ln\left[\frac{\left[\overline{\mathcal{D}}_g^{\mathrm{LN}}\right]^2}{\sqrt{\mathrm{Cov}_{\boldsymbol{\mathcal{D}}\boldsymbol{\mathcal{D}}}^{(\mathrm{LN})}(E_g, E_g) + \left[\overline{\mathcal{D}}_g^{\mathrm{LN}}\right]^2}}\right]. \tag{A.0.13}$$

Appendix B

Propagation of input model uncertainties with different marginal distributions using a hybrid polynomial chaos expansion

This appendix has been adapted from the following technical note "Propagation of input model uncertainties with different marginal distributions using a hybrid polynomial chaos expansion" [88]. The major changes are notational which have been done to be consistent with the thesis and parts of the theory and literature review have been replaced by references to avoid repetition of previous chapters.

B.1. Introduction

In many engineering applications, including reactor physics and criticality calculations, a situation may arise where the uncertainties associated with

input parameters are described with different probability distributions. For example, a reactor lattice pin cell may have nuclear data uncertainties described with a Gaussian distribution whereas the temperature of the fuel and moderator etc. are described using a uniform distribution. In this note we extend the work in [85]. We propose a combination of the optimal expansions for each probability distribution to form a hybrid polynomial basis. We first show that a tensor product of different Askey polynomials is a basis for the tensor product of their corresponding probability spaces. We then illustrate the theory using a simple numerical example which employs both uniform and Gaussian distributions.

B.2. Theory

In section (2.3) we have seen that when the input data are uncertain they may be modelled parametrically using a set of IID random variables $\boldsymbol{\xi}$. The response to a model, R, involving such uncertain quantities may itself be represented as a function of these IID random variables, namely: $R(\boldsymbol{\xi})$. The mean and variance of $R(\boldsymbol{\xi})$ may be calculated using the following expressions

$$\overline{R} = \int d\xi_1 \cdots \int d\xi_M R(\boldsymbol{\xi}) p(\boldsymbol{\xi}) \tag{B.2.1}$$

$$\mathrm{Var}[R] = \int d\xi_1 \cdots \int d\xi_M R^2(\boldsymbol{\xi}) p(\boldsymbol{\xi}) - \overline{R}^2 \tag{B.2.2}$$

with $\overline{R}$ and $\mathrm{Var}[R]$ representing the mean and variance respectively. The function $p(\boldsymbol{\xi})$ is the probability density function (PDF) of the random variable $\boldsymbol{\xi}$. Since all variables in the set $\boldsymbol{\xi}$ are independent, the PDF has the

form

$$p(\boldsymbol{\xi}) = \prod_{i=1}^{M} p(\xi_i). \tag{B.2.3}$$

As in Section (3.2), we only consider $\mathbb{R}$-valued random variables R which belong to the probability space $L_2(\Theta, P)$. In this case, each second order random variable $R \in L_2(\Theta, P)$ admits the following PC representation

$$\begin{aligned} R(\boldsymbol{\xi}(\theta)) = r_0 I_0 & \\ + \sum_{i_1=1}^{\infty} r_{i_1} I_1(\xi_{i_1}(\theta)) & \\ + \sum_{i_1=1}^{\infty} \sum_{i_2=1}^{i_1} r_{i_1,i_2} I_2(\xi_{i_1}(\theta), \xi_{i_2}(\theta)) & \\ + \sum_{i_1=1}^{\infty} \sum_{i_2=1}^{i_1} \sum_{i_3=1}^{i_2} r_{i_1,i_2,i_3} I_3(\xi_{i_1}(\theta), \xi_{i_2}(\theta), \xi_{i_3}(\theta)) & \\ + \cdots & \end{aligned} \tag{B.2.4}$$

where $I_n(\xi_{i_1}(\theta), \cdots, \xi_{i_n}(\theta))$ denotes the Wiener-Askey polynomial chaos of order n in terms of the random vector $\boldsymbol{\xi} = \{\xi_{i_1}, \cdots, \xi_{i_n}\}$. For notational convenience, we may write

$$R(\boldsymbol{\xi}) = \sum_{i=1}^{\infty} r_i \Phi_i(\boldsymbol{\xi}) \tag{B.2.5}$$

where there is a one-to-one correspondence between the functions $I_n(\xi_{i_1}, \cdots, \xi_{i_n})$ and $\Phi_i(\boldsymbol{\xi})$.

Consider now a random process Y which belongs to the space $\mathcal{H} = \mathcal{H}_1 \otimes \mathcal{H}_2$ where $\mathcal{H}_1 = L_2(\Theta_1, \mathcal{B}_1, \mu_1)$ and $\mathcal{H}_2 = L_2(\Theta_2, \mathcal{B}_2, \mu_2)$ are Hilbert spaces.

Supposing that $\{\phi_i\}$ and $\{\eta_i\}$ are GPC bases for $\mathcal{H}_1$ and $\mathcal{H}_2$ respectively, then we wish to know if we may expand Y with the following

$$Y = \sum_{i=1}^{\infty}\sum_{j=1}^{\infty} \alpha_{ij}\phi_i(\xi)\eta_j(\zeta) \tag{B.2.6}$$

For $X_1 \in \mathcal{H}_1$ and $X_2 \in \mathcal{H}_2$ we may write

$$X_1(\boldsymbol{\xi}) = \sum_i c_i\phi_i(\boldsymbol{\xi}) \quad ; X_2(\boldsymbol{\zeta}) = \sum_j d_j\eta_j(\boldsymbol{\zeta}) \tag{B.2.7}$$

where ϕ and η are the optimal polynomial bases corresponding to the probability measures μ_1 and μ_2 respectively. We can see straight away that the hybrid basis is orthogonal from the following

$$< \phi_1 \otimes \eta_1, \phi_2 \otimes \eta_2 > = < \phi_1, \phi_2 >< \eta_1, \eta_2 > \tag{B.2.8}$$

we also have $\sum_i |c_i|^2 < \infty$ and $\sum_j |d_j|^2 < \infty$. Thus $\sum_{ij} |c_i d_j| < \infty$, and therefore, $\sum_{ij} |c_i d_j| < \infty$. Consequently, we know that $\sum_{i<m,j<n} c_i d_j \phi_i \otimes \eta_j$ converges as $n, m \to \infty$. Therefore,

$$\left|\left| X_1 \otimes X_2 - \sum_{i<m,j<n} c_i d_j \phi_i \otimes \eta_j \right|\right| \to 0 \quad \text{as } m, n \to \infty \tag{B.2.9}$$

Thus, $\{\phi_i \otimes \eta_j\}$ is a basis for $\mathcal{H}_1 \otimes \mathcal{H}_2$.

The mean and variance of Eqn.(B.2.6) can now be calculated in the usual

way, namely

$$\overline{Y} = \alpha_{00} \tag{B.2.10}$$

$$v_Y = \sum_{i=1}^{\infty}\sum_{j=1}^{\infty} \alpha_{ij} < \phi_i^2 >< \eta_j^2 > \tag{B.2.11}$$

B.3. Numerical Example

As an example, we investigate the simple expression for the infinite multiplication factor k_∞:

$$k_\infty(\xi, \zeta) = \frac{\nu(\xi)\Sigma_f}{\Sigma_a(\zeta)} \tag{B.3.1}$$

where ν is the average number of neutrons produced per fission and Σ_f and Σ_a are the fission and absorption cross sections respectively. We assume that the absorption cross section and ν have an associated uncertainty which we represent parametrically using the random variables ξ and ζ, namely

$$\nu(\xi) = \overline{\nu}(1 + R\xi) \quad \xi \in [-\infty : \infty] \tag{B.3.2}$$

$$\Sigma_a(\zeta) = \overline{\Sigma_a}(1 + \sqrt{3}R\zeta) \quad \zeta \in [-1 : 1] \tag{B.3.3}$$

The fission cross section is assumed to have no uncertainty. Here R is the relative uncertainty and is defined as

$$R = \frac{\sigma}{\mu} \tag{B.3.4}$$

where σ is the standard deviation and μ is the mean.

In Eqns.(B.3.2) and (B.3.3) we note that the random variables have different supports. With the following probability distributions:

$$p(\xi) = \frac{1}{\sqrt{2\pi}} \exp\left\{-\frac{\xi^2}{2}\right\} \tag{B.3.5}$$

$$p(\zeta) = \frac{1}{2} \tag{B.3.6}$$

we can see that ν is described by a Gaussian distribution and Σ_a by a uniform distribution.

The mean and variance of Eqn.(B.3.18) using (B.2.1) and (B.2.2) can be calculated exactly and are given by the following:

$$\begin{aligned} \mu_{k_\infty} &= \int_{-\infty}^{\infty}\int_{-1}^{1} k_\infty(\xi,\zeta)p(\xi)p(\zeta)d\xi d\zeta \\ &= -\frac{\overline{\nu}\Sigma_f}{2\overline{\Sigma_a}R\sqrt{3}} \log\left\{\frac{1-\sqrt{3}R}{1+\sqrt{3}R}\right\} \end{aligned} \tag{B.3.7}$$

$$\begin{aligned} v_{k_\infty} &= \int_{-\infty}^{\infty}\int_{-1}^{1} k_\infty^2(\xi,\zeta)p(\xi)p(\zeta)d\xi d\zeta - \mu_{k_\infty}^2 \\ &= \frac{\overline{\nu}^2\overline{\Sigma_f}^2(1+R^2)}{\overline{\Sigma_a}(1-3R^2)} - \mu_{k_\infty}^2 \end{aligned} \tag{B.3.8}$$

We must note that solutions to Eqns.(B.3.7) and (B.3.8) are only available for values of $R \leq \frac{1}{\sqrt{3}} \approx 57.7\%$.

From [85] we note that the optimal polynomial basis for the Gaussian distribution defined in Eqn.(B.3.2) is the Hermite polynomials and the optimal basis for the uniform distribution in (B.3.3) is the Legendre polynomials. We now assume that $k_\infty(\xi,\zeta)$ belongs to the tensor product space of the uniform and Gaussian probability spaces. We may now expand Eqn.(B.3.18)

using the hybrid polynomial chaos expansion in Eqn.(B.2.6):

$$k_\infty(\xi,\zeta) = \sum_{i+j=0}^{\infty} \alpha_{ij} H_i(\xi) P_j(\zeta) \tag{B.3.9}$$

where H_i and P_j are the Hermite and Legendre polynomials of order i and j respectively. For numerical purposes, it is necessary to truncate the expansion in Eqn.(B.3.9) to a maximum polynomial order p, namely

$$k_\infty(\xi,\zeta) \approx \sum_{i+j=0}^{p} \alpha_{ij} H_i(\xi) P_j(\zeta) \tag{B.3.10}$$

To calculate the coefficients, α, in Eq.(B.3.10) we use the non-intrusive approach [58, 60]. Using this technique, the coefficients are calculated via the following integral

$$\begin{aligned}\alpha_{ij} &= \frac{\int_{-1}^{1}\int_{-\infty}^{\infty} k_\infty(\xi,\zeta) H_i(\xi) P_j(\zeta) p(\xi) p(\zeta) d\zeta d\xi}{\int_{-1}^{1}\int_{-\infty}^{\infty} H_i^2(\xi) P_j^2(\zeta) p(\xi) p(\zeta) d\zeta d\xi} \\ &= \frac{2j+1}{i!}\frac{1}{2\sqrt{2\pi}}\int_{-1}^{1}\int_{-\infty}^{\infty} k_\infty(\xi,\zeta) H_i(\xi) P_j(\zeta) e^{-\xi^2/2} d\zeta d\xi \end{aligned} \tag{B.3.11}$$

where we have made use of Eqns.(B.3.5), (B.3.6) and the following

$$\int_{-1}^{1} P_j^2(\zeta) p(\zeta) d\zeta = \frac{1}{2j+1} \quad \text{and} \quad \int_{-\infty}^{\infty} H_i^2(\xi) p(\xi) d\xi = i!$$

For values of $\overline{\nu}\Sigma_f = 2.0$ and $\overline{\Sigma_a} = 1.4$ exact values of the mean and variance can be computed using Eqns.(B.3.7) and (B.3.8) and the convergence of the expansion in (B.3.10) can be investigated. In Fig.(B.1) the relative error

$$\epsilon = \frac{|v_{k_\infty} - v_{k_\infty}^p|}{v_{k_\infty}} \tag{B.3.12}$$

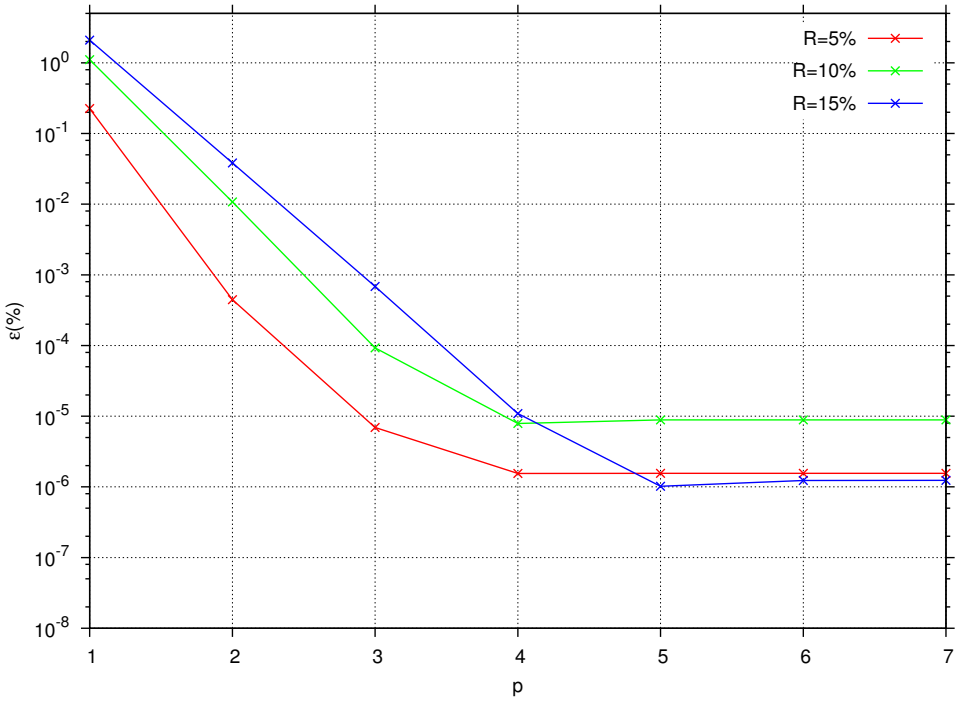


Figure B.1.: Convergence of the Hermite-Legendre polynomial expansion for relative uncertainties $R = 5\%, 10\%$ and 15%.

of the expansion is plotted versus the polynomial expansion order p. The values v_{k_∞} and $v^p_{k_\infty}$ in Eqn.(B.3.12) denote the exact variance calculated with (B.3.8) and polynomial chaos variance at order p calculated using (B.2.11) respectively. From Fig.(B.1) we can see that the Hermite-Legendre basis converges exponentially with the polynomial order p.

It is also informative to look at the convergence when the uniform probability is mapped to a Gaussian variable and $k_\infty(\xi_1, \xi_2)$ is expanded purely with Hermite polynomials in terms of the Gaussian random variables ξ_1 and ξ_2. This way we can check if the hybrid Hermite-Legendre basis provides benefit. To perform the mapping we equate probabilities, namely

$$p(\xi)d\xi = p(Z)dZ \tag{B.3.13}$$

where $\xi \in [-\infty : \infty]$ and $Z \in [a : b]$. The probability density functions are given by

$$p(\xi) = \frac{1}{\sqrt{2}\pi} \exp\left\{-\frac{\xi_\nu^2}{2}\right\} \tag{B.3.14}$$

$$p(Z) = \frac{1}{b-a} \tag{B.3.15}$$

Integrating yields:

$$\begin{aligned} \int_{-\infty}^{\xi} p(\xi)d\xi &= \int_a^Z p(Z)dZ \\ \frac{1}{2}\left[1 + \text{erf}\left(\frac{\xi}{\sqrt{2}}\right)\right] &= \frac{Z-a}{b-a} \\ \therefore Z &= \frac{1}{2}(a+b) + \frac{b-a}{2}\text{erf}\left(\frac{\xi}{\sqrt{2}}\right) \end{aligned} \tag{B.3.16}$$

where "erf" is the error function.

Now if we let

$$a = \overline{\Sigma_a}(1 - \sqrt{3}R) \quad , \quad b = \overline{\Sigma_a}(1 + \sqrt{3}R) \quad \text{and} \quad Z = \Sigma_a(\xi)$$

then we find

$$\Sigma_a(\xi) = \overline{\Sigma_a}\left[1 + \sqrt{3}R\ \text{erf}\left(\frac{\xi}{\sqrt{2}}\right)\right] \tag{B.3.17}$$

k_∞ is now written explicitly as

$$k_\infty(\xi_1, \xi_2) = \frac{\overline{\nu\Sigma}_f}{\overline{\Sigma_a}} \frac{1 + R\xi_1}{1 + \sqrt{3}R \text{ erf}\left(\frac{\xi_2}{\sqrt{2}}\right)} \tag{B.3.18}$$

and in a polynomial chaos expansion as

$$k_\infty(\xi_1, \xi_2) \approx \sum_{i+j=0}^{p} \alpha_{ij} H_i(\xi_1) H_j(\xi_2) \tag{B.3.19}$$

with the coefficients calculated using

$$\alpha_{ij} = \frac{1}{2\pi} \frac{1}{j!i!} \int_{-\infty}^{\infty} \int_{-\infty}^{\infty} k_\infty(\xi_1, \xi_2) H_i(\xi_1) H_j(\xi_2) e^{-(\xi_1^2 + \xi_2^2)/2} d\xi_1 d\xi_2 \tag{B.3.20}$$

In Fig.(B.2) the convergence of the variance using the Hermite-Hermite (HH) basis is plotted along-side results from Fig.(B.1) for the Hermite-Legendre (HL) basis. Here we can see that the convergence rate of the HH basis is considerably deteriorated when compared to the exponential convergence of the HL basis. From this simple example, the HL basis appears to be the optimal choice.

B.4. Discussion and Conclusions

In this note we have shown how a hybrid polynomial basis can be constructed to model problems involving input parameters which are described using different probability distributions. The optimal bases are chosen according to the probability density functions of the input parameters and a hybrid basis constructed through a tensor product. We have illustrated the use of this hybrid approach using a simple example and shown exponential rates of convergence. We also demonstrated the sub-optimal rates of con-

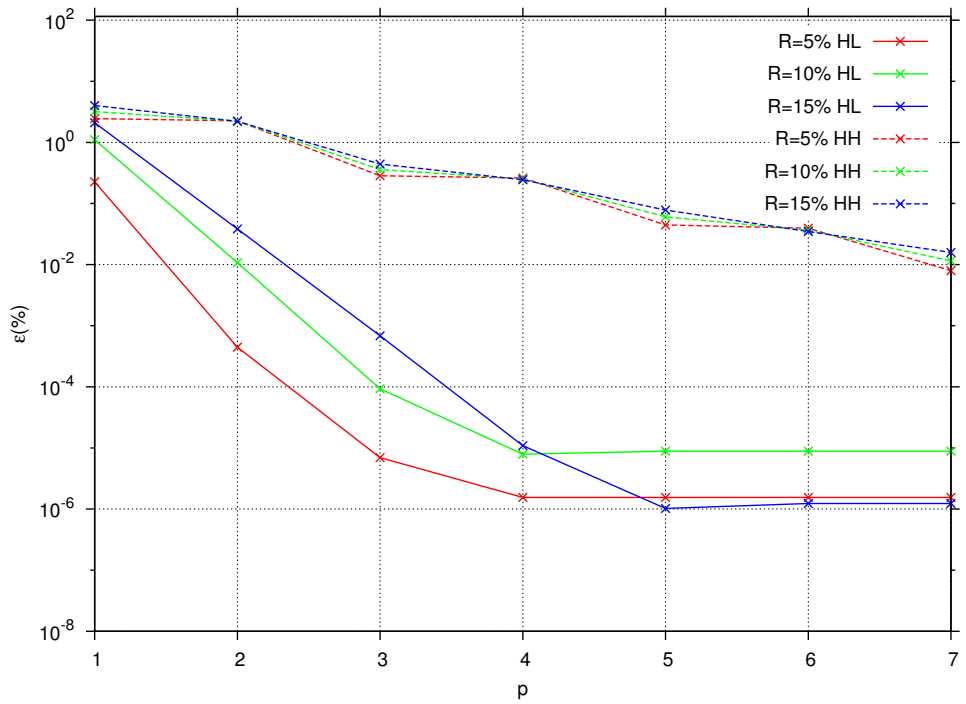


Figure B.2.: Convergence of the Hermite-Hermite and Hermite-Legendre expansions for relative uncertainties $R = 5\%, 10\%$ and 15%.

vergence when all probabilities are mapped to a common distribution and the same polynomials are used in the construction of the basis.

Appendix C

Integration of Functions with Associated Statistical Uncertainties

In this note we wish to asses the effect of using a statistically noisy set of integration points to project a model response on to a polynomial basis. As an illustrative example we have chosen an infinite, mono-energetic, multiplying system where an exact result for k_∞ is available:

$$k_\infty(\xi_\nu.\xi_c, \xi_c) = \frac{\nu(\xi_\nu)\Sigma_f(\xi_f)}{\Sigma_c(\xi_c) + \Sigma_f(\xi_f)} \tag{C.0.1}$$

In Eqn.(C.0.1) we have assumed that the fission cross section Σ_f, capture cross section Σ_c and average number of neutrons per fission ν are uncertain. The uncertainty is parametrised with the random variable ξ which, in-turn, is described using a Gaussian distribution. The nuclear data parameters, $\alpha = \{\nu, \Sigma_f, \Sigma_c\}$ may be written in terms of the relative uncertainty, R, as follows:

$$\alpha_i(\xi) = \overline{\alpha}_i(1 + R\xi_i) \tag{C.0.2}$$

In the first example we assume that only the fission cross section is uncertain, therefore: $\nu(\xi_\nu) = \overline{\nu}$ and $\Sigma_c(\xi_c) = \overline{\Sigma}_c$. The mean and variance of k_∞ due solely to the variation in the fission cross section has been calculated using quadrature and values for $R = 0.01$ and $R = 0.1$ are given in the table below.

R	Mean	Var
0.01	1.1333081447	$1.4276692150\times10^{-5}$
0.1	1.1307804641	$1.4799411850\times10^{-3}$

Table C.1.: Mean and variance in k_∞ of a homogeneous, mono-energetic problem due to uncertainty in the fission cross section.

As ξ_f, the variable describing the uncertainty in Σ_f, moves through its range of allowed values, a response is induced in the value of k_∞. The response of k_∞ to changes in ξ_f are plotted in Fig.(C.1) for $R = 0.01$ and $R = 0.1$. The response is also projected onto a set of polynomial chaos basis functions which are also plotted along side the response surface. Here we can see that as the order of the polynomial increases, the approximation converges to the actual response curve. The convergence is faster for $R = 0.01$ which is to be expected as there is less structure in the response, i.e. the response curve is ostensibly linear and is approximated accurately using a first order polynomial.

The projection of the k_∞ response on to the polynomial basis proceeds via an integration of the product of the response and the basis polynomial,

viz

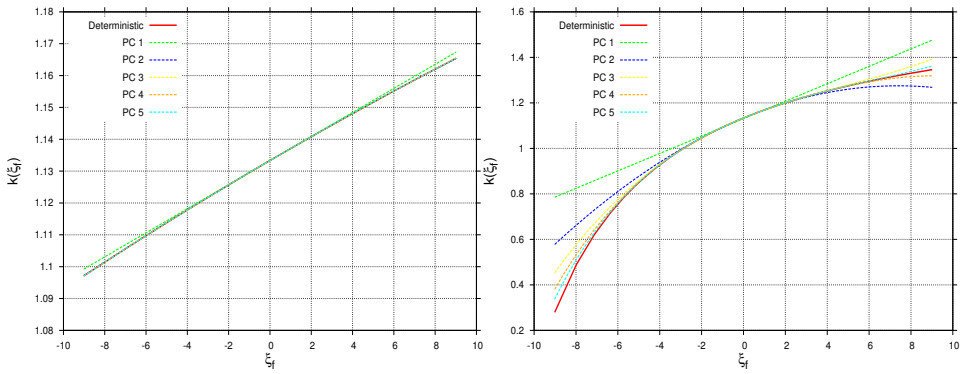
$$k_i = \frac{\int k_\infty(\xi_f)\Phi_i(\xi_f)}{N_i^2} \approx \frac{1}{N_i^2}\sum_{n=1}^{N_Q} w_n k_\infty(\xi_f^{(n)})\Phi(\xi_f^{(n)}) \tag{C.0.3}$$

The integration is performed using quadrature which is a weighted sum of function evaluations at a predetermined set of points. We now introduce an additional uncertainty into each of the evaluations as follows:

$$\begin{aligned} k_\infty(\xi_f^{(n)}, \eta_n) = k_\infty^{(n)}(\eta_n) &= \overline{k}_\infty^{(n)} + \sigma_n\eta_n \\ &= \frac{\overline{\nu}\Sigma_f(\xi_f^{(n)})}{\overline{\Sigma}_c + \Sigma_f(\xi_f^{(n)})} + \sigma_n\eta_n \end{aligned} \tag{C.0.4}$$

The uncertainty associated with each of the function evaluations is independent of one another. The magnitude of this variation is controlled via the standard deviation σ which scales the unit Gaussian variable η. The purpose of these extra variables is to provide an additional uncertainty onto the evaluations of the response surface.

To investigate the effect of uncertainty associated with each function evaluation, a polynomial expansion is computed for $R = 0.01$ and $R = 0.1$ for values of $\sigma = 1 \times 10^{-2}$ and $\sigma = 1 \times 10^{-3}$. The results are shown in Figs.(C.2) and (C.3). In Fig. (C.2a) the random response for $R = 0.01$ and $\sigma = 1 \times 10^{-2}$ is plotted. Here we can see that the size of the uncertainty in each of the function evaluations is relatively large compared to the variation in the response. Here the polynomial approximation is very oscillatory and poorly represents the deterministic response (Deterministic

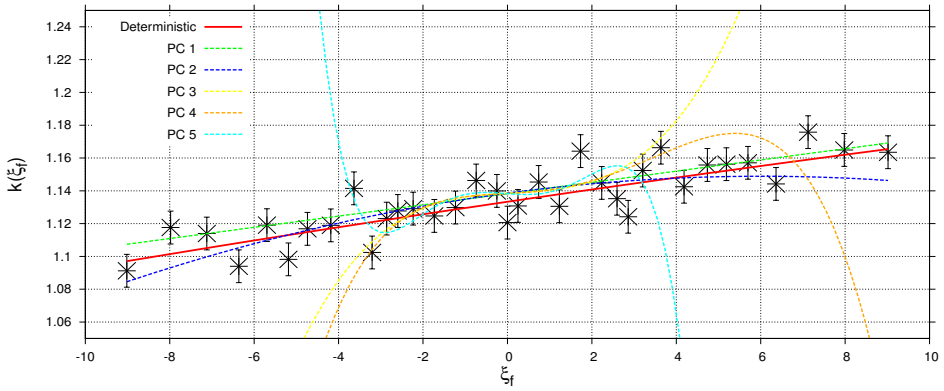


(a) $R = 0.01$ (b) $R = 0.1$

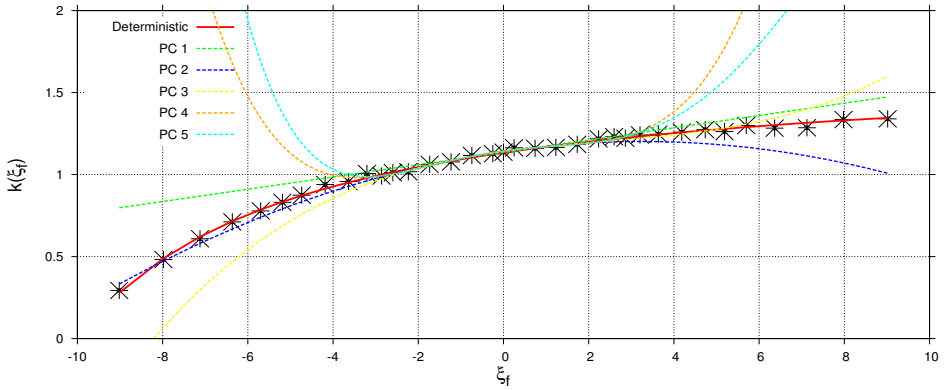
Figure C.1.: Polynomial approximation of a response surface using function evaluations with no statistical uncertainty.

in this sense corresponds to the situation where the function evaluations have no associated uncertainty). In Fig. (C.2b) the value of the relative uncertainty is increased to $R = 0.1$ and we can see that the magnitude of the data variation is a lot smaller relative to changes in the response. The polynomial representation also provides a much better approximation of the deterministic response, particularly in the region around the nominal value. However, the data is still oscillatory and the polynomial approximation rapidly diverges from the deterministic response at the extremes of the parameter space.

In Fig. (C.3a) the random response for $R = 0.01$ and $\sigma = 1 \times 10^{-3}$ is plotted. The variation of the data points is this time much smaller with respect to changes in the deterministic response when compared to the results in Fig.(C.2a). The polynomial approximation is reasonable around the nominal value but diverges quickly at the extremes of the parameter space. This is to be expected since the data is still visibly oscillatory around the deterministic response. In Fig. (C.3b) the relative uncertainty is increased



(a) $R = 0.01$, $\sigma = 1 \times 10^{-2}$

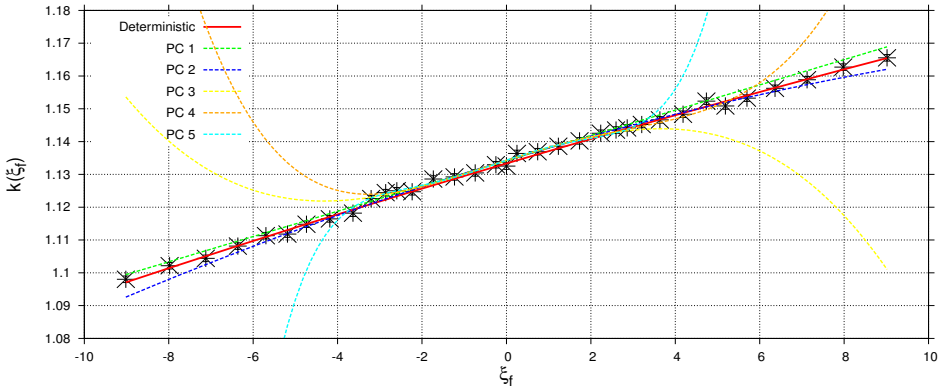


(b) $R = 0.1$, $\sigma = 1 \times 10^{-2}$

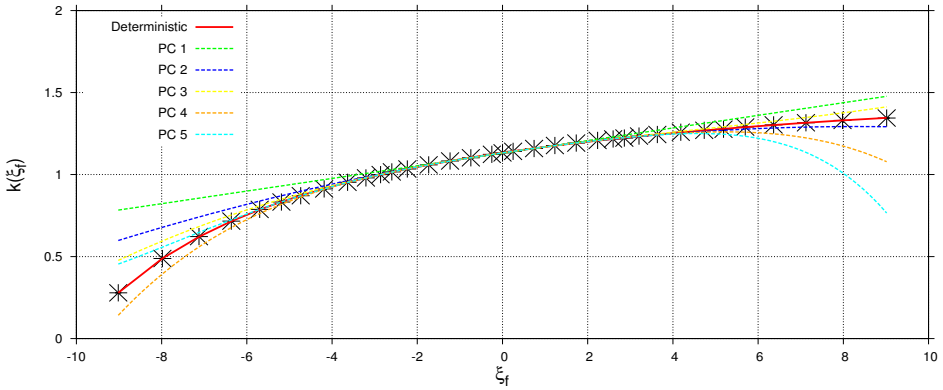
Figure C.2.: Polynomial chaos representation of a stochastic response surface with standard deviation $\sigma = 1 \times 10^{-2}$

to $R = 0.1$. In this situation the data is a much better representation of the deterministic response and, as such, the polynomial expansion provides a much better approximation. The expansion does start to diverge at the extremes of the parameter space for the higher order polynomials.

For the problems presented in Figs.(C.2) and (C.3), a Level 4 (35 points in 1 dimension) Genz-Keister quadrature rule was used to perform the integrations. To minimise the number of quadrature points, an adaptive procedure is available which automatically selects the quadrature points according to



(a) $R = 0.01$, $\sigma = 1 \times 10^{-3}$



(b) $R = 0.1$, $\sigma = 1 \times 10^{-3}$

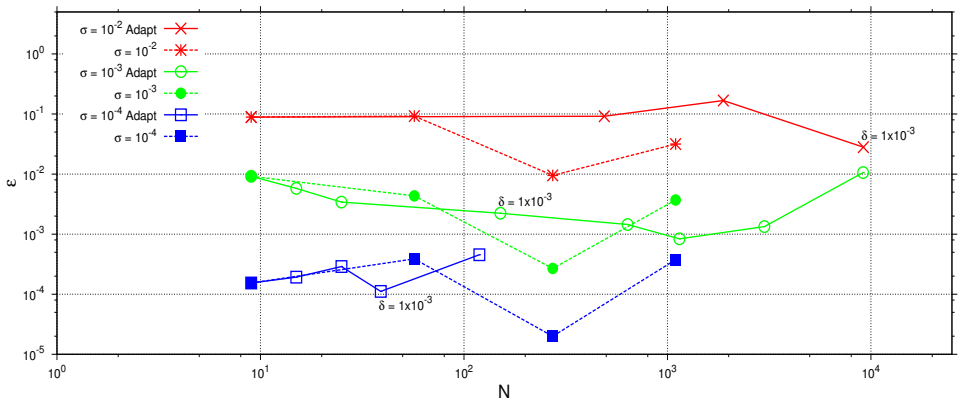
Figure C.3.: Polynomial chaos representation of a stochastic response surface with standard deviation $\sigma = 1 \times 10^{-3}$

a measure of the error in the calculated variance. We now wish to asses the feasibility of using the adaptive procedure for situations involving stochastic integration points. For the following examples we again use Eqn.(C.0.3) for k_∞ but with uncertainty also in the capture cross section and nu-bar. The resulting response surface for k_∞ is three dimensional. As a measure of how good the adaptive procedure is, the relative error is calculated in the parameter variance. The reference solution in this case is taken to be a level $L = 4$ quadrature of the response surface when the integration points

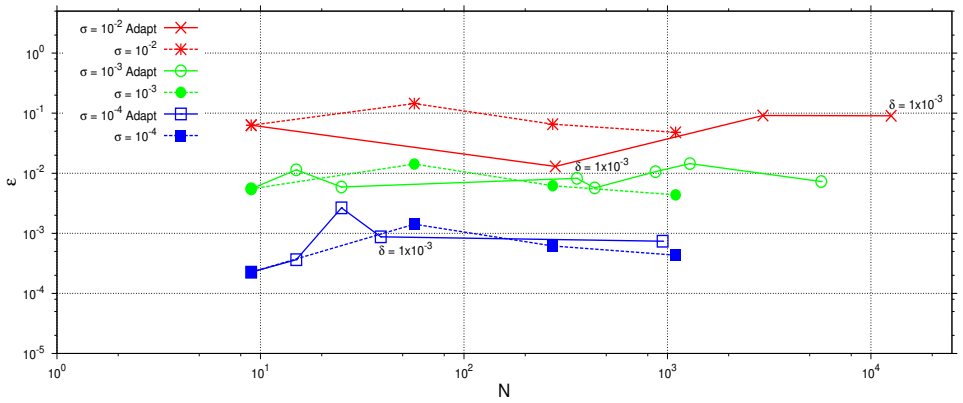
are completely deterministic. The error ϵ is given by the following

$$\epsilon = \frac{|V - V^{\mathrm{R}}|}{V^{\mathrm{R}}} \tag{C.0.5}$$

where V si the solution computed using the stochastic integration points and V^{R} is the reference solution.



(a) Seed = 123



(b) Seed = 32

Figure C.4.: Relative error in the parameter variance calculated using stochastic integration points.

In Fig.(C.4) the relative error is plotted versus the number of integration points N. Results have been calculated using standard deviations $\sigma = 10^{-2}$,

$\sigma = 10^{-3}$ and $\sigma = 10^{-4}$ for the quadrature points using two random number seeds. For both of the random seeds, the results show that the computed variance converges towards the reference value as the standard deviation decreases which is to be expected. There is also little difference between the results for the adaptive quadrature and the non-adaptive quadrature. For a given value of σ, the error does not appear to reduce appreciably as N is increased. For the adaptive quadrature the number of integration points is increased by decreasing the adaptive quadrature tolerance δ. In both figures (C.4a) and (C.4b), the data point corresponding to $\delta = 1 \times 10^{-3}$ is marked. For both values of the random number seed, as σ increases, the number of quadrature points increases and the accuracy of the integral decreases. In other words, the adaptive method become more inefficient as the uncertainty in the integration points increases. As σ increases, the magnitude of the random oscillations in the response surface increases. Because the quadrature scheme is based upon polynomials with a global support, it is unable to capture these local oscillations. The error measures calculated during the adaptive procedure will decrease slowly and non-monotonically, causing the adaptive procedure use an exhaustive number of integration points.